Gaussian Critical Line in Anisotropic Mixed Quantum Spin Chains

Der Fakultät für Physik und Geowissenschaften
der Universität Leipzig
genehmigte

DISSERTATION

zur Erlangung des akademischen Grades

doctor rerum naturalium
(Dr. rer. nat.)

vorgelegt

von Dipl.-Ing. Rainer Bischof
geboren am 02.06.1979 in Rottenmann (Österreich)

Gutachter: Prof. Dr. Wolfhard Janke
Prof. Dr. Matthias Vojta

Tag der Verleihung: 18.02.2013

"T'ing? Can be manyt'ing."
Byron, a Caribbean

For Heidi, Roan and Viggo.

Abstract

By numerical methods, two models of anisotropic mixed quantum spin chains, consisting of spins of two different sizes, $S^a = 1/2$ and $S^b = 1$ as well as $S^b = 3/2$, are studied with respect to their critical properties at quantum phase transitions in a selected region of parameter space. The quantum spin chains are made up of basecells of four spins, according to the structure $S^a - S^a - S^b - S^b$. They are described by the XXZ Hamiltonian, that extends the quantum Heisenberg model by a variable anisotropic exchange interaction. As additional control parameter, an alternating exchange constant between nearest-neighbour spins is introduced. Insight gained by complementary application of exact diagonalization and quantum Monte Carlo simulations, as well as appropriate methods of analysis, is embedded in the broad existing knowledge on homogeneous quantum spin chains. In anisotropic homogeneous quantum spin chains, there exist phase boundaries with continuously varying critical exponents, the *Gaussian critical lines*, along which, in addition to standard scaling relations, further extended scaling relations hold. Reweighting methods, also applied to improved quantum Monte Carlo estimators, and finite-size scaling analysis of simulation data deliver a wealth of numerical results confirming the existence of a Gaussian critical line also in the mixed spin models considered. Extrapolation of exact data offers, apart from confirmation of simulation data, furthermore, insight into the conformal operator content of the model with $S^b = 1$.

Kurzfassung

Mittels numerischer Methoden werden zwei Modelle anisotroper gemischter Quantenspinketten, bestehend aus Spins zweier unterschiedlicher Größen, $S^a = 1/2$ und $S^b = 1$ sowie $S^b = 3/2$, hinsichtlich ihrer kritischen Eigenschaften an Quanten-Phasenübergängen in einem ausgewählten Parameterbereich untersucht. Die Quantenspinketten sind aus Basiszellen zu vier Spins, gemäß der Struktur $S^a - S^a - S^b - S^b$, aufgebaut. Sie werden durch den XXZ Hamiltonoperator beschrieben, der das isotrope Quanten-Heisenberg Modell um eine variable anistrope Austauschwechselwirkung erweitert. Als zusätzlicher Kontrollparameter wird eine alterniernde Kopplungskonstante zwischen unmittelbar benachbarten Spins eingeführt. Die durch komplementäre Anwendung exakter Diagonalisierung und Quanten-Monte-Carlo Simulationen, sowie entsprechender Analyseverfahren, gewonnenen Erkenntnisse werden in das umfangreiche existierende Wissen über homogene Quantenspinketten eingebettet. Im Speziellen treten in anisotropen homogenen Quantenspinketten Phasengrenzen mit kontinuierlich variierenden kritischen Exponenten auf, die *Gaußschen kritischen Linien*, auf denen neben den herkömmlichen auch erweiterte Skalenrelationen Gültigkeit besitzen. Umgewichtungsmethoden, speziell auch angewandt auf verbesserte Quanten-Monte-Carlo Schätzer, und Endlichkeitsskalenanalyse von Simulationsdaten liefern eine Fülle von numerischen Ergebnissen, die das Auftreten der Gaußschen kritischen Linie auch in den untersuchten gemischten Quantenspinketten bestätigen. Die Extrapolation exakter Daten bietet, neben der Bestätigung der Simulationsdaten, darüber hinaus Einblick in einen Teil des konformen Operatorinhalts des Modells mit $S^b = 1$.

Acknowledgement

My ex-girlfriend suffered the most under my fascination for the world of quantum spins that caused an endless amalgamation of me and textbooks, or me and… *the computer*.

To marry Heidi and make her two formidable boys was, hopefully, the best I could do to ease here pain. Thank you, Heidi!

Of all my fellow students and researchers in Leipzig, who I very much appreciate for the good atmosphere of collegiality, I want to particularly thank Elmar Bittner and Andreas Nußbaumer, as well as their successors in duty, Martin Marenz, Hannes Nagel and Johannes Zierenberg, for keeping the vital computer structure going.

Je remercie profondément les collègues de la Groupe Physique Statistique de Nancy et mes colocs dans la rue de Metz à Nancy. I am especially grateful for Malte Henkel's interest in and support of my work, particularly concerning matters of conformal invariance at critical phenomena. The time in Nancy has always been extraordinarily motivating, inspiring and rewarding. I thank the Deutsch-Französische Hochschule (DFH-UFA) whose funding made that intercultural experience possible.

I thank Stefan Wessel for the hint of where to find a wealth of information on the spin-$\frac{1}{2}$ chain at an early stage of this work, and Andreas Läuchli who put my attention onto the Gaussian model at a late stage of this work that finally turned out to be intermediate. I gratefully acknowledge helpful communication with Jesus Salas, Ralph Kenna and Lev Shchur on the matter of logarithmic corrections. Discussions on crosscorrelations with Martin Weigel also proved fruitful. Thankfully, I appreciate stimulating conversation with Robert Swendsen.

Many thanks go to all my friends in Leipzig and elsewhere, e.g. Peter Jessner, but particularly to Philipp Buchholtz, who guided me the way to Marc Zlotowski (Kompetenzschule ELSYS), Viola Gründemann (Research Academy Leipzig), and Dr. Sabine Kaiser, who granted me invaluable support in a critical situation at the end of this work.

A very important thanks goes to the Rektorat of the University of Leipzig, who funded my work for three years by the Doktorandenförderplatz 00056. This funding was succeded by a three months grant of the Freistaat Sachsen, which is also gratefully acknowledged.

I thank the secretaries of the Institute of Theoretical Physics, Susan Hussack, Gabriele Menge and Lea Voigt, for their ever friendly and competent support, which I enjoyed as much as I appreciated.

Last, but not least I am indebted and grateful to my supervisor Wolfhard Janke, who throughout the years supported my fascination and interest with money, patience, faith and precise advice on all matters of statistical physics.

Contents

1 Introduction 1

2 Materials 7

I Theory and Methods 11

3 Relation Between Quantum and Classical Systems or (1+1)=2 13
- 3.1 Quantum–Classical Mapping 13
- 3.2 The Vertex Model 15
- 3.3 Correlations 17

4 Critical Exponents and Scaling Dimensions 19
- 4.1 Critical Exponents at Second-Order Critical Points 19
- 4.2 Renormalization Group: Idea and Eigenvalues 22
- 4.3 Conformal Invariance and Scaling Dimensions 26

5 XXZ Spin Chains 31
- 5.1 Mixed Spin Models: MA and MB 32
- 5.2 Valence Bonds and Surfaces of Solids 33
- 5.3 Phase Diagrams and Critical Exponents 36
- 5.4 Hidden Symmetry and String Observables 40
- 5.5 Gaussian Description and the Fundamental Scaling Dimension 48
- 5.6 Logarithmic Corrections at the Isotropic Point 52

6 Computational Methods 57
- 6.1 Exact Diagonalization and Extrapolation 58
  - 6.1.1 Exploiting Symmetries 58
  - 6.1.2 Lanczos Tridiagonalization 60
  - 6.1.3 BST Extrapolation 63
  - 6.1.4 Test Application 64
- 6.2 Loop Algorithm 67
  - 6.2.1 Setup: Configurations are Paths 68
  - 6.2.2 Update: Breakups and Loops 72
  - 6.2.3 $S \geq 1$: Subspins and Projectors 80
  - 6.2.4 Measurement: Estimators and Errors 81
- 6.3 Reweighting 87
- 6.4 Finite-Size Scaling 96

II Results and Discussion 103

7 Phase Boundary 105
7.1 Extrapolation of Exact Data 105
7.1.1 MA with basecell $\frac{1}{2}-\frac{1}{2}-1-1$ 106
7.1.2 MB with basecell $\frac{1}{2}-\frac{1}{2}-\frac{3}{2}-\frac{3}{2}$ 110
7.2 Finite-Size Scaling of Quantum Monte Carlo Data 112
7.3 Summary 121

8 Critical Exponents 123
8.1 γ/ν 125
8.2 $1/\nu$ 132
8.3 α/ν 145
8.4 β_z/ν 150
8.5 β_x/ν 159
8.6 x_λ 163
8.7 Matching Universality Classes 166
8.8 Summary 167

9 Gaussian Parameters and Central Charge 169

10 Finite-Size Spectra 175

11 Corrections to Finite-Size Scaling 185
11.1 Power-Law Corrections 185
11.2 Logarithmic Corrections 187

12 Summary, Conclusion and Outlook 197

III Appendix 203

A Plots 205
A.1 Quality of Reweighted Datasets 205

B Numbers 219
B.1 Finite-Size Scaling of the Location of Pseudocritical Points 219
B.2 Finite-Size Scaling of the Values at (Pseudo)Critical Points 224

C Some further points on the string observable D_z 231

List of Figures

3.1 Checkerboard representation of the spin-$\frac{1}{2}$ chain. 16

5.1 VBS configurations of homogeneous and mixed spin chains. 34
5.2 Examples of spin configurations. 34
5.3 "Haldane" phase in spin-$\frac{1}{2}$ dimers. 35
5.4 Phase diagrams of homogeneous spin chains. 37
5.5 Snapshots of the staggered magnetization of the spin-$\frac{1}{2}$ chain. 38
5.6 Exact critical exponents of the spin-$\frac{1}{2}$ chain. 39
5.7 Symmetry group D_4. 41

6.1 BST extrapolation depends on the choice of the free parameter ω. . . 65
6.2 Typical configuration in the loop algorithm. 68
6.3 Local approach to the loop algorithm. 73
6.4 Graphical representation of infinitesimal plaquettes. 76
6.5 Loops at work. 78
6.6 Subspin representation of $S \geq 1$. 81
6.7 Histograms, $S = 1/2$, excellent quality. 93
6.8 Histograms, MA, bad quality. 93
6.9 Reweighted data of the spin-$\frac{1}{2}$ chain at $\Delta = 1.0$, $L = 128$ and $\beta = 384$. 94
6.10 Reweighted data of MB at $\Delta = 0.0$, $L = 128$ and $\beta = 768$. 95
6.11 Irrelevant RG eigenvalues of the spin-$\frac{1}{2}$ chain. 100
6.12 Logarithmic corrections, the ratio $f_{\mathrm{a}}^{(3)}/f_{\mathrm{c}}^{(3)}$. 101

7.1 MA, extrapolation of exact data. 107
7.2 MB, extrapolation of exact data. 111
7.3 MA, pseudocritical points obtained from the twist parameter. 113
7.4 MB, pseudocritical points obtained from the twist parameter. 114
7.5 Comparing final estimates of critical points from ED and QMC. 117
7.6 Effective shift exponents. 118
7.7 Comparing the shift of pseudocritical points. 119
7.8 Shift of the susceptibility's maxima. 120
7.9 Phase boundaries of MA and MB, final result. 122

8.1 Susceptibility χ, finite-size growth of maxima. 126
8.2 χ, FSS analysis, $\Delta = 1$. 126
8.3 MA, χ, FSS analysis, $\Delta < 1$. 127
8.4 MB, χ, FSS analysis, $\Delta < 1$. 128
8.5 χ, background and amplitude. 129
8.6 γ/ν, final result. 131

8.7 MA, log-derivative of $|D_z|$, FSS analysis. 134
8.8 MA, log-derivative of D_x^2, FSS analysis. 135
8.9 MB, log-derivative of $|D_z|$, FSS analysis. 136
8.10 MB, log-derivative of D_x^2, FSS analysis. 137
8.11 Log-derivative D_z, background and amplitude. 138
8.12 $1/\nu$, $\Delta = 1$ 139
8.13 MA, $1/\nu$, $\Delta < 1$ 140
8.14 MB, $1/\nu$, $\Delta < 1$ 141
8.15 Correlation coefficients of different estimates of $1/\nu$. 142
8.16 $1/\nu$, final result. 144
8.17 MA, c_λ, FSS analysis. 146
8.18 MB, c_λ, FSS analysis. 147
8.19 α/ν, final result. 149
8.20 MA, D_z, FSS analysis. 152
8.21 MB, D_z^4, FSS analysis. 153
8.22 Effective correction exponent ω of D_z. 154
8.23 MA, asymmetric distribution of D_z. 156
8.24 β_z/ν, final result. 158
8.25 Finite-size dependence of D_x. 160
8.26 β_x/ν, FSS analysis. 161
8.27 β_x/ν, final result. 162
8.28 Fundamental scaling dimension x_λ, final result. 164
8.29 Matching universality classes. 167

9.1 Direct estimate of the Gaussian coupling $K = x_\lambda$. 171
9.2 Direct estimate of the Gaussian velocity v. 173

10.1 MA, $L = 20$, $\Delta = 0.3$, exact finite-size spectrum. 181
10.2 MA, $L = 20$, $\Delta = 1.0$, exact finite-size spectrum. 182
10.3 MA, Δ-dependence of extrapolated energy levels. 183
10.4 MA, selected exact finite-size energy levels. 184
10.5 MA, the central charge c, from extrapolation. 184

11.1 Visible sub-leading corrections in ξ/L. 186
11.2 Slow convergence of χ and ξ at $\Delta = 1$. 188
11.3 Asymptotic linearity of logarithmic corrections. 190
11.4 $S = 1/2$, susceptibility χ. 192

12.1 Main result: Critical exponent ratios versus effective Δ. 199

A.1 Reweighted data of MA at $\Delta = 1$, $L = 36$ and $\beta = 108$. 206
A.2 Reweighted data of MA at $\Delta = 0.2$, $L = 36$ and $\beta = 144$. 207
A.3 Reweighted data of MA at $\Delta = 0.0$, $L = 36$ and $\beta = 180$. 208
A.4 Reweighted data of MA at $\Delta = 1.0$, $L = 384$ and $\beta = 1152$. 209
A.5 Reweighted data of MA at $\Delta = 0.2$, $L = 384$ and $\beta = 1536$. 210
A.6 Reweighted data of MA at $\Delta = 0.0$, $L = 384$ and $\beta = 1920$. 211
A.7 Reweighted data of MB at $\Delta = 1.0$, $L = 32$ and $\beta = 96$. 212

A.8 Reweighted data of MB at $\Delta = 0.4$, $L = 32$ and $\beta = 128$. 213
A.9 Reweighted data of MB at $\Delta = 0.0$, $L = 32$ and $\beta = 192$. 214
A.10 Reweighted data of MB at $\Delta = 1.0$, $L = 256$ and $\beta = 768$. 215
A.11 Reweighted data of MB at $\Delta = 0.4$, $L = 256$ and $\beta = 1024$. 216
A.12 Reweighted data of MB at $\Delta = 0.0$, $L = 256$ and $\beta = 1536$. 217

C.1 β_z/ν, FSS analysis, dependence on the estimate of λ_c. 231
C.2 Effective background of D_z and its moments. 232
C.3 MA, D_z, FSS analysis. 233
C.4 Illustration of the quotients method. 234
C.5 MA, β_z/ν, result from quotients method. 235
C.6 MB, β_z/ν, result from quotients method. 236
C.7 Estimate of the expectation value $\langle D_{z,L} \rangle$. 238

List of Tables

2.1 Ions and the spin S. 7

3.1 Plaquettes and vertices. 17

5.1 Operator transformation under mapping $\mathrm{H}^{\mathrm{qAT}} \rightarrow \mathrm{H}^{\mathrm{XXZ}}$. 43
5.2 Coefficients of RG equations for the spin-$\frac{1}{2}$ Heisenberg chain. 53
5.3 Logarithmic exponents. 56

6.1 Number representation of the basis states. 59
6.2 Dimensions of symmetry-sectors. 60
6.3 BST extrapolants, $S = 1/2$, $\Delta = 0.5$. 66
6.4 Selected results of BST extrapolation, $S = 1/2$. 66

7.1 Extrapolation table of MA at $\Delta = 0.7$. 106
7.2 Selected extrapolation results of MA. 109
7.3 Selected extrapolation results of MB. 111
7.4 MA, extrapolation of exact data, $\lambda_{\mathrm{c}}(\Delta)$. 115
7.5 MB, extrapolation of exact data, $\lambda_{\mathrm{c}}(\Delta)$. 116
7.6 Final estimates of the phase boundaries $\lambda_{\mathrm{c}}(\Delta)$, from ED and QMC. . 117

8.1 γ/ν, final result. 130
8.2 Susceptibility χ, effective correction exponent ω. 131
8.3 MA, $\Delta = 1$, correlation coefficients of different estimates of $1/\nu$. 142
8.4 $1/\nu$, final result. 144
8.5 MA, logarithmic divergence of the specific heat at $\Delta = 0.4$. 148
8.6 MB, logarithmic divergence of the specific heat at $\Delta = 0.6$. 148
8.7 α/ν, final result. 149
8.8 β_z/ν, final result. 159
8.9 β_x/ν, final result. 162
8.10 MA, final comparison of x_λ. 165
8.11 MB, final comparison of x_λ. 165

9.1 Gaussian parameters K and v, and central charge c. 174

10.1 MA, selected values of extrapolated scaling dimensions. 179

11.1 Hatted exponents of logarithms. 191
11.2 Various fits of the susceptibility of the spin-$\frac{1}{2}$ chain. 193
11.3 Fitting logarithmic corrections with an effective version of $\mathcal{Z}$. 194
11.4 Fits of ξ to various (effective) forms of logarithmic corrections. 194

B.1 MA, FSS fit, zeros of the twist parameter. 220
B.2 MA, FSS fit, crossing points of the twist parameter. 220
B.3 MA, Polynomial fit, zeros of the twist parameter. 220
B.4 MA, FSS fit, maxima of ξ. 221
B.5 MA, FSS fit, maxima of χ. 221
B.6 MB, FSS fit, zeros of the twist parameter. 221
B.7 MB, FSS fit, crossing points of the twist parameter. 222
B.8 MB, Polynomial fit, zeros of the twist parameter. 222
B.9 MB, FSS fit, maxima of ξ. 222
B.10 MB, FSS fit, maxima of χ. 223
B.11 Comparing final and preliminary estimates of $\lambda_c(\Delta)$. 223
B.12 MA, γ/ν, double-log linear fits. 225
B.13 MA, individual estimates of $1/\nu$. 225
B.14 MA, α/ν, power-law fits. 225
B.15 MA, β_z/ν, FSS fits with additive L^{-1}-correction. 226
B.16 MA, β_z/ν, double-log linear fits. 226
B.17 MA, β_z/ν, quotients method. 226
B.18 MA, β_x/ν, double-log linear fits. 227
B.19 MB, γ/ν, double-log linear fits. 227
B.20 MB, individual estimates of $1/\nu$. 227
B.21 MB, α/ν, power-law fits. 228
B.22 MB, β_z/ν, FSS fits with additive L^{-1}-correction. 228
B.23 MB, β_z/ν, double-log linear fits. 229
B.24 MB, β_z/ν, quotients method. 229
B.25 MB, β_x/ν, double-log linear fits. 229

1 Introduction

A fundament to many theoretical and numerical approaches to quantum spin systems was laid in 1928 by W. Heisenberg who, during his professorship in Leipzig, presented a microscopic model to describe macroscopic properties of magnetic materials [1, 2]. The orbital overlap of localized electrons produces correlation of their magnetic moments. Heisenberg's ideas were later reformulated in terms of a spin Hamiltonian, which is now known as the *Heisenberg model* [see 2, pg. 509ff, and references therein].

A first climax in the long-standing history of interest in one-dimensional, and more generally low-dimensional, quantum magnets has been reached by Haldane's famous conjecture for isotropic and uniformly coupled, antiferromagnetic (AF) spin chains. With all spins of the same size and integer-valued, the groundstate is separated from the lowest lying excitations by an energy gap [3]. This has been verified experimentally [4] and numerically [5] soon after its formulation. Modern approaches, such as the application of quantum field theory to problems of condensed matter physics [6], and bosonization [7], that is particularly powerful in the world of one dimension [8], have pushed the limits of understanding considerably.

The interest in AF quantum spin chains and various generalizations of Heisenberg's model has strongly influenced the refinement of numerical methods. It is intimately linked to the development of new quantum Monte Carlo algorithms, such as the loop algorithm [9, 10], which is a main method of data production in this thesis, or algorithms based on the stochastic series expansion (SSE) [11], or conceptually new methods like the density matrix renormalization group (DMRG) algorithm [5].

The ability to control microscopic properties in the synthetization of new magnetic materials has considerably improved in the recent years, thus the number of compounds exhibiting quasi one-dimensional spin structures has grown significantly (see Sect. 2). Consequently, the study of quantum spin chains and other low-dimensional structures in experiments remains a highly active field of research [12–15], in addition to ongoing theoretical [16–19] and numerical [20–23] efforts.

One of the most intriguing phenomena studied in quantum spin chains is quantum criticality [24]. Quantum critical points occur at zero temperature. Usually, they mark the boundary between different quantum phases. Various quantum phase transitions may occur in quantum spin chains, most of them being of second order. As a consequence, quantum spin chains serve as fruitful ground that critical phenomena, and the underlying concepts of scaling and universality, can be observed and studied on [25, 26]. In addition to the fundamental significance as quantum magnets that may or may not set the stage for quantum critical phenomena, low-dimensional quantum spin systems enter various fields of modern research. Below is a list, far from being complete, of examples:

- High-temperature superconductors [27], based on doped cuprates, have been found to be quasi 2D spin-$\frac{1}{2}$ quantum antiferromagnets at small doping [28]. The quasi-1D spin-ladder material $\mathrm{SrCu_2O_3}$ exhibits superconductivity when doped with either holes or electrons [29].
- Structural chemistry and magnetic design aim at the controlled synthetization of materials with designated magnetic properties, such as molecular magnets and single chain magnets (spin chains) for use in various applications, such as spintronics or quantum computation (see Sect. 2).
- Complementary to magnetic design, recent progress in filling carbon-nanotubes with spin-carrying heterofullerenes [30] offers promising perspectives to spin-engineering and spintronics (see Sect. 2).
- Many molecular machines, such as a recently discovered magnetic switch [31], have fascinating spin-nanostructures.
- Quantum computation needs the realization of stable qubits. Spins or antiferromagnetically coupled mixed-spin dimers are considered good candidates [32, 33].
- Entanglement close to quantum phase transitions [34], and, generally, quantities that measure the degree of entanglement in a quantum system, in particular entanglement entropy, have raised considerable and increasing interest in the recent years [16]. Highly entangled groundstates of antiferromagnetic or XY-like quantum spin systems provide an ideal ground for testing and developing theories.
- Bose–Einstein condensation of magnons [35, 36].
- etc.

The XXZ Hamiltonian. The nearest-neighbour Heisenberg Hamiltonian in its simplest form is a spin Hamiltonian with a three-component two-spin interaction

$$\mathrm{H} = J \sum_{\langle i,j \rangle} \vec{\mathrm{S}}_i \vec{\mathrm{S}}_j = J \sum_{\langle i,j \rangle} \mathrm{S}_i^x\,\mathrm{S}_j^x + \mathrm{S}_i^y\,\mathrm{S}_j^y + \mathrm{S}_i^z\,\mathrm{S}_j^z\,, \tag{1.1}$$

where $\langle i,j \rangle$ indicates the summation over nearest-neighbour pairs of sites. If the coupling constant J is positive the interaction is antiferromagnetic, while for J negative it is ferromagnetic. The operators S_i^γ are the three components of the spin vector operator $\vec{\mathrm{S}}_i$, the square of which has the eigenvalue $S_i(S_i+1)$, with S_i the size of the spin at site i. In a matrix representation in which S^z is diagonal, the matrix elements of raising and lowering operators of any spin size, $\mathrm{S}^\pm = \mathrm{S}^x \pm \mathrm{i}\mathrm{S}^y$, can be calculated by (with $\hbar = 1$)

$$\left\langle S, m' \right| \mathrm{S}^\pm |S, m\rangle = \delta_{m',m\pm1} \sqrt{S(S+1) - m(m\pm1)}\,, \tag{1.2}$$

where $m = -S, -S+1, \ldots, S$, is the eigenvalue of the z-operator. The action of raising and lowering operators is to generate a state with S^z-eigenvalue raised, respectively lowered by 1, which is compactly expressed by the commutator

$$\left[\mathrm{S}^z, \mathrm{S}^\pm\right] = \pm \mathrm{S}^\pm\,. \tag{1.3}$$

This commutator embodies the reason why, despite the appealingly simple formulation (1.1), the Heisenberg Hamiltonian encapsulates many intriguing and fundamental aspects that make the quantum world special and unintuitive. As the size of the spin itself, the orientation is *quantized*. In a general eigenstate of a quantum spin Hamiltonian the state of an individual spin may be a *superposition* of more than one or even all possible orientations. Depending on the degree of *entanglement*, the measurement on a single spin (or an arbitrary part of the system) restricts or completely determines the possible outcome of measurements on other spins.

This work is focused on the one-dimensional Heisenberg model with XXZ *exchange anisotropy* and *bond alternation*, modelled by the spin chain Hamiltonian

$$\begin{aligned} \mathrm{H} = \sum_{i \text{ even}} & \big(J_{xy}\big(\,\mathrm{S}_i^x\,\mathrm{S}_{i+1}^x + \mathrm{S}_i^y\,\mathrm{S}_{i+1}^y\,\big) + J_z\,\mathrm{S}_i^z\,\mathrm{S}_{i+1}^z\,\big) \\ + \sum_{i \text{ odd}} & \big(J'_{xy}\big(\,\mathrm{S}_i^x\,\mathrm{S}_{i+1}^x + \mathrm{S}_i^y\,\mathrm{S}_{i+1}^y\,\big) + J'_z\,\mathrm{S}_i^z\,\mathrm{S}_{i+1}^z\,\big)\,. \end{aligned} \tag{1.4}$$

The set of couplings will be parameterized by two dimensionless control parameters, λ and Δ, such that

$$\Delta = \frac{J_z}{J_{xy}} = \frac{J'_z}{J'_{xy}}\,, \quad \lambda = \frac{J'_{xy}}{J_{xy}} = \frac{J'_z}{J_z}\,. \tag{1.5}$$

The XXZ exchange anisotropy is controlled by Δ. One set of bonds (from even to odd sites here) is set to $J_{xy} = 1$ and $J_z = \Delta$, while the other is set to $J'_{xy} = \lambda$ and $J'_z = \Delta\lambda$. We shall distinguish between the two types of bonds by calling them *unit-bonds* and λ-*bonds*, respectively. Using this parameterization, the XXZ Hamiltonian can be written

$$\mathrm{H}^{\mathrm{XXZ}}(\lambda, \Delta) = \sum_i \frac{1 + \lambda + (-1)^i(1-\lambda)}{2}\big(\,\mathrm{S}_i^x\,\mathrm{S}_{i+1}^x + \mathrm{S}_i^y\,\mathrm{S}_{i+1}^y + \Delta\,\mathrm{S}_i^z\,\mathrm{S}_{i+1}^z\,\big)\,. \tag{1.6}$$

With yet unspecified spin operators, this is the fundamental Hamiltonian of this thesis.

Mixed spin chains. Generally, the size of the spin can be different at every site. Marshall's theorems [37, 38], which also apply to anisotropic and mixed spin models [39, 40], imply that the minimal combination of at most two different kinds of spin S^a and S^b that has a singlet groundstate is constructed from a basecell of four spins with spins of equal size arranged in pairs,

$$-S^a - S^a - S^b - S^b-\,. \tag{1.7}$$

The simply alternating pattern $-S^a - S^b-$, with a basecell of two sites results in a ferrimagnet. This type shall not be considered here. In this thesis, the critical properties of two minimal versions of pattern (1.7) are studied numerically,

model A (MA): $(S^a, S^b) = (1/2, 1)$, with basecell $-\frac{1}{2} - \frac{1}{2} - 1 - 1-$,
and model B (MB): $(S^a, S^b) = (1/2, 3/2)$, with basecell $-\frac{1}{2} - \frac{1}{2} - \frac{3}{2} - \frac{3}{2}-$.

In the course of this work we have become used to the labels "MA" and "MB", these acronyms shall be used most frequently in this thesis. To the uniform case – all spins are of the same size S – we shall refer to as spin-S XXZ chain, or simply spin-S chain.

MA and MB at the isotropic point $\Delta = 1$ have been studied theoretically by mapping on the non-linear σ-model [41–44], establishing the picture that there are transitions between phases that can be described by different valence bond configurations [45–47]. By means of quantum Monte Carlo simulations of MA at $\Delta = 1$, critical values of bond alternation have been determined in [48] ($\lambda_{\mathrm{c}} = 0.77(1)$), and in [49] ($\lambda_{\mathrm{c}} = 0.762(1)$) along with the critical bond alternation of a mixed spin model with $(S^a, S^b) = (1, 3/2)$ (showing two transitions at $\lambda_{\mathrm{c}} = 0.479(1)$ and $1.318(1)$).[1] The critical values thus obtained differ from the theoretic predictions [43, 44]. The groundstate entanglement entropy of MA has been studied numerically in [52]. An unpublished estimate of the critical bond alternation of MB is $\lambda_{\mathrm{c}} = 0.621(1)$,[2] which has been confirmed numerically in [50]. Apart from that, MB has never been examined numerically in the literature. Numerical values of thermodynamic critical exponents or the effect of exchange anisotropy in mixed spin chains have, to the best of the author's knowledge, never been presented. It is the purpose of this thesis to fill these gaps.

Outline, methods and news. This thesis is organized as follows. In Sect. 2, a quick survey of materials related to the topics of this work will be given. The important relation between quantum models and classical models with an extra dimension will be motivated in Sect. 3. In that context, Sect. 3 serves to introduce a special case of the vertex model, on which exact knowledge of critical properties of the spin-$\frac{1}{2}$ chain, as well as the derivation of the quantum Monte Carlo method used in this is thesis, are based. Second-order critical points and the essential quantities to characterize them, i.e. critical exponents, will be discussed in Sect. 4 from various points of view. The purpose of Sect. 5 is to lay the theoretical background in which the results of our simulations will be interpreted. Even though being spelled out to large parts in terms of the spin-$\frac{1}{2}$ XXZ chain with occasional hints on the spin-1 chain, it is a basic assumption of this work that the matters discussed apply qualitatively to mixed spin chains also. In particular, the novel definition of a non-local string observable that is similar to known string observables of the homogeneous chains, but applicable to mixed spin chains, will be presented in Sect. 5.4, while Sect. 5.5 on the Gaussian model will state the main hypothesis of this thesis.

The methods of data production in this thesis, are exact diagonalization (ED) by the Lanczos algorithm [53] and quantum Monte Carlo (QMC) using the loop algorithm [9, 10] in continuous time path integral representation [54, 55]. Both will be presented in Sect. 6, along with the corresponding methods of data analysis, extrapolation [25] and finite-size scaling (FSS) [56, 57], respectively. Originally, the loop algorithm has been the primary method of choice, for flexibility in prospect of future projects involving more general basecell setups and, in particular, randomly disordered mixed spin chains, while ED has been implemented to produce test data. *A posteriori*, however, it turned out that for MA (but not MB), final ED results are of comparative

---

[1] These estimates of λ_{c} at the isotropic point have been confirmed numerically by the author of this thesis and co-workers [50, 51].

[2] Z. Xu (2005), private communication.

and competitive accuracy, which is why in that case the power of ED and extrapolation appears equivalent or, taking into account the considerably less computation time consumed, even superior. This is because, generally, applied to one-dimensional quantum spin chains, ED is particularly powerful due to the implications of conformal invariance in two (effective) dimensions [25]. However, the efficiency and applicability of the ED approach crucially depends on the presence of symmetries, in order to manage the fast growing Hilbert space when the chain length is increased. Size limitations are not as severe in (quantum) Monte Carlo methods but data is statistical. The loop algorithm offers easy access to off-diagonal observables via improved estimators [10], and due to the subspin representation, the generalization to higher spins ($S \geq 1$) [58] and mixed basecells thereof is straightforward. To locate pseudocritical points which are fed into the FSS analysis, we apply reweighting methods [59, 60] the application of which to data obtained from QMC simulations was described in [61]. We are not aware of any published literature that reports the specific application of reweighting to data obtained from the loop algorithm in path integral representation. We, furthermore, successfully generalized and applied for the first time the method to improved estimators. This will be discussed in Sect. 6.3.

Finally, but most importantly, Sects. 7–12 contain the results of our analysis, and a discussion thereof: the phase boundary (Sect. 7), critical exponents (Sect. 8), and Gaussian parameters (Sect. 9) of mixed spin models MA and MB, as well as the extrapolation of exact finite-size spectra of MA (Sect. 10) and a devoted consideration of corrections to the leading finite-size scaling behaviour (Sect. 11), which will also be discussed along Sects. 7 and 8. The results part is backed up by a variety of numbers and plots put into the appendix.

2 Materials

In real materials, localized spins are delivered by outer-shell *d*-electrons of transition metal ions (Sc-Zn) or *f*-electrons of rare earth ions (La-Lu). According to Hund's rules, in the groundstate electrons populate orbitals such that the total spin and total angular momentum are maximized [62, 63]. Most common examples are Cu^{2+} and Ni^{2+} that deliver $S = 1/2$ and $S = 1$, respectively. Exceptions to Hund's rules are, e.g., the ions Fe^{2+}-ion and Fe^{3+}-ion, with a close to half-filled outer *d*-shell, where, depending on the crystal field, spins can combine into a high-spin (hs) or low-spin (ls) configuration [62, 63]. A small selection of ions that occur more or less frequently in experimental reports are listed in Table 2.1. A special case of spin carriers are radicals, that may be organic and host a single unpaired electron giving $S = 1/2$ [64].

Table 2.1: Ions and the spin S.

ion	S
Zn^{2+}, Mg^{2+}, Fe^{2+}(ls)	0
Cu^{2+}, Co^{2+}, Fe^{3+}(ls)	$\frac{1}{2}$
Ni^{2+}, V^{3+}	1
Cr^{3+}, V^{2+}	$\frac{3}{2}$
Mn^{3+}, Fe^{2+}(hs)	2
Mn^{2+}, Fe^{3+}(hs)	$\frac{5}{2}$

One-dimensional spin systems are realized in materials with a crystal structure such that the spin carriers arrange in chains that are magnetically well isolated from each other. The remnant presence of weak interchain coupling usually leads to 3D effects, such as ordering, at sufficiently low temperatures. Examples of materials that host one-dimensional $S = 1/2$ structures are:

- $CuGeO_3$ [65–68]: Well-known spin-Peierls [69] material, where isolated uniform spin chains spontaneously dimerize below 14 K due do lattice vibrations [65, 66].
- IPA-$CuBr_3$ and IPA-$CuCl_3$: The couplings in IPA-$CuBr_3$ have AF–AF bond alternating structure with $\lambda \approx 0.5$ [70], whereas the couplings in IPA-$CuCl_3$ have a supposed FM–AF structure with $\lambda \approx -0.4$ [71]. However, recent experiments suggest that the latter is more appropriately modelled by an asymmetric $S = 1/2$ two-leg ladder [72].
- CuHpCl [73]: Strongly coupled dimers form the rungs of two-leg ladders [74–76].
- $SrCu_2O_3$: Gapped two-leg ladder material that shows superconductivity by doping either holes or electrons in the Sr layer [29, and refs. therein].
- F_5PNN [13, 64, 77, 78]: Purely organic, bond-alternating material with radicals as spin carriers, $\lambda \approx 0.4$ [64].

Spin-1 chains are realized in an ever growing number of compounds. Some examples of materials with uniformly coupled chains are:

- $CsNiCl_3$: First experimental verification of Haldane gap. Isotropic spin chains with weak single-ion anisotropy[1] and moderate interchain coupling that leads to

---

[1] A field that couples to $(S^z)^2$, which induces another form of XXZ anisotropy.

3D Néel order at low temperatures [4]. Recently, the presence of spin-$\frac{1}{2}$ degrees of freedom has been suggested [79].

- $AgVP_2S_6$: Another early experimental verification of an isotropic [80] Haldane gap material with a particularly large gap [81, 82]. This is one of the rare examples where spin-1 is not delivered by Ni^{2+}- but V^{3+}-ions.
- NENP [83], NINO [83], NDMAP [84] and NDMAZ [84]: Ni^{2+}-chain compounds with moderate single-ion anisotropy.
- DTN: Weakly coupled chains with strong single-ion anisotropy [85]. Spin-1 degrees of freedom (magnons) form a 3D Bose–Einstein condensate above a critical magnetic field, $H_c \approx 2\,\mathrm{T}$ [35].
- $PbNi_2V_2O_8$ [86–89]: Very recent material of weakly interacting chains [89] with weak negative single-ion anisotropy [88].
- R_2BaNiO_5 [90, 91]: Mixed spin rare earth (R) compounds that hosts spin-1 chains coupled to spin-$\frac{1}{2}$ R^{3+}-ions at interchain sites. In particular, the Haldane gap in Y_2BaNiO_5 has been measured several times [92–94].

Asymmetric molecular basecells lead to different bridging structures between the spin carrying metal ions and thus bond alternation occurs, as in

- NDOAP [95], NMAOP [96, 97] and NTENP [97, 98]: Ni^{2+}-chain compounds in the dimer phase with bond alternation parameter $\lambda \approx 0.1$, 0.25 and 0.45, respectively. Recent experiments on NTENP [14, 99] revealed the different structure of excitations in dimer and Haldane phase systems such as NDMAP.
- NTEAP [97, 100]: Isotropic Ni^{2+}-chain compound very close to the gapless point, $\lambda \approx 0.6$.

In homometallic materials staggered interaction necessarily is a feature of the crystal structure, that is subject to increasing control in the synthetization of new materials. A modular design strategy with bi- or polynuclear molecular building blocks [101] and the variety of ligands that can be utilized to bridge the building blocks offer promising perspectives for the design at need, not just of homogeneous bond alternating spin chains, but in particular of mixed spin chains as well.

However, to the best of our knowledge no exact realization of chains with mixed spin setup (1.7) exists. Nonetheless, a number of mixed spin materials is known, such as the rare earth compounds listed above, R_2BaNiO_5, that show ferrimagnetic behaviour. At low temperatures the interaction between AF spin-1 chains and interchain spin-$\frac{1}{2}$ Cu^{2+} ions leads to 3D magnetic long range order [90, 91]. Truly quasi-1D mixed spin materials exclusively show the simple alternating pattern $-S^a - S^b-$. Depending on the specific crystal structure that determines the exchange of neighbouring spins, a chain of Cu^{2+}–Ni^{2+} ions can be a single chain $\frac{1}{2} - 1$ ferromagnet [102, 103] or, if the interaction is antiferromagnetic, a ferrimagnet [104, 105]. An exotic and fascinating representative of a finite one-dimensional mixed spin structure is the ferrimagnetic molecular wheel of Fe^{3+}–Mn^{3+} ions [106].

In terms of magnetic design or structural chemistry, a basecell of the mixed spin setup (1.7) is a linear (other shapes exist) bimetallic tetranuclear complex. Such complexes do exist with various metals and interactions and the basecell of one of the models studied in this thesis is indeed realized in a Cu^{2+}–Ni^{2+}–Ni^{2+}–Cu^{2+} complex reported in [32]. Numerical calculations suggest strongly alternating AF intramolecular interactions with an "alternation" parameter $\lambda = 0.0008$. The building blocks crystallize in 2D sheets with neighbouring linear molecules oriented in perpendicular directions. Each Cu^{2+}–Ni^{2+} pair is strongly AF coupled to give an effective spin-$\frac{1}{2}$ that couples very weakly with its neighbour(s), thus the crystal is a quasi-2D assembly of mixed spin dimers weakly coupled to each other. This complex has been proposed as prototype of a stable two-qubit gate for quantum computation. Another similar realization of a mixed spin basecell is a Ni^{2+}–Cu^{2+}–Cu^{2+}–Ni^{2+} complex reported in [107]. The basecell molecules assemble in two different architectures one of which is linear in shape, but with basecells tilted with respect to the chain axis. Intramolecular interactions are yet unknown and, due to the tilt of the basecells, a ladder-like behaviour seems more reasonable to be expected. High-spin bimetallic tetranuclear Mn^{2+}–Mn^{3+}–Mn^{3+}–Mn^{2+} complexes have been reported with alternating FM–AF exchange [108] and, quite recently, with overall FM exchange [109]. Generally, heterometallic polynuclear complexes promise to realize an almost unlimited variety of mixed spin basecells. Note that, quite in contrast to homogeneous (or homometallic) chains, variation of interaction strengths, with bond alternation simply being a special case, is more the rule than the exception in mixed spin chains. Exchange of different spin species and crystal structure alike determine the coupling constants.

Another promising method to realize spin chains in general is the filling of carbon nanotubes [30]. Single-wall carbon nanotubes can be filled with heterofullerenes $C_{59}N$, where one carbon atom is replaced by nitrogen, resulting in a radical with one unpaired electron [110], or by endohedral fullerenes where a nitrogen atom is enclosed in the molecular sphere of the fullerene [111]. The filled tubes host homogeneous spin-$\frac{1}{2}$ chains. Bond alternation can, in principal, be controlled by adding functional groups attached to the fullerenes [30]. Using other agents, such as rare earth metals encapsulated in fullerenes [30], greatly enlarges the possible outcome of spin chains. It is thus far from speculation that, in the near future, filled carbon nanotubes can realize various homogeneous and mixed spin chains with coupling strengths being tunable to some extent. However, it is to be expected that thus realized mixed spin chains are subject to defects or, put in another way, randomness more strongly, compared with materials synthesized by the molecular design strategy discussed above.

With an ever growing chemist's toolbox there can be no doubt that the realization of mixed spin chains as studied in this theses is only a question of time – and interest. Once realized as coordination polymers or filled tubes (or experimentally implemented in optical lattices [112]), spin chains of arbitrary setups can, in principle, be subject to various experimental techniques that range from the direct measurement of thermodynamic properties, such as magnetization and susceptibility measurements [12, 88, 113], to relaxational and scattering methods that test dynamical features, such as nuclear magnetic resonance (NMR) [77, 114, 115], electron spin resonance (ESR) [14, 36, 85, 89], and magnetic neutron scattering [13, 99, 116, 117].[2]

---

[2] Given references refer to recent applications, for a brief description of NMR, ESR and neutron scattering see, e.g., [62] or [63] and references therein.

Part I

Theory and Methods

3 Relation Between Quantum and Classical Systems or (1+1)=2

In almost every aspect of this thesis on 1D quantum spin chains, the key idea is "to think 2D": in this thesis 1D quantum critical points "behave" like 2D classical critical points (Sect. 4); the 1D spin-$\frac{1}{2}$ XXZ chain is intimately related to various 2D classical models (here and Sect. 5); finite-size spectra of 1D quantum spin chains can be analyzed exploiting conformal invariance in 2D (Chaps. 4 and 6); the loop algorithm to simulate 1D quantum spin chains acts on 2D configurations (Sect. 6); etc.; The relation of D-dimensional quantum systems and $(D+1)$-dimensional classical systems, which shall be briefly introduced in this chapter, is quite general.

3.1 Quantum–Classical Mapping

Let O be an operator that represents some observable of interest and H the Hamiltonian of a quantum system. In the canonical ensemble, the quantum statistical expectation value of O is given by

$$\langle \mathrm{O} \rangle = \frac{1}{Z} \mathrm{Tr}\Big(\mathrm{e}^{-\beta \mathrm{H}} \mathrm{O}\Big) \,, \tag{3.1}$$

where Tr denotes the trace. The canonical partition function Z is the trace of the Boltzmann operator,

$$Z = \mathrm{Tr}\, \mathrm{e}^{-\beta \mathrm{H}} = \sum_n \langle n | \mathrm{e}^{-\beta \mathrm{H}} | n \rangle \,, \tag{3.2}$$

where the sum runs over all states of an arbitrary, complete set of, here, discrete basis states labelled by n. The partition function contains all information about equilibrium thermodynamic properties of the quantum system. The Boltzmann operator can be interpreted as evolution operator in imaginary time over a period given by the inverse temperature $\beta = 1/k_\mathrm{B}T$. This observation shows that dynamic properties contribute to static equilibrium properties.

The terms in the sum of (3.2) are transition amplitudes in imaginary time. By the usual time-slicing procedure used to obtain path integrals [118], the continuous evolution in imaginary time can be discretized into $(N+1)$ finite steps of size $\varepsilon = \beta/(N+1)$,

$$Z = \sum_{n_0} \langle n_0 | \underbrace{\mathrm{e}^{-\varepsilon \mathrm{H}} \cdots \mathrm{e}^{-\varepsilon \mathrm{H}}}_{(N+1)\,\text{factors}} | n_0 \rangle = \sum_{\{n_i\}} \prod_{i=0}^{N} \langle n_i | \mathrm{e}^{-\varepsilon \mathrm{H}} | n_{i+1} \rangle \,, \tag{3.3}$$

where N resolutions of the identity, $\sum_{n_i} |n_i\rangle\langle n_i|$, have been inserted in the last equation, $\sum_{\{n_i\}} \equiv \sum_{n_0} \cdots \sum_{n_N}$, and periodic boundary conditions $n_0 = n_{N+1} \equiv n$, naturally imposed by the trace in (3.2), have been implicitly assumed. Nothing prevents from interpreting imaginary time as another spatial dimension, with ε being the lattice constant. The task is to find a new reduced Hamiltonian $\mathcal{H}$, such that the partition function can be written in the form

$$Z = C \sum \mathrm{e}^{-\mathcal{H}}\,, \tag{3.4}$$

with C an unimportant constant. Note, that this is "inverse" to the famous transfer matrix approach or extremely anisotropic Hamiltonian limit [25]. Comparison to (3.3) shows that this can be accomplished by

$$\mathcal{H} = -\sum_{i=0}^{N} \ln \langle n_i| \,\mathrm{e}^{-\varepsilon \mathrm{H}}\, |n_{i+1}\rangle \ . \tag{3.5}$$

By construction, $\mathcal{H}$ is diagonal and, if D is the dimension of the original quantum model, it describes a *classical* $(D+1)$-dimensional model. But the new classical degrees of freedom need not necessarily be identical to the original ones. The trick is to find a clever parameterization of $\mathcal{H}$.

A simplistic example is a single Pauli spin in a transversal field, $h > 0$, [24, Chap. 2],

$$\mathrm{H} = -h\sigma^x = \begin{pmatrix} 0 & -h \\ -h & 0 \end{pmatrix}\,, \tag{3.6}$$

where the eigenstates $|\sigma\rangle$ of σ^z, with $\sigma^z\,|\sigma\rangle = \sigma\,|\sigma\rangle$ and $\sigma = \pm 1$, have been used as basis, that is, in fact, highly inadequate for obvious reasons. In this basis

$$\mathrm{e}^{\varepsilon h \sigma^x} = \begin{pmatrix} \cosh \varepsilon h & \sinh \varepsilon h \\ \sinh \varepsilon h & \cosh \varepsilon h \end{pmatrix} =: \begin{pmatrix} a & d \\ d & a \end{pmatrix}\,, \tag{3.7}$$

and the terms in the sum of (3.5) can be parameterized in terms of the original degrees of freedom, two classical spins,

$$\ln \langle \sigma_i| \,\mathrm{e}^{\varepsilon h \sigma^x}\, |\sigma_{i+1}\rangle = \mathcal{J}_0 + \mathcal{J}_1 \sigma_i \sigma_{i+1}\,, \tag{3.8}$$

with $2\mathcal{J}_0 = \ln(ad)$, and $2\mathcal{J}_1 = \ln(a/d)$. The resulting reduced Hamiltonian is

$$\mathcal{H}(\{\sigma_i\}) = -(N+1)\mathcal{J}_0 - \mathcal{J}_1 \sum_{i=0}^{N} \sigma_i \sigma_{i+1}\,, \tag{3.9}$$

which is just the energy shifted version of an Ising chain of $(N+1)$ spins with reduced coupling $\mathcal{J}_1$, that is determined by the field h and the step size ε.

In pretty much the same way as the single Pauli spin (3.6), the 1D Ising model in a transversal field (also called quantum Ising model) [24, Chap. 2],

$$\mathrm{H} = -J \sum_j \sigma^z_j \sigma^z_{j+1} - h \sum_j \sigma^x_j\,, \tag{3.10}$$

can be mapped onto the 2D classical Ising model. But this mapping depends on the Campbell–Baker–Hausdorff factorization,

$$\mathrm{e}^{-\varepsilon \mathrm{H}} = \mathrm{e}^{-\varepsilon \mathrm{H_d}}\, \mathrm{e}^{-\varepsilon \mathrm{H_o}}\, \mathrm{e}^{\frac{1}{2}(\varepsilon)^2 [\mathrm{H_d}, \mathrm{H_o}] + \cdots}\,, \tag{3.11}$$

where $\mathrm{H_d}$ refers to the diagonal and $\mathrm{H_o}$ to the off-diagonal part of H. Omitting the last factor in (3.11) induces a discretization error of order ε^2 which vanishes only in the *continuous time limit* $\varepsilon \to 0$. The diagonal part $\mathrm{H_d}$, simply generates Ising interactions in the new model in the original spatial direction with reduced coupling $\mathcal{J}_{1,\mathrm{s}} = \varepsilon J$. The off-diagonal part contains only single-site terms that commute with each other and the exponential can be factorized without further approximation. This results in Ising interactions of strength $\mathcal{J}_{1,\tau}$, in the extra dimension independently for each single (quantum) spin of the original model, just like for the single spin model (3.6).

It is a bit more involved to find a classical model that corresponds to two spins (or a chain thereof) coupled via XYZ-interaction, because of the appearance of zero-valued matrix elements in the operator $\mathrm{e}^{-\varepsilon \mathrm{H}}$, and, furthermore, because the terms in the off-diagonal part of a general XYZ Hamiltonian are bond terms that do not commute with each other. Using the Trotter–Suzuki breakup, however, instead of (3.11), permits the identification of the spin-$\frac{1}{2}$ XYZ quantum spin chain with a special case of the classical 2D vertex model. This important identification will described in the next section.

3.2 The Vertex Model

Usually, the square-lattice vertex model is defined by assigning weights to different vertex configurations. A vertex consists of four arrows, each pointing either towards or away from a common center. The spin-$\frac{1}{2}$ XYZ Hamiltonian corresponds to a special case called symmetric zero-field 8-vertex model, and the spin-$\frac{1}{2}$ XXZ Hamiltonian to the symmetric zero-field 6-vertex model [119].

The mapping is approximate, being exact in the continuous time limit, and achieved by applying the Trotter–Suzuki breakup [10, 120]. It has been the starting point in the derivation of the loop algorithm [10]. First, the Hamiltonian is split into pieces such that each contains only terms that commute with each other. On a chain with L sites and nearest neighbour interactions only (we apply periodic boundary conditions, $\mathrm{H}_{L-1,L} = \mathrm{H}_{L-1,0}$), this is simply

$$\mathrm{H} = \sum_{j=0}^{L/2-1} \mathrm{H}_{2j,2j+1} + \sum_{j=0}^{L/2-1} \mathrm{H}_{2j+1,2j+2} = \mathrm{H}_{\mathrm{even}} + \mathrm{H}_{\mathrm{odd}}\,, \tag{3.12}$$

where now

$$\mathrm{H}_{i,j} = J_x\, \mathrm{S}_i^x\, \mathrm{S}_j^x + J_y\, \mathrm{S}_i^y\, \mathrm{S}_j^y + J_z\, \mathrm{S}_i^z\, \mathrm{S}_j^z = \frac{1}{4}\begin{pmatrix} J_z & J_- & 0 & 0 \\ J_- & J_z & 0 & 0 \\ 0 & 0 & -J_z & J_+ \\ 0 & 0 & J_+ & -J_z \end{pmatrix}, \tag{3.13}$$

is a general XYZ two-spin interaction. Expressed in the basis $|\sigma,\tau\rangle = |\uparrow\uparrow\rangle\,, |\downarrow\downarrow\rangle\,, |\uparrow\downarrow\rangle$ and $|\downarrow\uparrow\rangle$, where $\uparrow(\downarrow)$ stands for $\sigma,\tau = +1(-1)$, it is block-diagonal. Now, second, Trotter's formula

$$\mathrm{e}^{-\beta(\mathrm{H}_{\mathrm{even}}+\mathrm{H}_{\mathrm{odd}})} = \lim_{N\to\infty} \left(\mathrm{e}^{-\varepsilon \mathrm{H}_{\mathrm{even}}} \mathrm{e}^{-\varepsilon \mathrm{H}_{\mathrm{odd}}}\right)^{N+1}, \tag{3.14}$$

allows for the factorization of the Boltzmann operator into even and odd contributions such that

$$\langle n_i|\mathrm{e}^{-\varepsilon \mathrm{H}}|n_{i+1}\rangle = \sum_{n_i'} \langle n_i|\mathrm{e}^{-\varepsilon \mathrm{H}_{\mathrm{even}}}|n_i'\rangle\langle n_i'|\mathrm{e}^{-\varepsilon \mathrm{H}_{\mathrm{odd}}}|n_{i+1}\rangle + O(\varepsilon^2)\,. \tag{3.15}$$

Using the fact that the two-spin Hamiltonian (3.13) acts only on the two-spin sub-state $|m_i\, m_j\rangle$ of state $|n\rangle = |m_0 \cdots m_{L-1}\rangle$,

$$\langle n_i|\mathrm{e}^{-\varepsilon \mathrm{H}_{\mathrm{even}}}|n_i'\rangle = \prod_{j=0}^{L/2-1} \langle m_{i,2j}\, m_{i,2j+1}|\mathrm{e}^{-\varepsilon \mathrm{H}_{2j,2j+1}}|m_{i,2j}'\, m_{i,2j+1}'\rangle\,, \tag{3.16}$$

and similar for the odd part. For finite ε this leads to the famous discrete time “checkerboard” representation [10] (see Fig. 3.1). A two-spin evolution is specified by four spin states and called “plaquette” in this context. The shaded plaquettes of the checkerboard can be identified with the vertices of the vertex model, tilted by 45°, and the non-zero matrix elements of the two-spin exponential operator $\mathrm{e}^{-\varepsilon \mathrm{H}_{i,j}}$, which is of the form

$$\mathrm{e}^{-\varepsilon \mathrm{H}} = \begin{pmatrix} a & d & 0 & 0 \\ d & a & 0 & 0 \\ 0 & 0 & c & b \\ 0 & 0 & b & c \end{pmatrix}\,, \tag{3.17}$$

with the corresponding vertex weights (see Table 3.1 for a definition of the symbols). In the general XYZ case ($J_x \neq J_z$) there are eight non-zero matrix elements, while in the XXZ case ($J_x = J_z$) there are six. Due to absence of an external magnetic field, inversion of spins does not change matrix elements. This leads to the same symmetry in the vertex model under inversion of arrows. The correspondence of matrix elements and weights of vertices is shown in Table 3.1. For $J_{x,y,z} > 0$, weight b is always

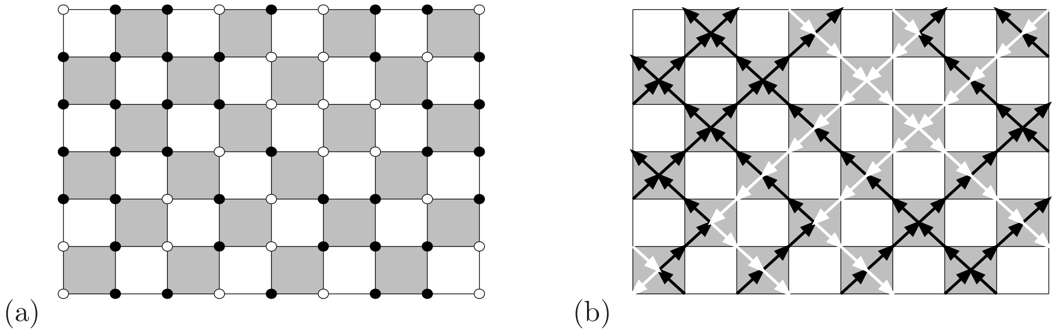

Figure 3.1: Checkerboard representation. Vertical axis is the discrete imaginary time. Only the shaded plaquettes evolve in a time step. (**a**) Filled (open) circles denote spin up (down). (**b**) Using arrows that point to the center of shaded plaquettes, instead of circles, the spatio-temporal configuration of classical spins looks like a classical 2D vertex model tilted by 45° [10, 119].

Table 3.1: Identification of spin-plaquettes with vertices of the vertex model. Baxter's symbols are widely used in the literature. The vertex weights are given by matrix elements of the two-spin evolution operator over a small step in imaginary time. Plaquettes and vertices in the last line appear only in the 8-vertex model.

plaquette	vertex	Baxter's symbol [119]		matrix element $\langle m_1 m_2 \vert \mathrm{e}^{-\varepsilon \mathrm{H}_{i,j}} \vert m_1' m_2' \rangle$
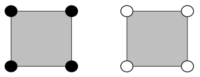	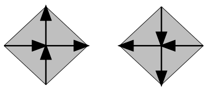	a	$=$	$\mathrm{e}^{-\varepsilon J_z/4}\cosh(+\varepsilon J_-/4)$
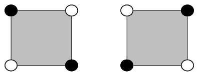	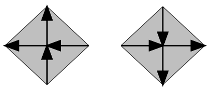	b	$=$	$\mathrm{e}^{+\varepsilon J_z/4}\sinh(-\varepsilon J_+/4)$
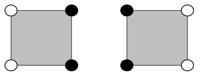	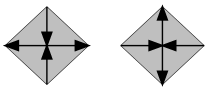	c	$=$	$\mathrm{e}^{+\varepsilon J_z/4}\cosh(+\varepsilon J_+/4)$
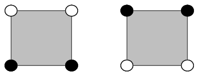	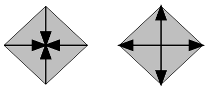	d	$=$	$\mathrm{e}^{-\varepsilon J_z/4}\sinh(-\varepsilon J_-/4)$

negative, and weight d is negative if $J_x > J_y$. In the XXZ case, if the length L of the spin-$\frac{1}{2}$ chain is even, the negative sign can be eliminated by a unitary sublattice basis rotation [10], that acts on, say, all spins at even sites,

$$\mathrm{S}^x_{2i} \to -\,\mathrm{S}^x_{2i}\,, \quad \mathrm{S}^y_{2i} \to -\,\mathrm{S}^y_{2i}\,, \quad \mathrm{S}^z_{2i} \to \mathrm{S}^z_{2i}\ . \tag{3.18}$$

The effect is to change the sign of all off-diagonal elements. The XXZ Hamiltonian (1.6) transforms as $\mathrm{H}^{\mathrm{XXZ}}(\lambda,\Delta) \to \tilde{\mathrm{H}}^{\mathrm{XXZ}}(\lambda,\Delta) = -\mathrm{H}^{\mathrm{XXZ}}(\lambda,-\Delta)$.

Thanks to the exact solution of the 8-vertex model [119, 121, 122] (with the 6-vertex model a special case thereof) it is, e.g., possible to obtain exact expressions for critical exponents of the spin-$\frac{1}{2}$ XYZ and XXZ chains.

3.3 Correlations

Let O_i be a real symmetric local operator of interest, such as S^z_i or S^x_i. The connected correlation function

$$G_{\mathrm{c},\mathcal{O}}(i,j) = \langle \mathrm{O}_i \mathrm{O}_j \rangle - \langle \mathrm{O}_i \rangle \langle \mathrm{O}_j \rangle\,, \tag{3.19}$$

measures the correlation of fluctuations of O, between sites i and j. In a non-critical system, the correlation between fluctuations decays exponentially at large distances, which in a translationally invariant system and for $\langle \mathrm{O}_i \rangle = 0$, is usually expressed as

$$G_{\mathcal{O}}(r) = \langle \mathrm{O}_r \mathrm{O}_0 \rangle \sim \mathrm{e}^{-r/\xi_{\mathcal{O}}}\ . \tag{3.20}$$

The exponential decay at large distances defines the correlation length $\xi_{\mathcal{O}}$.

To consider correlations in the extra dimension, it is, following [24, Chap. 2], convenient to use the temporal interpretation in the continuous limit and introduce the imaginary time variable τ. Then, using translation invariance in imaginary time, the time-ordered temporal correlation function of the time dependent operator $\mathrm{O}(\tau)$, can be calculated in the Heisenberg picture, where $\mathrm{O}(\tau) = \mathrm{e}^{\tau \mathrm{H}} \mathrm{O} \mathrm{e}^{-\tau \mathrm{H}}$, by

$$G_{\mathcal{O}}(\tau) = \langle \mathrm{O}(\tau)\mathrm{O}(0) \rangle = \frac{1}{Z} \sum_n \mathrm{e}^{-\beta E_n} \langle E_n | \mathrm{e}^{\tau \mathrm{H}} \mathrm{O} \mathrm{e}^{-\tau \mathrm{H}} \mathrm{O} | E_n \rangle \,, \tag{3.21}$$

where $\tau > 0$, and the eigenstates $|E_n\rangle$ of the quantum Hamiltonian, with $\mathrm{H}\,|E_n\rangle = E_n\,|E_n\rangle$, now serve as basis. Insertion of complete sets of eigenstates yields in the zero-temperature limit

$$\lim_{\beta\to\infty} G_{\mathcal{O}}(\tau) = \sum_n \mathrm{e}^{-\tau(E_n - E_0)} \, |\langle E_0 | \mathrm{O} | E_n \rangle|^2 \sim \mathrm{e}^{-\tau/(E_{1,\mathcal{O}} - E_0)} \,, \tag{3.22}$$

where E_0 denotes the energy of the groundstate. The temporal correlation decays exponentially. The decay at large distances is dominated by the inverse energy gap between groundstate and first excited state $|E_n\rangle = |E_{1,\mathcal{O}}\rangle$, for which the corresponding matrix element $\langle E_0|\mathrm{O}|E_n\rangle$ does not vanish. The important consequence is that correlation lengths in the extra dimension are given by the excitation gaps of the quantum spin system,

$$\xi_{\tau,\mathcal{O}} = \frac{1}{E_{1,\mathcal{O}} - E_0} \,. \tag{3.23}$$

In this thesis, the important correlations are the staggered components of spin–spin correlation functions. The off-critical exponential decay of the longitudinal (z) and transversal (x) staggered correlation functions[1]

$$G_{z/x}(r) = (-1)^r \langle \mathrm{S}_r^{z/x} \, \mathrm{S}_0^{z/x} \rangle \sim \mathrm{e}^{-r/\xi_{z/x}} \,, \tag{3.24}$$

define correlation lengths ξ_z and ξ_x. The XXZ spin chain is U(1)-symmetric, and thus consequently $\langle \mathrm{S}_r^x \, \mathrm{S}_0^x \rangle = \langle \mathrm{S}_r^y \, \mathrm{S}_0^y \rangle$. It is then convenient to use the Green's function $G_{\pm}(r) = (-1)^r \langle \mathrm{S}_r^+ \, \mathrm{S}_0^- \rangle$, instead. Temporal longitudinal and transversal correlation lengths, $\xi_{\tau,z}$ and $\xi_{\tau,x}$, respectively, can be defined via (3.22) and (3.23). The operators S_i^z and S_i^z connect the groundstate to different excited states. Generally, $\xi_{\tau,z} \neq \xi_{\tau,x}$, only at the fully SU(2)-symmetric istropic point, the two correlation lengths must be equal. The same holds, of course, for the spatial correlation lengths. It is thus, in principle, important to specify on which observable the definition is based on, when speaking of *the* correlation length.

---

[1] To be precise, mixed spin chains are not fully translationally invariant, the correlation function does depend on the position of both spins. But the exponential large distance decay is dominated by long-wavelength Fourier components of the correlation function which are not affected by the spin modulation within a basecell.

4 Critical Exponents and Scaling Dimensions

It is the purpose of this chapter to give meaning to the numbers that have been distilled from statistical and exact data in the course of this work and that will be presented in Part II. These numbers are critical exponents and scaling dimensions (or renormalization group eigenvalues). Above that, this chapter intends to set the background for the means of how to extract thermodynamic limit information from numerical data of finite systems. We shall not dive into the depths of statistical mechanics and thermodynamics of phase transitions in this chapter. The necessary background can be found in any standard textbook on these topics, such as [123–125], or in many specialized books, such as, e.g., [25, 26, 126], as introductory chapters. After a short introduction of second-order critical phenomena and critical exponents in Sect. 4.1, Sects. 4.2 and 4.3 are devoted to picking the raisins of the renormalization group idea [26] and the theory of conformal invariance [25], both applied to second-order critical phenomena.

4.1 Critical Exponents at Second-Order Critical Points

Second-order critical points are a particular and the most common class of continuous phase transitions. In contrast to abrupt first-order phase transitions, physical observables change continuously at a continuous phase transition, but in a non-analytic, singular way. The collective effect of critical fluctuations on all length scales is necessary to change continuously from one phase into another. Critical phenomena are characterized by scale invariance, i.e. the absence of an intrinsic length scale. This is reflected in critical quasi-long-range correlations of fluctuations, which decay asymptotically with a power-law at large distances in contrast to the off-critical exponential decay. Power-law decay of correlations implies an infinite correlation length. [124, 127]

The signature of a second-order critical point is the asymptotic power-law behaviour of the divergent correlation length (which can be for example ξ_z or $\xi_\pm$, defined in Sect. 3.3) upon approaching criticality,

$$\xi \sim |t|^{-\nu} \,, \tag{4.1}$$

where ν is the critical exponent of the correlation length ξ, and t is a dimensionless control parameter that drives the transition, with $t_\mathrm{c} = 0$, the critical point. This can be for example the reduced temperature $(T - T_\mathrm{c})/T_\mathrm{c}$, in a thermally driven classical phase transition, or some dimensionless coupling constant $(\lambda - \lambda_\mathrm{c})$, in a quantum phase transition. T_c or λ_c are the critical values of the control parameters. At the critical point, where the correlation length is infinite, the long-distance behaviour of the correlation function (which can be for example G_z or $G_\pm$, defined in Sect. 3.3) follows another power-law,

$$G(r) \sim |r|^{-D+2+\eta} , \tag{4.2}$$

controlled by another critical exponent η, also called anomalous dimension, with D the dimension of the system. If the critical point marks the boundary between two distinct phases, it is often possible to define a quantity that is zero in one phase and non-zero in the other, the order parameter. The definition of the order parameter depends on the presence of order in some sense, and the presence of order in some sense usually indicates the breaking of a symmetry in the ordered phase [124]. Let m be the order parameter density. The zero-field order parameter density can be defined by

$$m = \left.\frac{\partial f}{\partial H}\right|_{H=0} , \tag{4.3}$$

where H is the ordering field that couples to the order parameter, and $f = -\ln Z/(\beta V)$ the free energy density, with V the volume. If in the thermodynamic limit the order parameter has a nonzero expectation value even in the absence of the ordering field, i.e. if [127]

$$\lim_{H\to 0} \lim_{V\to\infty} \langle m \rangle \neq 0 , \tag{4.4}$$

the order is spontaneous and the corresponding symmetry is said to be spontaneously broken.[1] Let $t < 0$, be the ordered side. Then the order parameter vanishes non-analytically when the critical point is approached as

$$m \sim (-t)^\beta , \tag{4.5}$$

with β the critical exponent of the order parameter m.

Further critical exponents are usually labelled α and γ,[2] and defined by the singular behaviour of the specific heat c, and the zero-field order parameter susceptibility χ, i.e.

$$c = \frac{\partial e}{\partial T} \sim |t|^{-\alpha} , \quad \chi = \left.\frac{\partial m}{\partial H}\right|_{H=0} \sim |t|^{-\gamma} , \tag{4.6}$$

respectively, where $e = \partial(\beta f)/\partial\beta$, in the first equation is the internal energy density.

The critical exponents are universal quantities, their values do not depend on microscopic details of the model considered but on macroscopic features such as dimension and symmetries [128]. As a consequence, models that are significantly different in their microscopic description, can have the same set of critical exponents. The values of the critical exponents determine the *universality* class of a model. These values are

---

[1] Equivalently, spontaneous order may also be defined by the non-vanishing of long distance zero-field correlations of the local order parameter density, $\lim_{r\to\infty} \lim_{V\to\infty} \langle m(r)m(0)\rangle \neq 0$ [127].

[2] Another common exponent, usually labelled δ, is defined via the field-dependence of the order parameter at the critical point $t = 0$, $m \sim |H|^{-1/\delta}$. It does play no role in this thesis.

not independent from each other, but related through *scaling* relations [128]. For the standard critical exponents defined above the scaling relations read[3]

$$2\beta + \gamma + \alpha = 2\,, \tag{4.7}$$
$$\nu(2-\eta) = \gamma\,, \tag{4.8}$$
$$D\nu + \alpha = 2\,. \tag{4.9}$$

A consequence of the scaling relations is that the knowledge of only a few (two here) critical exponents suffices to determine all other critical exponents. Note, however, that stated as such the scaling relations only hold if temperature and the ordering field are the *only* control parameters, and if the exponent η is defined via the correlation of the order parameter fluctuations. But this is not precisely the case in the phase transitions considered in this thesis.

First of all, we have defined two different correlation functions G_z and $G_\pm$ which lead to two different exponents, η_z and $\eta_\pm$, and two different correlation lengths ξ_z and $\xi_\pm$. Scale invariance at the critical point implies, that close to criticality there is only one relevant length scale, and $\xi_z \sim \xi_\pm$. The exponent ν is the same for all correlation lengths. Second, staggered longitudinal magnetization, $m_\mathrm{s} = \sum_i (-1)^i m_i^z/V$, is not the order parameter here. Neither is the uniform magnetization nor their transversal counterparts. But the corresponding staggered susceptibilities χ_z and $\chi_\pm$ do diverge and give rise to definitions of two exponents, γ_z and $\gamma_\pm$. Formally it is possible to define also the exponents β_z and $\beta_\pm$, but they cannot be measured, $\langle \mathrm{S}_i^x \rangle = \langle \mathrm{S}_i^y \rangle = \langle \mathrm{S}_i^z \rangle = 0$ holds on both sides of the transitions considered and at the critical point. The corresponding scaling amplitudes are zero. We shall, however, define and measure order-parameter-like longitudinal and transversal observables and their critical exponents. There are considerably more exponents than in the standard case, and, as it seems, it should need the knowledge of more than just two critical exponents in order to determine the others via appropriate scaling relations. But, in fact, due to existence of extended scaling relations for the spin-$\frac{1}{2}$ XXZ chain [129–133] (and other Gaussian models), the knowledge of a *single* exponent is sufficient in that case. It is one of the main tasks of this thesis to tests if this is also true for mixed spin chains. Last but not least, the critical points considered here are quantum critical points and temperature is not a control parameter. This is about the most important difference to classical phase transitions. Apart from a few general subtleties in the difference of classical and quantum phenomena, there is not much difference between classical and quantum phase transitions.

Quantum critical points [24, 134]. Every transition at non-zero temperature can be described by classical theory, as thermal fluctuations will always dominate over quantum fluctuations sufficiently close to the critical point. However, at zero temperature there are no thermal fluctuations. A quantum phase transition can only be driven by quantum fluctuations of the groundstate. Thus, quantum phase transitions occur at zero temperature only, where the free energy density becomes the energy density in

---

[3] The scaling relation involving δ reads $\beta(\delta-1) = \gamma$.

the groundstate,

$$f = -\frac{1}{V}\frac{\ln Z}{\beta} \overset{\beta\to\infty}{\to} e_0 = \frac{E_0}{V}\,, \tag{4.10}$$

with V the volume. Quantum analogues of the internal energy and the temperature specific heat must be defined with respect to some control parameters that enter in the Hamiltonian. In our case, we choose the bond alternation parameter λ. We define an "internal" energy density $u_\lambda = \partial f/\partial\lambda$, and the corresponding specific heat c_λ, as[4]

$$c_\lambda = -\frac{\partial u_\lambda}{\partial\lambda} = -\frac{\partial^2 f}{\partial\lambda^2}\,. \tag{4.11}$$

Inverse excitation gaps of the quantum system give correlation lengths in imaginary time. At the quantum critical point the gaps close and the corresponding correlation lengths become infinite. In the vicinity of the critical point there is only a single relevant length scale given by the spatial correlation length. Both, spatial and imaginary temporal length scales must be related. This is generally expressed by

$$\xi \sim \xi_{\mathrm{s}}^z\,, \tag{4.12}$$

which can be considered the definition of the dynamic critical exponent [24]. The name emphasizes that z relates dynamic temporal to spatial properties.

At low temperature, dynamics is determined by low-energy excitations, which may be elementary quasi-particle excitations with energy-momentum dispersion relation $E(k)$. If the low-energy dispersion is linear

$$E(k) = v|k|\,, \tag{4.13}$$

with v a characteristic velocity, the dynamic critical exponent is $z = 1$ [25, 134].

4.2 Renormalization Group: Idea and Eigenvalues

Long distance behaviour is governed by long-wavelength degrees of freedom. In the renormalization group idea, short-wavelength degrees of freedom are integrated out in a systematic way in order to extract the interesting long-wavelength properties. It is the iterative attempt to express a model in terms of less degrees of freedom until a solvable or known model turns up [8]. Renormalization steps can be carried out in real space or momentum space or any other suitable representation [26, 135]. The presentation in this section largely follows [26].

A prominent simple example is Kadanoff's real space block spin renormalization scheme. Starting from the original D-dimensional system with spin degrees of freedom

---

[4] From our definition of the Hamiltonian (1.6), it follows that u_λ is the normalized or "reduced" energy density stored on λ-bonds. With u_{u} the energy stored on unit-bonds, the total energy density can be written $e = u_{\mathrm{u}} + \lambda u_\lambda$. At zero temperature, u_λ gives the change of the groundstate energy density with λ, and thus can also be seen as some kind of "specific heat". To be in accordance with usual scaling relations however, it is convenient to use definition (4.11).

s and a set of coupling constants $\{K\}$, b^d spins are combined into a new variable, the block spin s'. Then, new coupling constants

$$\{K'\} = \mathcal{R}(\{K\}) , \tag{4.14}$$

are calculated. The transformation is chosen such that the partition function and probability measure of long wavelength degrees of freedom are preserved, when expressed in terms of the new block spin variables and couplings. Under repeated transformation, the set of couplings will approach a renormalization group fixed point $\{K^*\} = \mathcal{R}\{K^*\}$. The fixed point contains all long distance or long wavelength information of the original system. "Trivial" fixed points, $\{K^*\} = 0$ and $\{K^*\} = \infty$, most commonly correspond to complete order and complete disorder. More importantly, however, a critical system is attracted into a non-trivial fixed point. Universal properties of a critical system, such as critical exponents or universal amplitude ratios, are completely determined by the corresponding attractive fixed point. This provides an explanation of universal phenomena and a definition of a universality class. "A universality class consists of all those models which flow into a particular fixed point. To each universality class will correspond a different critical fixed point." [26].

In real space, the renormalization group transformation is a scale transformation by some linear factor b. In the extreme case of an infinitesimal scale transformation, $b = 1 + \delta l$, with $\delta l \ll 1$, the couplings transform infinitesimally, $K_a \to K'_a \approx K_a + (\mathrm{d}K_a/\mathrm{d}l)\delta l$, and renormalization group equations (4.14) become differential equations,

$$\frac{\mathrm{d}K_a}{\mathrm{d}l} = -\beta_a(\{K\}) , \tag{4.15}$$

where the functions β_a are called renormalization group beta functions, their zeroes are the fixed points of renormalization. These equations determine the flow of the coupling constants under repeated renormalization. Linearized around the fixed point, the infinitesimal transformation can be written

$$K'_a - K^*_a \approx \sum_b \left(\delta_{ab} + \frac{\partial \beta_a}{\partial K_b} \delta l \right) (K_b - K^*_b) . \tag{4.16}$$

The matrix formed by $\delta_{ab} + (\partial\beta_a/\partial K_b)\delta l$, can be diagonalized to give eigenvalues $1 + y_i \delta l$, and left eigenvectors e^i. New *scaling variables* or *scaling fields* u_i, are chosen along the eigenvectors of the derivative matrix. They are linear combinations of deviations of the original couplings from their fixed point values, $u_i = \sum_a e^i_a (K_a - K^*_a)$, that transform as

$$u'_i \approx (1 + y_i \delta l) u_i . \tag{4.17}$$

If there are only two relevant variables, one even thermal variable t, and one odd variable h (e.g. a symmetry breaking ordering field), the scaling fields u_t and u_h can be chosen proportional to t and h, respectively. In a finite renormalization transformation the scaling variables transform as $u'_i = b^{y_i} u_i$. The y_i are called *renormalization group eigenvalues* of the scaling variable u_i. If $y_i > 0$, repeated renormalization will drive the system away from the fixed point and u_i is called a *relevant* scaling variable. If instead $y_i < 0$ renormalization will attract the system to the fixed point and u_i is called *irrelevant*. The special case $y_i = 0$ is called *marginal*. The linearized renormalization equations provide no information about the behaviour of a marginal scaling variable under repeated transformation.

The leading critical behaviour of observables is completely determined by the linearized differential equations of the relevant scaling fields. Going to higher than linear order leads to analytic correction terms. Considering irrelevant scaling fields gives rise to non-analytic corrections to scaling. To observe the effect of a marginal field, the differential equations must be written up to second order in the marginal field and its combinations with the relevant fields. The effect is to produce multiplicative logarithmic corrections to the leading power-law behaviour, usually followed by a tail of additive logarithmic corrections. The reasons for the presence of marginal scaling fields are manifold and depend on the model considered.

There is another special kind of scaling field, so-called *exact marginal* as opposed to the former which can also be called marginally relevant. An exact marginal field has vanishing contributions to the renormalization group differential equations even at (all) higher orders. It parameterizes, if present, a continuous line of fixed points, as for example in the Kosterlitz–Thouless transition of the XY model, or in Gaussian-like models as the spin-$\frac{1}{2}$ chain in the XY-like region.

Scaling relations. To leading order, the singular part of the free energy density transforms homogeneously under scale transformations,

$$f_s(t,h) = b^{-D} f_s(b^{y_t} t, b^{y_h} h) \,. \tag{4.18}$$

Fixing the scale factor, $b = t^{-1/y_t}$, gives the scaling form

$$f_s(t,h) \sim |t|^{\frac{D}{y_t}} \Phi_\pm \left(h t^{-\frac{y_h}{y_t}} \right) \,. \tag{4.19}$$

$\Phi_\pm(x)$ is a scaling function that is different on either side of the transition. It is universal, model-specific non-universal properties enter as constant scale factors of f_s (amplitude) and the argument but do not change the form of the function itself.

For a two-point correlation function of a local observable coupled to the field h, that depends only on the distance r, the homogeneity relation reads

$$G(r,t,h) = b^{-2(D-y_h)} G\left(\frac{r}{b}, b^{y_t} t, b^{y_h} h \right) \,. \tag{4.20}$$

Fixing the scale factor as before and setting $h = 0$, leads to the scaling form of the correlation function

$$G(r,t) \sim |t|^{2\frac{D-y_h}{y_t}} \Psi_\pm\left(r t^{\frac{1}{y_t}} \right) \,, \tag{4.21}$$

where $\Psi_\pm(x)$, again, is a universal scaling function and non-universal properties only determine the amplitude and a scale factor of the argument. Off criticality the correlation function decays exponentially at large distances as $\mathrm{e}^{-r/\xi}$. This can only be met if the argument of the scaling function is proportional to $r\xi^{-1}$, or $\xi \sim |t|^{-1/y_t}$.

Precisely at the critical point, $t = 0$ and the scaling function is merely a constant factor. The scale factor can be chosen $b = r$, i.e.

$$G(r, t = 0) \sim |r|^{-2(D-y_h)} . \tag{4.22}$$

The quantity

$$x_i = D - y_i , \tag{4.23}$$

that appears in the power of the above scaling form of the correlation function, is called *scaling dimension* of the observable the scaling field i couples to. This is, e.g., the spin operator S_i^z for the magnetic variable h or the local energy operator for the thermal (or thermal-like) variable t. In this context observables are called *scaling operators*.

From the usual thermodynamic definitions of standard observables as derivatives of the free energy density and from the scaling form of the correlation function, it follows that the standard critical exponents can be expressed in terms of two renormalization group eigenvalues y_t and y_h, or equivalently in terms of two scaling dimensions x_t and x_h (and the dimension of the system):

$$\alpha = 2 - \frac{D}{y_t} \quad \text{or} \quad \alpha = \frac{D - 2x_t}{D - x_t} , \tag{4.24}$$

$$\beta = \frac{D - y_h}{y_t} \quad \text{or} \quad \beta = \frac{x_h}{D - x_t} , \tag{4.25}$$

$$\gamma = \frac{2y_h - D}{y_t} \quad \text{or} \quad \gamma = \frac{D - 2x_h}{D - x_t} , \tag{4.26}$$

$$\eta = 2(D - y_h) \quad \text{or} \quad \eta = 2x_h , \tag{4.27}$$

$$\nu = \frac{1}{y_t} \quad \text{or} \quad \nu = \frac{1}{D - x_t} . \tag{4.28}$$

The standard scaling relations (4.7–4.9) follow immediately.

Ratios of critical exponents with ν are particularly important, they are quantities that can be estimated directly by finite-size scaling (see Sect. 6.4). Expressed via RG eigenvalues or scaling dimensions these are

$$\alpha/\nu = 2y_t - D = D - 2x_t , \tag{4.29}$$

$$\beta/\nu = D - y_h = x_h , \tag{4.30}$$

$$\gamma/\nu = 2y_h - D = D - 2x_h . \tag{4.31}$$

Quantum critical points. The thermal-like scaling variable is a coupling that in some way couples to the energy or some part of it. In this thesis, bond alternation λ couples to the total energy stored on λ-bonds. Temperature enters as a different variable, it is necessarily relevant at quantum critical points and the scaling of the free energy density is modified to [24, 134]

$$f_s(t, h, T) = b^{-(D+z)} f_s(b^{y_t} t, b^{y_h} h, b^z T) . \tag{4.32}$$

Precisely at $T = 0$ the quantum free energy density scales as that of a $(D + z)$-dimensional system. If the dimension D appears in scaling relation it must be replaced by $(D + z)$.

Finite-size scaling [56]. Finite systems do not exhibit critical singularities. Just like temperature, the inverse linear system size L^{-1} is a relevant scaling variable, it drives the system away from criticality if it is not precisely adjusted to its critical value, that is $L^{-1} = 0$. The scaling dimension of length is trivially known, and the homogeneity relation of the free energy density in finite quantum systems at zero temperature is

$$f_s(t, h, L^{-1}) = b^{-(D+z)} f_s(b^{y_t} t, b^{y_h} h, bL^{-1})\,. \tag{4.33}$$

Finite-size scaling is one of the main methods of data analysis in this thesis and will therefor be discussed in more detail in Sect. 6.4. The main idea behind is, that sufficiently close to the critical point the correlation length of the infinite system exceeds the finite linear length L, this is when the finite system begins to “feel” its finiteness. Then the correlation length that appears in scaling forms in the asymptotic form $|t|^{-\nu}$, can be replaced by L. Alternatively, L^{-1} can be included as a variable in the differential renormalization group equations [26],

$$\frac{\mathrm{d}L^{-1}}{\mathrm{d}l} = -L^{-1}(l) + \cdots\,. \tag{4.34}$$

4.3 Conformal Invariance and Scaling Dimensions

Systems at critical points are scale invariant, that is invariant under *global* scale transformations. Under the additional conditions of translational and rotational invariance and short-ranged interactions, critical systems are invariant not only under global but also under certain local scale transformations that leave the metric invariant, the group of conformal transformations. As the additional conditions are usually met in most critical systems, conformal invariance is the logical extension of scale invariance. After a short introduction to conformal invariance that closely follows [25], the main implications for this work will be outlined in this section.

Conformal transformations preserve angles. In more than two dimensions, these are translations, rotations, dilatations, i.e. global scale transformations, and the so-called special conformal transformation. These transformations form the group of projective conformal transformations that, using complex coordinates $z = x + \mathrm{i}y$, can be expressed by

$$z \to w_{\mathrm{p}}(z) = \frac{az + b}{cz + d}\,, \tag{4.35}$$

with the condition that $ad - bc = 1$. However, in two dimensions, *every* analytic function $w(z)$ is conformal! While projective conformal transformations do not change the geometry of space, this is not true for general analytic transformations. Invariance under all analytic transformations puts severe constraints on the structure of two dimensional critical systems, that can be exploited with great success.

Within the framework of conformal invariance, observables such as the energy density or the order parameter density are called scaling operators. All observables that can be written locally in terms of the fundamental degrees of freedom of the model considered, or as combinations of products of them, are scaling operators [26].

A scaling operator $\phi(z,\bar{z})$ is called *primary* if, under any conformal transformation $z \to z' = \omega(z)$, it transforms covariantly as

$$\phi(z,\bar{z}) \to \left(\frac{\partial\omega}{\partial z}\right)^{h} \left(\frac{\partial\bar{\omega}}{\partial\bar{z}}\right)^{\bar{h}} \phi(z',\bar{z}') \,, \tag{4.36}$$

where h and $\bar{h}$ are called holomorphic and antiholomorphic conformal weights, respectively. As can be easily seen from scale transformations $z \to bz$, the scaling dimension of the scaling operator ϕ is given by $x = h + \bar{h}$. Primary scaling operators exclusively exist in two dimensions. Every operator that is not primary, is called secondary. There exists a special class of secondary operators, called quasi-primary, these transform covariantly only under *projective* conformal transformations (4.35).

Invariance under projective conformal transformation is enough to completely determine the functional form of two-point functions of primary and quasi-primary operators,

$$\langle\phi_1\phi_2\rangle = \mathcal{C}_{12} z_{12}^{-2h} \bar{z}_{12}^{-2\bar{h}} = \mathcal{C}_{12} |z_{12}|^{-2x} \left(\frac{z_{12}}{|z_{12}|}\right)^{-2s} \,, \tag{4.37}$$

with $z_{12} = z_1 - z_2$ and $\bar{z}_{12} = \bar{z}_1 - \bar{z}_2$. The quantity $s = h - \bar{h}$, is called conformal spin, and $\mathcal{C}_{12}$ can fixed by normalization. Also, three-point functions of (quasi-)primary operators are completely determined. Properties of three-point functions in properly normalized conformally invariant systems are universal. In general, the structure of n-point functions is restricted up to $n-3$ free parameters, that introduce non-universal features.

Consequences of general analytic transformations of primary, quasi-primary and secondary operators are encoded in the algebraic language of the Virasoro algebra. The generators of the Virasoro algebra L_n and $\bar{L}_n$, with n integers, are the infinitesimal generators of conformal transformations in two dimensions. L_{-1}, L_0 and L_1, and their antiholomorphic counterparts generate the projective conformal transformations. The Virasoro generators satisfy the commutation relations

$$[L_n, L_m] = (n-m)L_{n+m} + \frac{c}{12} n(n^2-1)\delta_{n+m,0} \,, \tag{4.38}$$

$$[L_n, \bar{L}_m] = 0 \,. \tag{4.39}$$

The commutator of the antiholomorphic generators $\bar{L}_n$, reads analogous to the holomorphic commutator, both commute with each other and can be treated independently. The constant c is called central charge or conformal anomaly number. It is universal and parameterizes the effect due to a change of geometry under general analytic transformations. It is defined by the two-point function of the energy–momentum tensor

$$\langle T(z_1)T(z_2)\rangle = \frac{1}{2}\frac{c}{|z_1 - z_2|^4} \,. \tag{4.40}$$

The energy momentum tensor is defined as the scaling operator that couples to lowest order in $\partial\varepsilon$ under an infinitesimal general analytic transformation $z \to z' = z + \varepsilon(z)$.

In a quantum system with one spatial and one imaginary temporal dimension, the components of the energy–momentum tensor can be interpreted as density and flux of energy and momentum, hence the name [136]. Invariance of the energy–momentum tensor under spatial and temporal translations corresponds to the conservation of energy and momentum. By rotational and scale invariance the energy–momentum tensor is symmetric and traceless and two decoupled independent components can be defined, one holomorphic and one antiholomorphic,

$$T(z) = T_{11}(x,y) - T_{22}(x,y) - 2\mathrm{i}T_{12}(x,y)\,, \tag{4.41}$$

$$\bar{T}(\bar{z}) = T_{11}(x,y) - T_{22}(x,y) + 2\mathrm{i}T_{12}(x,y)\,, \tag{4.42}$$

which is the reason for the decoupling of holomorphic and antiholomophic Virasoro algebras. Translational invariance in the complex plane implies $\langle T(z)\rangle = 0$. Fluctuations around the zero mean as given by (4.40) occur on all length scales and are sensitive to changes in geometry, i.e. introduction of boundaries, which is analogous to the Casimir effect of vacuum fluctuations.

Physical information is drawn from the representation theory of *highest weight* representations of the Virasoro algebras. Holomorphic and antiholomorphic algebras decouple and it is sufficient to discuss one representation. Physical properties, however, must be deduced from the direct product of holomorphic and antiholomorphic representations. A primary scaling operator with scaling dimension $(h + \bar{h})$ corresponds to the highest weight state, denoted $|h\rangle$, in a representation of the Virasoro algebra in a basis chosen to be the eigenstates of L_0, i.e. by definition

$$L_0|h\rangle = h|h\rangle\,, \tag{4.43}$$

$$L_n|h\rangle = 0\,, \quad n > 0\,, \tag{4.44}$$

where L_n acts as lowering operator by n, $L_n|h'\rangle = |h' - n\rangle$, as follows directly from commutator (4.38). The highest weight state is annihilated by all lowering operators. The conformal vacuum, denoted by $|0\rangle$, is defined to be the highest weight state of a representation of the Virasoro algebra with highest weight $h = 0$. This corresponds the the identity operator $\mathbb{1}$, viewed as scaling operator with obvious scaling dimension 0.

The hermitian conjugate of generator L_n is $L_n^\dagger = L_{-n}$, which implies that $L_0^\dagger = L_0$, and conformal weights are real. Repeated application of raising operators, i.e. negatively indexed generators, on a highest weight state $|h\rangle$, creates descendant or secondary states $L_{-n_k} \cdots L_{-n_1}|h\rangle = |h + n_1 + \cdots + n_k\rangle$. All secondary states are eigenstates of L_0 to the eigenvalue $h + N$, where $N = n_1 + \cdots + n_k$ is called the level of the descendant. By convention, the indices are ordered, $n_1 \leq \cdots \leq n_k$. There are infinitely many secondary states, they form the *conformal tower* or *Verma module* of the primary scaling operator associated with the highest weight state $|h\rangle$. The Verma module of the conformal vacuum $|0\rangle$ or vacuum representation, is called conformal tower of the identity. The conformal tower of a primary scaling operator is a representation of the conformal symmetry.

Unitary representations of the conformal symmetry have in their Verma module only states with non-negative norm. The condition of unitarity puts restrictions on the possible values of central charge and conformal weights, both must be real, non-negative numbers. There exists a special class of states called null-states, higher-level states the norm of which is zero. The existence of null-states leads, for $c < 1$, to the series of so-called unitary minimal models for which the number and values possible conformal weights h is restricted. These include for example the Ising model with central charge $c = 1/2$ or the 3-state Potts model with central charge $c = 4/5$. The possible values of conformal weights in the Ising model are 0, 1/16 and 1/2. A unitary minimal model with central charge $c = 4/5$ has 10 different possible values of conformal weights, of which only 6 are realized in the 3-state Potts model. Thus, not every possible representation of the conformal symmetry is necessarily realized in a model. For $c \geq 1$ no further constraints arise. Those representations that are realized in a model are called *operator content*. The vacuum representation is always present.

Conformal weights give scaling dimensions. The central charge and operator content of a model determine which conformal weights and consequently which scaling dimensions are present. Scaling dimensions determine critical exponents and the linearized renormalization group flow of a critical system. This gives a definition of universality class in terms of conformal invariance. All models models with the same central charge and the same operator content belong to the same universality class.

Consequences for quantum systems. Conformal invariance applies to the singular part of the groundstate energy density. A regular background must be subtracted, such that the groundstate energy is zero, which amounts to a shift of the energy spectrum. Critical 1D quantum systems are effectively $(1+z)$-dimensional, and $z = 1$ is the condition that conformal invariance as described above can be exploited with maximal effect. For the quantum system to be truly invariant under rotations, that mix space and imaginary time, correlation functions must be equivalent in both directions and the correlation lengths equal. Correlation lengths in imaginary time are inverse energy gaps, and to satisfy the condition $\xi = \xi_\tau$, amounts to a rescaling of energy gaps, or *normalization* of the Hamiltonian. If $z = 1$, the dispersion law of elementary excitations is linear as in (4.13), and the proper conformal normalization is v, the velocity of elementary excitations. If $z \neq 1$, the condition of rotational invariance is necessarily violated.

One of the key consequences of conformal invariance that is of fundamental importance to the present work is that it tells how the energy–momentum tensor transforms under the map $w(z) = N/(2\pi) \ln Z$, that maps a system of infinite linear size at zero temperature (infinite extent in imaginary time) onto the semi-finite geometry of a system of linear extent N at zero temperature. A properly shifted and normalized Hamiltonian of a finite system with periodic boundary conditions, that is critical in the thermodynamic limit can be written

$$\frac{1}{v}(\mathrm{H} - e_\infty N) = \frac{2\pi}{N}\left(L_0 + \bar{L}_0 - \frac{c}{12}\right), \tag{4.45}$$

with e_∞ the non-singular part of the (unnormalized) groundstate energy density. The momentum part of the energy–momentum tensor gives

$$\mathrm{P} = \frac{2\pi}{N}\,(L_0 - \bar{L}_0)\,. \tag{4.46}$$

Every representation of the Virasoro algebra that is present in the Hamiltonian gives rise to a tower of integer spaced finite-size energy levels. The energy of eigenstates and the momentum-sector the states belong to are determined by the scaling dimension x_i, and the conformal spin s_i, of a primary scaling operator labelled by i and its descendant states. This is a one-to-one correspondence between the conformal towers of primary scaling operators and the finite-size energy levels [26, 136].

Thus, the eigenstates can be organized by

$$\frac{E^i_{j,j'}(N) - E_0(N)}{v} = \frac{2\pi}{N}(x_i + j + j') + \cdots \,, \tag{4.47}$$

$$P^i_{j,j'}(N) = \frac{2\pi}{N}(s_i + j - j') \,, \tag{4.48}$$

where the ellipses in the first equation represent higher order finite-size corrections, and j and j' parameterize the conformal tower of scaling operator i. The conformal normalization v is generally unknown, but it can be deduced from the condition that energy levels belonging to the same conformal tower must be integer spaced. In particular, the conformal tower of the identity ($\mathbb{1}$ with $x_{\mathbb{1}} = 0$) is always present and it must have states in the sectors with momentum $P = \pm 2(2\pi/N)$, and with energy gap $|P|$. This demand fixes the conformal normalization,

$$\frac{E^{\mathbb{1}}_{2,0}(N) - E_0(N)}{v} = \frac{E^{\mathbb{1}}_{0,2}(N) - E_0(N)}{v} \overset{!}{=} 2\frac{2\pi}{N} \,. \tag{4.49}$$

The groundstate itself corresponds to the conformal vacuum. It has the energy

$$E_0 = -\frac{\pi c v}{6N} \,, \tag{4.50}$$

and belongs to the sector of zero momentum. This gives a way to determine the central charge from the groundstate energy of finite-size systems, once the normalization is known.

5 XXZ Spin Chains

A variety of properties of XXZ chains, with a significant emphasis on the spin-$\frac{1}{2}$ chain and occasional side-views on the spin-1 chain, will be discussed. Thus a framework will be established within which properties of the mixed spin models can be understood. As an introduction to basic properties of the XXZ Hamiltonian, that will not be covered explicitly in this chapter, the book of Auerbach [38], which also contains advanced material, shall be recommended.

Section 5.1 states the Hamiltonian of the two mixed spin models, denoted MA and MB, that are the central models of interest in this thesis. Section 5.2 explains the structure of phases, the transitions in-between which are the central topic of this thesis, in terms of valence bonds between subspins and compares this picture to surfaces of solids. The phase diagrams and critical exponents of the spin-$\frac{1}{2}$ and the spin-1 chain, to which the phase diagrams of the mixed spin models are to be compared, will be presented and discussed in Sect. 5.3. The spin-$\frac{1}{2}$ XXZ chain is not only closely related to the vertex model, which we encountered in Sect. 3.2 and a special model to describe solid surfaces, but also to a host of other 2D classical and 1D quantum models. After a discussion of the (quantum) Ashkin–Teller model, which reveals a hidden symmetry of the spin-$\frac{1}{2}$ XXZ chain, and a brief review of the hidden symmetry of the spin-1 chain, which both lead to the definition of non-local string observables, a novel generalization of string observables to mixed spin chains will be presented in Sect. 5.4. The Gaussian model, and the sine-Gordon model, provide, among many other benefits, a unified framework in order to understand the existence of extended scaling relations [129–133], as will be explained, before stating the main hypothesis of this thesis, in Sect. 5.5. Finally, the structure of logarithmic corrections to scaling, which appear at the isotropic point in the critical spin-$\frac{1}{2}$ and spin-1 chain, and supposedly also in higher-spin isotropic and uniform chains, will be examined in Sect. 5.6, making heavy use of results derived for the 4-state Potts model.

5.1 Mixed Spin Models: MA and MB

The models of interest, in this thesis are two mixed quantum spin chains. The basecell in both models contains four sites. Four spins of two different sizes, S^a and S^b, reside on the sites of the basecell, according to the pattern

$$-S^a - S^a - S^b - S^b - . \tag{5.1}$$

Specifically, the following two setups, denoted model A (MA) and model B (MB) , are studied:

$$\begin{aligned} &\text{model A (MA):} \quad (S^a, S^b) = (1/2, 1), \quad \text{with basecell} \quad -\tfrac{1}{2} - \tfrac{1}{2} - 1 - 1 -, \\ &\text{model B (MB):} \quad (S^a, S^b) = (1/2, 3/2), \quad \text{with basecell} \quad -\tfrac{1}{2} - \tfrac{1}{2} - \tfrac{3}{2} - \tfrac{3}{2} -. \end{aligned}$$

Nearest-neighbour spins interact via all three components of the spin vector operator. To tune the models to critical points, two control parameters have been introduced. Bond alternation is controlled by λ, such that spins of equal size interact with unit strength and spins of different size with strength λ. The corresponding bonds are called unit- and λ-bonds respectively, in this thesis. XXZ exchange anisotropy is controlled by Δ, such that Δ gives the relative strength of the interaction between z-components of neighbouring spins.

Implicitly assuming periodic boundary conditions in a spin chain of length L, and using $\mathrm{S}_i^{\alpha,S}$, in order to denote the α-component of a spin operator $\vec{\mathrm{S}}_i$, that represents a spin of size S at site i, MA refers to the following bond alternating XXZ Hamiltonian,

$$\begin{aligned} \mathrm{H}^{\mathrm{MA}}(\lambda, \Delta) = \sum_{i=0}^{L/4} \Big[& \mathrm{S}_{4i}^{x,\frac{1}{2}} \mathrm{S}_{4i+1}^{x,\frac{1}{2}} + \mathrm{S}_{4i}^{y,\frac{1}{2}} \mathrm{S}_{4i+1}^{y,\frac{1}{2}} + \Delta\, \mathrm{S}_{4i}^{z,\frac{1}{2}} \mathrm{S}_{4i+1}^{z,\frac{1}{2}} \\ & + \lambda\, \mathrm{S}_{4i+1}^{x,\frac{1}{2}} \mathrm{S}_{4i+2}^{x,1} + \lambda\, \mathrm{S}_{4i+1}^{y,\frac{1}{2}} \mathrm{S}_{4i+2}^{y,1} + \Delta\lambda\, \mathrm{S}_{4i+1}^{z,\frac{1}{2}} \mathrm{S}_{4i+2}^{z,1} \\ & + \mathrm{S}_{4i+2}^{x,1} \mathrm{S}_{4i+3}^{x,1} + \mathrm{S}_{4i+2}^{y,1} \mathrm{S}_{4i+3}^{y,1} + \Delta\, \mathrm{S}_{4i+2}^{z,1} \mathrm{S}_{4i+3}^{z,1} \\ & + \lambda\, \mathrm{S}_{4i+3}^{x,1} \mathrm{S}_{4i+4}^{x,\frac{1}{2}} + \lambda\, \mathrm{S}_{4i+3}^{y,1} \mathrm{S}_{4i+4}^{y,\frac{1}{2}} + \Delta\lambda\, \mathrm{S}_{4i+3}^{z,1} \mathrm{S}_{4i+4}^{z,\frac{1}{2}} \Big] , \end{aligned} \tag{5.2}$$

and MB to

$$\begin{aligned} \mathrm{H}^{\mathrm{MB}}(\lambda, \Delta) = \sum_{i=0}^{L/4} \Big[& \mathrm{S}_{4i}^{x,\frac{1}{2}} \mathrm{S}_{4i+1}^{x,\frac{1}{2}} + \mathrm{S}_{4i}^{y,\frac{1}{2}} \mathrm{S}_{4i+1}^{y,\frac{1}{2}} + \Delta\, \mathrm{S}_{4i}^{z,\frac{1}{2}} \mathrm{S}_{4i+1}^{z,\frac{1}{2}} \\ & + \lambda\, \mathrm{S}_{4i+1}^{x,\frac{1}{2}} \mathrm{S}_{4i+2}^{x,\frac{3}{2}} + \lambda\, \mathrm{S}_{4i+1}^{y,\frac{1}{2}} \mathrm{S}_{4i+2}^{y,\frac{3}{2}} + \Delta\lambda\, \mathrm{S}_{4i+1}^{z,\frac{1}{2}} \mathrm{S}_{4i+2}^{z,\frac{3}{2}} \\ & + \mathrm{S}_{4i+2}^{x,\frac{3}{2}} \mathrm{S}_{4i+3}^{x,\frac{3}{2}} + \mathrm{S}_{4i+2}^{y,\frac{3}{2}} \mathrm{S}_{4i+3}^{y,\frac{3}{2}} + \Delta\, \mathrm{S}_{4i+2}^{z,\frac{3}{2}} \mathrm{S}_{4i+3}^{z,\frac{3}{2}} \\ & + \lambda\, \mathrm{S}_{4i+3}^{x,\frac{3}{2}} \mathrm{S}_{4i+4}^{x,\frac{1}{2}} + \lambda\, \mathrm{S}_{4i+3}^{y,\frac{3}{2}} \mathrm{S}_{4i+4}^{y,\frac{1}{2}} + \Delta\lambda\, \mathrm{S}_{4i+3}^{z,\frac{3}{2}} \mathrm{S}_{4i+4}^{z,\frac{1}{2}} \Big] . \end{aligned} \tag{5.3}$$

Throughout this thesis, the acronyms MA and MB shall be used consistently. Uniform or homogeneous spin-S quantum spin chains, modelled by the same bond alternating XXZ Hamiltonian, but with $S^a = S^b$, shall be referred to as spin-S chains.

5.2 Valence Bonds and Surfaces of Solids

The phases of interest in this thesis can be conveniently "visualized" in terms of *subspins*. A spin of general size S can be represented by $2S$ symmetrized subspins of size $S = 1/2$. The symmetrization projects onto the space of maximized total spin of combined subspins thereby restoring the original size of the Hilbert space. If two subspins that belong to spins on different sites form a singlet, this is called a *valence bond* [45]. A formal definition of valence bonds can be given by use of Schwinger boson operators [38]. The groundstates of spin chains in phases characterized by a given valence bond configuration are generally not exact valence bond states, which serve merely as trial wavefunctions to approximate the groundstate wavefunction. However, it is possible to explicitly construct spin Hamiltonians that have exact valence bond groundstates [46, 47].

For bond alternating chains with nearest-neighbour couplings, it is sufficient to consider valence bonds between neighbouring subspins only. The valence bond configuration can only change by crossing a critical phase boundary. There are $2S + 1$ different successive valence bond configurations separated by $2S$ critical points for a spin-S chain and bond alternation can be used to tune between them [137, 138]. The special cases $S = 1/2$ and $S = 1$ are depicted in Fig. 5.1a. The mixed spin chains MA and MB only have two different nearest-neighbour valence bond configurations and one phase transition. The spin-$\frac{1}{2}$ pairs serve as bottleneck that prevents further transitions (see Fig. 5.1b).

Setting the bond alternation $\lambda = 0$, the chain decouples into isolated dimers that each form a singlet in the groundstate, thus giving a perfect valence bond configuration. Elementary excitations are isolated triplet excitations of dimers. Turning on a small coupling between dimers, the valence bond structure remains unchanged, but excitations may spread across the chain. In homogeneous spin chains at the opposite end with λ sufficiently large, dimers are shifted by one lattice site, giving essentially the same valence bond configurations. These two dimer configurations already exhaust the possible phases of the spin-$\frac{1}{2}$ chain. The boundary is the isotropic and uniformly coupled spin-$\frac{1}{2}$ Heisenberg chain with $\lambda = 1$ (see Sect. 5.3). Both dimer configurations break translational symmetry by one lattice site as a direct consequence of the explicit breaking of translational symmetry by bond alternation. The spin-1 chain offers an intermediate valence bond configuration that remains fully translationally invariant. The phase characterized by this intermediate valence bond configuration is called *Haldane phase* [142]. The bottleneck of spin-$\frac{1}{2}$ pairs in mixed spin chains MA and MB also prevents the formation of a Haldane phase. From the dimerized phase MA and MB transit into a quadrumerized one (see Fig. 5.1b).

From the point of view of individual spins both, dimer and Haldane phase, are disordered, yet there is a structural difference. A closer inspection of valence bond configurations shows that in the Haldane phase a spin in state $m = +1$, is always followed by a spin in state $m = -1$, and *vice versa*, but separated by an arbitrary number of zeroes, which is why the order in the Haldane phase is also called liquid Néel order [142]. On the other hand, in the dimer phase a state $m = +1$, if it occurs, is always immediately followed by $m = -1$, and *vice versa*. Figure 5.2b shows examples of possible subspin states of a spin-1 chain in the dimer and in the Haldane phase.

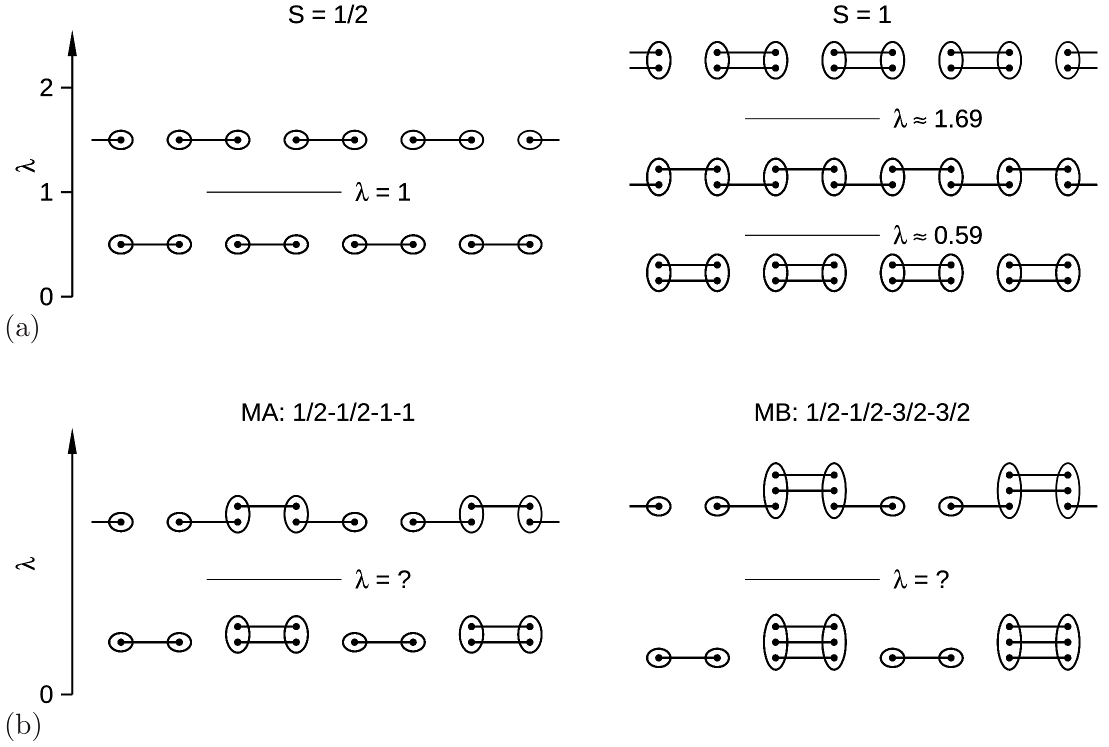

Figure 5.1: Valence bond configuration of homogeneous (**a**) and mixed spin chains (**b**). Dots symbolize subspins and connecting horizontal lines symbolize singlets between subspins, the valence bonds. Bond alternation λ is symbolized on the vertical axis. The numerical values given for the phase boundaries in (**a**) refer to the isotropic point, $\Delta = 1$, (the values of the spin-1 chain are numerical estimates [139–141]).

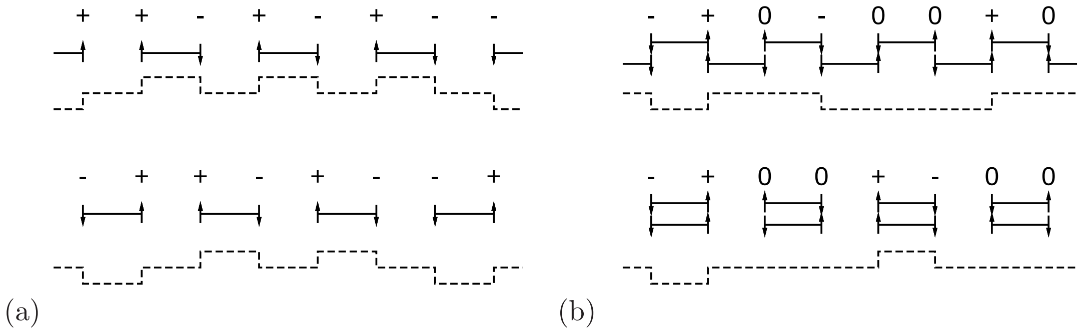

Figure 5.2: Examples of spin configurations of homogeneous spin chains. Arrows represent the orientation of subspins, "±" and "0" refer to the total spin state, and the dashed horizontal step curve shows the spin states translated into the surface of a solid. (**a**) $S = 1/2$. Both dimerized phases are equivalent. (**b**) $S = 1$. In the dimerized phase (bottom) "+" is always followed immediately by "−" and *vice versa* which corresponds to small "islands" in the solid surface. In the Haldane phase (top) "+" and "−" can be separated by an arbitrary number of sites. The solid surface is disordered flat.

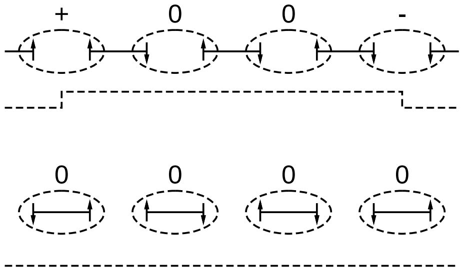

Figure 5.3: "Haldane"-phase-like structure in the dimers of the spin-$\frac{1}{2}$ chain. Bottom: With respect to reference dimers (dashed ellipses) the chain is ordered, which corresponds to a perfectly flat surface (dashed horizontal line). Top: Order in the other dimers generates a Haldane-phase-like structure on the reference dimers. The surface is disordered flat.

There is yet another interpretation of the Haldane phase given by den Nijs and Rommelse [142]. They showed that a general spin-1 model can be obtained as the extremely anisotropic Hamiltonian limit of the classical 2D restricted solid-on-solid model (RSOS). The RSOS model is used to model the behaviour of crystal surfaces. The lattice degrees of freedom are the local integer heights of the surface, and the difference in heights on neighbouring sites is restricted to $-1, 0, 1$, i.e. the state of a spin gives the step size of the RSOS model. The Haldane phase corresponds to the disordered flat phase of the RSOS model. It was argued by den Nijs and Rommelse [142] that the appearance of the disordered flat phase is not a special feature of the spin-1 chain or integer spin chains in general. The spin-$\frac{1}{2}$ chain, and half-odd integer spin chains in general, may also exhibit a disordered flat phase. However, they correspond to body-centered solid-on-solid models (BCSOS). The absence of the $m = 0$ state in half-odd integer spin chains enforces a minimum step size of ±1 in BCSOS models (see Fig. 5.2a). Both dimer phases of the spin-$\frac{1}{2}$ chain correspond to disordered flat phases in the BCSOS model. The Haldane-phase-like character becomes visible when looking at the spin-$\frac{1}{2}$ chain on the dimer level, as illustrated in Fig. 5.3. Two spins that are connected by a valence bond give a singlet of total spin zero. Thus from the perspective of valence bond dimers the spin chain is perfectly ordered with all dimers giving zero spin, and the BCSOS model is in a completely flat phase. When the reference dimers are kept fixed, but the valence bond configuration is switched, the reference dimers become disordered with a structure equivalent to that of the Haldane phase. A dimer of total $m = +1$ is followed by a dimer with $m = -1$, and *vice versa*, separated by an arbitrary number of dimers with $m = 0$. From this point of view, the two dimer phases are distinct. It is, however, important to keep in mind that this distinction depends on the particular choice of fixed reference dimers. Both dimerized spin-$\frac{1}{2}$ phases are supposed to connect smoothly (without phase transition) to the spin-1 Haldane phase, when either tuning λ or the coupling on unit-bonds to $-\infty$ [143–145].

Twist Order. About two decades before Haldane published his famous conjecture that homogeneous integer spin chains are gapped, Lieb et al. [146] argued from the other side, that half-odd integer spin chains are gapless. They introduced the unitary twist operator [38, 146]

$$\mathrm{U_T} = \mathrm{e}^{\mathrm{i}\frac{2\pi}{L}\sum_{j=1}^{L} j \mathrm{S}_j^z} , \tag{5.4}$$

which creates a magnon-like excitation by twisting every spin about an angle of $2\pi/L$, with respect to its predecessor. The energy of this excitation vanishes linearly with the inverse system size. If the excitation is orthogonal to the groundstate, it becomes degenerate with the groundstate in the thermodynamic limit, i.e. closes the excitation gap. It turns out that this is always the case for half-odd integer spin chains, which proves the gaplessness in that case.

The real part of the ground state expectation value,

$$z = \mathrm{Re}\,\langle E_0|\mathrm{e}^{\mathrm{i}\frac{2\pi}{L}\sum_{j=1}^{L} jS_j^z}|E_0\rangle\,, \tag{5.5}$$

serves as a convenient indicator for the presence of a valence bond structure and consequently for phase transitions between various valence bond configurations [141]. At the critical point the twist order parameter z is zero and it approaches the critical point in a non-analytic manner.

5.3 Phase Diagrams and Critical Exponents

The λ–Δ phase diagram of the homogeneous spin-$\frac{1}{2}$ chain was obtained in [147] (and in [148] for slightly different version of the model) from series expansion methods with the original aim to study universality classes of the 2D classical Ashkin–Teller model. The critical bond alternation, $\lambda_{\mathrm{c}} \approx 0.6$, of the spin-1 chain at the isotropic point has been determined in [139] via DMRG, and later refined [140, 141]. The full λ–Δ phase diagram of the spin-1 chains was calculated numerically in [149, 150], by exact diagonalization using the Lanczos method. The phase diagrams are sketched in Fig. 5.4. They contain several different regions:

- Two equivalent dimerized phases, D1 and D2.
- The Neél ordered phase, N, where the staggered magnetization develops a non-zero expectation value in ground state, spontaneously breaking a Z_2 symmetry.
- The XY-like phase, C, is critical everywhere and fans out of the phase boundary D1–D2 at $\Delta = -1/\sqrt{2}$
- The Haldane phase, H.

Not shown in Fig. 5.4 is a ferrormagnetic phase at $\Delta < -1$. The phase boundaries are altogether critical, and they belong to the following universality classes:

- D1–D2 for $S = 1/2$, and H–D1 and H–D2 for $S = 1$: Critical exponents vary continuously with Δ, along the phase boundary. It belongs to the *Gaussian universality class*. The equivalent boundary in mixed spin chains, where it separates a dimerized from a quadrumerized phase, is the focus of this work.
- N–D1, N–D2 and N–H: These phase boundaries belong to the Ising universality class, the critical exponents are the Ising model critical exponents [147, 151].
- D1–C, D2–C and C–H: These phase boundaries are of Kosterlitz–Thouless (KT) type [152], where the correlation length diverges exponentially.

As discussed in the previous section, phases D1 and D2 are completely disordered with respect to individual spins, that randomly take states up or down. The staggered magnetization is zero in both phases, no spontaneous Z_2 symmetry breaking

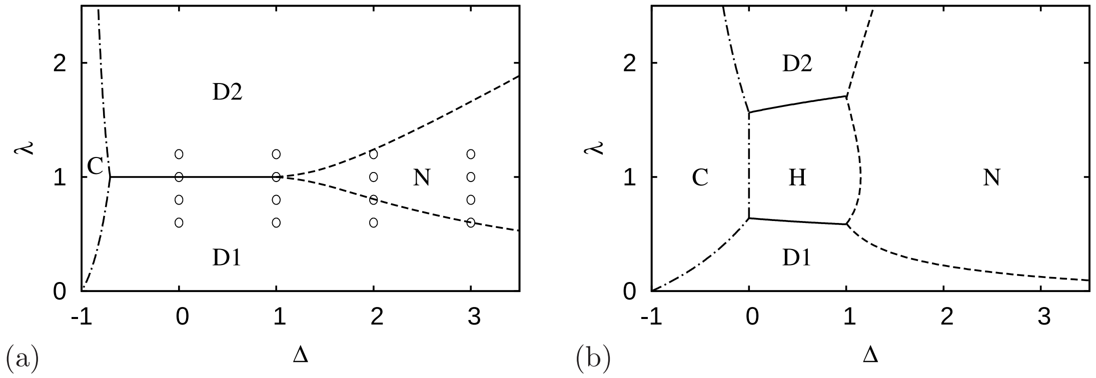

Figure 5.4: Phase diagrams of homogeneous spin chains with exchange anisotropy Δ, and bond alternation λ: D1/D2…dimer phases; N…Neél phase; C…critical XY-like phase; H…Haldane phase. The full lines are phase boundaries of the Gaussian universality class. Boundaries of the Neél phase (dashed) are in the Ising and that of the XY-like critical phase (dashed-dotted) in the Kosterlitz–Thouless universality class. (**a**) $S = 1/2$. Small circles indicate the location of snapshots in Fig. 5.5. (**b**) $S = 1$. (Pictures are reproductions of the phase diagrams published in [147] for $S = 1/2$, and [149, 150] for $S = 1$.)

occurs. That is, staggered magnetization is not an order parameter (and neither is the uniform magnetization, of course) that can be used to distinguish the two phases, as both phases are completely equivalent from that point of view. Staggered magnetization is an order parameter only for the Neél ordered phase N. Snapshots of the staggered magnetization that illustrate this are shown in Fig. 5.5. Thus, the critical exponent β cannot be observed with respect to staggered magnetization. Nonetheless, both dimerized phases respond to staggered magnetic fields, and with XXZ anisotropy the response to a longitudinal field (in z direction) will be different from that to a transversal field (oriented somewhere in the xy–plane). The response is measured by staggered susceptibilities which by the fluctuation–dissipation theorem are related to staggered spin–spin correlation functions.

The exact dependence of the critical exponents of the spin-$\frac{1}{2}$ XXZ chain on Δ can be inferred from Baxter's solution of the classical 2D 8-vertex (8V) model [121, 122]. The correlation length exponent of the 8-vertex model is

$$\nu^{8\mathrm{V}} = \frac{\pi}{2\mu} \quad \text{with} \quad \cos\mu = \frac{a'b' - c'd'}{a'b' + c'd'}\,, \tag{5.6}$$

where $a' > 0$, $b' > 0$, $c' > a' + b' + d'$ and $d' > 0$, are four different weights of the vertices in the principal domain of the symmetric 8V model. The spin-$\frac{1}{2}$ XXZ chain maps onto the 6-vertex (6V) model, a special case of the 8V model with $d = 0$. By symmetry considerations [154, 155] the weights of the 6V model can be mapped into the principal domain of the 8V phase diagram where then $\cos\mu = (a^2 + b^2 - c^2)/(2ab)$ [156], with a, b and c the weights given in Table 3.1. Taking the limit $\varepsilon \to 0$, it follows that $\cos\mu = \Delta$, and the exponent becomes

$$\nu^{8\mathrm{V}} = \frac{\pi}{2\arccos\Delta}\,. \tag{5.7}$$

$\nu^{8\mathrm{V}}$ controls the asymptotic power-law behaviour of the 8V correlation length when the thermal control parameter is tuned to criticality. The thermal control parameter

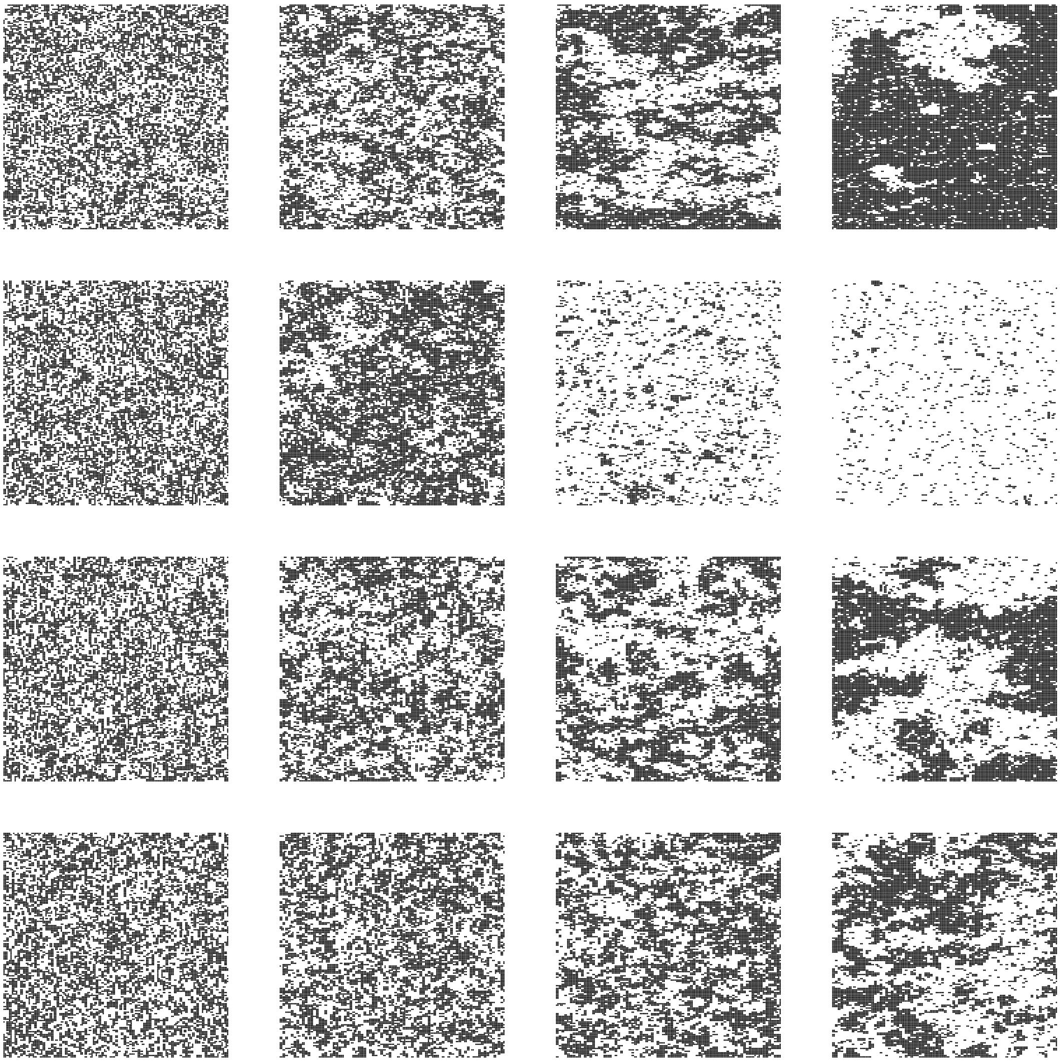

Figure 5.5: Snapshots of the staggered magnetization of the spin-$\frac{1}{2}$ chain. Imaginary time (on the vertical axis) is coarse-grained to obtain a discrete 2D picture of classical spins. All images are (160×160) close-ups of a system with $L = 256$ and coarse-grained $\beta = 3L$. Images are arranged as to correspond to the circles in Fig. 5.4a. The third column shows, from top to bottom, the transition from a nearly critical state in the Néel ordered phase to the dimerized phase, which is disordered with respect to staggered magnetization. This corresponds to the Ising-like Z_2 symmetry breaking, thus the resemblance to the well-known snapshots of the critical and ordered Ising model (see, e.g., [124, 153]). Quite in contrast, the snapshots in the first column do not really show a difference. Staggered magnetization cannot be used to distinguish the two dimerized phases.

of the 8V is the temperature. The control parameter in the quantum phase transition of the spin-$\frac{1}{2}$ XXZ chain, i.e. the bond alternation parameter λ, does, however, not correspond to the temperature of the 8V model. It rather corresponds to the temperature of the classical 2D Ashkin–Teller (AT) model [155]. It is thus ν^{AT}, that has to be identified with the exponent ν of the spin-$\frac{1}{2}$ XXZ chain. The AT and the 8V model are very similar. Both can be phrased in terms of two coupled Ising models, yet they differ in their topology [119]. A relation can be established by a duality transformation on one of the two Ising models. In essence, this results in the following exact expression, which for compactness we write in terms of the RG eigenvalue of the 8V thermal control parameter $y = (\nu^{8\mathrm{V}})^{-1} = (2/\pi) \arccos \Delta$,

$$\nu = \frac{2-y}{3-2y} \,. \tag{5.8}$$

In a standard second-order transition, knowing two exponents is sufficient to calculate the other exponents from scaling relations. It turns here, that due to existence of extended scaling relations [129–133], which can be, e.g., stated as

$$\eta^z = (\eta^{\pm})^{-1} = 4 - 2\nu^{-1} \,. \tag{5.9}$$

it is, in fact, sufficient to know a single exponent only. These relation follows from duality properties [157] of the Gaussian model [133] or the relation between the 8V and Ashkin–Teller model [155]. Using standard scaling relations (4.7)–(4.9), the critical exponents of the longitudinal and transversal susceptibilities can be obtained as

$$\gamma^z = \frac{2-2y}{3-2y} \,, \quad \gamma^{\pm} = \frac{4-y^2}{6-4y} \,. \tag{5.10}$$

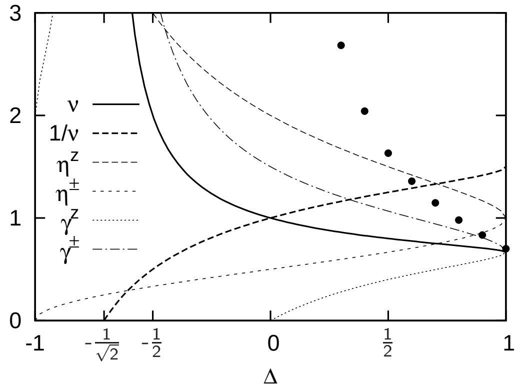

Figure 5.6: Exact critical exponents of the spin-$\frac{1}{2}$ chain (curves) and the numerical estimates of ν of the spin-1 chain [150] (dots).

The Δ-dependence of the exponents in the region $|\Delta| \leq 1$ is shown in Fig. 5.6. There are some notable points. The critical line fans out to become a region at $\Delta = -1/\sqrt{2}$, where $\gamma^{\pm}$ and ν, both diverge. At $\Delta = 0$, ν takes the value 1. There, the spin-$\frac{1}{2}$ XXZ chain is equivalent to two decoupled transversal Ising models, yet not in the Ising model's universality class. The central charge of the transversal Ising model is 1/2, taking two of them the central charges of both add up to 1. Below $\Delta = 0$, γ^z is negative, the critical singularity of the longitudinal staggered susceptibility χ^z is convergent instead of divergent, whereas precisely at $\Delta = 0$, χ^z diverges logarithmically. At the isotropic point $\Delta = 1$, due to SU(2) symmetry the susceptibility exponents necessarily become equal and take the value 2/3. But also $\nu = 2/3$, and the exponent of the specific heat with respect to λ, $\alpha = 2/3$,[1] the values of the 4-state Potts model, which

---

[1] It can be verified by inspection of the corresponding scaling dimensions (see Sect. 5.5), that, in fact, $\alpha = \gamma^z$ for all Δ.

is in the same universality class as the spin-1/2 XXZ chain. In the 4-state Potts model $\gamma = 7/6$, which is not a contradiction to the fact that $\gamma^z = \gamma^\pm = 2/3$ at the isotropic point. The magnetic field of the Potts model is *not* the magnetic field of the XXZ chain. This will become apparent in the next section, where the mapping between XXZ chain and quantum Ashkin–Teller model will be explained, the classical version of which contains the 4-state Potts model as a special case.

The critical exponent ν of the spin-1 chain is also shown in Fig. 5.6 (dots). It has been calculated in [150]. The behaviour is qualitatively the same as for the spin-$\frac{1}{2}$ chain, but the precise numerical dependence on Δ differs. The boundaries H–D1/2 in the spin-1 chain and the boundary D1–D2 in the spin-$\frac{1}{2}$ chain are in the same universality class. But only at the AF isotropic point the the numerical values of ν of the spin-$\frac{1}{2}$ and the spin-1 chain meet as a consequence of the SU(2) symmetry. In the spin-1 chain, ν diverges at $\Delta = 0$ which marks the entrance of the critical XY-like region.

5.4 Hidden Symmetry and String Observables

It is, in our opinion, a startling fact, that the transition D1–D2 in the spin-$\frac{1}{2}$ chain and the transitions H–D1/2 in the spin-1 chain are in the same universality class. The reason is, that in both cases there is a spontaneous breaking of *hidden* $Z_2 \times Z_2$ symmetries involved, signalled by non-local string observables. For the spin-$\frac{1}{2}$ chain, the discussion of the hidden symmetry will be more detailed than for the spin-1 chain, because we consider it the clue to a definition of string observables in mixed spin chains, which will follow at the end of this section. Our interest in string observables of mixed spin chains is two-fold. First, the need of an order parameter-like quantity to obtain a direct estimate of the exponent ratio $1/\nu$ from our quantum Monte Carlo simulations. Second, and more importantly, to “see” the spontaneous breaking of a hidden symmetry. The results chapter will show, that the first point is matched. However, our generalization of the string observables to mixed spin chains is rather heuristic. We have no proof that it does indeed indicate the spontaneous breaking of a hidden $Z_2 \times Z_2$ symmetry.

Spin-$\frac{1}{2}$ and the quantum Ashkin–Teller Model. The classical 2D Ashkin–Teller model is a model of four-state variables on a square lattice [158], which may represent four different atoms. It is closely related to several other models and has been studied thoroughly in the literature [132, 147, 154, 159, 160]. The symmetric version of the AT model can be written in terms of two Ising models coupled via four-spin interaction. Using two sets of Pauli operators or Ising variables, $\sigma^z = \pm 1$ and $\tau^z = \pm 1$, the Hamiltonian reads [147]

$$\mathrm{H}^{\mathrm{AT}} = -\sum_{\langle i,j\rangle} \left[K_2 \left(\sigma_i^z \sigma_j^z + \tau_i^z \tau_j^z \right) + K_4 \sigma_i^z \sigma_j^z \tau_i^z \tau_j^z \right], \tag{5.11}$$

where the sum runs over all nearest-neighbour pairs $\langle i, j\rangle$ of sites. The on-site variable (σ_i^z, τ_i^z), represents the four different states. The special case $K_2 = K_4$, is just a complicated disguise of the four-state Potts model.

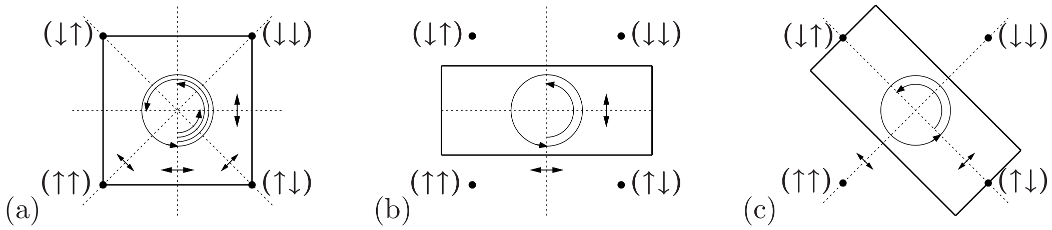

Figure 5.7: Symmetry operations of D_4, the symmetry group of the AT and qAT model. (**a**) D_4 is the symmetry of a square. (**b**) and (**c**) show the two invariant subgroups isomorphic to $Z_2 \times Z_2$, the symmetry of a rectangle.

The 1D quantum version of the AT model (qAT) can be obtained from its classical counterpart by introducing different couplings in x and y direction, $K_2^{x/y}$ and $K_4^{x/y}$, and taking the anisotropic Hamiltonian limit $K_2^{x/y} \to 0$ and $K_4^{x/y} \to \infty$, such that $\Delta = K_4^x/K_2^x$, and $\lambda = \exp(2(K_4^y - K_2^y))$, giving (see [25, 147])

$$\mathrm{H}^{\mathrm{qAT}} = -\sum_i \Big[\underbrace{\sigma_i^x + \lambda \sigma_i^z \sigma_{i+1}^z}_{\text{quantum Ising}} + \underbrace{\tau_i^x + \lambda \tau_i^z \tau_{i+1}^z}_{\text{quantum Ising}} + \Delta \left(\sigma_i^x \tau_i^x + \lambda \sigma_i^z \sigma_{i+1}^z \tau_i^z \tau_{i+1}^z \right) \Big] , \tag{5.12}$$

which consists of two quantum Ising models (Ising models in a transversal field) coupled by four-spin interaction with strength $\lambda\Delta$, and another transversal field of strength Δ, that couples to the x-polarization $\sigma^x\tau^x$. Note the unconventional parameterization that keeps the transversal field at unity, and that the z-coupling of the individual quantum Ising models favors ferromagnetic alignment if $\lambda > 0$.

Hamiltonians (5.11) and (5.12) remain unchanged under the following symmetry operations, and combinations thereof, [132, 147]

$$\sigma^z \to -\sigma^z , \quad \tau^z \to -\tau^z , \quad \sigma \to \tau . \tag{5.13}$$

Together with the identity this gives eight operations that form a group isomorphic to the dihedral group of order four, D_4 [25, 147]. This is the symmetry group of a square, it contains four rotations or cyclic permutations and four reflections as is illustrated in Fig. 5.7. The group D_4 contains several subgroups four of which are invariant or normal in D_4. The four invariant subgroups are Z_2 (rotation of π), Z_4 (all rotations), and two times $Z_2 \times Z_2$ (rotation of π and two reflections, either with respect to the diagonals or to the axes that bisect the sides of the square) [161].

Suppose $\Delta > -1$, and the transversal fields in $\mathrm{H}^{\mathrm{qAT}}$ are turned off. Then, the 1D qAT model reduces to the 1D classical AT model. The groundstate is fully ordered as the two-spin Ising interaction enforces parallel alignment of the spins on each of the two individual Ising chains. The four-spin interaction does not discriminate between the relative orientations of the two Ising chains, thus the ordered groundstate is fourfold degenerate. Each of the four groundstates *spontaneously* breaks the D_4 symmetry. Now, when the transversal fields are turned on and set to unity, the order will prevail for sufficiently large values of λ. Yet, when lowering λ, quantum fluctuations induced by the transversal fields will eventually destroy the order at a critical value λ_c. The large-λ phase is ordered and the small-λ phase is disordered and, in this sense, λ plays the role of an inverse temperature.

Order parameters that signal D_4 symmetry breaking are, for example, the magnetizations of the individual Ising systems $m^\sigma = 1/L\sum_i \sigma_i^z$, and $m^\tau = 1/L\sum_i \tau_i^z$ [147], that, in order to reflect the fourfold degeneracy of the classical groundstate, can be combined to a complex order parameter

$$m = \frac{m^\sigma + m^\tau}{2} + \mathrm{i}\,\frac{m^\sigma - m^\tau}{2}\,. \tag{5.14}$$

A groundstate of the qAT model, that has a nonzero expectation value $\langle m\rangle \neq 0$, fully breaks the D_4 symmetry. If it does so in the absence of an external magnetic field, the symmetry breaking is spontaneous. Another order parameter is the polarization [147]

$$p = \frac{1}{L}\sum_i \sigma_i^z \tau_i^z\,. \tag{5.15}$$

It is, however, important and interesting to note that the polarization is itself $Z_2 \times Z_2$ symmetric (see Fig. 5.7c). One of the two $Z_2 \times Z_2$ subgroups of D_4, the one that contains the operations which change either both or no signs of (σ_i, τ_i), remains unbroken when a polarizing field is introduced in $\mathrm{H}^{\mathrm{qAT}}$ that couples to $\sigma_i^z\tau_i^z$. Consequently, a nonzero groundstate expectation value of the polarization can only indicate a partial breaking of the D_4 symmetry.

There exists a non-local unitary transformation that maps the qAT model onto a spin-$\frac{1}{2}$ XXZ chain of doubled length, the transformation is given in [147]. Since the number of sites is doubled when mapping the qAT model onto the XXZ chain by placing the duals of τ-spins on interstitial sites, it is convenient to rewrite $\mathrm{H}^{\mathrm{qAT}}$ with the lattice constant doubled,

$$\mathrm{H}^{\mathrm{qAT}} = -\sum_i \sigma_{2i}^x + \tau_{2i}^x + \Delta p_{2i}^x + \lambda\left(\sigma_{2i}^z\sigma_{2i+2}^z + \tau_{2i}^z\tau_{2i+2}^z + \Delta p_{2i}^z p_{2i+2}^z\right)\,, \tag{5.16}$$

with $p_{2i}^z = \sigma_{2i}^z\tau_{2i}^z$. Define the duality transformation,

$$\sigma_{2i}^z \to \prod_{k\leq i}\sigma_{2k}^x\,,\quad \sigma_{2i}^x \to \sigma_{2i-1}^z\sigma_{2i+1}^z\,, \tag{5.17}$$

and likewise for the τ-spins, which connects the large-λ to the small-λ region by mapping $\mathrm{H}^{\mathrm{qAT}}(\lambda) \to \lambda\mathrm{H}^{\mathrm{qAT}}(1/\lambda)$. Then, the non-local unitary transformation of an infinite system consists of the following five steps:

1. Duality transformation on τ-spins and renaming.
2. Duality transformation on all spins.
3. Use $\sigma^z\sigma^x = \mathrm{i}\sigma^y$.
4. Rotation $\sigma^z \to \sigma^y$ and $\sigma^y \to -\sigma^z$.
5. Sublattice basis rotation $\sigma_{2i+1}^{x/y} \to -\sigma_{2i+1}^{x/y}$.

The detailed effect of each transformation step is shown in Table 5.1. Steps 1 and 2 use $(\sigma^{x/z})^2 = \mathbb{1}$, a property of spin-$\frac{1}{2}$ Pauli matrices $\sigma^x = 2\mathrm{S}^x$. Transformed τ-variables are placed on odd (interstitial) sites, which is why in step 2 they can be

Table 5.1: Operator transformation under mapping $\mathrm{H}^{\mathrm{qAT}} \to \mathrm{H}^{\mathrm{XXZ}}$. The three lines at the top are the local order parameters of the qAT model. The middle block maps on unit-bonds and the last three lines on λ-bonds of the XXZ chain.

	step 1	step 2	step 3	step 4	XXZ
σ^z_{2i}	$\cdots$	$\prod\limits_{k\leq 2i} \sigma^x_k$	$\cdots$	$\cdots$	$\prod\limits_{k\leq 2i} 2(-1)^k \mathrm{S}^x_k$
τ^z_{2i}	$\prod\limits_{k\leq i} \sigma^x_{2k-1}$	$\prod\limits_{k\leq 2i} \sigma^z_k$	$\cdots$	$\prod\limits_{k\leq 2i} \sigma^y_k$	$\prod\limits_{k\leq 2i} 2(-1)^k \mathrm{S}^y_k$
p^z_{2i}	$\sigma^z_{2i} \prod\limits_{k\leq i} \sigma^x_{2k-1}$	$\prod\limits_{k\leq 2i} \sigma^x_k \sigma^z_k$	$\prod\limits_{k\leq 2i} -\mathrm{i}\sigma^y_k$	$\prod\limits_{k\leq 2i} \mathrm{i}\sigma^z_k$	$\prod\limits_{k\leq 2i} 2\mathrm{i}\mathrm{S}^z_k$
σ^x_{2i}	$\cdots$	$\sigma^z_{2i}\sigma^z_{2i+1}$	$\cdots$	$\sigma^y_{2i}\sigma^y_{2i+1}$	$-4\mathrm{S}^y_{2i}\mathrm{S}^y_{2i+1}$
τ^x_{2i}	$\sigma^z_{2i-1}\sigma^z_{2i+1}$	$\sigma^x_{2i}\sigma^x_{2i+1}$	$\cdots$	$\cdots$	$-4\mathrm{S}^x_{2i}\mathrm{S}^x_{2i+1}$
p^x_{2i}	$\sigma^z_{2i-1}\sigma^x_{2i}\sigma^z_{2i+1}$	$\sigma^z_{2i}\sigma^x_{2i}\sigma^z_{2i+1}\sigma^x_{2i+1}$	$-\sigma^y_{2i}\sigma^y_{2i+1}$	$-\sigma^z_{2i}\sigma^z_{2i+1}$	$-4\mathrm{S}^z_{2i}\mathrm{S}^z_{2i+1}$
$\sigma^z_{2i}\sigma^z_{2i+2}$	$\cdots$	$\sigma^x_{2i+1}\sigma^x_{2i+2}$	$\cdots$	$\cdots$	$-4\mathrm{S}^x_{2i+1}\mathrm{S}^x_{2i+2}$
$\tau^z_{2i}\tau^z_{2i+2}$	σ^x_{2i+1}	$\sigma^z_{2i+1}\sigma^z_{2i+2}$	$\cdots$	$\sigma^y_{2i+1}\sigma^y_{2i+2}$	$-4\mathrm{S}^y_{2i+1}\mathrm{S}^y_{2i+2}$
$p^z_{2i}p^z_{2i+2}$	$\sigma^z_{2i}\sigma^x_{2i+1}\sigma^z_{2i+2}$	$\sigma^x_{2i+1}\sigma^z_{2i+1}\sigma^x_{2i+2}\sigma^z_{2i+2}$	$-\sigma^y_{2i+1}\sigma^y_{2i+2}$	$-\sigma^z_{2i+1}\sigma^z_{2i+2}$	$-4\mathrm{S}^z_{2i+1}\mathrm{S}^z_{2i+2}$

renamed and labelled σ. The identity used in step 3, again, only holds for spin-1/2 Pauli matrices. Step 5 is just the unitary transformation (3.18) that can be used to invert the sign of off-diagonal elements in XXZ Hamiltonians on bipartite lattices. Finally, after step 5, $\mathrm{H}^{\mathrm{qAT}}$ takes the form of the XXZ Hamiltonian (1.4) [147],

$$\begin{aligned}\mathrm{H}^{(5)} = \sum_i \big[&\sigma^x_{2i}\sigma^x_{2i+1} + \sigma^y_{2i}\sigma^y_{2i+1} + \Delta\sigma^z_{2i}\sigma^z_{2i+1} \\ &+\lambda\left(\sigma^x_{2i+1}\sigma^x_{2i+2} + \sigma^y_{2i+1}\sigma^y_{2i+2} + \Delta\sigma^z_{2i+1}\sigma^z_{2i+2}\right)\big]\,,\end{aligned} \tag{5.18}$$

and it follows that $\mathrm{H}^{\mathrm{qAT}}(\lambda,\Delta) \to 4\mathrm{H}^{\mathrm{XXZ}}(\lambda,\Delta)$. The D_4 symmetry of the qAT model is thus a hidden symmetry of the XXZ chain.

With the mapping at hand, (dis)order parameters of the qAT model give observables to characterize the phases of the XXZ chain with respect to the hidden order. Local magnetizations (σ^z_{2i} and τ^z_{2i}) and polarization (p^z_{2i}) can be read off directly from the first three lines in Table 5.1. They transform into non-local string observables in the XXZ chain. The local polarization becomes

$$p^z_{2i} \to P_z(i) = \prod_{k\leq 2i} 2\mathrm{i}\mathrm{S}^z_k\,, \tag{5.19}$$

a longitudinal string observable in the XXZ chain. Based on [147], Yamanaka et al. [148] defined a similar quantity D_z, which transforms from a string of transversal local polarizations (see third line in the middle block of Table 5.1),[2]

$$\prod_{k\leq 2i} p^x_{2i} \rightarrow D_z(i) = \prod_{k\leq i} -4\mathrm{S}^z_{2k}\mathrm{S}^z_{2k+1} = \prod_{k\leq 2i+1} 2\mathrm{i}\mathrm{S}^z_k \,. \tag{5.20}$$

It is essentially the product of spins on unit-bonds in the XXZ chain. The last equation, which holds only if the string contains an even number of spins, shows the subtle difference to the polarization (5.19), the string extends a *single* site further. Thus, if $D_z(i)$ is made up of an even number of spins, $P_z(i)$ must be made up of an odd number. A nonzero expectation value of D_z signals order in the p^x-strings, which means disorder in the local order parameters of the qAT model. It is thus a *disorder* parameter [162, 163]. But from duality transformation (5.17), we see that the p^x-string is dual to the local polarization. It is thus also the *order* parameter of the dual system, that is obtained by performing duality transformation (5.17) an all spins (without renaming, of course). This is a consequence of the self-duality property of the qAT model. In the XXZ chain, the duality transformation translates into the simple shift by one lattice site. As discussed in Sect. 5.2, the notion of order and disorder depends on the deliberate choice of reference dimers, which corresponds to the deliberate choice of discussing order either in terms of the qAT (5.12) model or its dual.

From Table 5.1 it can be seen that the qAT magnetization order parameters become strings of transversal components of the spin operator. The alternating sign is the effect of step 5, the sublattice basis rotation. In strings of an even number of spins, the effect of the alternating sign is the same as that of the of the imaginary i, in the z-string, which comes from step 3. We could follow [147, 148] and define the following transversal string observable

$$D_{\pm}(i) = \prod_{k\leq i} -2(\mathrm{S}^+_{2k}\mathrm{S}^-_{2k+1} + \mathrm{S}^-_{2k}\mathrm{S}^+_{2k+1})\,, \tag{5.21}$$

the nonzero expectation value of which signals disorder of the qAT model. However, in Sect. 6.2, we shall find it more convenient to construct an (improved) estimator for the following quantity,

$$D_x(i) = \prod_{k\leq i} -4(\mathrm{S}^x_{2k}\mathrm{S}^x_{2k+1})\,, \tag{5.22}$$

which may, at first sight, look like the equivalent of the local qAT magnetization τ^z_{2i}, but is its dual, a string of τ^x_{2i} (see Table 5.1). It is thus a disorder parameter [162, 163] of the qAT model, but again we suppose that D_x can equally well be considered an order parameter of the dual system. Contrary to D_z, D_x is related to a full breaking of the D_4 symmetry (as is $D_{\pm}$).

So far, the discussion applies to the infinite system, we have neither specified an origin (or starting value in sums and products), nor a chain length L of the qAT model. With the doubling of sites, when mapping the qAT model onto the XXZ chain, the number of spins in the XXZ chain is always even. Periodic boundary conditions

---

[2] The product rule is reversed here in comparison to the original work [148], which is merely a matter of convention.

(pbc) in the XXZ chain correspond to pbc in the qAT model, but with the added feature of explicitly selecting a sector with even parity with respect to the product operators $\prod_i \sigma_i^x$ and $\prod_i \tau_i^x$ [159, 164], where the products run over all L sites of the qAT model. The effect of these operators is to flip all σ- and τ-spins, respectively. Thus, by considering the XXZ chain with pbc, one is restricted to consideration of states in the qAT model that are symmetric under global flips of all σ- and/or τ-spins. With these considerations in mind, we define the following sum of strings for further use in measurements related to the hidden D_4 symmetry,

$$D_{z/x} = \frac{1}{L} \sum_{i=0}^{L-1} D_{z/x}(i) \,, \tag{5.23}$$

where we have artificially introduced an origin, such that all products in the definition of string observables start at 0, and L is the number of sites in the qAT model, i.e. half the number of sites in XXZ chain. Note that if we let the string of the polarization (5.19) start at index 0, it becomes imaginary. We could alternatively let it start at 1, it can then be viewed as bound to λ-bonds in contrast to the string D_z which is bound to unit-bonds.

Spin-1 and the String Order Parameter. The valence bond solid picture, and the structure of the disordered flat phase in RSOS models, translated into the language of the spin-1 chains, reveal that the Haldane phase has antiferromagnetic order but positional disorder, also called liquid Néel order [142] (see Sect. 5.2). The groundstate of the uniformly coupled isotropic spin-1 chain is located inside the Haldane phase and breaks a hidden $Z_2 \times Z_2$ symmetry [165, 166]. By a non-local unitary transformation the AF spin-1 chain can be mapped onto a ferromagnetic model that explicitly exhibits the $Z_2 \times Z_2$ symmetry. A state of perfect liquid Neél order will be transformed into a state with all nonzero spins aligned. An operator that performs this task is given by [166, 167]

$$\mathrm{U} = \mathrm{U}^{-1} = \prod_{j<k} \mathrm{e}^{\mathrm{i}\pi\, \mathrm{S}_j^z\, \mathrm{S}_k^x} \,. \tag{5.24}$$

After the transformation, the spin-1 XXZ Hamiltonian takes the form

$$\mathrm{UHU}^{-1} = \sum_j \mathrm{S}_j^x\, \mathrm{e}^{\mathrm{i}\pi\, \mathrm{S}_{i+1}^x}\, \mathrm{S}_{i+1}^x + \mathrm{S}_j^y\, \mathrm{e}^{\mathrm{i}\pi(\mathrm{S}_i^z + \mathrm{S}_{i+1}^x)}\, \mathrm{S}_{i+1}^y + \Delta\, \mathrm{S}_j^z\, \mathrm{e}^{\mathrm{i}\pi\, \mathrm{S}_i^z}\, \mathrm{S}_{i+1}^z \,, \tag{5.25}$$

which in fact holds for arbitrary integer spin. In the special case $S = 1$, the Hamiltonian simplifies to [165, 166]

$$\mathrm{UHU}^{-1} = -\sum_j \mathrm{S}_j^x\, \mathrm{S}_{i+1}^x + \mathrm{S}_j^y\, \mathrm{e}^{\mathrm{i}\pi(\mathrm{S}_i^z + \mathrm{S}_{i+1}^x)}\, \mathrm{S}_{i+1}^y + \Delta\, \mathrm{S}_j^z\, \mathrm{S}_{i+1}^z \,, \tag{5.26}$$

due to the fact that $\mathrm{e}^{\mathrm{i}\pi\, \mathrm{S}_i^\alpha}\, \mathrm{S}_i^\alpha = -\,\mathrm{S}_i^\alpha$. U(1) symmetry is destroyed by the transformation, yet there remains a discrete $Z_2 \times Z_2$ symmetry under rotations of π about the x

and z axes. The order parameters that measure spontaneous breaking of this symmetry are magnetizations in the x and z-direction in the transformed system. Translated back into the original system, these become string observables [166], such as

$$\tilde{\mathrm{S}}_j^z = \mathrm{e}^{\mathrm{i}\pi \sum_{l=1}^{j-1} \mathrm{S}_l^z}\, \mathrm{S}_j^z\,, \tag{5.27}$$

which acts as order parameter of the Haldane phase [142]. Alternatively, the string order parameter can be defined in terms of a string correlation function [168]. Note the parallels to the previous discussion on the qAT model, i.e. a non-local string observable to detect the spontaneous breaking of a hidden $Z_2 \times Z_2$ symmetry, but also the different mechanism, though non-local in both cases, to make the hidden symmetry visible and the difference in the definition of the string observable.

However, den Nijs and Rommelse [142] also introduced a string without spin(s) at the end which they termed a "familiar type of disorder operator", and which has only recently gained attention again [17],

$$G_{ji}^z = \prod_{k=j}^{i} \mathrm{e}^{\mathrm{i}\pi\, \mathrm{S}_k^z}\,. \tag{5.28}$$

In terms of the RSOS model (see Sect. 5.2), it is the order parameter of the RSOS flat phase which corresponds to a disordered singlet phase in the spin-1 chain reached, e.g., by introducing a sufficiently strong single-ion anisotropy which favours the state with local $m_i = 0$. This phase is not the same as the dimerized phase, which is, however, also a disordered singlet phase.[3] If we define for the spin-1 chain

$$D_z(i) = \prod_{k\le i} \mathrm{e}^{\mathrm{i}\pi\, \mathrm{S}_k^z}\,, \tag{5.29}$$

then, in the thermodynamic limit, $1/L \sum_i D_z(i)$ is zero in the Haldane phase, because G_{ji}^z is zero in the Haldane phase [142], but nonzero in the dimerized phases D1 and D2, which follows from the similarity of the dimerized phases and the RSOS flat phase, but can also be seen easily from considering the extreme points of isolated two-spin systems (i.e. λ being either 0 or ∞). It thus serves as order parameter in the transition H–D1/2. Note, that there is no need here, to artificially introduce reference dimers, because there is no direct transition between the physically equivalent phases D1 and D2 as in the spin-$\frac{1}{2}$ chain. In order to distinguish D1 from D2, however, this would be indeed necessary.

The same considerations, concerning the hidden breaking of a $Z_2 \times Z_2$ symmetry and detection by a generalized version of the string order parameter (5.27), also apply to homogeneous spin-S chains with larger spins, $S > 1$ [169–172].

String observables in mixed spin chains. A mapping $\mathrm{S}^z \to \mathrm{S}^z - 1/2$, for the small spins in a ferrimagnetic mixed spin chain ($S = 1, 1/2$) with single-ion anisotropy has

---

[3] The RSOS flat phase is a "gas" of disordered (±1)-excitations in a background of $m = 0$ spins, while the dimerized phase can be considered a "gas" of disordered dimer "excitations", with ±1 followed immediately by ∓1, in a "background" of 0-0 dimers (see Fig. 5.2 in Sect. 5.2).

been proposed and tested in [173]. This transforms $m = \pm 1/2$ into a variable with values 0 and 1, which can then be inserted into an exponential operator to give real values just like with spin-1's. Critical exponents based on this extended string order parameter were shown to satisfy a standard scaling relation [173]. Here, we follow a different route, mainly because this mapping is designed to reveal the Haldane-like structure of "trimers" [174] in the phase with small single-ion anisotropy, but also because a natural generalization to other half-odd integer spins, such as $S = 3/2$ in MB, is not so obvious.

First, we note that the basic element in the definition of the string observables (5.19) and (5.20) is $2\mathrm{i}\mathrm{S}_i^z = \mathrm{i}\sigma^z$. The next thing we note is that, if we define a similar string for the spin-1 chain in terms of subspins $\vec{\mathrm{s}}_{i1}$ and $\vec{\mathrm{s}}_{i2}$, the order parameters of the RSOS flat phase (5.28), and (5.29), emerges, because $2\mathrm{i}\mathrm{s}_{i1}^z 2\mathrm{i}\mathrm{s}_{i2}^z = \mathrm{i}\sigma_{i1}^z \mathrm{i}\sigma_{i2}^z$, is the same operator as $\mathrm{e}^{\mathrm{i}\pi\,\mathrm{S}_i^z}$ (for symmetrized subspins!). It takes the value $-1(+1)$, if the subspins are equally (oppositely) aligned, i.e. if $m_i = \pm 1(0)$.

To formalize the definition of string observables for general mixed spin chains, we define Σ-variables on every site as

$$\Sigma_i^{z/x} = \prod_{j=1}^{2S_i} \mathrm{i}\sigma_{ij}^{z/x} , \tag{5.30}$$

where $2S_i$, is the number of (symmetrized) subspins at site i, constituting a spin of size S_i. Now we define finite-system strings simply as

$$D_{z/x,2i} = \prod_{k=0}^{i-1} \Sigma_{2k}^{z/x} \Sigma_{2k+1}^{z/x} = \prod_{k=0}^{2i-1} \Sigma_k^{z/x} , \tag{5.31}$$

which gives (5.20) if $S_i = 1/2$, and every second of (5.29) if $S = 1$, with a slight change in the meaning of i, which we have here chosen such that the index $2i$ in (5.31) counts the number of spins contained in the string. And the observable to be measured will be

$$D_{x/z} = \frac{2}{L} \sum_{i=1}^{L/2} D_{x/z,2i} . \tag{5.32}$$

We are aware, that we have not presented a conclusive line of arguments to show that longitudinal and transversal strings defined in terms of Σ-variables relate to a hidden spontaneous symmetry breaking, presumably of a $Z_2 \times Z_2$ symmetry or sub-symmetry. This, however, is our *conjecture*. With the emphasis on computation, we have not the theoretical means to give a proof, and consider the issue unresolved and future work. We shall, however, briefly sketch possible ways to proceed in the following.

In general mixed spin chains it is always possible to define a backbone of subspins, such that subspins that are neighbours on the backbone belong to different sublattices of the original spin chain, and view every subspin as located on a single site. For uniform couplings, this backbone can be mapped on a qAT model, thus revealing the hidden D_4 symmetry. More general couplings would have to be caught by introduction of coupling parameters λ and Δ that differ from site to site. Symmetrization of subspins can be "simulated" by the introduction of a sufficiently strong ferromagnetic coupling in-between subspins of the same spin. Due to symmetrization, and even more, the interaction between subspins on neighbouring sites, however, interactions beyond the nearest neighbour on the backbone are inevitably generated. This non-nearest-neighbour interactions would lead to non-local multi-site interactions in the qAT model. We conjecture, that this complex of non-local multi-site interactions does not change the symmetry group of the qAT model. It would further have to be shown, that it only comprises irrelevant operators. Alternatively, one might consider a reduced backbone, by choosing only a single subspin at every site. This corresponds to the idea, that the critical boundary between different VBS configurations of general mixed and uniform spin chains, "hosts" a critical spin-$\frac{1}{2}$ subchain [43, 44]. The reduced backbone can be mapped on the qAT model, with, again, non-local interactions generated by symmetrization of subspins, but also of the remaining subspins that do not belong to the reduced backbone.

To conclude this section on hidden symmetry, we anticipate the results chapter of this thesis, and state that the string observables defined above, do indeed show (dis)order-parameter-like behaviour, with critical exponents that seem to fit into the framework set in the next section when tolerating another unresolved intriguing aspect.

5.5 Gaussian Description and the Fundamental Scaling Dimension

In two-dimensional Euclidean space the Gaussian model describes a free bosonic massless (gapless) scalar field, a string of coupled quantum oscillators [7]. Its Hamiltonian can be written

$$\mathrm{H}^{\mathrm{G}} = \frac{v}{2\pi} \int \mathrm{d}r \, \frac{1}{K} (\partial_r \Phi)^2 + K (\partial_r \Theta)^2 \,. \tag{5.33}$$

The fields Φ and Θ are dual to each other, and $\Pi = -\partial_r \Theta / \pi$ and Φ are canonically conjugate with commutation relation $[\Pi(r_1), \Phi(r_2)] = -\mathrm{i}\pi\delta(r_1 - r_2)$.

The Gaussian model is critical for every value of the dimensionless coupling $K > 0$, and can be solved exactly. The asymptotic form of correlation functions of exponentials of the fundamental degrees of freedom, the fields Φ and Θ, is [24, 133]

$$\left\langle \mathrm{e}^{\mathrm{i}n\Theta(r)} \mathrm{e}^{-\mathrm{i}n\Theta(0)} \right\rangle \sim |r|^{-n^2/(2K)} \,, \quad \left\langle \mathrm{e}^{\mathrm{i}m\Phi(r)} \mathrm{e}^{-\mathrm{i}m\Phi(0)} \right\rangle \sim |r|^{-m^2 K/2} \,. \tag{5.34}$$

The elementary excitations of the Gaussian model are two types of topological excitations with integer topological charges n and m. The topological excitations are usually interpreted as spin-wave and vortex excitations, and the topological charges are the wave number and vorticity, respectively. The duality transformation $\Phi \leftrightarrow \Theta$, $K \to 1/K$, maps spin-wave into vortex excitations and *vice versa*. The differentiation between spin-wave and vortex excitations is a matter of convention. Combined spin-wave and vortex operators are the primary scaling operators of the Gaussian model, with scaling dimension [133] and conformal spin [7] given by

$$x_{n,m} = \frac{n^2}{4K} + \frac{m^2 K}{4} \,, \tag{5.35}$$

and

$$s_{n,m} = \frac{nm}{2}\,, \tag{5.36}$$

respectively. The scaling dimensions $x_{n,m}$, of the Gaussian model are parameterized by the single dimensionless coupling constant K, with which they vary continuously. It follows that dual excitations satisfy $x_{n,0}x_{0,m} = n^2m^2/16$. If a model can be brought into Gaussian form, exact or by approximations, all its correlation functions are known. Generally, the mapping is non-trivial, and approximations form an essential ingredient.

In this section, the Gaussian model will be introduced for the spin-$\frac{1}{2}$ chain, which is sufficient to set the framework. It is established that critical fluctuations at, e.g., bond alternation driven transitions in the XXZ spin-1 chain [149, 150, 175, 176], and even in higher spin-S chains [175, 177], can be described by a Gaussian critical theory with continuously varying critical exponents. The transformation to a Gaussian model, however, is considerably more complicated in that case [178, 179], involving, for example, different species of fermions [180] and non-abelian bosonization [7, 181]. The isotropic spin-1 chain with bond alternation has been studied theoretically and numerically in [182]. The Gaussian behaviour, that critical exponents depend on the exchange anisotropy, has been confirmed numerically in [149, 150, 175]. On the critical boundary H–D1/2 it can, like the spin-$\frac{1}{2}$ chain on the boundary D1–D2 also, be described by a Wess–Zumino–Witten (WZW) model with Kac–Moody central charge $k = 1$ [183], which is equivalent to a Gaussian model, that has Virasoro central charge $c = 3k/(2+k) = 1$ [181, 184].[4] The mapping of the spin-$\frac{1}{2}$ XXZ chain to the Gaussian model is described in detail for example in [8, 24]. The following is a brief summary.

The first step is, after a sublattice basis rotation (3.18), to express the spin Hamiltonian in terms of hopping spinless fermions. Presence of a fermion represents a spin-up, absence a spin-down. In order to obtain purely fermionic commutators, the simple identification does not work. The Jordan–Wigner transformation [146, 189, 190] introduces an operator string that takes care of this, at the cost of a non-local transformation law which creates subtleties in the definition of boundary conditions. The number of fermions is the number of up-spins, and the (shifted) fermion density corresponds the magnetization. Zero magnetization corresponds to half-filling, and a magnetic field is the chemical potential in the fermion language. The spin-flip term becomes the kinetic fermionic hopping term and the z-interaction of spins induces interaction of fermions. At the XY-point, $\Delta = 0$, the fermions are free and can be solved exactly after Fourier transforming into momentum space [190, 191]. The energy of elementary excitations of free fermions is given by the dispersion [191], $E = -\cos k$. In the groundstate, states are filled up to the Fermi level, which at half-filling is $k_\mathrm{F} = \pi/2$, and the velocity of elementary excitations at the Fermi level is $v = \sin k_\mathrm{F} = 1$, also called Fermi velocity.

The next step is to make the discrete hopping Hamiltonian continuous by introducing fermionic fields and approximating the dispersion of elementary excitation by a

---

[4] Sometimes general spin-S chains are referred to as WZW models with Kac–Moody central charge $k = 2S$, which are not equivalent to the Gaussian model with Virasoro central charge $c = 1$. This refers to integrable spin-S chains [185], where the Hamiltonian is polynomial in the spin–spin interaction [175, 186]. The bond alternating spin-1 XXZ chain is not the integrable spin-1 chain. A crossover from $k = 2S = 2$ criticality, i.e. $c = 3/2$, to $c = 1$ was studied in [187, 188].

straight line. This model, i.e. one-dimensional moving fermions with linear dispersion, is also called Tomonaga–Luttinger model, or Luttinger liquid [8, 130, 192], in reference to its higher-dimensional equivalent, the Fermi liquid. The linearization of the dispersion law makes it necessary to introduce two different kinds of fermionic fields, left- and right-moving ones, and creates a Dirac sea of infinitely many negative energy fermions. The contribution of the Dirac sea to the energy must be taken care of by normal ordering of fermionic operators.

Due to the presence of a Dirac sea, which is a consequence of the linearized dispersion, and due to the fact that in one dimension, the Fermi surface consists of two points only, it is possible to express fermionic particle–hole excitations by bosonic creation operators. This step is called *bosonization*. As a result, two fields are introduced, Φ and Θ, the gradients of which measure fermionic densities [7, 8, 24],

$$\nabla\Phi(x) = \partial_x\Phi(x) = \pi(\rho_{\mathrm{R}}(x) + \rho_{\mathrm{L}}(x))\,, \quad \nabla\Theta(x) = \partial_x\Theta(x) = \pi(\rho_{\mathrm{R}}(x) - \rho_{\mathrm{L}}(x))\,, \tag{5.37}$$

where ρ_{R} and ρ_{L} are the densities of right- and left-moving fermions, respectively. Written in terms (of gradients) of the fields Φ and Θ, the XXZ Hamiltonian at $\Delta = 0$ becomes exactly that of the Gaussian model (5.33). The Gaussian parameters, also called Luttinger parameters in that context, are $v = 1$ and $K = 1$, here. Periodic boundary conditions in the fermionic fields lead to $\Phi(x + L) = \Phi(x) + \pi N$ and $\Theta(x + L) = \Theta(x) + \pi J$, with the topological charges N (total fermion number) and J (difference of total charges of the left- and right-moving fermions) [8, 24]. This periodicity condition for bosonic fields motivates the interpretation of Φ and Θ as angular variables [8, 24, 192].

The linearization of the dispersion is the crucial approximation that makes bosonization possible, and consequently the interacting ($\Delta \neq 0$) model solvable. Interacting fermions scatter, at low temperature this scattering processes will take place close to the Fermi surface, where the assumption of linear dispersion is well justified. For left- and right-moving spinless fermions, there are essentially three possible scattering processes. The effect of backward and forward scattering is to modify the Luttinger parameters. As the interaction is controlled by Δ, these parameters become functions thereof, $v = v(\Delta)$ and $K = K(\Delta)$. Another process, called umklapp scattering, however, introduces a new term in the Gaussian Hamiltonian, which becomes

$$\mathrm{H} = \frac{v}{2\pi}\int \mathrm{d}x \left[\frac{1}{K}(\partial_x\Phi)^2 + K(\partial_x\Theta)^2 - u\cos(4\Phi)\right]\,. \tag{5.38}$$

This is the sine-Gordon model [193], its a Gaussian model of non-interacting bosons, subject to a “potential” term $\cos(4\Phi)$ [24]. The effect of this term is to couple sectors of different topological charge J. It has scaling dimension $x_{0,4} = 4K$, so for $K < 1/2$ it becomes relevant and drives the system away from criticality, this is where the Gaussian type critical behaviour of the sine-Gordon model ends. Precisely at $K = 1/2$, the term is marginal and induces logarithmic corrections. For $K > 1/2$ and $u > 0$ the flow is towards the Néel ordered fixed point.

Spin operators in terms of bosonic fields are composed of staggered and uniform parts. The staggered parts take the form [8, 179]

$$\mathrm{S}^z(r) \sim (-1)^r\cos(2\Phi(r))\,, \quad \mathrm{S}^+(r) \sim (-1)^r\mathrm{e}^{-\mathrm{i}\Theta(r)}\,, \tag{5.39}$$

from which, with (5.34), the leading long-distance behaviour of longitudinal and transversal equal-time correlation functions of the XXZ chain follow [8, 130, 179],

$$G_z(r) \sim |r|^{-2K}\,, \quad G_\pm(r) \sim |r|^{-\frac{1}{2K}}\,. \tag{5.40}$$

These two correlation functions must be equal at the SU(2) symmetric, isotropic point, which forces $K(\Delta = 1) = 1/2$, so the isotropic point is the point, where the cosine term in the sine-Gordon Hamiltonian generates the logarithmic corrections [8, 24].

Staggered exchange adds another term to the sine-Gordon Hamiltonian, in terms of the bosonic fields it is given by [24],

$$(-1)^i \vec{\mathrm{S}}_i \vec{\mathrm{S}}_{i+1} \sim \sin(2\Phi) \sim \mathrm{e}^{\mathrm{i}2\Phi} - \mathrm{e}^{-\mathrm{i}2\Phi}\,. \tag{5.41}$$

Staggered exchange is, of course, bond alternation and in the XXZ chain, the coupling of the above term to the sine-Gordon Hamiltonian is zero at the critical point. We call the scaling dimension of this term the *fundamental* scaling dimension, because it relates to our fundamental control parameter. It is

$$x_\lambda = x_{0,2} = K\,. \tag{5.42}$$

$K(\Delta = 0) = 1$ and $K(\Delta = 1) = 1/2$, but the precise functional dependence of the Luttinger parameter K, and also of v, on the control parameter Δ has been lost during bosonization [8, 24]. Only the knowledge of the exact solution of the XXZ chain permits reconstruction of $K(\Delta)$ and $v(\Delta)$. The energy operator of the 8-vertex model has scaling dimension $x_{2,0}$, and depends on Δ as [133, 147],

$$x_{2,0} = x_{\mathrm{T}}^{8\mathrm{V}} = 2 - \frac{2}{\pi}\arccos(\Delta)\,. \tag{5.43}$$

The energy operator of the Ashkin–Teller model is dual to the energy operator of the 8V model. It has the scaling dimension $x_{0,2}$, with $x_{0,2}x_{2,0} = 1$, which is by (5.42) equal to x_λ or K, thus finally

$$K = x_\lambda = \frac{1}{x_{\mathrm{T}}^{8\mathrm{V}}} = \frac{\pi}{2\arccos(-\Delta)}\,. \tag{5.44}$$

From this dependence on Δ, all other scaling dimensions follow. Note, that at the aforementioned special point $\Delta = -1/\sqrt{2}$, $K = 2$, bond alternation therefore becomes irrelevant below.

An alternative method, if no exact solution is at hand, is to use the spin stiffness [20, 24, 194, 195], which relates to vK. The spin stiffness is the equivalent of the change in fermion density with a change of the chemical potential [8]. It is the response of the system to an energy flux, introduced by twisted boundary conditions $\mathrm{S}_L^z = \mathrm{e}^{i\Omega}\,\mathrm{S}_0^z$ [8],

$$L\frac{\partial^2 E}{\partial \Omega^2} = \frac{vK}{\pi}\,. \tag{5.45}$$

The Luttinger parameter v, is the velocity of elementary excitations. The exact solution gives for the spin-1/2 XXZ chain [164, 196–198], with $\gamma = \arccos\Delta$,

$$v = \frac{\pi}{2}\frac{\sin\gamma}{\gamma}\,. \tag{5.46}$$

Considering mixed spin models we now state the following:

Mixed spin models, MA and MB, are Gaussian.

This statement is to be understood in the sense, that critical properties of mixed spin chains, MA and MB, as defined in Sect. 5.1, can be described by the sine-Gordon model, which is a *Gaussian* model with a perturbing cosine-term. This is our *main hypothesis*, and we consider it the purpose of this thesis to test it by numerical methods. Put in a more conservative way, the above statement is the *main assumption* of this thesis, which can be used to self-consistently explain the observed data. We shall not present any further theoretical backup for our main hypothesis. However, the fact that mixed spin models do indeed exhibit bond alternation driven second-order phase transitions, suggests that the spin-size modulation can be (at least effectively) described by an irrelevant operator in (5.38). The presence of an irrelevant operator does not change the universality class of a critical phase transition, but it can, among other effects, renormalize coupling constants of relevant operators [199] and thus change the location of the critical point.

5.6 Logarithmic Corrections at the Isotropic Point

At the isotropic point the spin-$\frac{1}{2}$ chain shows logarithmic corrections in practically all of its observables. The leading singular behaviour of the inverse energy gap, i.e. the temporal correlation length, is modified by a multiplicative logarithmic factor [191, 200, 201],

$$\xi_\tau \sim |\delta|^{-2/3} |\ln|\delta||^{1/2} \,, \tag{5.47}$$

with δ a symmetric parameterization of bond alternation, i.e. $\delta = (\lambda - 1)/(\lambda + 1)$.[5] Similarly, the singular part of the free energy density, which in a quantum phase transition corresponds to the energy density of the groundstate, acquires a logarithmic modification [191, 200, 201]

$$f_\mathrm{s} \sim |\delta|^{4/3} |\ln|\delta||^{-1} \,, \tag{5.48}$$

and the asymptotic critical behaviour ($\delta = 0$) of the staggered spin–spin correlation function at large distances is [8, 179, 202]

$$G_\mathrm{s}(r) \sim r^{-1} (\ln r)^{1/2} \,. \tag{5.49}$$

The same type of corrections is supposed to be present also in the spin-1 chain [175, 182, 203–205], and in general isotropic spin-S [206]. The origin of the logarithmic corrections is the marginal irrelevance of the cosine-term in the sine-Gordon model at the isotropic point. This term originates from the umklapp scattering process.

Analysis of experimental data [207] showed, that the asymptotic regime, where the log-modified leading behaviour dominates, can only be seen vaguely very close to the critical point, where $\delta \lesssim 0.005$ or $\lambda \gtrsim 0.99$ (cf. Fig. 30 in [207]). Moreover, multiplicative logarithmic corrections are usually accompanied by a tail of additive

---

[5] For the spin-$\frac{1}{2}$ chain, $\delta_\mathrm{c} = 0$. More generally, the thermal critical singularities depend on $t = |\delta - \delta_\mathrm{c}|$. For small t, $|\delta - \delta_\mathrm{c}| \sim |\lambda - \lambda_\mathrm{c}|$ and δ can be replaced by λ.

logarithmic terms. To estimate exponents of logarithmic modification factors from scratch on the basis of simulation or experimental data is virtually impossible without detailed *a priori* knowledge of the corrections.

The renormalization group equations to the order necessary and sufficient here, for the thermal field $t \sim |\delta|$ (or more generally $t \sim |\delta - \delta_c|$) and possible other relevant fields h_i of the even or odd sector are [191, 208, 209]

$$\frac{\mathrm{d}t}{\mathrm{d}l} = (y_t - y_t b_t u)t\,, \tag{5.50}$$

$$\frac{\mathrm{d}h_i}{\mathrm{d}l} = (y_i - y_i b_i u)h_i\,. \tag{5.51}$$

The coefficients y_t and y_i are the RG eigenvalues that determine the standard critical exponents, while b_t and b_i can, in principle, be determined from what is called "operator product expansion" [25, 26], which will not be uttered here. The differential equation of the marginal field u through third order is [191, 209–211]

$$\frac{\mathrm{d}u}{\mathrm{d}l} = -a_2 u^2 - a_3 u^3\,, \tag{5.52}$$

where, owing to the marginality of the field, the linear term is missing and a_2 is given by the corresponding operator product expansion coefficient [25, 26]. Normalizing the two-point function of the operator that couples to the marginal field, yields $a_2 = \pi 4/\sqrt{3}$ [192, 206] in the spin-$\frac{1}{2}$ chain. The precise value of a_2, however, is not so important, it is non-universal and depends on the choice of the scale of u. The units of the marginal field can always be chosen such that, e.g. $a_2 = 1$. Ratios of b_t, b_i and a_2, and the ratio a_3/a_2^2, however, do not depend on the specific choice of the scale of u, they are universal. In the spin-$\frac{1}{2}$ chain, $a_3/a_2^2 = 1/2$ [210, 212]. Following Spronken et al. [191] we use $a_2 = 1$. For clarity, the coefficients are summarized in Table 5.2, where b_h is included as follows from the known logarithmic correction to the spin–spin correlation function (5.49).

The renormalization group equations (5.50)–(5.52) have been carefully studied for the dilute 4-state Potts model in two dimensions [209, 211, 213, 214]. In the dilute Potts model sites that carry the four-state variable can be unoccupied. An energy amount D is added for every occupied site and the standard Potts model emerges in the limit of large negative $D \to -\infty$. The dilution field is marginally irrelevant for all negative values $D < 0$ [209, 213]. Coefficients that turn the RG differential equations (5.50)–(5.52), into those studied in [209, 211, 213, 214], are included in Table 5.2 for comparison.. Universal quantities that follow from the RG coefficients y_t, b_t, y_h, b_h and a_2, are the same for the 4-state Potts model and for the spin-$\frac{1}{2}$ Heisenberg chain. However, it must be emphasized that the magnetic field of the Potts model is not the magnetic field of the Heisenberg chain, thus $y_h^{\mathrm{Potts}} \neq y_h^{\mathrm{HB}}$!

Table 5.2: Coefficients of RG equations (5.50)–(5.52) for the spin-$\frac{1}{2}$ Heisenberg chain (HB), as used in this thesis, and the 2D 4-state Potts (P) model.

	y_t	b_t	y_h	b_h	a_2	a_3
HB:	$\frac{3}{2}$	$\frac{1}{2}$	$\frac{3}{2}$	$-\frac{1}{6}$	1	$\frac{1}{2}$
P:	$\frac{3}{2}$	$-\frac{1}{2\pi}$	$\frac{15}{8}$	$-\frac{1}{30\pi}$	$-\frac{1}{\pi}$	$\frac{1}{2\pi^2}$

Structure of logarithmic corrections. The following presentation of solutions to the RG equations adopts the results of [211], and [214]. The solution to (5.51) is

$$\mathcal{X}_i(l)^{-1} := \frac{h_i(l)}{h_{i0}} = \mathrm{e}^{y_i l} \mathcal{Z}(l)^{-y_i b_i / a_2} \,, \tag{5.53}$$

where, for $h_i = t$, the solution of (5.50) follows with y_t and b_t. The function $\mathcal{Z}(l)$ is a shorthand for

$$\mathcal{Z}(l) := \frac{u_0}{u(l)} \frac{a_2 + a_3 u(l)}{a_2 + a_3 u_0} \,, \tag{5.54}$$

where $u(l)$ is the solution of (5.52). It can be written as

$$u(l) = u^{(2)}(l) f_{\mathrm{c}}^{(3)}(l) \,. \tag{5.55}$$

with

$$u^{(2)}(l) = \frac{u_0}{1 + a_2 u_0 l} \,, \tag{5.56}$$

the solution of (5.52) up to second order only, i.e. with $a_3 = 0$, and a multiplicative correction $f_{\mathrm{c}}^{(3)}(l)$, which accounts for the third order in (5.52).

The initial values of the scaling fields, t_0, h_{i0} and u_0, are model dependent and thus non-universal. The leading behaviour of observables at small t, with all other relevant fields set to zero, can be obtained by fixing the scale factor. Choosing the logarithmic scale factor $l = l^*$ such that $t(l^*) = 1$ (or some constant of $\mathcal{O}(1)$), the equation for l^* follows from (5.53),

$$l^* = -\nu \ln t_0 + \hat{\nu} \ln \mathcal{Z}(l^*) \,, \tag{5.57}$$

with the usual identification $\nu = 1/y_t$, and the universal hatted exponent

$$\hat{\nu} = \frac{b_t}{a_2} \,. \tag{5.58}$$

Note, that if $a_2 = 0$, $\mathcal{Z}(l) \equiv 1$ and the solution of (5.57), $l^* = -\nu \ln t_0$, produces the standard leading power-law behaviour. Logarithmic corrections enter the stage on the next level, when $a_2 \neq 0$ but $a_3 = 0$. In this case $\mathcal{Z}(l) = u_0/u^{(2)}(l) = 1 + u_0 a_2 l$ and (5.57) becomes a transcendental fixed point equation in l^* or, alternatively, in $\mathcal{Z}(l^*)$,

$$\mathcal{Z} = 1 + u_0 a_2 (-\nu \ln t_0 + \hat{\nu} \ln \mathcal{Z}) \,, \tag{5.59}$$

which can be solved approximately by iteration. Choosing $\mathcal{Z} = 1$ as initial guess gives $\mathcal{Z} \approx 1 - u_0 a_2 \nu \ln t_0$, where the error due to necessarily incomplete iteration is of order $\mathcal{O}(\mathcal{Z}^{-1})$. Depending on the value of $u_0 a_2$, it may be that the asymptotic regime $-u_0 a_2 \nu \ln t_0 \gg 1$, is entered only very close to the critical point, i.e. for very small values of t_0. Naturally, a second iteration produces further logarithmic terms. However, it was argued by many authors that it is not sufficient to consider RG equations (5.52) up to second order only [210, 211, 214, 215], i.e. then the third order term must be considered as well. The function $f_{\mathrm{c}}^{(3)}$ in (5.55), that considers corrections due to third order, was treated asymptotically as

$$f_{\mathrm{c}}^{(3)}(l) \sim 1 - \frac{a_3}{a_2^2}\frac{\ln l}{l} + O\left(\frac{1}{l}\right) , \tag{5.60}$$

by Salas and Sokal [211], and Shchur et al. [214], and approximately as

$$f_{\mathrm{c}}^{(3)}(l) \approx 1 - \frac{a_3}{a_2^2}\frac{\ln(l + 1/(a_2 u_0) + a_3/a_2^2)}{l + 1/(a_2 u_0)} , \tag{5.61}$$

by Nomura [210]. The significance and differences of the two above forms become important in numerical analysis via finite-size scaling where $l = \ln L$ (see Sect. 6.4).

The notation in $\mathcal{X}$ and $\mathcal{Z}$ can be conveniently used to express the scaling behaviour of observables. The scaling of the correlation length becomes

$$\xi_\tau(t_0, u_0) = \mathrm{e}^l \xi_\tau(t(l), u(l)) = \mathcal{X}^{-\nu}\mathcal{Z}^{\hat{\nu}}\xi_\tau(t_0\mathcal{X}^{-1}, u) \sim t_0^{-\nu}(-\ln t_0)^{\hat{\nu}} . \tag{5.62}$$

The singular part of the free energy density can be written

$$f(t_0, u_0) = \mathrm{e}^{-Dl} f(t(l), u(l)) = \mathcal{X}^{D\nu}\mathcal{Z}^{-D\hat{\nu}} f(t_0\mathcal{X}^{-1}, u) , \tag{5.63}$$

where thermodynamic observables follow from the derivatives with respect to t_0 and h_{i0}, i.e. [214]

$$C_t(t_0, u_0) = \mathcal{X}^{D\nu-2}\mathcal{Z}^{-D\hat{\nu}} C_t(t_0\mathcal{X}^{-1}, u) \sim t_0^{-\alpha}(-\ln t_0)^{\hat{\alpha}} , \tag{5.64}$$

$$M_i(t_0, u_0) = \mathcal{X}^{D\nu-\rho_i}\mathcal{Z}^{-D\hat{\nu}+\kappa_i} M_i(t_0\mathcal{X}^{-1}, u) \sim t_0^{\beta_i}(-\ln t_0)^{\hat{\beta}_i} , \tag{5.65}$$

$$\chi_i(t_0, u_0) = \mathcal{X}^{D\nu-2\rho_i}\mathcal{Z}^{-D\hat{\nu}+2\kappa_i} \chi_i(t_0\mathcal{X}^{-1}, u) \sim t_0^{-\gamma_i}(-\ln t_0)^{\hat{\gamma}_i} , \tag{5.66}$$

with

$$\rho_i = \frac{y_i}{y_t} \quad \text{and} \quad \kappa_i = \frac{y_i}{a_2}(b_t - b_i) , \tag{5.67}$$

and the hatted notation of the exponents of leading logarithms

$$\hat{\alpha} = -D\hat{\nu} , \tag{5.68}$$

$$\hat{\beta}_i = -D\hat{\nu} + \kappa_i , \tag{5.69}$$

$$\hat{\gamma}_i = -D\hat{\nu} + 2\kappa_i . \tag{5.70}$$

Finally, the scaling of the correlation function follows from the free energy density by the second derivative with respect to local fields, $\mathrm{d}^2 f/\mathrm{d}h_i(r_1)\mathrm{d}h_i(r_2)|_{h_i=0}$ [213],

$$G_i(r; t_0, u_0) = \mathrm{e}^{-2(D-y_i)l}\mathcal{Z}^{-2y_i b_i/a_2} G(r/e^l; t(l), u(l)) ,$$

with $r = |r_1 - r_2|$. Choosing $l = \ln r$, we get at criticality where $t_0 = 0$, the following asymptotic behaviour at sufficiently large r,

$$G_i(r; 0, u_0) = r^{-2(D-y_i)}\mathcal{Z}(\ln r)^{-2y_i b_i/a_2} G(1; 0, u(\ln r)) \sim r^{-2(D-y_i)}(\ln r)^{-2y_i b_i/a_2} , \tag{5.71}$$

which, of course, identifies the standard critical exponent of the correlation function via $\eta_i + D - 2 = 2(D - y_i)$, but also the corresponding hatted exponent

$$\hat{\eta}_i = -2y_i\frac{b_i}{a_2} . \tag{5.72}$$

The values of the exponents of leading logarithms are summarized in Table 5.3.

Table 5.3: Exponents of the leading logarithms for the spin-$\frac{1}{2}$ Heisenberg chain (HB) and the 2D 4-state Potts (P) model.

	$\hat{\nu}$	$\hat{\alpha}$	$\hat{\beta}$	$\hat{\gamma}$	$\hat{\eta}$
HB:	$\frac{1}{2}$	-1	0	1	$\frac{1}{2}$
P:	$\frac{1}{2}$	-1	$-\frac{1}{4}$	$\frac{3}{4}$	$-\frac{1}{8}$

From the definition of hatted exponents in terms of the coefficients of RG equations, scaling relations among them can be inferred, just as is the case for standard critical exponents. For example [216],

$$\hat{\alpha} = 2\hat{\beta}_i - \hat{\gamma}_i \,, \tag{5.73}$$

which follows directly from (5.68)–(5.70), or [217]

$$\hat{\eta}_i = \hat{\gamma}_i - \hat{\nu}(2 - \eta_i) \,, \tag{5.74}$$

following from (5.58)–(5.72) and the standard definition of η. Another important exponent, denoted $\hat{q}$, controls the logarithmic modification of the linear dependence of the correlation length on the system size L, i.e. $\xi \sim L(\ln L)^{\hat{q}}$, and it is related to the other exponents via [216]

$$\hat{q} = \hat{\nu} + \frac{\nu}{2-\alpha}\hat{\alpha} \,. \tag{5.75}$$

If hyperscaling holds, $D\nu = 2 - \alpha$, and the above relation becomes $\hat{q} = \hat{\nu} + \alpha/D$. Recalling the definition of $\hat{\alpha} = -D\hat{\nu}$ (5.68), it follows immediately that valid hyperscaling implies $\hat{q} = 0$ [216].

6 Computational Methods

This is the final chapter that covers background material. A detailed account of the two self-implemented numerical methods of data production, Lanczos diagonalization and the loop algorithm, will given in Sect. 6.1 and Sect. 6.2, respectively. This is followed by a description of analysis of statistical data obtained from the loop algorithm, reweighting (in Sect. 6.3) and finite-size scaling (in Sect. 6.4). The method to analyze exact data, extrapolation, is included in Sect. 6.1. Section Sect. 6.3 contains a description of the novel application of the reweighting method to improved estimators.

This is not intended to be a programmer's thesis. We shall therefore refrain from presenting examples of code, or a detailed discussion of our implementations. The code, partially commented, can be downloaded from the web.[1] It is free to be used, modified and distributed. Some remarks, however, will be given along the presentation in this chapter. We shall further not give a detailed account of numerical methods used as black boxes, but for completeness state them here, in the preamble to this chapter. Black box code that was used in this thesis, include: various routines from Numerical Recipes (NR) [218] in order to fulfill tasks such as minimization, root finding, diagonalization of small matrices and Levenberg–Marquardt minimization in non-linear least-χ^2 fits; routines from the LAPACK[2] to efficiently perform vector–matrix multiplication and diagonalization of real symmetric and complex Hermitian matrices; the MATPACK[3] library that provides various tested random number generators (RNG). The art of random number generation shall not be discussed either. We have tested several promising candidates of MATPACK, including the RNG's called Ran088, Ran255 and R19937 (the famous Mersenne twister), but for performance reasons Ran088 has become our standard choice. After comparing results to our own implementation of linear and non-linear fits, using NR routines, we used the convenient interactive plotting tool "gnuplot" instead.

Wherever possible, i.e. for the spin-$\frac{1}{2}$ chain, we checked the output of our implementations of the Lanczos method and the loop algorithm with exact analytical results, and compared the two methods to each other (as well as to results from implementations using the ALPS library [219] at an early stage of code production) on small systems where no exact analytical results are available. After a considerable time of debugging we considered our implementations to be correct to best of our testing abilities. With one exception in Sect. 6.1.4, we shall not present any test results, because there is not much to learn from them.

---

[1] Available at: `http://www.physik.uni-leipzig.de/~bischof`

[2] Available at `http://www.netlib.org/lapack`

[3] Available at `http://www.matpack.de`

6.1 Exact Diagonalization and Extrapolation

Energy levels of finite systems are related to scaling dimensions that, in turn, determine the critical exponents of a theory. From this point of view the exact diagonalization of Hamiltonians, or at least the exact knowledge of a few low-lying energy levels is of great value. The Hilbert space grows exponentially with system size and it is crucial to exploit symmetries, in order to pre-diagonalize the Hamiltonian into blocks of invariant symmetry-sectors and use degeneracies between sectors. Symmetries are discussed in in Sect. 6.1.1. The Lanczos algorithm to diagonalize large Hermitian matrices and the BST algorithm to extrapolate a series of exact finite-size estimates of energy levels or critical points will be outlined in Secs. 6.1.2 and 6.1.3. Final a test application shall be used to discuss some subtleties of the BST extrapolation method in Sect. 6.1.4.

6.1.1 Exploiting Symmetries

In its essence, the exploitation of symmetries[4] follows a simple and obvious recipe:

1. Construct a basis $|\phi\rangle$, that is invariant under given symmetries.
2. Calculate the matrix elements $\mathrm{H}_{\phi,\phi'} = \langle\phi|\,\mathrm{H}\,|\phi'\rangle$ to transform the Hamiltonian H to the new basis.

We choose the eigenstates of $\mathrm{S}^z_{\mathrm{tot}}$ as basis, and, first of all, introduce the scheme to represent the basis states numerically. A single spin of size S can take the values $m = -S, -S+1, \ldots, S$. Shifting by S gives an unsigned integer,

$$m^{\#} = m + S = 0, \ldots, 2S\,, \tag{6.1}$$

that serves as label of a single-spin state. States of L spins are then represented by L integers $m_i^{\#}$, $i = 1, \ldots, L$. For the spin-$\frac{1}{2}$ chain, $m_i^{\#} = 0, 1$ and the multi-spin state can be labelled by an unsigned integer given by the bit-pattern of single-spin states. For models involving general spins, such as MA (5.2) and MB (5.3), a generalized “bit pattern” can be used to define an integer label n of a basis state $|n\rangle \equiv |m_1^{\#}, \ldots, m_L^{\#}\rangle \equiv |m_1, \ldots, m_L\rangle$, e.g., by

$$n = \sum_{i=1}^{L} m_i^{\#} B_i\,, \quad B_i = B_{i+1}(1 + 2S_{i+1})\,, \quad B_L = 1\,. \tag{6.2}$$

Labels n and n', then conveniently serve as row- and column-index in the numerical representation of the full Hamiltonian matrix with matrix elements $\langle n|\,\mathrm{H}\,|n'\rangle$.

Conservation of the total magnetization M, can be trivially implemented by sorting out the corresponding basis states,

$$\left|\tilde{n}^M\right\rangle = |m_0, \ldots, m_{L-1}\rangle\,, \quad \text{with } \sum_i m_i = M\,, \tag{6.3}$$

---

[4] See [25, Sect. 9] for a detailed guide that shall be followed here.

Table 6.1: Number representation of the basis states of a small chain with $L = 4$, $|m_1^\#, \ldots, m_L^\#\rangle = |n\rangle$. The label n is calculated from (6.2) with the B_i given in brackets in the second line. The second and third column give the basecell of MA and MB, respectively.

spin setup:	$\frac{1}{2}-\frac{1}{2}-\frac{1}{2}-\frac{1}{2}$	$\frac{1}{2}-\frac{1}{2}-1-1$	$\frac{1}{2}-\frac{1}{2}-\frac{3}{2}-\frac{3}{2}$
$\{B_i\}$:	$\{8,4,2,1\}$	$\{18,9,3,1\}$	$\{32,16,4,1\}$
	$\lvert 0000\rangle = \lvert 0\rangle$	$\lvert 0000\rangle = \lvert 0\rangle$	$\lvert 0000\rangle = \lvert 0\rangle$
	$\lvert 0001\rangle = \lvert 1\rangle$	$\lvert 0001\rangle = \lvert 1\rangle$	$\lvert 0001\rangle = \lvert 1\rangle$
	$\lvert 0010\rangle = \lvert 2\rangle$	$\lvert 0002\rangle = \lvert 2\rangle$	$\lvert 0002\rangle = \lvert 2\rangle$
	$\lvert 0011\rangle = \lvert 3\rangle$	$\lvert 0010\rangle = \lvert 3\rangle$	$\lvert 0003\rangle = \lvert 3\rangle$
	$\vdots$	$\vdots$	$\vdots$
	$\lvert 1111\rangle = \lvert 16\rangle$	$\lvert 1122\rangle = \lvert 35\rangle$	$\lvert 1133\rangle = \lvert 63\rangle$

where $\tilde{n}^M$ is a new label. In the absence of an external magnetic field, the XXZ Hamiltonian is invariant under spin inversion and the spectra of sectors M and $-M$ are degenerate.

If periodic boundary conditions are applied, which will always be the case in this thesis, translation invariance implies the conservation of momentum. Generally, translation invariance can only hold with respect to the basecell. Let T denote the operator that shifts the spins by one lattice site. If the size of the basecell is l, T must be applied l times to shift the spins by one basecell, $\mathrm{T}^l |m_1, \ldots, m_L\rangle = |m_{l+1}, \ldots, m_L, m_1, \ldots, m_l\rangle$. The states

$$\left|\tilde{n}^{MP}\right\rangle = \frac{1}{\sqrt{N_{\mathrm{bc}}}} \sum_{j=0}^{N_{\mathrm{bc}}-1} \mathrm{e}^{\mathrm{i}\frac{2\pi}{N_{\mathrm{bc}}} jP}\, \mathrm{T}^{jl} \left|\tilde{n}^M\right\rangle , \tag{6.4}$$

are normalized eigenstates of T, that form an orthonormal basis of the sector with magnetization M and momentum $2\pi P/N_{\mathrm{bc}}$. $N_{\mathrm{bc}} = L/l$, is the number of basecells. The quantum number P, that takes the values $P = 0, \ldots, N_{\mathrm{bc}} - 1$, is the scaled momentum with respect to the basecells. We shall use P to label the corresponding sectors with conserved momentum. In homogeneous spin chains the size of a basecell is $l = 1$ (or 2 with bond alternation) and one can maximally profit from translational invariance by constructing bases of L (or $L/2$) orthogonal sectors, while the mixed spin chains MA and MB have $l = 4$, where a chain of, e.g., length $L = 20$ permits only five invariant P-sectors.

If the basecell is symmetric under space inversion (or reflection), the XXZ Hamiltonian is symmetric under space inversion. A reflection invariant basis can be constructed from

$$\left|\tilde{n}^{\pm}\right\rangle = \frac{1}{\sqrt{2}} \left(|n\rangle \pm \mathcal{P}\,|n\rangle\right) , \tag{6.5}$$

with the parity operator $\mathcal{P}$, defined by $\mathcal{P}\,|m_1, \ldots, m_L\rangle = |m_L, \ldots, m_1\rangle$. The eigenvalues of $\mathcal{P}$ are $\mathcal{S} = \pm 1$, and a state that conserves parity is either symmetric or

Table 6.2: Dimensions of invariant symmetry-sectors. This table compares the total dimension of a sector with magnetization M to the dimensions of its P-subsectors. $L = 20$ for MA, and 16 for MB. If two values are given, the sector is real and the first (second) value corresponds to the (anti-)symmetric parity-invariant subsector with $\mathcal{S} = +(-)$. Using the triple $MP\mathcal{S}$ to label the sectors (see main text), the largest sectors to be treated in this thesis were the complex sectors 010 and 020 of MA.

model	M	dimension	$P = 0$	$P = 1$	$P = 2$
MA	0	7 873 260	787 330+787 330	1 574 650	1 574 650
	1	7 473 840	748 074+746 694	1 494 768	1 494 768
	2	6 389 880	638 988+638 988	1 277 976	1 277 976
	3	4 912 850	491 850+490 720	982 570	982 570
MB	0	1 901 638	238 112+237 466	475 248	237 782+237 782
	1	1 828 656	228 582+228 582	457 164	228 582+228 582
	2	1 625 472	203 559+202 959	406 218	203 259+203 259
	3	1 334 032	166 754+166 754	333 508	166 754+166 754

antisymmetric under reflection. For $N_{\mathrm{bc}} \geq 3$, one can profit from combined exploitation of translation and reflection invariance. The quantum numbers P in (6.4) are only defined modulo N_{bc}, the sector $(N_{\mathrm{bc}} - P)$ is the same as sector $-P$ and reflection invariance ensures that sectors P and $-P$ are degenerate. The special sectors with $P = 0$, and – if the number of basecells is even – $P = N_{\mathrm{bc}}/2$, can be blocked into symmetric and antisymmetric parts. In the course of this work, we have become used to consider $S^a - S^a - S^b - S^b$ as the structure of basecells. This is, of course, not symmetric under reflection. Here, a better choice would have been $S^a - S^b - S^b - S^a$. We, however, trivially circumvented this problem by placing the center of reflection one site shifted with respect to the origin.

Thus, finally, the original basis of $\mathrm{S}^z_{\mathrm{tot}}$-eigenstates is decomposed into bases of different sectors labelled by the triple $MP\mathcal{S}$,

$$\left|\tilde{n}^{MP\mathcal{S}}\right\rangle = \begin{cases} \left|\tilde{n}^{MP\pm}\right\rangle = \frac{1}{\sqrt{2}}\left(\left|\tilde{n}^{MP}\right\rangle \pm \mathcal{P}\left|\tilde{n}^{MP}\right\rangle\right) & \text{if } P = 0, N_{\mathrm{bc}}/2\,, \\ \left|\tilde{n}^{MP0}\right\rangle = \left|\tilde{n}^{MP}\right\rangle & \text{else.} \end{cases} \tag{6.6}$$

For convenience, we use the labels $\mathcal{S} = \pm$ for $\mathcal{S} = \pm 1$, and $\mathcal{S} = 0$ for sectors that cannot be further decomposed by reflection symmetry. A sector $MP0$ is two-fold degenerate if $M = 0$, and four-fold degenerate if $M \neq 0$. The importance of symmetries becomes obvious when comparing the dimensions of various sectors. In Table 6.2 some numbers are listed for MA with $L = 20$, and (total dimension is 36^5) and MB with $L = 16$ (total dimension is 64^4).

6.1.2 Lanczos Tridiagonalization

The Lanczos algorithm [53] is a powerful iterative method to approximate one or a few dominant (usually the lowest) eigenvalues and eigenvectors of large Hermitian matrices. It starts with a suitable normalized initial state $|\phi_0\rangle$, that should have a finite overlap with the groundstate (or any other state the procedure aims at). Then, a set of orthonormal vectors is generated by successive application of the Hamiltonian accompanied by Gram–Schmidt orthogonalization,

$$|\phi'_{n+1}\rangle = \mathrm{H}|\phi_n\rangle - \sum_{i=0}^{n} H_{in}|\phi_i\rangle \,, \tag{6.7}$$

and normalization,

$$|\phi_{n+1}\rangle = \frac{|\phi'_{n+1}\rangle}{\|\phi'_{n+1}\|} \,. \tag{6.8}$$

The coefficients H_{in} in (6.7) are the components of the vector $\mathrm{H}|\phi_n\rangle$ along the previously generated vectors $|\phi_i\rangle$, in other words the matrix elements $\langle\phi_i|\mathrm{H}|\phi_n\rangle$. Using the hermiticity of H, inspection of matrix elements for $m \leq n$ yields

$$\begin{aligned} H_{mn} &= \langle\, \phi_m |\, \mathrm{H}|\phi_n\rangle = (\langle\, \phi_n |\, \mathrm{H}|\phi_m\rangle)^* \\ &= \left(\langle\phi_n|\phi'_{m+1}\rangle + \sum_{i=0}^{m} \langle\phi_i|\mathrm{H}|\phi_m\rangle\, \langle\phi_n|\phi_i\rangle \right)^* \\ &= \|\phi'_{m+1}\|\, \delta_{n,m+1} + \langle\phi_m|\mathrm{H}|\phi_n\rangle\, \delta_{nm} \\ &= \begin{cases} H_{nn} & \text{if } m = n\,, \\ \|\phi'_n\| & \text{if } m = n-1\,, \\ 0 & \text{else}\,. \end{cases} \end{aligned} \tag{6.9}$$

The case $m = n$ is a tautological statement, but the cases $m \neq n$ show that every new vector only needs to be orthogonalized with its two predecessors. Moreover, the norm $\|\phi'_2\|$ that needs to be calculated in step n, can be reused in the construction of the new vector in step $n + 1$.

In the orthonormal basis $\{|\phi_n\rangle\}$, the Hamiltonian takes a tridiagonal form

$$\begin{pmatrix} H_{00} & \|\phi'_1\| & & \\ \|\phi'_1\| & H_{11} & \|\phi'_2\| & \\ & \|\phi'_2\| & H_{22} & \ddots \\ & & \ddots & \ddots \end{pmatrix} \,. \tag{6.10}$$

The eigenvalues of this tridiagonal matrix approximate the eigenvalues of the original Hamiltonian. They can be calculated by standard full diagonalization methods [218]. It is the distinct power of the Lanczos algorithm that, compared to the dimension of the original Hilbert space, relatively few iterations are sufficient to reach machine precision in the approximation of a few low-lying energy levels.

In summary, the Lanczos algorithm to compute the groundstate energy can be stated as follows:

1. Choose a random but suitable initial vector.
2. Construct a new normalized vector according to (6.7)–(6.9).

3. Compute the lowest eigenvalue of the truncated tridiagonal matrix (6.10).
4. Repeat steps 2 and 3 until convergence.

The procedure is a bit more intricate if more than one eigenvalue is desired. Due to rounding errors new vectors will eventually loose their orthogonality with the initial vectors. This results in another eigenvalue converging to the groundstate, even if the groundstate is unique. Without control of rounding errors spurious degeneracies will occur, that are not really present the spectrum of H. In fact, the Lanczos algorithm as stated above is not able to resolve degeneracies, thus spurious eigenvalues can, in principle, be identified easily. A way to eliminate them is regular re-orthogonalization of new vectors with the previous ones. We shall use a simple recipe that is certainly non-optimized though rather fail-proof in the implementation:

1. Choose a random but suitable initial vector.
2. Orthogonalize it with all previously found eigenvectors.
3. Construct only *two* new vectors according to (6.7)–(6.9).
4. Compute the eigenvector to the lowest eigenvalue of the 3×3 matrix (6.10).
5. Repeat steps 2–4 with the eigenvector as new initial vector until convergence.
6. Add the converged eigenvector to the set of found eigenvectors and restart.

This way, re-orthogonalization is automatic but costly. In particular, step 2 is not necessary in every subsequent iteration and computation intense when the number of found eigenvectors increase. We found, however, that apart from very few exceptions up to six eigenvalues could be computed within acceptable time even in the largest symmetry-sectors.

Remarks on the implementation. The Lanczos method is extremely powerful, yet relatively simple to implement. Our implementations follow exactly the recipes with and without reorthogonalization, given above. The crucial and time consuming part (for the longest chains), however, is the generation, respectively transformation, of the Hamiltonian in the desired symmetry sector. Of the two possible variants, either generating the matrix elements on-the-fly or generation of the complete matrix which is then written to disk, we chose the latter. This was because we aimed at numerous diagonalization procedures at various different values of the two control parameters, Δ and λ. To this end, we had to split the Hamiltonian into four parts,

$$\mathrm{H} = \mathrm{H}_{\mathrm{o,u}} + \lambda \mathrm{H}_{\mathrm{o},\lambda} + \Delta \mathrm{H}_{\mathrm{d,u}} + \lambda\Delta \mathrm{H}_{\mathrm{d},\lambda} ,$$

each part of which had to be generated and transformed individually and for every symmetry sector considered. Once, the four pieces had been stored on disk, the Hamiltonian with arbitrary values of Δ and λ, could be generated within a few tens of seconds (for the longest chains). Transforming, however, both off-diagonal parts of the real sector 10+ of MA, $L = 20$, took in sum about 800 CPU hours. Off-diagonal parts of the complex sector 120 took about 1500 CPU hours. All four parts of sector 10+ take 174M (compressed: 34M) of disk space, that of sector 120 take 447M (compressed: 67M). In both, generation and tridiagonlization, we made extensive use of efficient LAPACK routines, in order to perform real and complex sparse matrix–vector multiplications. The final diagonalization of the truncated tridiagonal matrix has been done using standard routines of Numerical Recipes [218].

The calculation of the lowest eigenvalue of one sector, which does not need costly reorthogonalization, took for MA, $L = 20$, and the largest real sectors, roughly 20 to 30 seconds to reach a precision of 8 digits, and a few minutes for the largest complex sectors. Finding the minimum of the energy gap required the calculation of the lowest level of two sectors. With a decent minimization routine, such as `brent` from NR [218], it required 30 to 100 individual gaps to reach a reasonable precision. The gap for any value of Δ has been found in at most roughly an hour.

Calculating more than one level, significantly blew up computation time because of the need for reorthogonalization. Calculating six levels of MA, $L = 20$, in the largest real sectors took generally about 10 hours for each set of parameters, in the largest complex sector up to two days.[5]

6.1.3 BST Extrapolation

Full exact diagonalization and the Lanczos algorithm provide a series of finite-size estimates of energy levels (or energy gaps). Wrapping diagonalization by minimization algorithms, pseudocritical couplings defined, e.g., by the minimum of the excitation gap can be calculated and provide a series of exact finite-size estimates of the true critical value. Even though generally being only a few and stemming from small systems, exact values can give valuable and accurate information about infinite volume limits due to the existence of powerful extrapolation algorithms.

Here, the application of the Burlisch–Stoer (BST) [220] algorithm shall be explained. If finite-size estimates $T(L)$ are supposed to be subject to power-law corrections, i.e.,

$$T(L) = T_\infty + \mathcal{A}_1 L^{-\omega_1} + \mathcal{A}_2 L^{-\omega_2} + \cdots \,, \tag{6.11}$$

the BST algorithm accelerates the convergence of the series of exact finite-size estimates by iteratively creating new series from the following prescription [25],

$$\begin{aligned} T_{-1}^{(i)} &= 0\,, \\ T_0^{(i)} &= T(L_i)\,, \\ T_m^{(i)} &= T_{m-1}^{(i+1)} + \frac{\left(T_{m-1}^{(i+1)} - T_{m-1}^{(i)}\right)}{\left(\frac{L_{i+1}}{L_i}\right)^{\omega}\left(1 - \frac{T_{m-1}^{(i+1)} - T_{m-1}^{(i)}}{T_{m-1}^{(i+1)} - T_{m-2}^{(i+1)}}\right) - 1}\,. \end{aligned} \tag{6.12}$$

The exponent ω is a free parameter of the algorithm, it can be adjusted to optimize the outcome of the extrapolation with respect to some suitably chosen criteria. It can

---

[5] The numbers are supposed to give a rough idea of the computational effort, but in particular illustrate the importance of exploiting symmetries. All numbers given refer to a standard desktop machine of our institute (Intel Core2 Quad CPU Q6600 @ 2.40GHz and 3.9GB RAM) and will, certainly, vary significantly from machine to machine.

be convenient to organize the extrapolants $T_m^{(i)}$ in the form of a table [25],

$$\begin{array}{ccc} T_0^{(0)} & & \\ & T_1^{(0)} & \\ T_0^{(1)} & & T_2^{(0)} \\ & T_1^{(1)} & \\ T_0^{(2)} & & \ddots \end{array} \tag{6.13}$$

The first column then contains the original exact finite-size estimates $T(L_i)$ and the accelerated and shortened series of each iteration follow in next columns. If there are $M+1$ original finite-size estimates, the algorithm can be iterated M times. The final estimate is $T_M^{(0)}$, and it depends on the choice of ω. For sufficiently large M, the quantity

$$\varepsilon \equiv \varepsilon_M^{(0)} = 2|T_{M-1}^{(0)} - T_{M-1}^{(1)}| \,. \tag{6.14}$$

is supposed to give an estimate of the error of the extrapolated value $T_M^{(i)}$ [221]. To minimize ε, seems to be a reasonable criterion for the choice of an optimal ω. One can also define the "error" of an intermediate estimate $T_m^{(i)}$ by

$$\varepsilon_m^{(i)} = 2|T_{m-1}^{(i)} - T_{m-1}^{(i+1)}| \,, \tag{6.15}$$

and use as criterion to minimize all $\varepsilon_m^{(i)}$ simultaneously [25]. If this is implemented as criterion to minimize the sum

$$\varepsilon_{\text{tot}} = \sum_{m=1}^{M} \sum_{i=0}^{M-m} \varepsilon_m^{(i)} \,, \tag{6.16}$$

this basically and mostly[6] means to minimize the total extent $|T_j^0 - T_j^{M-j-1}|$, of each accelerated series j.

6.1.4 Test Application

To test our implementation of the Lanczos algorithm and BST extrapolation, we calculated the conformal normalization $v(\Delta)$, of the spin-$\frac{1}{2}$ chain at the critical point $\lambda_c = 1$, for some selected values of the exchange anisotropy Δ. Additionally, this test proved particularly useful in order to gain experience in handling BST extrapolation. The conformal normalization of the spin-$\frac{1}{2}$ chain is exactly known to be [164, 196–198] (see Sect. 5.5)

$$v_{\text{ex}}(\Delta) = \frac{\pi}{2} \frac{\sin(\arccos\Delta)}{\arccos\Delta} \,. \tag{6.17}$$

The groundstates of finite chains belong to sector 00+, if $L/2$ is even, and to sector $0(L/2)-$, if $L/2$ is odd. As in [177], we use the lowest level in the sector with $P=1$, if $L/2$ is even, and $P = L/2+1$, if $L/2$ is odd, to normalize the spectrum and obtain a series of 8 finite-size estimates for $L = 4, 6, \ldots, 18$.

---

[6] If the accelerated series are monotonous. For particular ω it may occur that this is not true.

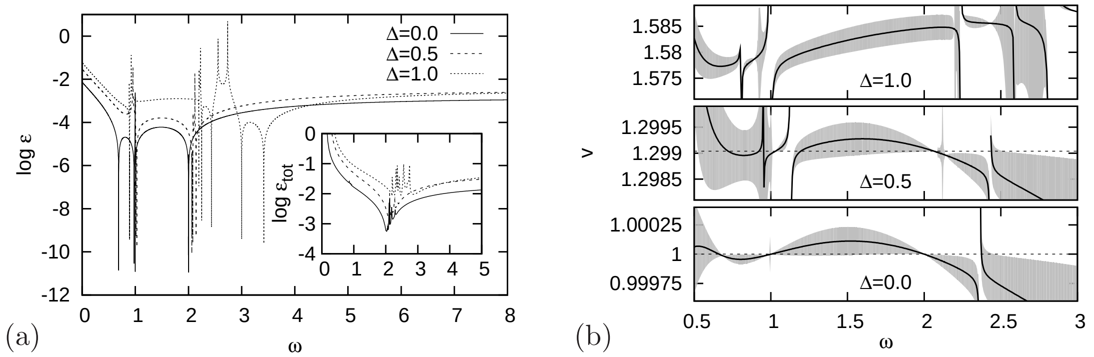

Figure 6.1: Dependence of BST extrapolation on the choice of ω. (**a**) The error ε, of the final estimate shows a rich structure of local minima. The values of some minima can be arbitrarily lowered by fine-tuning the search. The overall error ε_{tot} (inset) permits the identification of an absolute minimum for $\Delta < 1$. **(b)** The final estimate v depends on the choice of ω. Dashed lines show the exact infinite volume limit $v_{\text{ex}}(\Delta)$. At $\Delta = 1$ it is $v_{\text{ex}}(1) = \pi/2 \approx 1.571$.

We studied the dependence of the error ε of the final estimate v, and of the overall error ε_{tot} on the choice of ω. Figure 6.1a shows a rich structure of local minima of ε. For $\Delta \neq 1$, there seems to be an accumulation of minima in the vicinity of $\omega = 1$ and 2. The value of some of the minima depends on the parameters of the minimization routine, they can be arbitrarily lowered by fine-tuning the search and it becomes impossible to decide which of the minima is the absolute minimum. Quite in contrast, the overall error does show a distinct absolute minimum at $\omega \approx 2$, where, again, the isotropic point is a notable exception. Studying the Δ-dependence of the location of the minima, it turns out that most minima shift continuously with Δ, and a generic rule that either $\omega = 1$ or $\omega = 2$ were a “good” choice becomes less optimal close to $\Delta = 1$. The range of final estimates v, when ω is varied between 0.5 and 3, can be seen in Fig. 6.1b.

A sample table of extrapolants is shown in Table 6.3 for $\Delta = 0.5$. The choice $\omega = 2.06284$ is a local minimum of the error of the final estimate with $\varepsilon < 10^{-8}$. We compare the corresponding final estimate denoted by $v_{\text{opt},2}$, to other estimates:

$$\begin{aligned} v_1 &= 1.2989858 \pm 0.0008551 && \text{with} \quad \omega = 1, \\ v_2 &= 1.2990961 \pm 0.0000674 && \text{with} \quad \omega = 2, \\ v_{\text{opt},1} &= 1.2990105 && \text{with} \quad \omega = 1.01362, \\ v_{\text{opt},2} &= 1.2990401 && \text{with} \quad \omega = 2.06284, \\ \text{and} \quad v_{\text{opt,o}} &= 1.2990025 \pm 0.0000959 && \text{with} \quad \omega = 2.10020. \end{aligned}$$

The estimate $v_{\text{opt},1}$ comes from a local minimum of ε close to $\omega = 1$, and $v_{\text{opt,o}}$ is the minimum of the overall error ε_{tot}. We would conclude that $v_{\text{f}} = 1.2990(1)$, but comparison to the exact value $v_{\text{ex}}(0.5) = 1.2990381$, shows that we could, in fact, do much better using the estimate $v_{\text{opt},2}$. In Table 6.4 we list the same set of different estimates for other values of Δ and find that $v_{\text{opt},2}$ indeed gives a remarkably good, in fact, the best estimate at least up to $\Delta < 0.6$. The problem is that, without comparison to the exact result we, would not know. Moreover, we would have no reasonable error estimate. This would be provided automatically by fixing ω to either 1 or 2, which can be verified by comparing to the exact result (!) – which, however, is generally *unknown*. The criterion to minimize ε_{tot} does also provide error estimates, but a look at Table 6.4 shows that it does not work as purely "objective" criterion in the general case either. For $\Delta = 0.6$ and $\Delta = 1$, the error is hopelessly too small. But the pathological case is $\Delta = 0$, the absolute minimum of ε_{tot} lies at $\omega = 2.026247$, which is different from the obviously excellent choice $\omega = 2$, which also hosts a local minimum of ε itself. As result we would obtain $v_{\text{f,opt,o}} = 0.999988(11)$ and even "miss" the correct answer slightly. Objectively, we would have to be content with the values labelled by v_∞ in Table 6.4.

Table 6.3: BST extrapolants $T_j^{(i)}$, of the conformal normalization of spin-$\frac{1}{2}$ chain at $\Delta = 0.5$. The index j refers to the column and the superscript (i) to the row within a column. The first column gives the original exact finite-size estimates. The choice of ω corresponds to a local minimum of ε with error $\varepsilon < 10^{-8}$. The exact infinite volume limit is $v_{\text{ex}}(0.5) = 1.2990381$.

L	$\omega = 2.06284$							
4	1.0734305							
		1.3094985						
6	1.1955801		1.2993436					
		1.3016057		1.2990524				
8	1.2408186		1.2991011		1.2990431			
		1.2999505		1.2990443		1.2990398		
10	1.2619961		1.2990586		1.2990406		1.2990401	
		1.2994398		1.2990414		1.2990401		1.2990401
12	1.2734992		1.299047		1.2990402		1.2990401	
		1.2992417		1.2990405		1.2990401		
14	1.2804095		1.299043		1.2990401			
		1.2991523		1.2990403				
16	1.2848726		1.2990415					
		1.2991072						
18	1.2879166							

Table 6.4: Exact finite-size estimates of the conformal normalization of spin-$\frac{1}{2}$ chain from chains of length L, and results of BST extrapolation at different values of ω in comparison to the exact infinite volume limit v_{ex}. $v_{1(2)}$… BST extrapolation with $\omega = 1(2)$; $v_{\text{opt},1(2)}$… local minima in the vicinity of $\omega = 1(2)$; $v_{\text{opt,o}}$… absolute minimum of ε_{tot}; v_∞… final estimate based on the previous estimates.

L	$\Delta = 0$	$\Delta = 0.2$	$\Delta = 0.4$	$\Delta = 0.6$	$\Delta = 0.8$	$\Delta = 1$
4	0.9003163	0.9662263	1.0365989	1.1113365	1.1902841	1.2732395
6	0.9549297	1.0504197	1.1467148	1.2451482	1.3470128	1.4534022
8	0.9744954	1.0818748	1.1877918	1.2942644	1.4036007	1.5181534
10	0.9836316	1.0967903	1.2071686	1.3170259	1.4292557	1.5472518
12	0.9886159	1.1049873	1.2177664	1.3292647	1.4426972	1.5622964
14	0.9916286	1.1099619	1.2241722	1.3365446	1.4504609	1.5708297
16	0.9935869	1.1132036	1.2283324	1.3412015	1.4552678	1.5759887
18	0.9949308	1.1154318	1.2311839	1.3443482	1.4584015	1.5792510
v_1	1.0000000	1.123862(1)	1.24185(1)	1.355(1)	1.46451(7)	1.555(2)
v_2	1.0000000	1.1238623(4)	1.24187(2)	1.3554(2)	1.467(1)	1.585(3)
$v_{\text{opt},1}$	0.9999994	1.1238509	1.2418313	1.3550875	1.4645294	1.5786442
$v_{\text{opt},2}$	1.0000000	1.1238618	1.2418520	1.3553066	1.4664166	1.5844823
$v_{\text{opt,o}}$	0.999988(11)	1.12384(6)	1.2418(1)	1.3553265(1)	1.4668(3)	1.5844823(4)
v_∞	1	1.12386(1)	1.24185(2)	1.3552(2)	1.466(1)	1.57(2)
v_{ex}	1	1.1238620	1.2418564	1.3551640	1.4646094	1.5707963

6.2 Loop Algorithm

In Monte Carlo methods large sums or integrals are evaluated stochastically. As discussed in Sect. 3.1, interpreting the Boltzmann operator as evolution operator in imaginary time, the partition function of a quantum system,

$$Z = \mathrm{Tr}\,\mathrm{e}^{-\beta \mathrm{H}} = \sum_n \langle n | \mathrm{e}^{-\beta \mathrm{H}} | n \rangle \,, \tag{6.18}$$

is a sum over transition amplitudes with initial and final states equal. This can formally be written as a *path integral* in imaginary time, after the usual time-slicing procedure [118],

$$Z = \oint \mathcal{D}[n(\tau)]\, W[n(\tau)] \,, \tag{6.19}$$

where the imaginary-time variable τ is running from 0 to β, the circle symbolically denotes the condition $n(0) = n(\beta) = n$, $W[n(\tau)]$ is the weight of a particular path and $\mathcal{D}[n(\tau)]$ a "measure" of integration.

The loop(-cluster) algorithm [9, 10] in continuous time path integral representation [54, 55] is a quantum Monte Carlo algorithm that samples the canonical ensemble by generating a Markov chain of **paths** or **configurations**,

$$\mathcal{C}_1 \to \mathcal{C}_2 \to \mathcal{C}_3 \to \cdots \,, \tag{6.20}$$

that contribute to the partition function. Each configuration $\mathcal{C}_{i+1} = y$, with weight W_{i+1} is constructed from the previous one $\mathcal{C}_i = x$, with a suitably chosen update probability $p_{x,y}$. A Monte Carlo algorithm generates a valid and well-defined Markov chain of configurations if the following three conditions are met (see, e.g., [153]):

1. **Normalization**: $\sum_y p_{x,y} = 1\,.$
2. **Ergodicity**: From every configuration every other configuration that contributes to the partition function must be reachable within a finite sequence of updates.
3. **Detailed Balance**: $W_x\, p_{x,y} = W_y\, p_{y,x}$, which is sufficient but not necessary.

In Sect. 6.2.1, the interpretation of configurations as paths and the meaning of weights and measures as used in the symbolic notation of (6.19) of integration will be discussed in more detail. The update scheme of the loop algorithm meeting the conditions for a Markov process will be described in Sect. 6.2.2. Being able to perform global updates[7], the loop algorithm completely eliminates critical slow down, that makes simulations with local update algorithms inefficient in the vicinity of a critical point. Furthermore, the loop algorithm allows for the implementation of improved estimators, which have a reduced variance on the one hand, and on the other hand offer easy access to off-diagonal observables [10, 223]. After a short intermezzo to explain how to simulate spins of magnitude $S \geq 1$ in Sect. 6.2.3, improved and unimproved

---

[7] The loop algorithm can be viewed as the generalization of the classical Swendsen–Wang cluster algorithm [222] to quantum systems.

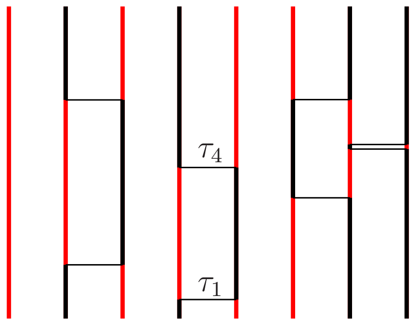

Figure 6.2: Typical configuration in the loop algorithm. Vertical direction is imaginary time, the length of each line is β. Black (red) lines represent spin up (down). Staring and ending time (τ_1 and τ_4) are indicated. In our notation, they border the segments $\mathfrak{s}_{3,2}$ and $\mathfrak{s}_{4,2}$, which have orientation $m_{3,2} = +1/2$ and $m_{4,2} = +1/2$, and length $|\mathfrak{s}_{3,2}| = |\mathfrak{s}_{4,2}| = \tau_4 - \tau_1$.

estimators of observables will be presented in Sect. 6.2.4, along with consideration of autocorrelation and error estimation.

The loop algorithm can also be formulated in a stochastic series expansion (SSE) representation of the partition function [11]. Further related methods are, e.g., the directed loop algorithm [224–226], the worm algorithm [227, 228] or projector quantum Monte Carlo methods [229, 230].

6.2.1 Setup: Configurations are Paths

The canonical basis of S^z-eigenstates is discrete, thus a configuration $\mathcal{C}$ or path $[n(\tau)]$ in *continuous* imaginary time is a discrete sequence of basis states that change from one to another instantaneously at distinct times [54, 55]. We shall call these changes of basis states *jumps*. A configuration that contains J jumps at times τ_i,

$$\mathcal{C} \equiv [n(\tau)] \equiv \{\mathcal{S}_1, \mathcal{S}_2, \ldots, \mathcal{S}_{J+1}\}\,, \tag{6.21}$$

consists of $(J+1)$ time intervals which we will denote by $\mathcal{S}_i = (n_i, \tau_i)$, where τ_i specifies the end of the interval and $\tau_{J+1} = \beta$. We define for convenience $\tau_0 = 0$ and omit the starting time in the specification of an interval. The state n_i extends from τ_{i-1} to τ_i where it jumps to n_{i+1}. Due to the periodic boundary conditions we have $n_1 = n_{J+1}$.

In a spin chain with $S = 1/2$, at each time $0 \le \tau \le \beta$ the state $|n(\tau)\rangle$ is made up of L individual spins with the local magnetic moment $m_i(\tau) = \pm 1/2$. The time evolution of a single spin is a piecewise constant function that alternates between the two orientations, it is chopped into $k_i + 1$ time intervals which we shall call *segments* or *edges*,

$$[m_i(\tau)] \equiv \{\mathfrak{s}_{i1}, \mathfrak{s}_{i2}, \ldots, \mathfrak{s}_{ik_i}, \mathfrak{s}_{i(k_i+1)}\}\,, \quad \mathfrak{s}_{ij} = (m_{ij}, \tau_{ij})\,, \quad \mathfrak{s}_{i(k_i+1)} = (m_{i1}, \beta)\,, \tag{6.22}$$

where the orientation or state of segment $\mathfrak{s}_{ij}$ is m_{ij} and its length is

$$l_{ij} := |\mathfrak{s}_{ij}| = \tau_{ij} - \tau_{i,j-1}\,, \qquad \sum_{j=1}^{k_i+1} l_{ij} = \beta\,. \tag{6.23}$$

A typical configurations is shown in Fig. 6.2.

Weights of configurations. The assignment of weights to configurations starts with the standard time-slicing procedure to obtain the path integral formulation [118]. In (3.3), the factorization of the Boltzmann operator yielded

$$Z = \sum_{\{n\}_N} \prod_{i=0}^{N} \langle n_{i+1}| \, \mathrm{e}^{-\varepsilon \mathrm{H}} \, |n_i\rangle \ , \tag{6.24}$$

with $\sum_{\{n\}_N} \equiv \sum_{n_0} \cdots \sum_{n_N}$, and implicitly assumed periodic boundary conditions $n_0 = n_{N+1}$.

Using a notation for diagonal and off-diagonal parts of the Hamiltonian [55, 231]

$$E_{n,n'} = \langle n|\mathrm{E}|n'\rangle = \delta_{n,n'}\langle n|\mathrm{H}|n'\rangle =: \delta_{n,n'} E_n \, , \tag{6.25}$$

$$V_{n,n'} = \langle n|\mathrm{V}|n'\rangle = \begin{cases} \langle n|\mathrm{H}|n'\rangle & \text{if } n \neq n' \\ 0 & \text{else} \end{cases} \, , \tag{6.26}$$

the small-time amplitudes that appear in the product of (6.24) can be approximated by use of the Campbell–Baker–Hausdorff formula and the expansion of $\mathrm{e}^{-\varepsilon \mathrm{V}}$,

$$\begin{aligned} W_{n_i,n_{i+1}} := \langle n_{i+1}| \, \mathrm{e}^{-\varepsilon \mathrm{H}} \, |n_i\rangle &\approx \langle n_{i+1}| \, (\mathbb{1} - \varepsilon \mathrm{V})\mathrm{e}^{-\varepsilon \mathrm{E}} \, |n_i\rangle \\ &= (\delta_{n_{i+1},n_i} - \varepsilon V_{n_{i+1},n_i})\mathrm{e}^{-\varepsilon E_{n_i}} \\ &= \begin{cases} \mathrm{e}^{-\varepsilon E_{n_i}} & \text{if } n_{i+1} = n_i \\ -\varepsilon V_{n_{i+1},n_i} \mathrm{e}^{-\varepsilon E_{n_i}} & \text{if } n_{i+1} \neq n_i \end{cases} \, , \end{aligned} \tag{6.27}$$

where the error due to the approximation in the first line is of order $O(\varepsilon^2)$ [10]. This amplitude can be used to assign a weight $W_{n_i,n_{i+1}}$ to what is called a *timeslice*. In the continuous limit the temporal extent of a timeslice becomes zero or rather *infinitesimal*. The above relation becomes exact and one may write for the weight of an infinitesimal timeslice,

$$\lim_{N\to\infty} W_{n_i,n_{i+1}} = W(\tau) \equiv W_{n(\tau),n(\tau+\mathrm{d}\tau)} = \begin{cases} \mathrm{e}^{-\mathrm{d}\tau E(\tau)} & \text{if } n(\tau+\mathrm{d}\tau) = n(\tau) \\ -\mathrm{d}\tau V(\tau)\mathrm{e}^{-\mathrm{d}\tau E(\tau)} & \text{if } n(\tau+\mathrm{d}\tau) \neq n(\tau) \end{cases} \, , \tag{6.28}$$

where the continuum generalization of E_{n_i} and V_{n_{i+1},n_i},

$$E(\tau) \equiv E_{n(\tau)} = \langle n(\tau)|\mathrm{E}|n(\tau)\rangle \, , \tag{6.29}$$

$$V(\tau) \equiv V_{n(\tau+\mathrm{d}\tau),n(\tau)} = \langle n(\tau+\mathrm{d}\tau)|\mathrm{V}|n(\tau)\rangle \, , \tag{6.30}$$

has been introduced. Insertion of (6.27) into the time-sliced version (6.24) of the partition function and use of the limiting expression (6.28) makes contact with the symbolic path integral notation (6.19) [231],

$$\begin{aligned} Z &= \lim_{N\to\infty} \sum_{\{n\}_N} \mathrm{e}^{-\varepsilon \sum_{i=0}^{N} E_{n_i}} \prod_{j=1}^{J} \left(-\varepsilon V_{n_{j+1},n_j}\right) \\ &= \oint_{\mathcal{C}} \mathrm{e}^{-\int_0^\beta \mathrm{d}\tau E(\tau)} (-\mathrm{d}\tau)^J \prod_{j=1}^{J} V(\tau_j) =: \oint \mathcal{D}[n(\tau)] \, W[n(\tau)] \, , \end{aligned} \tag{6.31}$$

where the symbol of integration $\oint_{\mathcal{C}}$, is to be understood as $\oint_{\mathcal{C}} \equiv \lim_{N\to\infty} \sum_{n_0} \cdots \sum_{n_N}$, with the circle a reminder of periodic boundary conditions in imaginary time. The existence of the continuous limit of the time-slicing procedure is ensured by the Farhi–Gutmann construction of the path integral [231], or by the formulation in terms of time-dependent perturbation theory [55, 61]. Both do not make reference to any time-slicing at all.

The merit of the time-slicing construction of the path integral is, that from the knowledge of the infinitesimal weights of infinitesimal timeslices it is possible assign a weight, that is itself infinitesimal in general, to continuous time configurations that consist of infinitely many infinitesimally small timeslices. The separation of the weight of a configuration into a weight and a measure is arbitrary, as pointed out in [231], but convenient. Thus, we define the weight as

$$W_{\mathcal{C}} \equiv W[n(\tau)] = (-1)^{J_{\mathcal{C}}} \mathrm{e}^{-\beta E_{\mathcal{C}}} \prod_{i=1}^{J_{\mathcal{C}}} V(\tau_i)\,, \tag{6.32}$$

where by the index in $J_{\mathcal{C}}$, the number of jumps in configuration $\mathcal{C}$, we indicate the dependence on the specific configuration, and similarly by the index in $E_{\mathcal{C}}$, which is given by [61]

$$E_{\mathcal{C}} \equiv E[n(\tau)] = \frac{1}{\beta} \lim_{N\to\infty} \varepsilon \sum_{i=0}^{N} E_{n_i} = \frac{1}{\beta} \int_0^\beta \mathrm{d}\tau E(\tau)\,, \tag{6.33}$$

i.e. the average contribution of diagonal elements of the Hamiltonian to the energy of a configuration, which we shall further simply call the *diagonal energy* of a configuration. The measure $\mathcal{D}[n(\tau)] = (\mathrm{d}\tau)^{J_{\mathcal{C}}}$, then is the $J_{\mathcal{C}}$-dimensional volume-element of imaginary time.

The factor $(-1)^{J_{\mathcal{C}}}$ in (6.32) is at the core of the notorious sign problem. It allows for the possibility of the weight becoming negative, which makes the probability interpretation of normalized weights problematic. However, in many cases the sign does not matter. In the definition of the XXZ spin Hamiltonian (1.6), we have only positive off-diagonal elements, i.e. configurations could indeed have negative sign. However, in spin chains with an even number of sites the periodic boundary conditions in imaginary time and the fact that only nearest neighbour interaction is considered demand that only an even number of jumps can occur in any allowed path.

All QMC simulations in this thesis are restricted to chains with an even number of spins which ensures the positivity of total weights of configurations. Moreover, having chosen bond alternation λ, and exchange anisotropy Δ, as the only control parameters, the off-diagonal elements take only two different values, $J_{xy}/2$ and $\lambda J_{xy}/2$. Restricting notation without further indication to non-zero-weight paths only, we can write the weight (6.32) of a configuration as

$$W_{\mathcal{C}} = (-1)^{J_{\mathrm{u}}+J_\lambda} \mathrm{e}^{-\beta E_{\mathcal{C}}} \left(\frac{J_{xy}}{2}\right)^{J_{\mathrm{u}}} \left(\lambda \frac{J_{xy}}{2}\right)^{J_\lambda} = \frac{\mathrm{e}^{-\beta E_{\mathcal{C}}}}{2^{J_{\mathcal{C}}}} \lambda^{J_\lambda}\,, \tag{6.34}$$

where by J_{u} and J_λ we denote the number of jumps due to two-spin-flips on unit- and λ-bonds, respectively, and $J_{xy} = 1$ as well as the fact that $J_{\mathrm{u}} + J_\lambda = J_{\mathcal{C}}$ is always an even number in this thesis were used in the last equation.

Factorization of timeslices. The weight of an infinitesimal timeslice (6.28) is not the end of the story in order to derive the local update rules of the loop algorithm (see Sect. 6.2.2). In discrete time, when N is finite, the Trotter–Suzuki decomposition [10, 120] is used to reduce the time evolution of an L-spin state on a single timeslice to L independent two-spin evolutions at the cost of an intermediate time step (see Sect. 3.2). This way the weight of a time slice factorizes into a product of the weights of two-spin evolutions [10, 54]. Under the all-embracing protection of the continuous time limit $N \to \infty$, however, the Trotter–Suzuki breakup is not necessary.

The XXZ Hamiltonian is the sum of two-spin interactions between spins on neighbouring sites only and so are the operators $\mathrm{E} = \sum_i \mathrm{E}_{i,i+1}$, and $\mathrm{V} = \sum_i \mathrm{V}_{i,i+1}$. For the diagonal operator it follows immediately that the corresponding weight of the timeslice factorizes into two-spin contributions,

$$\mathrm{e}^{-\mathrm{d}\tau E(\tau)} = \mathrm{e}^{-\mathrm{d}\tau \sum_{i=0}^{L-1} E_{i,i+1}(\tau)} = \prod_{i=0}^{L-1} \mathrm{e}^{-\mathrm{d}\tau E_{i,i+1}(\tau)} \,. \tag{6.35}$$

In order to see the factorization of the off-diagonal contribution, consider

$$\begin{aligned} \langle n_{i+1}|\mathrm{V}|n_i\rangle &= \langle m_{i+1,0}\cdots m_{i+1,L-1}| \sum_{j=0}^{L-1} \mathrm{V}_{j,j+1} |m_{i,0}\cdots m_{i,L-1}\rangle \\ &= \sum_{j=0}^{L-1} \langle m_{i+1,j} m_{i+1,j+1}|\mathrm{V}_{j,j+1}|m_{i,j} m_{i,j+1}\rangle \prod_{l\neq j,j+1} \delta_{m_{i+1,l},m_{i,l}} \,. \end{aligned} \tag{6.36}$$

The product of Kronecker-δ's takes care that $\langle n_{i+1}|\mathrm{V}|n_i\rangle$ is non-zero only if two neighbouring spins flip. The matrix elements of one and only one local operator $\mathrm{V}_{j,j+1}$ then determine the two-spin contribution to the weight of the timeslice. In the continuous time limit we write

$$\begin{aligned} \langle n(\tau+\mathrm{d}\tau)|\mathrm{V}|n(\tau)\rangle &= \sum_{j=0}^{L-1} \langle m_j(\tau+\mathrm{d}\tau) m_{j+1}(\tau+\mathrm{d}\tau)|\mathrm{V}_{j,j+1}|m_j(\tau) m_{j+1}(\tau)\rangle \\ &\qquad \times \prod_{l\neq j,j+1} \delta_{m_l(\tau+\mathrm{d}\tau),m_l(\tau)} \\ &=: \sum_{j=0}^{L-1} V_{j,j+1}(\tau) \prod_{l\neq j,j+1} \delta_l(\tau) \,. \end{aligned} \tag{6.37}$$

If now the weight of an infinitesimal two-spin evolution is defined by

$$W_{j,j+1}(\tau) = \begin{cases} \mathrm{e}^{-\mathrm{d}\tau E_{j,j+1}(\tau)} & \text{if } n(\tau+\mathrm{d}\tau) = n(\tau) \\ -\mathrm{d}\tau V_{j,j+1}(\tau) \mathrm{e}^{-\mathrm{d}\tau E_{j,j+1}(\tau)} \prod_{l\neq j,j+1} \delta_l(\tau) & \text{if } n(\tau+\mathrm{d}\tau) \neq n(\tau) \end{cases} , \tag{6.38}$$

the factorization of the weight of an infinitesimal timeslice can be written

$$W(\tau) = W_{n(\mathrm{d}\tau+\tau),n(\tau)} = \prod_{j=0}^{L-1} W_{j,j+1}(\tau) \,. \tag{6.39}$$

If more than two spins are different in the states $|n(\tau{+}\mathrm{d}\tau)\rangle$ and $|n(\tau)\rangle$ the weight of the timeslice is zero. This is because this must be at least the result of two two-spin flips, the contribution of which, however, is of order $O(\varepsilon^2)$. In other words, in truly continuous time the chance that two two-spin flips on different bonds occur exactly at the same time vanishes. There is always at least an arbitrarily small but finite time interval in-between.

Remarks on the implementation. We consider the implementation of a QMC algorithm such as the loop algorithm considerably more complicated than that of diagonalization methods such as Lanczos. The ALPS project [219] does, in fact, provide a set of well-tested implementations of many state-of-the-art simulation algorithms for physics. For reasons of flexibility to adjust simulations precisely to our needs, however, we chose to build our own implementation.

The implementation maps precisely the picture, described in this section, of a configuration consisting of segments of constant orientation with an initial and final time. We used built-in types of the standard template library (STL) of C++, and made, progressing with the complexity of the algorithm, progressing use of the object-oriented programming paradigm.

The core unit of a configuration in our implementation is an edge (or segment). It contains the information of its final time, its current state, a label used to assign it to a loop(-cluster) (see next section), and a flag that indicates whether it belongs to a unit- or a λ-bond. In the special case of the isotropic point, the information of state and bond-type would not be needed (see next section), but this is different in the general XXZ case. An edge further contains two pointers to in- and outgoing edges, which are used for loop construction.

A spin, or subspin to be more precise (see Sect. 6.2.3), is, following Evertz [10], implemented as a doubly-linked list of pointers to edges. A spin is defined as class derived from the STL built-in type `list`. The use of pointers was necessary, in order to allow for dynamic allocation of new edges at new. In order to avoid permanent construction and destruction of edges, and thus permanent allocation and deallocation of memory, unused edges are gathered in a collector and given back at need.

6.2.2 Update: Breakups and Loops

Roughly speaking, the generation of a new configuration out of its predecessor consists of randomly chopping and flipping segments, followed by a recombination of segments. The difficulty is to avoid the generation of zero-weight configurations. The loop algorithm is an efficient method to accomplish this task.

The local, approach as presented in [54], is to construct a single loop. The loop's head and tail are planted in the configuration at an arbitrary site and arbitrary time. The tail remains fixed while the head is viewed as moving through the configuration. The direction of moving is determined by the orientation of the current segment. By convention the loop moves forward in time if the segment represents a spin up ($m = 1/2$) and backward if the spin is down ($m = -1/2$). At any moment in time the loop has three possible ways to proceed. It can move on or it can jump to another spin that interacts with the current spin and change or keep the direction of movement.

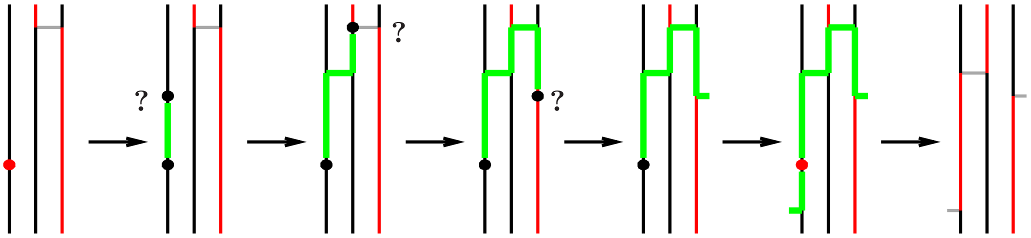

Figure 6.3: Illustration of the local approach to the loop algorithm. A loop head (red dot) is randomly planted and moves upwards (downwards) on black (red) segments. Every question mark marks the effect of a random decision, optional (anywhere) or forced (on breakups marked by horizontal lines) jumps to adjacent sites. Eventually the loop closes, thereby covering part of the configuration which can be flipped. The flip leads to an updated configuration.

This is where the typical randomness of Monte Carlo simulations enters the stage in a random decision of what the loop head does. The loop head leaves a mark everywhere it passes through, thereby covering part of the configuration. By leaving a mark the loop avoids to cover segments twice.[8] The construction ends when the loop's head meets its tail and then all segments that are marked by the loop are flipped. A typical loop construction is sketched in Fig. 6.3. Depending on the Hamiltonian, there are even more things that can happen. Two or more loops can be glued together and form a cluster of loops, the loop's head may be annihilated without meeting the tail resulting in unfinished loop pieces that in turn may be glued to other unfinished pieces. The construction of a single loop generalizes to the construction of a single cluster of loops and/or loop pieces [10].

The self-implemented version of the loop algorithm that is used in this thesis, is based on a different global approach. It is a multi-loop(-cluster) update that makes use of all loops that are constructed randomly on a given configuration. The derivation of the multi-loop update in terms of an auxiliary concept called *graph* is described in great detail in the review by Evertz [10], which shall be followed closely here. Based on local decisions, a given configuration of non-zero weight is decomposed into or decorated by a set of loops (or clusters of loops). Each loop(-cluster) can then be flipped individually with a suitable probability. In the following we shall review the derivation adjusted to our needs and – avoiding the plaquette picture used in [10] – directly in continuous time. In doing so, we will establish the weight of a *decorated configuration* as the product of infinitely many decorated and factorized infinitesimal timeslices.

At each moment in imaginary time two spins whose interaction is given by an XXZ Heisenberg term are in one of six different states. By symmetry under spin-inversion the six states separate into three pairs of different type, each pair having the same weight. Two spins[9] can be equal (E), be different (D), or flip simultaneously

---

[8] A variant, called *worm* algorithm, does not leave a mark, but flips instantaneously on passing through and is thus able to undo flips that have already been performed.

[9] We shall always assume spins of size $S = 1/2$ here. The generalization to higher spins will be shown in Sect. 6.2.3.

(F), if they have different orientation (see Fig. 6.4a for a graphical representation). The weights follow from (6.38). Using the λ–Δ parameterization of the XXZ Hamiltonian (1.6), the weights are given by [10]

$$\begin{aligned}
W_1 = W_2 = W_\mathrm{E} &= \begin{cases} \mathrm{e}^{-\mathrm{d}\tau\Delta/4} & \text{on unit-bonds} \\ \mathrm{e}^{-\mathrm{d}\tau\lambda\Delta/4} & \text{on } \lambda\text{-bonds} \end{cases} , \\
W_3 = W_4 = W_\mathrm{D} &= \begin{cases} \mathrm{e}^{\mathrm{d}\tau\Delta/4} & \text{on unit-bonds} \\ \mathrm{e}^{\mathrm{d}\tau\lambda\Delta/4} & \text{on } \lambda\text{-bonds} \end{cases} , \\
W_5 = W_6 = W_\mathrm{F} &= \begin{cases} \mathrm{d}\tau/2 & \text{on unit-bonds} \\ \mathrm{d}\tau\lambda/2 & \text{on } \lambda\text{-bonds} \end{cases} .
\end{aligned} \tag{6.40}$$

The negative sign has disappeared. In fact, the weight W_F is originally negative. For the total weight of a configuration this does not matter, as discussed in the previous section. Here, the sign was eliminated by the sublattice basis rotation (3.18) [10]. This cancels the sign in the weights (6.38). From this point of view it is $\tilde{\mathrm{H}}^\mathrm{XXZ}(-\Delta)$ that is simulated. Clearly, diagonal observables, i.e. observables represented by a diagonal operator, the measurement of which depends on z-components of spin are not at all affected by this basis transformation, while off-diagonal observables of the XXZ chain acquire a staggering factor.

The update of a local two-spin state changes the weight or leaves it as it is. For every state six different updates are possible. This gives 36 update probabilities $p_{ij} = p(W_i \to W_j)$, to be defined. They must be normalized and satisfy detailed balance, i.e.

$$\sum_j p_{ij} \overset{!}{=} 1 , \quad \text{and} \quad W_i p_{ij} \overset{!}{=} W_j p_{ji} . \tag{6.41}$$

Symmetry under spin-inversion drastically reduces the number of different values the probabilities p_{ij} can take. The values can only depend on the change of type and not on the specific change of spin states [10, 54]. Every change of type implies four probabilities of the same value:

$$\begin{aligned}
\mathrm{E} \leftrightarrow \mathrm{D}: \quad & p_{13} = p_{14} = p_{23} = p_{24} , \quad p_{31} = p_{41} = p_{32} = p_{42} , \\
\mathrm{E} \leftrightarrow \mathrm{F}: \quad & p_{15} = p_{16} = p_{25} = p_{26} , \quad p_{51} = p_{61} = p_{52} = p_{62} , \\
\mathrm{D} \leftrightarrow \mathrm{F}: \quad & p_{35} = p_{36} = p_{45} = p_{46} , \quad p_{53} = p_{63} = p_{54} = p_{64} .
\end{aligned} \tag{6.42}$$

Similarly, probabilities that involve no change of type must be equal within each type,

$$x, y \in \mathrm{E} \text{ or } \mathrm{D} \text{ or } \mathrm{F} : \quad p_{xx} = p_{yy} = p_{xy} = p_{yx} . \tag{6.43}$$

The trick is to define new weights, $w_{ij} = W_i p_{ij}$ [10]. Due to (6.40), the new weights satisfy the same equalities, (6.42) and (6.43), as the probabilities. The normalization condition becomes $\sum_j w_{ij} \overset{!}{=} W_i$, and detailed balance turns into

$$w_{ij} \overset{!}{=} w_{ji} . \tag{6.44}$$

This adds a further set of restrictive equalities, which motivates the definition of another set of weights, called *local graph weights* [10],

$$\begin{aligned} w_{\mathrm{vb}}/2 &= w_{13} = w_{31} = w_{14} = w_{41} = w_{23} = w_{32} = w_{24} = w_{42}\,, \\ w_{\mathrm{hb}}/2 &= w_{35} = w_{53} = w_{36} = w_{63} = w_{45} = w_{54} = w_{46} = w_{64}\,, \\ w_{\mathrm{db}}/2 &= w_{15} = w_{51} = w_{16} = w_{61} = w_{25} = w_{52} = w_{26} = w_{62}\,, \\ w_{\mathrm{ge}}/2 &= w_{12} = w_{12} = w_{11} = w_{22}\,, \\ w_{\mathrm{gd}}/2 &= w_{34} = w_{43} = w_{33} = w_{44}\,, \\ w_{\mathrm{gf}}/2 &= w_{56} = w_{65} = w_{55} = w_{66}\,. \end{aligned} \tag{6.45}$$

These graph weights can be interpreted as locally stored information that tells a loop how to proceed. The indices refer to the names as motivated by the corresponding loop construction rules [10, 54] (see Fig. 6.4b for a graphical representation):

• vertical breakup	(vb):	loop proceeds.
• horizontal breakup	(hb):	loop jumps and changes direction.
• diagonal breakup	(db):	loop jumps and keeps direction.

The remaining three graphs refer to the construction rules of clusters of loops. Their presence forces two loops to be flipped simultaneously, which can be interpreted as two loops being glued together, hence the names: glue on equal spins (ge), glue on different spins (gd), glue on spins that flip (gf).

The normalization condition can now conveniently be written in terms of local graph weights giving three equations for six unknowns [10],

$$w_{\mathrm{ge}} + w_{\mathrm{vb}} + w_{\mathrm{db}} = W_{\mathrm{E}}\,, \quad w_{\mathrm{vb}} + w_{\mathrm{gd}} + w_{\mathrm{hb}} = W_{\mathrm{D}}\,, \quad w_{\mathrm{db}} + w_{\mathrm{hb}} + w_{\mathrm{gf}} = W_{\mathrm{F}}\,. \tag{6.46}$$

The optimal choice of local graph weights is achieved by minimizing the glue weights. It is a special feature of the XY-like region $-1 \leq \Delta \leq 1$ that all glue weights can be set to zero $w_{\mathrm{ge}} = w_{\mathrm{gd}} = w_{\mathrm{gf}} = 0$, leaving three equations for three unknowns and we end up with breakups only, the weights of which are [10]

$$w_{\mathrm{vb}} = \frac{W_{\mathrm{D}}+W_{\mathrm{E}}-W_{\mathrm{F}}}{2}\,, \quad w_{\mathrm{hb}} = \frac{W_{\mathrm{D}}-W_{\mathrm{E}}+W_{\mathrm{F}}}{2}\,, \quad w_{\mathrm{db}} = \frac{W_{\mathrm{E}}-W_{\mathrm{D}}+W_{\mathrm{F}}}{2}\,. \tag{6.47}$$

This is the result of the clever choice of auxiliary weights and, in particular, local graph weights (6.45). But even more important is the fact that due to (6.44), the local graph weights are independent from the underlying spin structure. Once, e.g., the vertical breakup is assigned, it doesn't matter what spin state it is assigned to, the weight of the vertical breakup remains fixed. By assigning a local graph at every moment (i.e. infinitesimal interval) in time between every interacting spin, a global graph is assigned to the total configuration. The global graph is a decomposition into loops (or clusters) [10]. Associated with the underlying spin configuration, every loop is oriented. Along the closed line defined by a loop every segment points into the same direction. The global weight, however, is independent from the orientation of loops. Thus, one could wipe out the information of spins completely and randomly assign

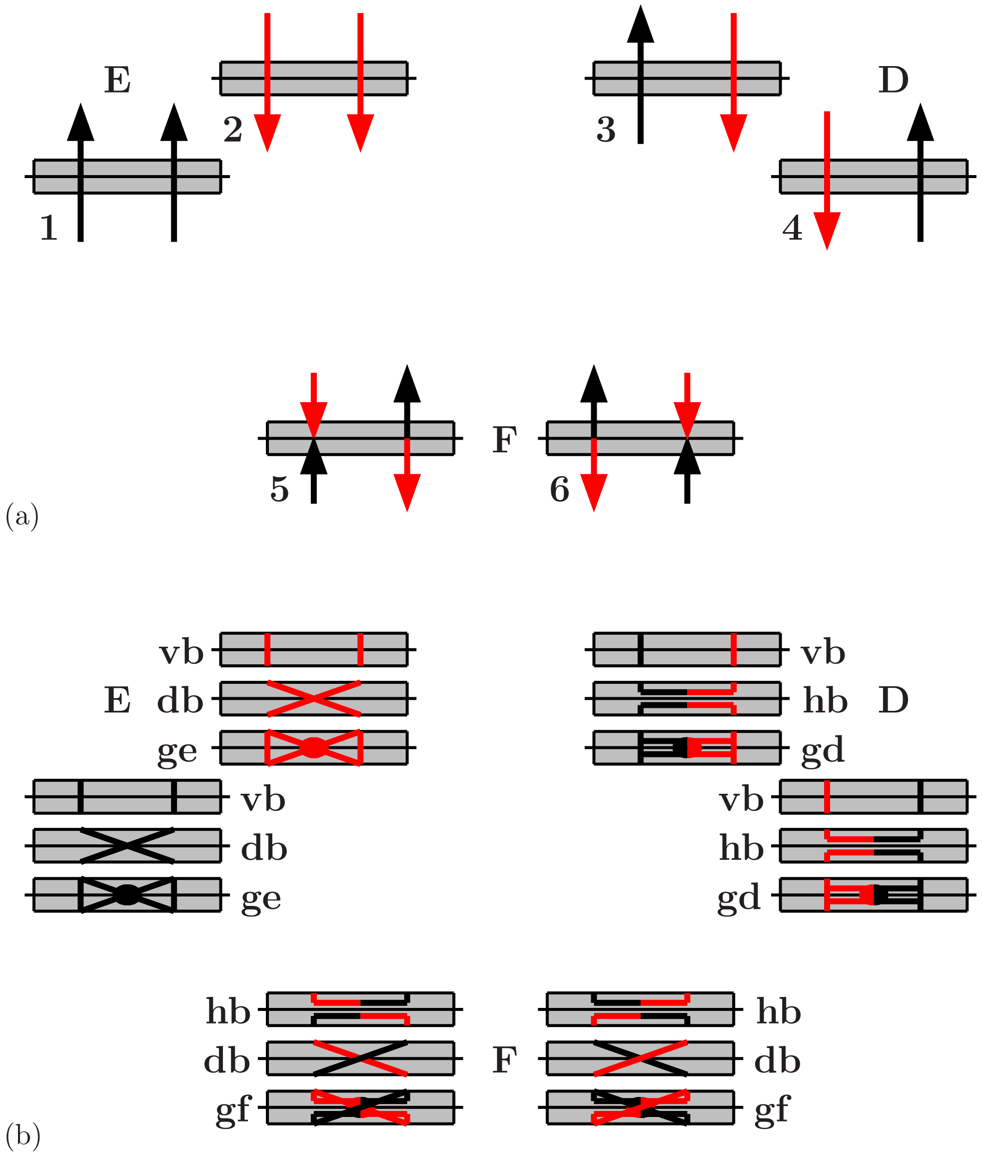

Figure 6.4: Graphical representation of infinitesimal “plaquettes”. (**a**) Coloured arrows denote the state of spins at a specific moment in imaginary time. Six configurations, that are compatible with U(1) symmetry of the XXZ spin chain, fall into three classes: spins are equal (E), different (D) or flip (F). (**b**) Colour refers to the underlying spin configuration. The weight of a local graph assigned to an infinitesimal plaquette, however, is independent thereof. Breakups and glues determine the loop movement: vertical (vb), diagonal (db) or horizontal breakup (hb), and glue on equal (ge), different (gd) or flipped (gf) spins.

a new orientation to each loop, thereby randomly choosing one of the 2^{N_L} possible spin configurations that can be reached from a graph that contains N_L loops. In other words, with respect to the original spin configuration every loop can be flipped or not with suitable probability. If the Hamiltonian is symmetric under spin-inversion, as in our case, this probability is simply $p_{\text{flip}} = 1/2$ [10].

The probability of assigning a local graph to a two-spin state is given by the normalized local graph weights. The normalization follows from (6.46) and the relevant weights in this work result from (6.40) and (6.47),

$$
\begin{aligned}
w_{\text{vb}} &= \begin{cases} \mathrm{e}^{-\mathrm{d}\tau/4} & \text{on unit-bonds} \\ \mathrm{e}^{-\mathrm{d}\tau\lambda/4} & \text{on } \lambda\text{-bonds} \end{cases}, \\
w_{\text{hb}} &= \begin{cases} \mathrm{d}\tau\frac{1+\Delta}{4} & \text{on unit-bonds} \\ \mathrm{d}\tau\frac{1+\Delta}{4}\lambda & \text{on } \lambda\text{-bonds} \end{cases}, \\
w_{\text{db}} &= \begin{cases} \mathrm{d}\tau\frac{1-\Delta}{4} & \text{on unit-bonds} \\ \mathrm{d}\tau\frac{1-\Delta}{4}\lambda & \text{on } \lambda\text{-bonds} \end{cases}.
\end{aligned}
\tag{6.48}
$$

Together with the weights (6.40), the probabilities $p(W_{\text{X}}; w_{\text{y}})$ of assigning local graphs with weight w_{y} to states with weight W_{X}, become

$$
\begin{aligned}
p(W_{\text{E}}; w_{\text{db}}) = 1 - p(W_{\text{E}}; w_{\text{vb}}) &= \mathrm{d}\tau\frac{1-\Delta}{4} \times \begin{cases} 1 & \text{on unit-bonds} \\ \lambda & \text{on } \lambda\text{-bonds} \end{cases}, \\
p(W_{\text{D}}; w_{\text{hb}}) = 1 - p(W_{\text{D}}; w_{\text{vb}}) &= \mathrm{d}\tau\frac{1+\Delta}{4} \times \begin{cases} 1 & \text{on unit-bonds} \\ \lambda & \text{on } \lambda\text{-bonds} \end{cases}, \\
p(W_{\text{F}}; w_{\text{hb}}) = 1 - p(W_{\text{F}}; w_{\text{db}}) &= \frac{1+\Delta}{2} \times \begin{cases} 1 & \text{on unit-bonds} \\ \lambda & \text{on } \lambda\text{-bonds} \end{cases}.
\end{aligned}
\tag{6.49}
$$

Just like the diagonal timeslices form a dense continuous background of an undecorated configuration with occasional isolated events, called jumps, vertical breakups form continuous intervals interrupted by horizontal and diagonal breakups. The difference is that in the decorated case there is only one type of background with a single weight, as the weight of the vertical breakup is independent from the underlying states of spins. The spin states enter only the choice of which non-vertical breakups may be assigned. On a time interval where two interacting spins have different orientation, for example, a horizontal breakup may appear with a constant probability density. This is the characteristic feature of a Poisson process, which motivates the comparison to a decay process [54, 231]. Time intervals between non-vertical breakups are thus distributed exponentially.

The global approach to the multi-loop update consists of the following steps [10]:

1. Randomly spread non-vertical breakups and glues.
2. Identify all loops (or clusters of loops).
3. Flip each loop with a suitable probability.

A typical multi-loop construction is illustrated in Fig. 6.5.

We conclude this section by a look at the…

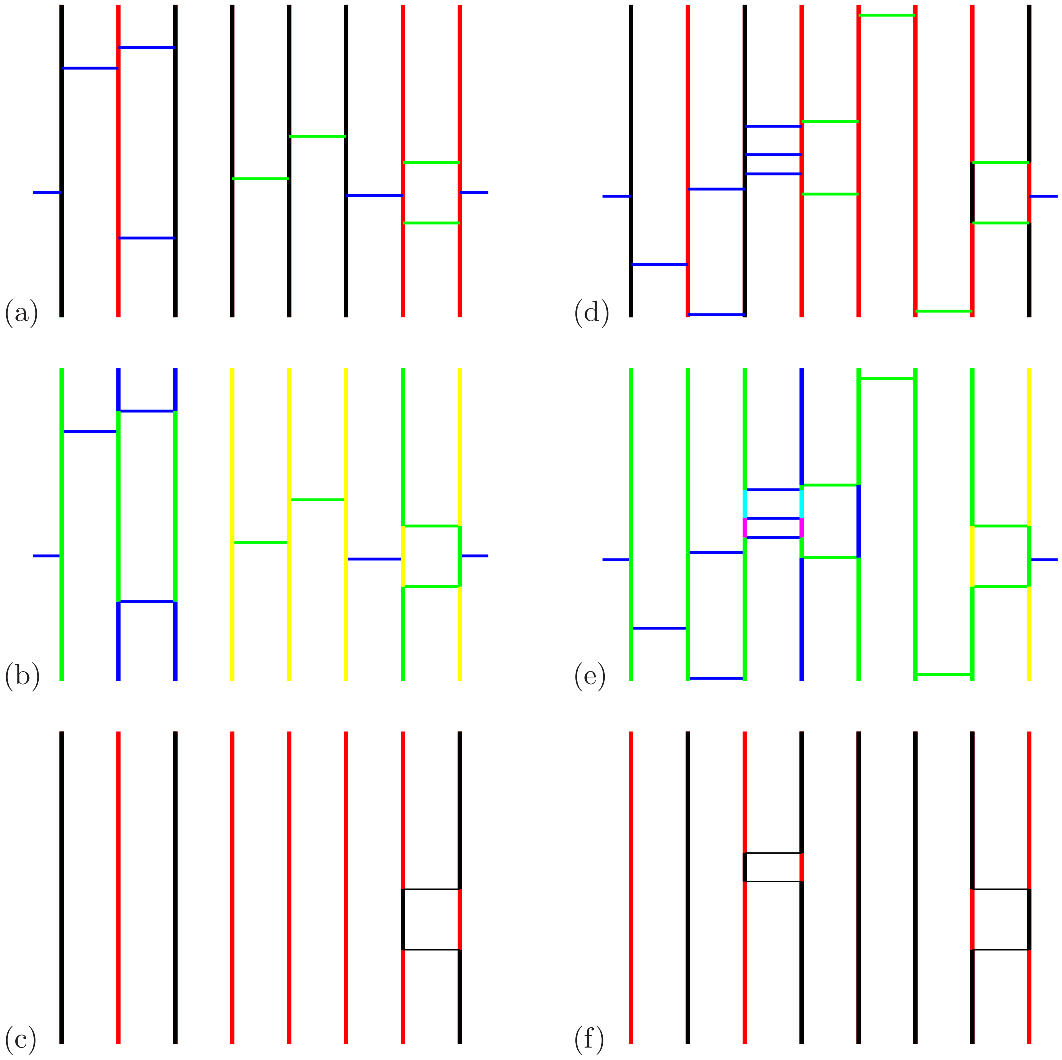

Figure 6.5: Loops at work. Imaginary time is in the vertical direction. Black (red) vertical lines represent segments of spin up (down). (**a**) A random initial configuration with no spin-flips is decorated with diagonal and horizontal breakups (blue and green horizontal lines, respectively). (**b**) Three different (color coded) loops can be identified. (**c**) Flipping the yellow loop leads to the new configuration with two spin-flips on the last bond. (**d**–**f**) The same procedure as every update. (After generation of this plot, we found exactly the same style of plots illustrating the multi-loop algorithm in the Ph.D. thesis of M. Troyer (ETH Zürich, 1994).)

. . . weight of a decorated configuration. Due to the factorization (6.39) of timeslices into a product of two-spin contributions, the weight of a decorated infinitesimal timeslice is the product over local graph weights,

$$
\begin{aligned}
w(\tau) \equiv w_{g(\tau)} &= \prod_{j=0}^{L-1} w_{j,j+1}(\tau) \\
&= \begin{cases} \mathrm{e}^{-\mathrm{d}\tau L/4} & \text{if } \forall_j : w_{j,j+1}(\tau) = w_{\mathrm{vb}} \\ \mathrm{e}^{-\mathrm{d}\tau (L-1)/4}\mathrm{d}\tau \frac{1+\Delta}{4} & \text{if } w_{k,k+1}(\tau) = w_{\mathrm{hb}} \wedge \forall_{j\neq k}\colon w_{j,j+1}(\tau) = w_{\mathrm{vb}} \\ \mathrm{e}^{-\mathrm{d}\tau (L-1)/4}\mathrm{d}\tau \frac{1-\Delta}{4} & \text{if } w_{k,k+1}(\tau) = w_{\mathrm{hb}} \wedge \forall_{j\neq k}\colon w_{j,j+1}(\tau) = w_{\mathrm{db}} \end{cases} .
\end{aligned} \tag{6.50}
$$

Then the total weight $w_{\mathcal{G}}$ of a decorated configuration becomes

$$
w_{\mathcal{G}} = \mathrm{e}^{-\beta L/4} \left(\frac{1+\Delta}{4}\right)^{h_{\mathcal{G}}} \left(\frac{1-\Delta}{4}\right)^{d_{\mathcal{G}}} (\mathrm{d}\tau)^{b_{\mathcal{G}}} , \tag{6.51}
$$

where $b_{\mathcal{G}} = h_{\mathcal{G}} + d_{\mathcal{G}}$ is the total number of non-vertical breakups, the sum of horizontal and diagonal breakups, respectively, in the decorated configuration $\mathcal{G}$. The knowledge of this weight permits the application of reweighting methods to improved estimators, which are observables of a decorated configuration (see Sect. 6.3).

Remarks on the implementation. A bond, or subbond to be more precise (see next section), in our implementation is represented by a class of the same name. This construct merely acts as an envelope to perform several different tasks. In a bond, among other auxiliary information, the coupling constants, respectively the decay constants as described in this sections, are stored, in addition with a reference to the subspins the bond connects (or couples). The primary task of a bond is to spread diagonal and horizontal breakups and to glue edges together.

To spread the breakups, a bond iterates through intervals of constant orientation of both connected subspins, and thereby inserts new edges at randomly chosen times, the time intervals being drawn from an exponential distribution. In parallel, the pointers in the edges are set as demanded by the specific type of breakup that has been inserted.

Loop construction could proceed in two ways, one of which is the well-known Hoshen–Kopelman method [232][10]. We, however, chose a different route. Starting form the origin, we construct one loop after the other, by proceeding through the configuration following the pointers stored in the edges, and systematically looking for uncovered edges. The states of the edges are flipped on-the-fly or not, according to a further random number. A final sweep through the spins (lists) cleans up edges that are not needed anymore, i.e. it removes every edge that is followed by an edge of the same orientation.

The increased complexity due to the presence of horizontal and diagonal breakups, spoils many useful features that simplify the implementation for the isotropic model. For example, if there are only horizontal breakups, the orientation of edges when iterated through a loop inevitably alternates, which is not the case in a diagonal breakup that connects edges of the same orientation. We do not claim to have built

---

[10] See also, e.g., [153].

the most efficient implementation. Programming is also an evolutionary process, thus, our implementation gradually grew less and less error-prone. Of the numerous bugs that we encountered and removed during this process we wish to comment on only one, a particularly difficult-to-track-down one.

The bug has to do with the question of what happens if two breakups are inserted precisely at the same time, both of which connect to a least one common subspin. The reason why the bug was difficult to track, was that drawing exactly equal insertion times on one subspin is an extremely rare event that occurred in the largest systems only. It happened only, when the random number generator generated a floating point number which was exactly the same as some number already generated[11], and the current position of spreading breakups was such that the two equal times could indeed collide. The error that occurred then, was that an edge of extent zero was inserted that had an invalid pointer stored, because it could not be accessed from one side. The fix of the bug was simply to include a test for exactly equal times in the neighbourhood of the current position of insertion.

6.2.3 $S \geq 1$: Subspins and Projectors

Spins of higher magnitude $S \geq 1$ can be represented by $2S$ symmetrized and normalized subspins of size $S = 1/2$ [233],

$$|m, S\rangle = \frac{1}{(2S)!} \sum_{i=1}^{(2S)!} \mathrm{X}_i |\sigma_1, \ldots, \sigma_{2S}\rangle =: \mathrm{P} |\sigma_1, \ldots, \sigma_{2S}\rangle \,. \tag{6.52}$$

where $\{\mathrm{X}_i\}$ is the set of operators that perform the $(2S)!$ possible permutations (including the unit operation) of $2S$ subspins. $2S$ subspins can be in 2^{2S} different states, while a spin of size S can only be in $2S + 1$ states. The symmetrization operator P projects onto the subspace of maximum total spin and thus restores the original size of the Hilbert space. It is symmetric and idempotent, i.e. $\mathrm{P}^2 = \mathrm{P}$, and its matrix elements

$$\langle \sigma'_1, \ldots, \sigma'_{2S} | \mathrm{P} | \sigma_1, \ldots, \sigma_{2S}\rangle = \frac{n_+! n_-!}{(2S)!} \delta_{n'_+, n_+} \,, \tag{6.53}$$

where n_+ (n_-) is the number of subspins that are up (down) in the state $|\sigma_1, \ldots, \sigma_{2S}\rangle$, can be used to define new update rules, or weights of local graphs assigned between subspins of one and the same spin.

The idempotence property of the projector P implies that it must be applied only once. It is suitable to insert the projector at the temporal boundary, where it can be interpreted as relaxed boundary condition [58]. It is not necessary that each single subspin satisfies the periodic boundary condition, as long as the total state of the spin does so. The projector at the boundary permits to randomly permute the links between first and last segments of the same orientation. In accordance with the matrix elements (6.53), each permutation has the same probability $(n_+! n_-!)/(2S)!$. The relaxed boundary conditions are illustrated in Fig. 6.6a.

---

[11] By ”same”, we mean really the same such that the boolean operator “==” evaluates to true. Generating random numbers that are the exactly the same in that sense, does occur inevitably even in the best random number generators.

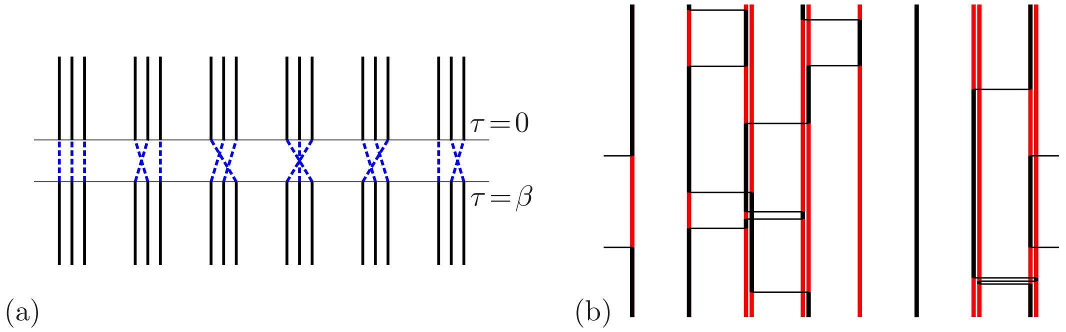

Figure 6.6: Subspin representation of spins with size $S \geq 1$. (**a**) Projectors as relaxed boundary conditions for $S = 3/2$. Dashed lines show the six different possible connections at the boundary if all subspins are in the same state. In the update one of them is chosen randomly. (**b**) A typical configuration of MA with basecell $\frac{1}{2} - \frac{1}{2} - 1 - 1$, where the spins of size $S = 1$ are now represented by two vertical lines.

A two-spin interaction of two large spins of size S_a and S_b decomposes into $4S_aS_b$ contributions. Every subspin of spin a interacts with every subspin of spin b. This leads to an increase of the possibility for two-subspin-flips. This can be seen in Fig. 6.6b, where a typical configuration of a mixed spin chain is shown. In the loop algorithm it leads to an increase of channels for a loop to jump. Or, in terms of the global approach, to an increase of two-subspin time intervals to which local graphs must be assigned. Everything described in the two previous sections, apart from the relaxed boundary conditions, can remain as it is, if the word "spin" is replaced by "subspin".

6.2.4 Measurement: Estimators and Errors

The expectation value of a physical observable $\mathcal{O}$ is *estimated* by the average over configurations

$$\langle \mathcal{O} \rangle_{\mathrm{MC}} = \frac{1}{N} \sum_i \mathcal{O}_i \,, \tag{6.54}$$

where $\mathcal{O}_i = \mathcal{O}(\mathcal{C}_i)$ is the measured value of $\mathcal{O}$ in configuration $\mathcal{C}_i$.

Observables that depend only on the z-components of spin are represented by diagonal operators, we shall call them *diagonal observables.* Diagonal observables, such as the the twist parameter or the longitudinal string observable, are trivial to measure in the sense that the measurement can be directly performed on the basis states. Taking the state of a given configuration at some time τ,

$$|\, n(\tau) \rangle = |\, m_1(\tau), \ldots, m_L(\tau) \rangle \ , \tag{6.55}$$

gives one possible state of the spin chain. All diagonal observables can be measured on that state. We call the corresponding estimator, a **slice** estimator,

$$\mathcal{O}_{\mathrm{sl},\tau} := \mathcal{O}(\tau) = \langle n(\tau) |\ \mathrm{O}\, | n(\tau) \rangle \ . \tag{6.56}$$

By standard, we take the measurement at $\tau = 0$. Alternatively, one may take all states that a configuration offers and average them, i.e. integrate over imaginary time defining an **integrated** estimator,

$$\mathcal{O}_{\text{int}} := \frac{1}{\beta} \int_0^\beta d\tau \mathcal{O}(\tau) \,. \tag{6.57}$$

The loop algorithm permits the construction of improved estimators. A decorated configuration in the loop algorithm that contains n_l loops permits access to 2^{n_l} new configurations $\mathcal{C}'$. Formally, an *improved* estimator is defined as a the observable's estimator averaged over all accessible configurations [10]

$$\mathcal{O}_{\text{imp}} := \frac{1}{2^{n_l}} \sum_{\mathcal{C}'} \mathcal{O}(\mathcal{C}') \,. \tag{6.58}$$

For correlation functions this definition gives an improved estimator – under special circumstances a very simple one indeed – that can be measured with an effort comparable to the measurement of the unimproved estimator (see below). The reduction of variance depends on the average number, and thus size, of loops that can be flipped individually. The size of loops is related to the correlation length. Consequently, the gain from using improved estimator can be moderate at or close to critical points. The main advantage then lies in the fact that improved estimators offer a way to efficiently measure *off-diagonal* observables.

Generalized susceptibilities. An important example for the application of improved estimators are generalized or *dynamic* susceptibilities. Correlation functions such as the spin–spin correlation $G^\alpha_{r_0,\tau_0}(r,\tau) \equiv \left\langle \mathrm{S}^\alpha_{r_0}(\tau_0)\, \mathrm{S}^{\alpha\dagger}_r(\tau) \right\rangle$, are key quantities in the description of critical phenomena. Fourier transforming the correlation function leads to the imaginary time dynamic structure factors

$$\widetilde{G}^\alpha_{r_0,\tau_0}(\omega,k) = \sum_{r=0}^{L-1} \int_0^\beta \mathrm{d}\tau \mathrm{e}^{-\mathrm{i}(kr-\omega\tau)} G^\alpha_{r_0,\tau_0}(r,\tau) \,, \tag{6.59}$$

which averaged over all origins become dynamic susceptibilities

$$\chi^\alpha(\omega,k) = \frac{1}{L\beta} \sum_{r_0=0}^{L-1} \int_0^\beta \mathrm{d}\tau_0 \widetilde{G}^\alpha_{r_0,\tau_0}(\omega,k) \,. \tag{6.60}$$

Of particular importance in this thesis are *staggered* susceptibilities

$$\chi^\alpha_{\mathrm{s}} = \chi^\alpha(0,\pi) \,, \tag{6.61}$$

which can be conveniently measured by the use of improved estimators.

The improved estimator for the longitudinal two-spin correlator is [10]

$$4\big(\mathrm{S}^z_i(\tau_i)\, \mathrm{S}^z_j(\tau_j) \big)_{\text{imp}} = \begin{cases} \sigma_i(\tau_i)\sigma_j(\tau_j) & \text{if the two points are in the same loop(-cluster),} \\ 0 & \text{otherwise,} \end{cases} \tag{6.62}$$

where $\sigma_i(\tau_i) = 2m_i(\tau_i) = \pm 1$. Only if both spins are in the same loop(-cluster), their product will be the same in all configurations that can be reached by loop-flips. In the other case, the two spins will be flipped independently, the product changes sign and contributions cancel. In the special case of isotropic AF interactions, only horizontal breakups between nearest neighbours occur, and within a loop the product $\sigma_i(\tau_i)\sigma_j(\tau_j) = (-1)^{|i-j|}$, always. Comparing with the subsequent definition (6.64), this reflects SU(2) symmetry [10].

The measurement of off-diagonal correlators is possible in decorated configurations but its derivation is a bit more involved [10, 223, 234]. For example, the correlator $\langle \mathrm{S}_i^+(\tau_i)\,\mathrm{S}_j^-(\tau_j)\rangle$, when "inserted" into a configuration, flips the spin at site i (j) and time τ_i (τ_j) from down (up) to up (down). That this flip occurs in the direction of imaginary time and not against it is a time ordering convention. A decorated configuration contributes to the expectation value of $\langle \mathrm{S}_i^+(\tau_i)\,\mathrm{S}_j^-(\tau_j)\rangle$ if the insertion of $\mathrm{S}_i^+(\tau_i)$ and $\mathrm{S}_j^-(\tau_j)$ does *not* produce conflicts in the loop orientations [223, 234]. A flip introduced within one loop "propagates" through the loop along the orientation of the loop (another convention) and must be compensated before the loop closes to avoid a conflict in the loop orientation. Thus, $\mathrm{S}_i^+(\tau_i)$ and $\mathrm{S}_j^-(\tau_j)$ must belong to the *same loop*[12] in order to contribute. It is convenient to take the measurement as an improved estimator, averaging over all possible loop orientations. Then half the configurations contribute to $\langle \mathrm{S}_i^+(\tau_i)\,\mathrm{S}_j^-(\tau_j)\rangle$ while the other half contributes to $\langle \mathrm{S}_i^-(\tau_i)\,\mathrm{S}_j^+(\tau_j)\rangle$, which results in the following prescription,[13]

$$2\big\langle \mathrm{S}_i^\pm(\tau_i)\,\mathrm{S}_j^\mp(\tau_j)\big\rangle_{\mathrm{imp}} = \begin{cases} (-1)^{|i-j|} & \text{if the two points are in the same loop,} \\ 0 & \text{otherwise.} \end{cases} \tag{6.63}$$

The staggering factor appears because of the sublattice basis rotation that has been applied. It cancels automatically, when the staggered correlator is considered. Noting that $\mathrm{S}_i^+(\tau_i)\,\mathrm{S}_j^+(\tau_j)$ and $\mathrm{S}_i^-(\tau_i)\,\mathrm{S}_j^-(\tau_j)$, can never produce consistent loop orientations, it is easy to see that with (6.63), we also obtain the following improved estimator

$$4\big\langle \mathrm{S}_i^x(\tau_i)\,\mathrm{S}_j^x(\tau_j)\big\rangle_{\mathrm{imp}} = \begin{cases} (-1)^{|i-j|} & \text{if the two points are in the same loop,} \\ 0 & \text{otherwise.} \end{cases} \tag{6.64}$$

The proof thereof, and of the same relation for $\mathrm{S}_i^y(\tau_i)\,\mathrm{S}_j^y(\tau_j)$, can be found in [223].

Now (6.62) and (6.63) can be inserted into (6.60) to define efficient measurements of staggered susceptibilities via generalized loop sizes by the following improved estimators [235]

$$4\chi^x_{\mathrm{s,imp}}(\omega,k) = 4\chi^x_{\mathrm{imp}}(\omega,k+\pi) = \frac{1}{L\beta}\sum_{\text{loops } \mathcal{L}} |\mathcal{L}(\omega,k)|^2\,, \tag{6.65}$$

$$4\chi^z_{\mathrm{s,imp}}(\omega,k) = 4\chi^z_{\mathrm{imp}}(\omega,k+\pi) = \frac{1}{L\beta}\sum_{\text{loops } \mathcal{L}} \left(|\mathcal{L}(\omega,k)|_{\mathrm{w}}\right)^2\,, \tag{6.66}$$

---

[12] The flip does not propagate through *clusters* of loops [10].

[13] We quote from [10], but there the factor on the left-hand side of the equation is 4. If this is a misprint or due to some uncommented convention on measurement and time ordering, we do not know. In our interpretation, however, only the factor 2 is consistent with SU(2) symmetry, i.e. that $\langle \mathrm{S}_i^x\,\mathrm{S}_j^x\rangle = \langle \mathrm{S}_i^y\,\mathrm{S}_j^y\rangle = \langle \mathrm{S}_i^z\,\mathrm{S}_j^z\rangle$. See also [223].

where by $|\mathcal{L}(\omega, k)|$ and $|\mathcal{L}(\omega, k)|_{\mathrm{w}}$, we denote the *generalized size* and the *generalized weighted size* of a loop, respectively. These quantities generalize the notion of the size of a single loop, given by the sum of the lengths of all segments that belong to a loop, to arbitrary Fourier-components, by generalizing the length of a segment that extends from τ_{s} to τ_{e} at site r,

$$|\mathfrak{s}(\omega, k)| = \frac{\mathrm{e}^{-\mathrm{i}\omega\tau_{\mathrm{e}}} - \mathrm{e}^{-\mathrm{i}\omega\tau_{\mathrm{s}}}}{-\mathrm{i}\omega}\mathrm{e}^{\mathrm{i}kr}\,, \quad \text{i.e. } |\mathcal{L}(\omega, k)| = \sum_{\mathfrak{s}\in\mathcal{L}} |\mathfrak{s}(\omega, k)|\,. \tag{6.67}$$

In the weighted size of a loop, the length of each segment is multiplied by the orientation $\sigma(\mathfrak{s}) = \pm 1$, of the segment,

$$|\mathcal{L}(\omega, k)|_{\mathrm{w}} = \sum_{\mathfrak{s}\in\mathcal{L}} |\mathfrak{s}(\omega, k)|_{\mathrm{w}} = \sum_{\mathfrak{s}\in\mathcal{L}} |\mathfrak{s}(\omega, k)|\sigma(\mathfrak{s})\,. \tag{6.68}$$

The “weighting” of loop sizes in the improved estimator is necessary due to the product $\sigma_i(\tau_i)\sigma_j(\tau_j)$ in (6.62).

The components of the imaginary time dynamic structure are particularly useful in order to measure finite-size correlation lengths via the moment definition. The second-moment [58, 235, 236],

$$\xi_\tau^{(2)} = \frac{\beta}{2\pi}\sqrt{\frac{\chi_{\mathrm{s}}^x}{\chi^x(2\pi/\beta, \pi)} - 1}\,, \tag{6.69}$$

and the fourth-moment estimator [58]

$$\xi_\tau^{(4)} = \frac{\beta}{4\pi}\sqrt{3\,\frac{\chi_{\mathrm{s}}^x - \chi^x(2\pi/\beta, \pi)}{\chi^x(2\pi/\beta, \pi) - \chi^x(4\pi/\beta, \pi)} - 1}\,, \tag{6.70}$$

of the temporal correlation length, are both estimates of the inverse finite-size energy gap. In the thermodynamic limit, their behaviour is supposed to converge to the behaviour of the “true” correlation length defined by the exponential decay of correlations. Similar quantities can be defined to estimate spatial correlation lengths.

String observables. The improved estimator of the two-point function (6.62) is readily generalized to longitudinal multi- or n-point functions, $\langle \mathrm{S}_{i_1}^z(\tau_{i_1}) \cdots \mathrm{S}_{i_n}^z(\tau_{i_n})\rangle$. For notational simplicity we shall focus on equal-time correlators of spin-$\frac{1}{2}$'s at arbitrary $\tau \equiv \tau_{i_1} = \cdots = \tau_{i_n}$, in the following. If n spins (or subspins) are considered, there will be $l \leq n$ loops (or loop-clusters) covering the n spins. Certainly, a loop may contain more than just one spin. If a loop occurs only once (or an odd number of times), flipping that loop will cause a change of sign in the measurement of the string. In the summation over all accessible configurations in the evaluation of the improved estimator (6.58), such contributions cancel. The flip of a loop that occurs an even number of times never changes the sign. Thus, the improved estimator can be formulated as

$$2^n\big(\,\mathrm{S}_{i_1}^z \cdots \mathrm{S}_{i_n}^z\,\big)_{\mathrm{imp}} = \begin{cases} \sigma_{i_1} \cdots \sigma_{i_n} & \text{if no loop(-cluster) occurs an odd number of times,} \\ 0 & \text{otherwise.} \end{cases} \tag{6.71}$$

Note that the improved estimator of z-strings made up of an odd number of spins (or subspins) is always zero.

It is a bit more complicated to consider general transversal n-point functions [10, 223, 234]. The demand that loop orientations are consistent, immediately implies, first of all, that only strings that contain an even number of operators can gather contributions from decorated configurations, but, second, also that the string must consist of an equal number of raising and lowering operators, and, third, that in each loop there must appear an even number of operators with raising and lowering operators in alternating order along the loop orientation. Consider for the start a four-point function [223, 234], e.g. the equal-time correlator $\langle \mathrm{S}_0^+\,\mathrm{S}_1^-\,\mathrm{S}_2^+\,\mathrm{S}_3^-\rangle$. It receives contributions from two loops, but only if sites 0 and 1 belong to one loop and sites 2 and 3 to the other, or if sites 0 and 3 belong to one loop and sites 1 and 2 to the other, but not if sites 0 and 2 belong to one loop and sites 1 and 3 to the other. Additionally, this four-point function receives contributions from one loop, but only if the loop traverses the sites in the following order: $0 \to 1 \to 2 \to 3$ (and cyclic permutations thereof, of course), or the other way round. When implementing this measurement, e.g. as improved estimator, it is therefore necessary to check the topology of the loop(s). It is, in fact, simpler to directly measure strings in x-components, such as the four-point function $\langle \mathrm{S}_0^x\,\mathrm{S}_1^x\,\mathrm{S}_2^x\,\mathrm{S}_3^x\rangle$. Using $\mathrm{S}_i^x = (\mathrm{S}_i^+ + \mathrm{S}_i^-)/2$, the x-string becomes the sum of 16 terms, only six of which contain two "+"- and two "−"-operators. Every decorated configuration that covers the four spins with either two loops or one, realizes exactly one of these six terms. This leads to the following estimator,

$$2^2\big(\,\mathrm{S}_0^x\,\mathrm{S}_1^x\,\mathrm{S}_2^x\,\mathrm{S}_3^x\,\big)_{\mathrm{imp}} = \begin{cases} (-1)^2 & \text{if covered by 1 or 2 loops,} \\ 0 & \text{otherwise,} \end{cases} \tag{6.72}$$

where $(-1)^2$ represents the staggering factor due to the sublattice basis rotation, which cancels here. This estimator can be interpreted as improved estimator, but does not need to be. The difference is only important when considering individual terms in S_i^+ and S_i^-, but not the sum thereof. The generalization to longer strings of S^x's is straightforward and can be verified inductively, by successively adding two-point single-loop contributions, contributions from permutations, and a new one-loop contribution. It reads similar to (6.71),

$$2^n\big(\,\mathrm{S}_{i_1}^x\cdots\mathrm{S}_{i_n}^x\,\big)_{\mathrm{imp}} = \begin{cases} (-1)^{n_{\mathrm{sbr}}} & \text{if no loop occurs an odd number of times,} \\ 0 & \text{otherwise,} \end{cases} \tag{6.73}$$

where n_{sbr} is the number of (sub)spins affected by the sublattice basis rotation. Note that, again, this estimator is zero, if an odd number of spins is considered and thus n_{sbr} could effectively be replaced by $n/2$, in our mixed spin models.

What we need are the improved estimators of string observables $D^{z/x}(i)$ defined in (5.31) via Σ-variables (5.30)[14]. From the above considerations their improved esti-

---

[14] Recall $\Sigma_i^{z/x} = \prod_{j=1}^{2S_i} \mathrm{i}\sigma_{ij}^{z/x}$, where the number of subspins at site i is $2S_i$.

mators follow immediately,

$$D^z_{\mathrm{imp}}(i) = \begin{cases} \prod_{k\leq i} \Sigma^z_{2k}\Sigma^z_{2k+1} & \text{if no loop(-cluster) occurs an odd number of times,} \\ 0 & \text{otherwise,} \end{cases} \tag{6.74}$$

while

$$D^x_{\mathrm{imp}}(i) = \begin{cases} 1 & \text{if no loop occurs an odd number of times,} \\ 0 & \text{otherwise.} \end{cases} \tag{6.75}$$

The factors in front of (6.71) and (6.73) disappear due to the use of $\sigma^{z/x} = 2\,\mathrm{S}^{z/x}$, and the alternating sign in (6.73) is cancelled in (6.75) due to appearance of the imaginary unit i, in the definition of Σ-variables.

Error estimation. Measured values of observables are random variables that are distributed with some – not necessarily Gaussian – distribution. The straightforward estimate of the statistical error of an observable's estimate is given by $\sqrt{\mathrm{var}(\mathcal{O})/N}$. But the variance, $\mathrm{var}(\mathcal{O}) = \langle\mathcal{O}^2\rangle - \langle\mathcal{O}\rangle^2$, must also be estimated from the simulation data, and the above expression is only valid for completely uncorrelated measurements. Successive configurations are, however, autocorrelated and the true variance and consequently the error is systematically underestimated if uncorrelated samples are assumed. This autocorrelation leads to a reduced effective sample size which is taken into account in the following error estimate [237]

$$\mathrm{err}(\mathcal{O}) = \sqrt{\frac{\mathrm{var}(\mathcal{O})}{N_{\mathrm{eff}}}}\,, \tag{6.76}$$

where $N_{\mathrm{eff}} = N/(2\tau_{\mathcal{O},\mathrm{int}})$, and $\tau_{\mathcal{O},\mathrm{int}}$ is the integrated autocorrelation time of observable $\mathcal{O}$, which is approximately defined as [237]

$$\tau_{\mathrm{O,int}} \approx \frac{1}{2} + \sum_{i=1}^{N} \frac{\langle\mathcal{O}_0\mathcal{O}_k\rangle - \langle\mathcal{O}_0\rangle\langle\mathcal{O}_k\rangle}{\mathrm{var}(\mathcal{O})}\,. \tag{6.77}$$

Practically, the binning and jacknife methods [238] can be used to calculate error estimates without explicitly calculating the integrated autocorrelation time. In both methods the original data series of N measurements is cut into n blocks, or bins, of length $l = N/n$. In the binning method the average of each bin is calculated. The statistical analysis is then performed on the n bin averages. If the length of a bin is much larger than the integrated autocorrelation time of the original data series, the bin averages are statistically uncorrelated and the bias-corrected variance of bin averages should lead to an estimate of the true statistical error. In practice, one may start with a moderate length of bins and successively increase it until a convergence of the error estimate is observed. The jacknife method is similar, but instead of averaging within bins, for each bin the average is calculated from all measurements that do not belong to the bin. This method is particularly suited for the error estimate of functions (or complicated analysis) of observable estimates, such as the second- and fourth-moment estimators of the imaginary time correlation length, (6.69) and (6.70), respectively. The functions can be evaluated on each jacknifed set containing almost all data. Let f be a function of the expectation value of an observable, or the results of some analysis thereof. Then the final estimate is

$$f = f_{\text{tot}} - (n-1)\left(f_{\text{jack}} - f_{\text{tot}}\right) , \tag{6.78}$$

where f_{tot} is the function applied to the average of the total series, and $f_{\text{jack}} = 1/n \sum_j f_j$, is the average of the function applied to the n bin averages. The second term in (6.78) constitutes a bias the jacknife method is capable of detecting. The error of $f_{\mathcal{O}}$ can be estimated to be

$$\text{err}(f) = \sqrt{\frac{n-1}{n} \sum_{j=1}^{n} \left(f_j^2 - f_{\text{jack}}^2\right)} . \tag{6.79}$$

6.3 Reweighting

Reweighting permits the use of data measured in a single simulation at some point in the space of control parameters, to estimate the expectation values of observables at different points in parameter space [59]. By now, reweighting methods are a standard tool in the analysis of classical Monte Carlo data, but only a few years ago the key idea, that is the formulation of the partition function in terms of the density and weight of configurations, has been presented in a way suitable to be applied to data obtained from QMC simulations Troyer et al. [61]. This presentation of the reweighting method, in particular single-histogram reweighting, follows the spirit of [153] and with conceptual aid from [61]. The multi-histogram method [60] is explained following [239]. The general outline of the method is followed by a specification to the needs of this work, and a critical discussion of the quality of reweighted data curves used in this thesis. To the best of our knowledge, reweighting has never been applied to statistical data obtained from QMC simulations with the loop algorithm in path integral formulation.

Let $\beta = \{\beta_1, \beta_2, \ldots\}$ denote the set of given values of different control parameters. Then, the probability $p_\beta(\alpha)$ to observe a specific configuration characterized by a set of different properties $\alpha = \{\alpha_1, \alpha_2, \ldots\}$, is

$$p_\beta(\alpha) = \frac{\rho(\alpha) W_\beta(\alpha)}{Z_\beta} , \tag{6.80}$$

where $\rho(\alpha)$ is the density of configurations with properties α, $W_\beta(\alpha)$ the weight of a configuration with properties α, if the control parameters are set to β, and $Z_\beta = \sum_\alpha \rho(\alpha) W_\beta(\alpha)$, is the partition function. The expectation value of an observable $\mathcal{O}$ at parameters β is

$$\langle \mathcal{O} \rangle_\beta = \sum_\alpha \mathcal{O}(\alpha) p_\beta(\alpha) , \tag{6.81}$$

where $\mathcal{O}(\alpha)$ is the microcanonical expectation value of $\mathcal{O}$ with the properties fixed, i.e. the average over all configurations $\mathcal{C} \in \{\mathcal{C}\}_\alpha$, that share properties α,

$$\mathcal{O}(\alpha) = \frac{1}{\rho(\alpha)} \sum_{\mathcal{C}\in\{\mathcal{C}\}_\alpha} \mathcal{O}(\mathcal{C}) \,. \tag{6.82}$$

Inverting (6.80) for $\rho(\alpha)$, the expectation value of $\mathcal{O}$, when control parameters are set to β' instead of β, can be rewritten in the following way,

$$\langle\mathcal{O}\rangle_{\beta'} = \sum_\alpha \mathcal{O}(\alpha) p_{\beta'}(\alpha) = \frac{Z_\beta}{Z_{\beta'}} \sum_\alpha \mathcal{O}(\alpha) p_\beta(\alpha) \frac{W_{\beta'}(\alpha)}{W_\beta(\alpha)} = \frac{\sum_\alpha \mathcal{O}(\alpha) p_\beta(\alpha) w_{\beta'\beta}(\alpha)}{\sum_\alpha p_\beta(\alpha) w_{\beta'\beta}(\alpha)} \,, \tag{6.83}$$

where in the last equation the normalization condition $\sum_\alpha p_{\beta'}(\alpha) \overset{!}{=} 1$, has been used, and the ratio of weights, $w_{\beta'\beta}(\alpha) = W_{\beta'}(\alpha)/W_\beta(\alpha)$, introduced. This is the fundament of all reweighting techniques.

Single-histogram reweighting. From a single MC simulation with control parameters set to β, the probability $p_\beta(\alpha)$ is approximated by a statistical estimate $p_{\mathrm{MC},\beta}(\alpha)$,

$$p_\beta(\alpha) \approx p_{\mathrm{MC},\beta}(\alpha) = \frac{H_\beta(\alpha)}{N} \,, \tag{6.84}$$

where the histogram $H_\beta(\alpha)$, recorded in N measurements, counts the number of configurations with properties α, that occur during the simulation. The unknown microcanonical averages $\mathcal{O}(\alpha)$ must also be estimated from the MC data. For practical reasons it is convenient to record another histogram,

$$H_{\mathcal{O},\beta}(\alpha) = \sum_{i=1}^{N} \begin{cases} \mathcal{O}(\mathcal{C}_i) & \text{if } \mathcal{C}_i \in \{\mathcal{C}\}_\alpha \\ 0 & \text{else} \end{cases} \,, \tag{6.85}$$

such that $\mathcal{O}(\alpha) \approx \mathcal{O}_{\mathrm{MC}}(\alpha) = H_{\mathcal{O},\beta}(\alpha)/H_\beta(\alpha)$. $H_{\mathcal{O},\beta}(\alpha)$ simply sums up all measurements of $\mathcal{O}$ performed on configurations that share properties α.

The expectation value of $\mathcal{O}$ at arbitrary β' can then be estimated by

$$\langle\mathcal{O}\rangle_{\beta'} \approx \frac{\sum_\alpha H_{\mathcal{O},\beta}(\alpha) w_{\beta'\beta}(\alpha)}{\sum_\alpha H_\beta(\alpha) w_{\beta'\beta}(\alpha)} \,. \tag{6.86}$$

In canonical MC simulations the probability distribution $p_\beta(\alpha)$ is use usually peaked, more or less sharply, around some central values of the properties. The relative errors of the entries in the estimated distribution grow with $1/\sqrt{p_{\mathrm{MC},\beta}(\alpha)}$ [237]. If the peak of $p_{\beta'}(\alpha)$ lies in the error-prone tails of the original distribution, then there will simply be not enough information stored in $p_{\mathrm{MC},\beta}(\alpha)$ to obtain a reliable estimate of $p_{\beta'}(\alpha)$. This limits the range of reweighting. The distributions $p_\beta(\alpha)$ and $p_{\beta'}(\alpha)$ must have a sizeable overlap in the region where the relative errors of $p_{\mathrm{MC},\beta}(\alpha)$ are still small.

Multi-histogram reweighting. If M simulations are carried out at M different sets of control parameters $\{\beta\}_m$, $m = 1, \dots, M$, one gets M different estimates of one and the same density of configurations [239],

$$\rho(\alpha) \approx \frac{Z_m}{N_m} \frac{H_m(\alpha)}{W_m(\alpha)}\,, \tag{6.87}$$

where N_m is the number of measurements in simulation m, and for convenience the shorthands $Z_m = Z_{\beta_m}$, $H_m(\alpha) = H_{\beta_m}(\alpha)$ and $W_m(\alpha) = W_{\beta_m}(\alpha)$ have been introduced. An optimized density of configurations can be constructed by the error-weighted combination of individual histograms, which results in [237, 239]

$$\rho(\alpha) \approx \frac{\sum_{m=1}^{M} H_m(\alpha)}{\sum_{m=1}^{M} \frac{N_m}{Z_m} W_m(\alpha)}\,. \tag{6.88}$$

Using this optimized combined density of configurations in (6.83), the estimate of the expectation value of $\mathcal{O}$ at arbitrary β' becomes

$$\langle \mathcal{O} \rangle_{\{\beta'\}} \approx \frac{\sum_\alpha \Big[M_{\mathcal{O}}(\alpha) \Big/ \sum_m \frac{N_m}{Z_m} w_{m'}(\alpha) \Big]}{\sum_\alpha \Big[M(\alpha) \Big/ \sum_m \frac{N_m}{Z_m} w_{m'}(\alpha) \Big]}\,, \tag{6.89}$$

with the shorthand $w_{m'}(\alpha) = W_m(\alpha)/W_{\beta'}(\alpha) = W_{\beta_m}(\alpha)/W_{\beta'}(\alpha)$ and the combined "master" histograms

$$M(\alpha) = \sum_{m=1}^{M} H_m(\alpha)\,, \quad M_{\mathcal{O}}(\alpha) = \sum_{m=1}^{M} H_{m,\mathcal{O}}(\alpha)\,. \tag{6.90}$$

The partition functions $Z_i = \sum_\alpha \rho(\alpha) W_i(\alpha)$, are unknown and must be determined from the self-consistency condition

$$Z_i \overset{!}{=} Z_i \sum_\alpha \frac{\sum_{m=1}^{M} H_m(\alpha)}{\sum_{m=1}^{M} \frac{N_m Z_i}{Z_m} w_{mi}(\alpha)}\,. \tag{6.91}$$

This can be done, for example, by iteration [239]. Starting with a reasonable initial guess the partition functions converge under iteration to some value $\tilde{Z}_i = Z_i/Z_0$, with an unknown but physically unimportant overall constant factor Z_0, that cancels out in (6.89).

Considerations that limit the reweighting range of the single-histogram also apply to the multi-histogram technique. Loosely speaking, the neighbouring histogram should set in where the first one does not provide enough information anymore. As a rule of thumb two neighbouring histograms should intersect at their half-widths.

Specialization. In the QMC simulations of this thesis, the control parameters are bond alternation, exchange anisotropy and inverse temperature, λ, Δ and β respectively. The properties of interest, that are needed to define the weight of a configuration of the loop algorithm are carefully discussed in Sect. 6.2.1. They are the averaged and "reduced" diagonal energies on unit- and λ-bonds, E_u and E_λ, respectively, and the total number of jumps n, as well as the number of jumps on λ-bonds, n_λ. The weight of a configuration with properties $\{E_\mathrm{u}, E_\lambda, n, n_\lambda\}$ and control parameters $\{\lambda, \Delta, \beta\}$ is

$$W_{\lambda,\Delta,\beta}(E_\mathrm{u}, E_\lambda, n, n_\lambda) = \mathrm{e}^{-\beta\Delta(E_\mathrm{u}+\lambda E_\lambda)} \frac{(\beta/2)^n}{n!} \lambda^{n_\lambda} \,. \tag{6.92}$$

With this weight it is possible to reweight in all three control parameters to an arbitrary set of new values $\{\lambda', \Delta', \beta'\}$ within the limits imposed by the statistical inaccuracy of the data. In this work, however, we will exclusively use the reweighting in λ, i.e. $\Delta = \Delta'$ and $\beta = \beta'$, and the important ratio of weights becomes

$$\frac{W_{\lambda',\Delta,\beta}(E_\mathrm{u}, E_\lambda, n, n_\lambda)}{W_{\lambda,\Delta,\beta}(E_\mathrm{u}, E_\lambda, n, n_\lambda)} = \mathrm{e}^{-\beta\Delta(\lambda'-\lambda)E_\lambda} \left(\frac{\lambda'}{\lambda}\right)^{n_\lambda} \,. \tag{6.93}$$

All histograms that need to be recorded are two-dimensional. Equation 6.93 is the key ingredient in the estimate of the expectation value of $\mathcal{O}$ at λ',

$$\langle \mathcal{O} \rangle_{\lambda'} \approx \frac{\int \mathrm{d}E_\lambda \sum_{n_\lambda} \mathrm{e}^{-\beta(\lambda'-\lambda)E_\lambda} (\lambda'/\lambda)^{n_\lambda} H_{\mathcal{O},\lambda}(E_\lambda, n_\lambda)}{\int \mathrm{d}E_\lambda \sum_{n_\lambda} \mathrm{e}^{-\beta(\lambda'-\lambda)E_\lambda} (\lambda'/\lambda)^{n_\lambda} H_{\lambda}(E_\lambda, n_\lambda)} \,. \tag{6.94}$$

The energy E_λ, however, is a continuous variable, and the sum over E_λ is an integral. The density of configurations $\rho(E_\lambda, n_\lambda)$, counts the number of configurations in the interval $E_\lambda + \mathrm{d}E_\lambda$ with n_λ jumps. Numerically, the integral over E_λ becomes again a sum over discrete intervals of a suitably chosen width ε_{E_λ}, and the histograms necessarily remain discrete.

Care is needed to be taken when reweighting, e.g., the total energy E. One cannot simply record the histogram $H_{\lambda,E}(E_\lambda, n_\lambda)$ and plug it into (6.94), because the total energy of a configuration is $E = \Delta(E_u + \lambda E_\lambda) - n/\beta$, and it depends explicitly on λ.[15] Correctly, the reweighting method (6.94) must be applied to the individual terms separately,

$$\langle E \rangle_{\lambda'} = \Delta(\langle E_u \rangle_{\lambda'} + \lambda' \langle E_\lambda \rangle_{\lambda'}) - \frac{1}{\beta} \langle n \rangle_{\lambda'} \,. \tag{6.95}$$

Similar considerations apply to the specific heat with respect to λ or λ-derivatives of observables, and all other observables the estimators of which depend explicitly on λ.

Reweighting of improved estimators. At first sight, the formal definition of improved estimators as averages over all configurations accessible in an update step may seem discouraging. The number 2^{n_l} of configurations that can be reached from a configuration decorated with n_l loops can become very large, and, generally, the attempt to record an improved histogram over all accessible configurations is hopeless. Decorated configurations are an intermediate though crucial step in the update of a spin configuration. A small change in the point of view makes the applicability of reweighting immediately obvious. What if the decorated configurations are *the* configurations

---

[15] Notation is unfortunate here. The index in E_λ does not indicate a dependence on λ but that the energy is measured on λ-bonds.

of the model and the spin configurations the intermediate step? Such a model is a pure loop model [10]. The weights of decorated configurations, i.e. configurations in the pure loop model, are known. They can easily be constructed from the weights of infinitesimal decorated plaquettes given in [10] and presented in Sect. 6.2.2. The whole machinery of reweighting can be applied to improved estimators. Even though a small step, neither the possibility of reweighting improved estimators of the loop algorithm nor the application thereof have been reported in the literature.

The weight of a decorated configuration does not depend on the diagonal energy but on the number of horizontal and diagonal breakups, d and h, respectively, and on the number of breakups (diagonal and horizontal ones) on λ-bonds, n_λ,

$$W_{\lambda,\Delta,\beta}(d,h,n_\lambda) = \mathrm{e}^{-\beta(1+\lambda)(1+\Delta)/4}\frac{(\beta/4)^{d+h}}{(d+h)!}(1-\Delta)^d(1+\Delta)^h\lambda^{n_\lambda}\,. \tag{6.96}$$

Again, only the ratio of weights is important which, for $\Delta = \Delta'$ and $\beta = \beta'$, is

$$\frac{W_{\lambda',\Delta,\beta}(d,h,n_\lambda)}{W_{\lambda,\Delta,\beta}(d,h,n_\lambda)} = \mathrm{e}^{-\beta(\lambda'-\lambda)(1+\Delta)/4}\left(\frac{\lambda'}{\lambda}\right)^{n_\lambda}\,. \tag{6.97}$$

The single property, n_λ, remains important and the histograms are one-dimensional. The exponential prefactor does not even depend on n_λ and therefor drops out in the expression for the expectation value of $\mathcal{O}$ at λ',

$$\langle\mathcal{O}\rangle_{\lambda'} \approx \frac{\sum_{n_\lambda}(\lambda'/\lambda)^{n_\lambda}H_{\mathcal{O},\lambda}(n_\lambda)}{\sum_{n_\lambda}(\lambda'/\lambda)^{n_\lambda}H_{\lambda}(n_\lambda)}\,. \tag{6.98}$$

With n_λ being a discrete variable, there is no need for the discretization of integrals. The generalization of the reweighting technique to improved estimators is, in fact, a simplification.

Quality of multi-histogram reweighted datasets. Multi-histogram reweighting depends on two parameters, the system size βL, and the spacing of λ-points. Generally, we found the quality of reweighted improved estimators to be more sensitive. Figure 6.7 shows examples of histograms that deliver excellent quality data, while the bad-case scenario is depicted in Fig. 6.8. $L = 128$, represents an intermediate chain length in our simulations, but for MB at $\Delta = 0$ we chose an aspect ratio $a = 6$, i.e. $\beta = 768$, resulting in an already relatively large system. Furthermore, the simulation points were rather widely spread in that case, which resulted in MB at $\Delta = 0$, being the worst case, as far as data quality is concerned.

Reweighted data, obtained from multi- and single-histogram reweighting, that correspond to the histograms shown in Figs. 6.7 and 6.8, can be found in Figs. 6.9 and 6.10. While the reweighted data of the twist parameter z (Fig. 6.10a), the zeroes of which are one definition of pseudocritical points needed in the finite-size scaling analysis (see Sects. 6.4 and 7.2), and the longitudinal string observable D_z (Fig. 6.10e) of MB can still be considered rather smooth curves of acceptable quality, the multi-histogram reweighted curve of the transversal string observable D_x (Fig. 6.10g), though still being smooth, exhibits a visible decrease in quality. Taking the (logarithmic) derivative of D_x, reveals the pathological case as shown in Fig. 6.10g. While the logarithmic derivative of D_z (Fig. 6.10d) does not look to good either, but can still be considered of containing at least some valuable information. Looking at the scale of Fig. 6.10g, this is clearly not the case for the logarithmic derivative of D_x. We consequently discarded the corresponding datasets (and a few more) from our final analysis (see Sect. 8.2.

D_z has been measured using an integrated estimator, which can be reweighted by the standard method for unimproved estimators, but the estimator of D_x is an improved one. The reweighting of improved estimators of the loop algorithm, has been described in this section. The reason for the different performance can be guessed from looking at the curves in Fig. 6.10, that originate from single-histogram reweighting. While for the standard estimators, where the single-histogram reweighted curves at least match the neighbouring datapoints, the improved estimators fail to do so. The combination of all single-histograms into one multi-histogram permits to calculate a continuous line in both cases, but in the case of improved estimators this line can at most be euphemistically considered a data based interpolation of statistically fluctuating datapoints.

Of special importance are extremal quantities that exhibit maxima, that can be used to define pseudocritical points (see Sect. 6.4), such as the susceptibility or the correlation length. It should be obvious from a look at Fig. 6.10b,c that the localization of the maximum can easily lead to wrong results in the case of bad-quality histograms. We have carefully checked all cases by common-sense judgement and comparison to fits to polynomials, whether the estimate of the maxima's location is reasonable, and, in fact, acceptable, and rejected the estimate if that was not the case. Fortunately the situation is different for the *values* at the maxima, which are not too much affected within the statistical accuracy that can be reached from low-quality histograms.

In Sect. A.1, plots of data and reweighted curves equivalent to those in Figs. 6.9 and 6.10, are shown (Figs. A.1–A.12), for a small and a large chain of MA and MB, and three selected values of Δ, a good ($\Delta = 1$), and intermediate ($\Delta = 0.2$ in MA, and $\Delta = 0.4$ in MB) and a bad one ($\Delta = 0$). Figs. A.1–A.12 in the appendix, are thus our most fundamental document of the databasis underlying the analysis presented in Sects. 7.2, 8, 9 and 11.

The decreasing quality of data and histograms with decreasing Δ, is a direct consequence of the rapidly dwindling energy gap, which forced us to chose a larger aspect ratio and consequently simulate considerably larger systems. A sub-optimal choice of possibly too few simulation points, certainly, put its own share into the decreasing quality.

In conclusion of this section, however, we want to put attention on Fig. 6.9, that shows test-data of the spin-$\frac{1}{2}$ chain. In particular Fig. 6.9b–d,g,h show excellent reweighted curves of improved estimators, which we take as confirmation of our correct generalization and application of the reweighting method to improved estimators of the loop algorithm. Pseudocritical points that could be obtained from this method proved crucial in a major part of the analysis in this thesis.

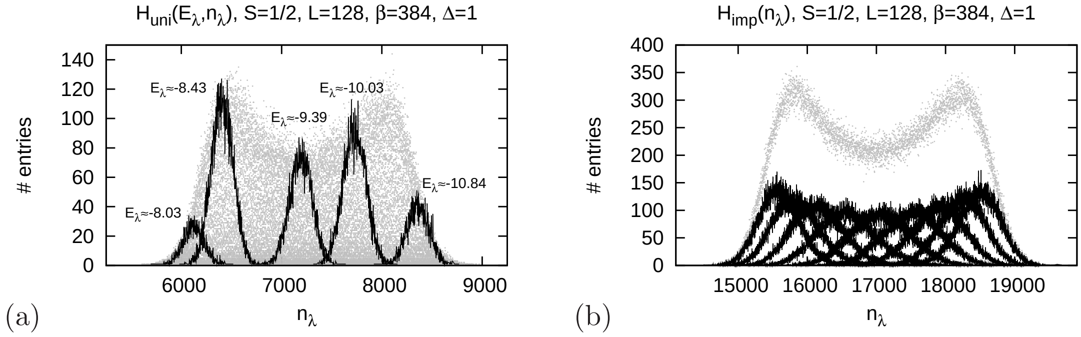

Figure 6.7: High-quality histograms of the spin-$\frac{1}{2}$ chain, $L = 128$ and $\beta = 384$, at the isotropic point, $\Delta = 1$. (**a**) The histogram $H_{\text{uni}}(E_\lambda, n_\lambda)$ is used to reweight "unimproved" or standard estimators, measured in an undecorated spin configuration. The full projected two-dimensional histogram is shown in grey, while the data in black shows the entries of selected values of E_λ. (**b**) The histogram $H_{\text{imp}}(n_\lambda)$ is used to reweight "improved" estimators, measured in a decorated configuration. The full histogram, that contains all entries obtained from simulations at nine different equally-spaced values of λ is shown in grey, while the histograms of each point (used for single-histogram reweighting) are depicted black.

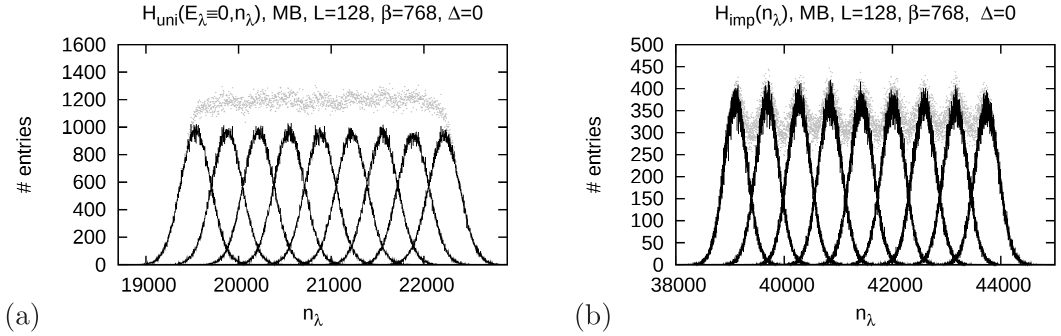

Figure 6.8: Low-quality histograms of the MB, $L = 128$ and $\beta = 768$, at the XY-like point $\Delta = 0$. Grey data shows the full histogram, combining entries the entries of single histograms (black data) obtained from simulation at nine different values of λ. (**a**) The histogram $H_{\text{uni}}(E_\lambda \equiv 0, n_\lambda)$, is effectively one-dimensional at $\Delta = 0$. (**b**) The single (grey) histograms overlap roughly at their half-width, but the combined histogram (black) still exhibits a visible undulation.

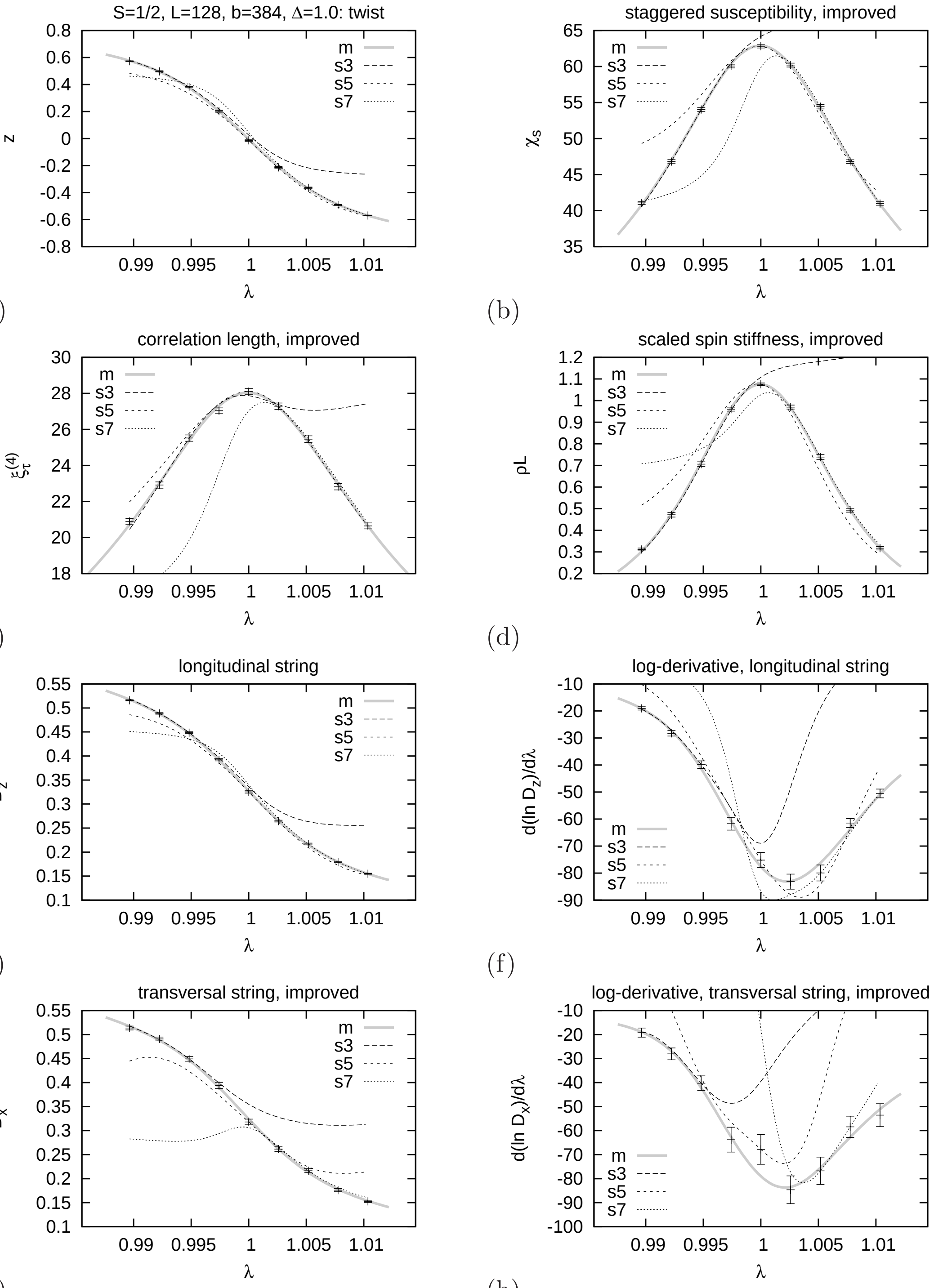

(a) (b) (c) (d) (e) (f) (g) (h)

Figure 6.9: Data of the spin-$\frac{1}{2}$ chain at $\Delta = 1.0$, $L = 128$ and $\beta = 384$. The label "si" (m) denotes data from single-(multi-)histogram reweighting of the i-th (all) point(s).

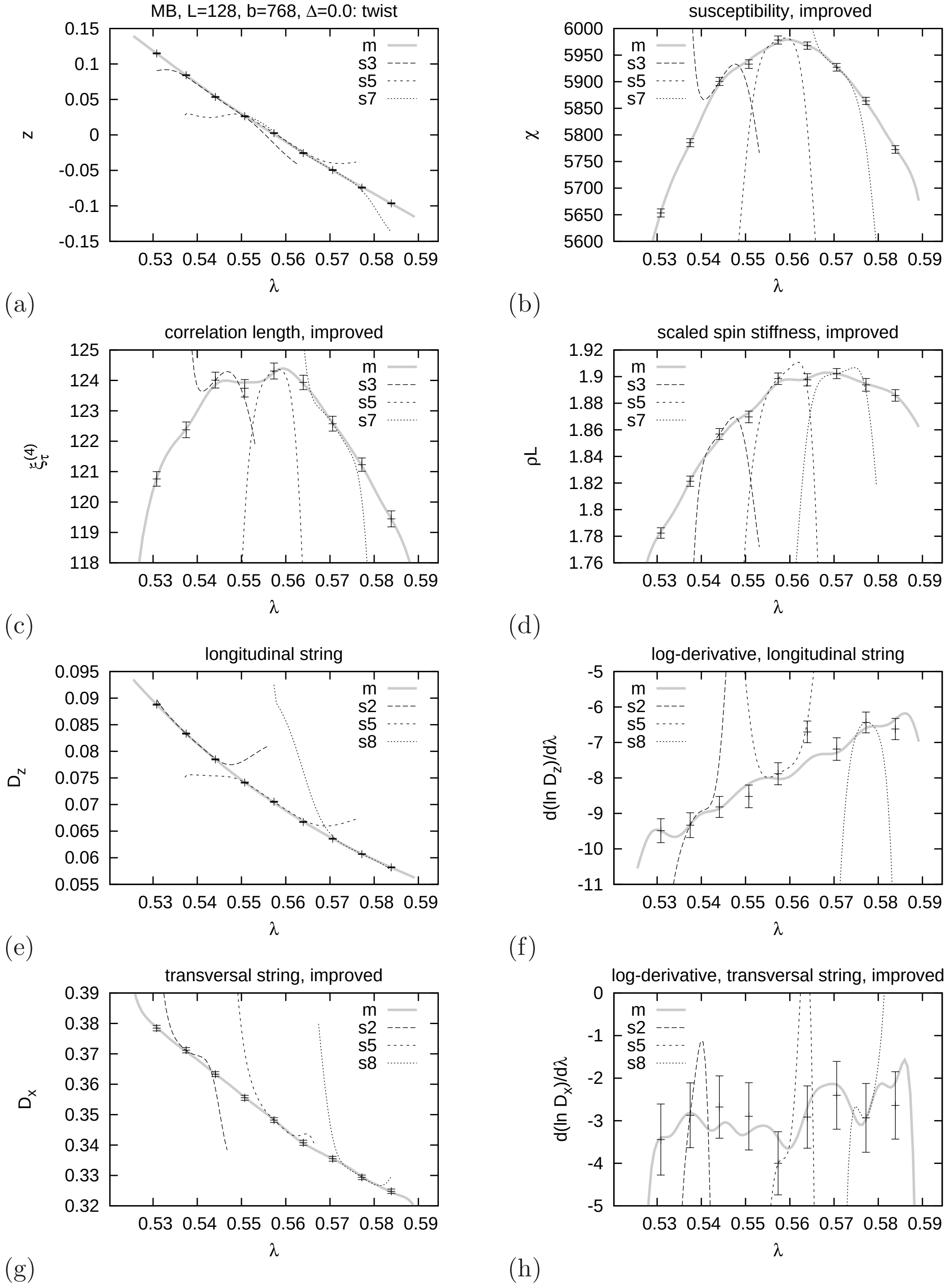

Figure 6.10: Data of MB at $\Delta = 0.0$, $L = 128$ and $\beta = 768$. The label "si" (m) denotes data from single-(multi-)histogram reweighting of the i-th (all) point(s).

6.4 Finite-Size Scaling

Singularities of thermodynamic observables only develop in the thermodynamic limit of infinite system size, and zero temperature in the case of quantum phase transitions. Statistical finite-size data of (quantum) Monte Carlo simulations needs to be extrapolated to the thermodynamic limit. The method to do so is called *finite-size scaling* [56, 57, and refs. therein].[16] It was originally derived phenomenologically and put on rigorous footing within the concept of renormalization [26]. In finite systems singular thermodynamic observables become analytic functions of the control parameters. Divergences are rounded off to yield distinct maxima that are generally shifted away from the critical point. In its essence, the idea of finite-size scaling is simple but effective. Sufficiently close to the critical point the correlation length ξ exceeds the linear system size L, and the (finite-size) correlation length ξ_L, wherever it appears in scaling relations, explicitly or implicitly, can be replaced by L. This is embodied in the main hypothesis of finite-size scaling that assumes ξ to be the *only* relevant length scale in the vicinity of the critical point, and that observables and finite-size effects depend only on the the ratio of the two fundamental length scales L/ξ. Far off criticality, where $L \gg \xi$, the system is not "aware" of its finiteness and observables exhibit the behaviour of the infinite system, traditionally called bulk behaviour in that context. On the contrary, finite-size effects dominate when $L \ll \xi$. The crossover sets in in a region where $L \approx \xi$. To leading order, this is the region where $L/\xi \sim Lt^{\nu} \approx 1$, or equivalently in terms of the *scaled* control parameter

$$r = tL^{1/\nu} \approx 1\,. \tag{6.99}$$

The behaviour of observables follows naturally from homogeneity laws derived by the renormalization technique when the inverse length L^{-1} is added as another control parameter or scaling field. It is necessarily relevant and its RG eigenvalue is trivially $y_{L^{-1}} = 1$. Considering quantum phase transitions, the temperature β^{-1} enters as another "length", being a relevant scaling field with RG eigenvalue $y_{\beta^{-1}} = z = 1$, here [26, 134]. By fixing the scale factor $b = \mathrm{e}^{l} = L$, scaling laws become FSS laws, which for the correlation length is

$$\xi(\{g_{i0}\}; L^{-1}, \beta^{-1}) = L\,\xi(\{r_i\}; 1, a)\,, \tag{6.100}$$

with $a = L\beta^{-1}$, the aspect ratio, and the scaled variables

$$r_i = r_i(\{g_{i0}\}; L, a)\,. \tag{6.101}$$

Keeping the aspect ratio a constant[17] one may write

$$\xi(\{g_{i0}\}; L^{-1}, \beta^{-1}) = L\,\xi(\{r_i\})\,. \tag{6.102}$$

---

[16] See also, for example, [25, chap. 3] or [237].

[17] The aspect ratio measures the "distance" from the groundstate. Assuming that it is chosen small enough in order to measure only the groundstate properties is equivalent to truncate an expansion in the aspect ratio after the zeroth-order term.

Similarly one may write for the singular part of the free energy density, again at constant aspect ratio,

$$f(\{g_{i0}\}; L^{-1}, \beta^{-1}) = L^{-D} f(\{r_i\}) \,. \tag{6.103}$$

The functions $\xi(\{r_i\})$ and $f(\{r_i\})$ are *universal* and *analytic* functions of their arguments. Non-universal model-dependent properties enter through the initial values $\{g_{i0}\}$ in the definition of the arguments (6.101). The initial values $g_{i0} = g_{i0}(t, h, u, \ldots)$, are to lowest order proportional to the control parameters of the model considered, but may, in principle depend on all other (relevant and irrelevant) parameters.

In order to avoid confusion it is useful to clarify the notation. Considering, e.g., the control parameter λ, we have the following identifications:

λ ... principal control parameter,
$t = |\lambda - \lambda_\mathrm{c}|$ ... redefined control parameter,[18]
$g_{t0} \sim t$ ... initial value of corresponding scaling field,[19]
$r_t = g_t(\ln L)$ ... scaled variable, rescaled scaling field.

Assuming that r_t is the only variable in (6.102) and (6.103) and that it does indeed take the form (6.99), i.e. neglecting all possible corrections to FSS, leads to *conventional second-order FSS*. By taking derivatives of the singular part of the free energy density (6.103), the generic (asymptotic) form of observables becomes

$$\mathcal{O}_L \sim L^{\rho/\nu} \mathcal{O}(r_t) \,, \tag{6.104}$$

with ρ the critical exponent of observable $\mathcal{O}$. This leads to the famous data-collapse of the scaled observable $\mathcal{O}/L^{\rho/\nu}$, is plotted against the scaled variable $r_t = tL^{1/\nu}$. The conventional FSS analysis then proceeds as, e.g., follows:

- From a series of suitably defined pseudocritical points $\lambda^*(L)$, determine the true critical value λ_c, from

  $$\lambda^*(L) = \lambda_\mathrm{c} + r^* L^{-\theta} \,, \tag{6.105}$$

  where r^* is the value of r_t where pseudocritical points collapse in the scaling plot, and θ is the shift exponent that is supposed to be equal to $1/\nu$.

- Determine critical exponent ratios ρ/ν, either from $\mathcal{O}(r_t = r^*)$, the values at the pseudocritical points which has the advantage of being independent from the

---

[18] To be precise, this discussion is based on the symmetric parameterization of bond alternation $\delta = (\lambda - 1)/(\lambda + 1)$. In terms of δ, the principal control parameter is $t = \delta - \delta_\mathrm{c}$ which translates into

$$t = \frac{2}{1+\lambda_\mathrm{c}} \sum_{n=1}^{\infty} \left(\frac{\lambda - \lambda_\mathrm{c}}{1+\lambda_\mathrm{c}}\right)^n \,.$$

Sufficiently close to the critical point $t \sim \lambda - \lambda_\mathrm{c}$. The powers in $(\lambda - \lambda_\mathrm{c})$, however, modify the amplitudes of analytic corrections that results from the expansion (6.109) (see below).

[19] Comparing to Sect. 5.6, g_{t0} corresponds to t_0.

estimate of the critical point, or from $\mathcal{O}(r_t = 0)$, the values at the critical point, via

$$\mathcal{O}_L = B + AL^{\rho/\nu}\,, \tag{6.106}$$

where B represents a possible background term and the amplitude A is either $\mathcal{O}(r^*)$ or $\mathcal{O}(0)$.

Suitably defined pseudocritical points are, e.g., the maxima of the susceptibility, zeroes of the twist parameter or crossing points of Binder cumulants [240–242] of the order parameter. Logarithmic derivatives of moments of the order parameter and derivatives of the Binder ratios of the order parameter give access to direct estimates of the important ratio $1/\nu$ [153, 240–242], i.e.,

$$\frac{\mathrm{d}\ln m^k}{\mathrm{d}\lambda} \sim L^{1/\nu}\,, \tag{6.107}$$

$$-\frac{\mathrm{d}}{\mathrm{d}\lambda}\frac{\langle m^{2k}\rangle}{\langle m^k\rangle^2} \sim L^{1/\nu}\,, \tag{6.108}$$

respectively. This is particularly useful when $\theta \neq 1/\nu$, which happens, e.g., if the presence of at least one irrelevant field cannot be neglected. Generally, conventional FSS must be modified if *corrections to FSS* cannot be neglected. These corrections fall into three classes: analytic, non-analytic and logarithmic corrections.

Analytic corrections to scaling and FSS are generated by non-linear dependencies of the initial values g_{i0} on the control parameter t, and cross-dependencies on other relevant control parameters [199]. Cross-dependencies on irrelevant control parameters can be absorbed by a redefinition of t [199]. Analytic corrections do not affect FSS precisely at the critical point, because there $t = 0$ (and so are all other relevant fields), but the shift of pseudocritical points does not simply follow (6.105) anymore. In conventional scaling plots, pseudocritical points do not collapse into the same point r^*, because the correct scaling argument is $r_t = g_{t0}L^{1/\nu}$ with [199]

$$g_{t0} = t + \tau_{h^2}h^2 + \tau_{t^2}t^2 + \tau_{t^3}t^3 + \tau_{th^2}th^2 + \tau_{h^4}h^4 + \cdots\,, \tag{6.109}$$

rather than $r_t = tL^{1/\nu}$. For demonstration we have included a magnetic field h, or general field from the odd sector, which together with t also enters in the expansion of g_{h0}, the initial value of the scaling field,

$$g_{h0} = h + \eta_{ht}ht + \eta_{ht^2}ht^2 + \eta_{h^3}h^3 + \cdots\,. \tag{6.110}$$

To obtain the shift behaviour of pseudocritical points defined by, say, extrema of observables, one would have to solve $\mathrm{d}\mathcal{O}_L/\mathrm{d}t|_{\lambda=\lambda_L^*} = 0$, which, generally, is impossible to do in closed form. One has to take refuge in expansions and asymptotics to obtain $\lambda_L^* \sim \lambda_\mathrm{c} + S_1L^{-1/\nu}(1 + S_2L^{-1/\nu} + \cdots)$, with the leading shift amplitude S_1 and the amplitude S_2 of the leading analytic correction. However, this is only valid for sufficiently large L. A similar modification appears in the values of observables at pseudocritical points, because $t_L^* = \lambda_L^* - \lambda_\mathrm{c}$ enters as argument.

As a secondary effect, cross-dependencies of relevant scaling fields may lead to non-analytic correction terms to scaling [199], but also to FSS, in second derivatives of the free energy density, such as the specific heat or the magnetic susceptibility. The primary source for *non-analytic* corrections, however, are irrelevant fields [26, 243].

The initial values of irrelevant scaling fields cannot be set to zero at the critical point. Non-analytic corrections do affect FSS at the critical point. To lowest order, the scaled variable corresponding to an irrelevant scaling field l with RG eigenvalue $y_l = -|y_l| < 0$, is [26, 243]

$$r_l = l L^{-|y_l|}\,, \tag{6.111}$$

where, for simplicity, we have assumed the initial value $g_{l0} = l$. This leads to the consequence that the amplitude A, in (6.106), is itself L-dependent even at the critical point, i.e. $A = A(r_l) = A(lL^{-|y_l|})$. Taylor expanding in the argument r_l [26] leads to

$$\mathcal{O}_L = B + A_0 L^{\rho/\nu}\left(1 + \frac{A_1}{A_0} l L^{-|y_l|} + \cdots\right)\,, \tag{6.112}$$

for every irrelevant field that is present and significant. The corrections are suppressed by $L^{-|y_l|}$ and vanish for sufficiently large L. What is sufficiently large, in fact, depends on the value of the exponent y_l and the amplitude $(A_1/A_0)l$, which depends on the generally unknown value of l. It might seem reasonable to assume a similar multiplicative modification of the conventional shift behaviour (6.105), but Privman and Fisher [244] stated[20] that an irrelevant field may modify, in fact, the shift exponent

$$\theta = \frac{1}{\nu} + k|y_l|\,, \tag{6.113}$$

with $k = 0, 1, 2\ldots$, the value depending on symmetry consideration [245]. Figure 6.11 shows some candidate exponents, i.e. irrelevant RG eigenvalues, of the Gaussian operator content of the spin-$\frac{1}{2}$ chain in the region $1 \leq \Delta \leq 1$. Every irrelevant operator can, in principle, generate a correction to FSS with exponent $y_{n,m}$. From the Taylor expansion in (6.112), it follows that also multiples of $y_{n,m}$ may appear as correction exponents. Furthermore, in addition to primary scaling operator, also the descendant operators may generate non-analytic corrections, yielding potential candidates $y_{n,m} - i$, for correction exponents at each level i of the corresponding conformal tower. This large set of candidates for correction exponents, can be drastically reduced by symmetry considerations, which, however, will not be uttered here.[21]

Last, but not least, there may be *logarithmic* corrections to FSS. The corresponding corrections to scaling have been discussed in Sect. 5.6. Logarithmic corrections appear when a marginal scaling field[22] with $y_l = 0$, is present. Based on the main hypothesis of this thesis, we have reason to expect logarithmic corrections in the observables of mixed spin models MA and MB at the isotropic points. SU(2) symmetry forces the perturbing cosine-term of the sine-Gordon model to be marginal at the isotropic point. Let u be the marginal field, r_u the corresponding scaling variable and $g_{u0} = u_0$, its initial value (we use u_0 instead of simply u, to be in agreement with Sect. 5.6).

---

[20] The statement being expanded into a two-liner by Henkel et al. [245].

[21] See, for example, [244, 246, 247], or the discussions in [245] or [214].

[22] A marginally (ir)relevant scaling field, to be precise.

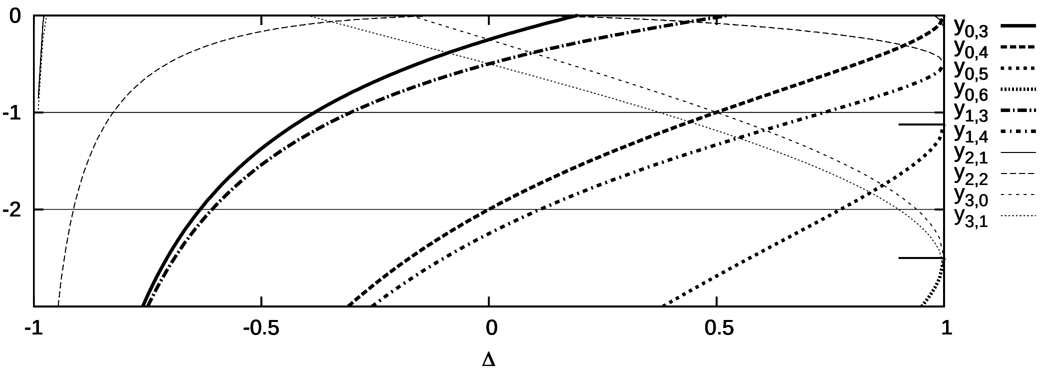

Figure 6.11: Some irrelevant RG eigenvalues of the Gaussian operator content of the spin-$\frac{1}{2}$ chain. Short lines at the right border indicate the values of the 4-state Potts model.

Then, using the results from Sect. 5.6 for logarithmic corrections, the relevant scaled variables r_t and r_h are modified to [214, 248]

$$r_t = g_{t0} L^{1/\nu} \mathcal{Z}^{-\hat{\nu}/\nu} , \tag{6.114}$$

$$r_h = g_{h0} L^{y_h} \mathcal{Z}^{-y_h b_h / a_2} , \tag{6.115}$$

and the scaled marginal variable is (5.55),

$$r_u = \frac{u_0 f_{\mathrm{c}}^{(3)}(\ln L)}{1 + u_0 a_2 \ln L} . \tag{6.116}$$

Then, the variable $\mathcal{Z}$, introduced in (5.54), takes the form

$$\mathcal{Z} = \frac{u_0}{a_2 + a_3 u_0} \left(a_3 + a_2 \frac{1 + a_2 u_0 \ln L}{u_0 f_{\mathrm{c}}^{(3)}} \right) , \tag{6.117}$$

which is linear in $\ln L$, apart from the function $f_{\mathrm{c}}^{(3)} = f_{\mathrm{c}}^{(3)}(\ln L)$. In scaling and finite-size scaling laws, usually powers of the variable $\mathcal{Z}$ appear. To observe the proclaimed leading asymptotic behaviour $\sim L^{\rho/\nu} (\ln L)^{\hat{\rho} - \rho\hat{\nu}/\nu}$, the term proportional to $\ln L$, must be much larger than the (approximately) constant terms. This is satisfied if $\ln L \gg 1/a_2 u_0 + f_{\mathrm{c}}^{(3)} a_3 / a_2^2$, or roughly equivalent $\ln L \gg 1/a_2 u_0$, which can be seen from a simple rearrangement of (6.117). If $a_2 u_0 = 2$, and $\ln L = 5$, say, can be considered large enough, this would imply a chain length $L \approx 150$, to be on safe grounds, while already for $a_2 u_0 = 1$, $L \approx 20000$ would be needed, and obviously much worse for even smaller values of $a_2 u_0$. Furthermore, the function $f_{\mathrm{c}}^{(3)}$ converges to unity with growing L, but very slowly, with the rate depending on $a_2 u_0$. Using the approximation [210] (see Sect. 5.6)

$$f_{\mathrm{c}}^{(3)}(l) \approx 1 - \frac{a_3}{a_2^2} \frac{\ln(l + 1/(a_2 u_0) + a_3/a_2^2)}{l + 1/(a_2 u_0)} , \tag{6.118}$$

with $a_2 u_0 = 0.5$ (and $a_3/a_2^2 = 1/2$), $f_{\mathrm{c}}^{(3)}$ takes the value 0.852 at $L = 100$, and 0.890 at $L = 10000$, while for $a_2 u_0 = 2$, $f_{\mathrm{c}}^{(3)}$ takes approximately the value 0.831 at

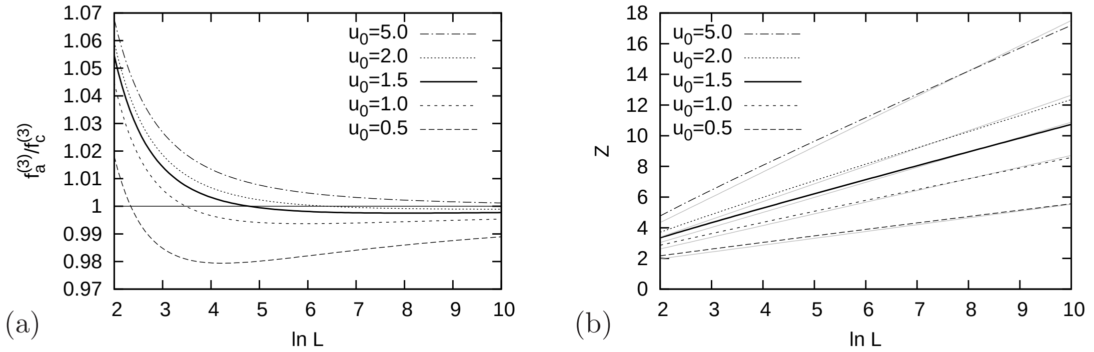

Figure 6.12: (**a**) Comparison of $f_\mathrm{c}^{(3)}$, which with $a_2 u_0 = 1.753(1)$ gives very good agreement with exact data [210], and $f_\mathrm{a}^{(3)}$, a truncated asymptotic form containing only the universal ratio a_3/a_2^2. Plotted is the ratio $f_\mathrm{a}^{(3)}/f_\mathrm{c}^{(3)}$. (**b**) The variable $\mathcal{Z}$, as given in (6.117), using $f_\mathrm{c}^{(3)}$. Full lines are added for comparison. They are really straight lines with $f_\mathrm{c}^{(3)}$ set to some appropriate value < 1.

$L = 100$, and 0.880 at $L = 10000$. None can be safely assumed to be equal to unity. Nomura [210] produced excellent agreement with exact Bethe ansatz data of very large spin-$\frac{1}{2}$ chains ($L = 1024 \ldots 16384$), from a fit using the above form of $f_\mathrm{c}^{(3)}$, that yielded $a_2 u_0 = 1.753(1)$. For a sufficiently small size of the L-window used, $f_\mathrm{c}^{(3)}$ can possibly be assumed approximately constant. From $L = 160$ to 384, or 512, being a typical and accessible L-window in QMC simulations, the values of $f_\mathrm{c}^{(3)}$ vary within 1–2%, which might, however, be too much with very accurate data.

With the ratio a_3/a_2^2 universal, $f_\mathrm{c}^{(3)}$ as stated above has the advantage of containing only a single free parameter, the product $a_2 u_0$. The asymptotic form (5.60), which we shall denote $f_\mathrm{a}^{(3)}$, here, i.e.

$$f_\mathrm{a}^{(3)} \sim 1 - \frac{a_3}{a_2^2} \frac{\ln l}{l} , \tag{6.119}$$

needs at least one further parameter, if one wants to somehow incorporate the $O(1/l)$-term, that has been ignored above. However, for $a_2 u_0 = 1.5$, $f_\mathrm{a}^{(3)}$ seems to already a good approximation for $\ln L > 4$, as can be seen in Fig. 6.12a. The quality of $f_\mathrm{a}^{(3)}$ compared to $f_\mathrm{c}^{(3)}$, depends crucially on the value $a_2 u_0$. To incorporate the $O(1/l)$-term, does not seem be so simple, because the ratio plotted in Fig. 6.12a is non-monotonous. For small L, $f_\mathrm{a}^{(3)}$ is larger than $f_\mathrm{c}^{(3)}$, while asymptotically $f_\mathrm{a}^{(3)}$ approaches $f_\mathrm{c}^{(3)}$ from below. To effectively model this difference by an $O(1/l)$-term, that is sufficiently simple, one possible has to go to, again, to rather large system sizes.

The linearity of the variable $\mathcal{Z}$ itself, can be studied in Fig. 6.12b, using $f_\mathrm{c}^{(3)}$ for different values of $a_2 u_0$. Comparison to real straight lines shows, that $\mathcal{Z}$ is indeed not exactly linear, and can only be assumed to be so in a sufficiently small L-window, but with effective discriminant and slope. Depending on the accuracy of the data, linear behaviour of $\mathcal{Z}$ in $\ln L$, might be a reasonable assumption, or not.

The slow behaviour is the general problem when trying to analyze logarithmic corrections numerically. Salas and Sokal [211] argued that in order to observe the dominance of the universal ($\ln\ln L/lnL$) term over the combined universal and non-universal contribution of order $1/\ln L$ correction in the susceptibility of the 4-state Potts model, it would be necessary to go to extremely large system sizes, $L \approx 10^{64}$. Another example for the pathological character of logarithmic corrections is Table I in [210], where finite-size estimates of the isotropic spin-$\frac{1}{2}$ chain, obtained from exact Bethe ansatz calculations [249, 250], are listed. While, for relatively[23] large $L = 16384$, the exact value $c = 1$ is reproduced up to three digits, while the scaling dimension x_{t}, of the elementary triplet excitation, which has the exact value 1/2, still gives the relatively poor effective estimate 0.478.

In the presence of logarithmic corrections (neglecting power-law correction here), the generic zero-field FSS form of observables is

$$\mathcal{O}_L(\lambda_{\mathrm{c}}) \sim L^{\rho/\nu} \mathcal{Z}^{\hat{\rho}-\rho\hat{\nu}/\nu} \sim L^{\rho/\nu} (\ln L)^{\hat{\rho}-\rho\hat{\nu}/\nu} \,, \tag{6.120}$$

where ρ and $\hat{\rho}$ are critical and logarithmic exponents, respectively, of observable $\mathcal{O}$ (see Sect. 5.6). From the form (6.114) of r_t it follows, that also the shift behaviour of pseudocritical points is modified. To leading order it looks

$$\lambda^*(L) = \lambda_{\mathrm{c}} + r^* L^{-1/\nu} \mathcal{Z}^{\hat{\nu}/\nu} (1 + \cdots) \sim \lambda_{\mathrm{c}} + r^* L^{-1/\nu} (\ln L)^{\hat{\nu}/\nu} \,, \tag{6.121}$$

but it is virtually impossible to observe this behaviour in finite-size simulations. Additionally, analytic and non-analytic power-laws may appear as pure terms as already discussed, but also mixed in with logarithmic terms.

Logarithmic corrections are difficult to track down quantitatively and they "spoil" the scaling and finite-size scaling behaviour of physical observables on virtually all length scales. If the presence of logarithmic corrections is unknown or neglected, the assumption of power-law behaviour inevitably leads to wrong estimates of critical exponents. However, results are wrong in a systematic way that has been investigated by Affleck and Bonner [204]. Under the assumption of pure power-law behaviour, the fundamental scaling dimension of the spin-$\frac{1}{2}$ Heisenberg chain, which has the exact value $x = 1/2$, may be overestimated to yield the *effective* value $x^{\mathrm{eff}} \approx 0.71$.

---

[23] Extremely large, from the QMC point of view, in fact.

Part II

Results and Discussion

7 Phase Boundary

The results for the critical line $\lambda_c(\Delta)$ are presented in two parts. Section 7.1 treats results obtained from extrapolation of exact data, and Sect. 7.2 those obtained from finite-size scaling of simulation data from quantum Monte Carlo. See Sect. 6 for a detailed description of the underlying numerical methods. A summary will be given at the end of this section in Sect. 7.3.

7.1 Extrapolation of Exact Data

We found the groundstates of both mixed spin chains in the sector with magnetization $M = 0$ and basecell momentum $P = 0$. The groundstate's parity of MA (5.2) alternates between even and odd for even and odd numbers of basecells, respectively, while the groundstate of MB (5.3) lies in the even sector for any number of basecells. This is in perfect agreement with Marshall's sign criterion [37, 38]. The lowest excited states belong to the first magnetized sector, $M = 1$, with momentum $P = 0$, and parity opposite to the groundstate sectors.

For fixed values of the exchange anisotropy Δ, we located the minimum of the energy gap between the groundstate and first excited state. We thus obtained a series of five finite-size estimates of the critical point for MA ($L = 4, 8, 12, 16$ and 20) and a series of four estimates for MB ($L = 4, 8, 12, 16$). To obtain an estimate of the true critical point ($L \to \infty$) we used the BST algorithm, which accelerates the convergence of the series and successively eliminates data points from the series until a final estimate is reached. See Sect. 6.1.3, for a description of the BST extrapolation method. The procedure can be organized in tables of the form [25]:

$$\begin{array}{ccc}
\lambda_0^{(0)} & & \\
 & \lambda_1^{(0)} & \\
\lambda_0^{(1)} & & \lambda_2^{(0)} \\
 & \lambda_1^{(1)} & \\
\lambda_0^{(2)} & & \ddots
\end{array}$$

The first column is the original series of finite-size estimates. A sample table is shown in Table 7.1. We used $\varepsilon_5^{(0)} = 2|\lambda_4^{(0)} - \lambda_4^{(1)}|$, to estimate the error of the final estimate $\lambda_c = \lambda_5^{(0)}$, for MA, and similarly $\varepsilon = \varepsilon_4^{(0)}$, for the final estimate $\lambda_c = \lambda_4^{(0)}$ of MB. We implemented the criterion to minimize all $\varepsilon_m^{(i)}$ simultaneously, as minimization of the sum $\varepsilon_{\text{tot}} = \sum_{i,m} \varepsilon_m^{(i)}$.

Table 7.1: Example of extrapolation table for MA at $\Delta = 0.7$.

L	$\omega = 2.379$				
4	0.47121815				
		0.79684943			
8	0.70340390		0.76025795		
		0.76193735		0.76041059	
12	0.73851463		0.76040544		0.76041067
		0.76068419		0.76041067	
16	0.74933809		0.76041009		
		0.76049000			
20	0.75389171				

7.1.1 MA with basecell $\frac{1}{2} - \frac{1}{2} - 1 - 1$

Like in our test application in Sect. 6.1.4, the error varies as a function of the exponent ω. We identify several distinct minima of ε, in the range $0.1 \leq \omega \leq 5$, some of which can be arbitrarily decreased by fine-tuning the search. Based on the absolute minimum of ε, it is thus impossible to choose *the* optimal ω. The interplay of different error estimates in ε_{tot}, leads to a similar but new structure of local minima. Quite in contrast to ε, however, the absolute minimum of ε_{tot} can always be uniquely identified, even though it is possible, that several local minima may exist in the close vicinity of the absolute minimum giving, in the worst case, significantly different final estimates of λ. This may happen if the absolute minimum is close to a pole of the function $\lambda(\omega)$. Interestingly enough, we find that the locations of all different minima that were studied in this work, vary continuously with the anisotropy parameter Δ.

Figure 7.1 gives a detailed graphical account of our analysis. Figure 7.1a shows a sample structure of minima, the errors, ε and ε_{tot}, are plotted as functions of the BST parameter ω, while Fig. 7.1b compares the dependence of the final estimate λ_{c} on ω for two different values of Δ. We shall focus in the following discussion on Fig. 7.1c, which shows the variation of the minima's locations and of various "final" estimates λ_{c}, on Δ. The first thing to note is the smooth shift of the minima in the largest portion of the interval of analysis. There is a general tendency of the minima to shift to smaller values with decreasing exchange anisotropy Δ, until at $\Delta \approx -0.6$, the shift reverts towards larger values again. Exceptions to this behaviour occur at the boundaries, $|\Delta| \approx 1$. Approaching the isotropic ferromagnetic point $\Delta = -1$, the tame structure of minima destabilizes and the analysis becomes increasingly difficult. We shall mostly ignore this region further on. At the other end, approaching $\Delta = 1$, the shift of the minima changes direction again, and, additionally, the three central minima come very close to each other. The two lowest branches of minima merge at $\Delta \approx -0.3$, and the first minimum appears to shift to zero at $\Delta \approx -0.55$. Considering the overall error ε_{tot}, it can be seen in Fig. 7.1a, that at $\Delta = 0$, two of its minima actually coincide with minima of ε, a feature that is retained throughout the Δ-interval of interest, in fact. The absolute minimum of ε_{tot}, which would give an objective criterion to choose a unique optimal ω, coincides with the fifth, respectively fourth, minimum of ε, but at $\Delta \approx 0.74$, the absolute minimum of ε_{tot} jumps to a smaller value of ω, that does not minimize ε. Thus, using the simultaneous minimization of all $\varepsilon_m^{(i)}$, as suggested in [25], we would have to choose $\omega > 2$ throughout, and accept that for $\Delta > 0.74$, our error estimate of the final value is not minimized.

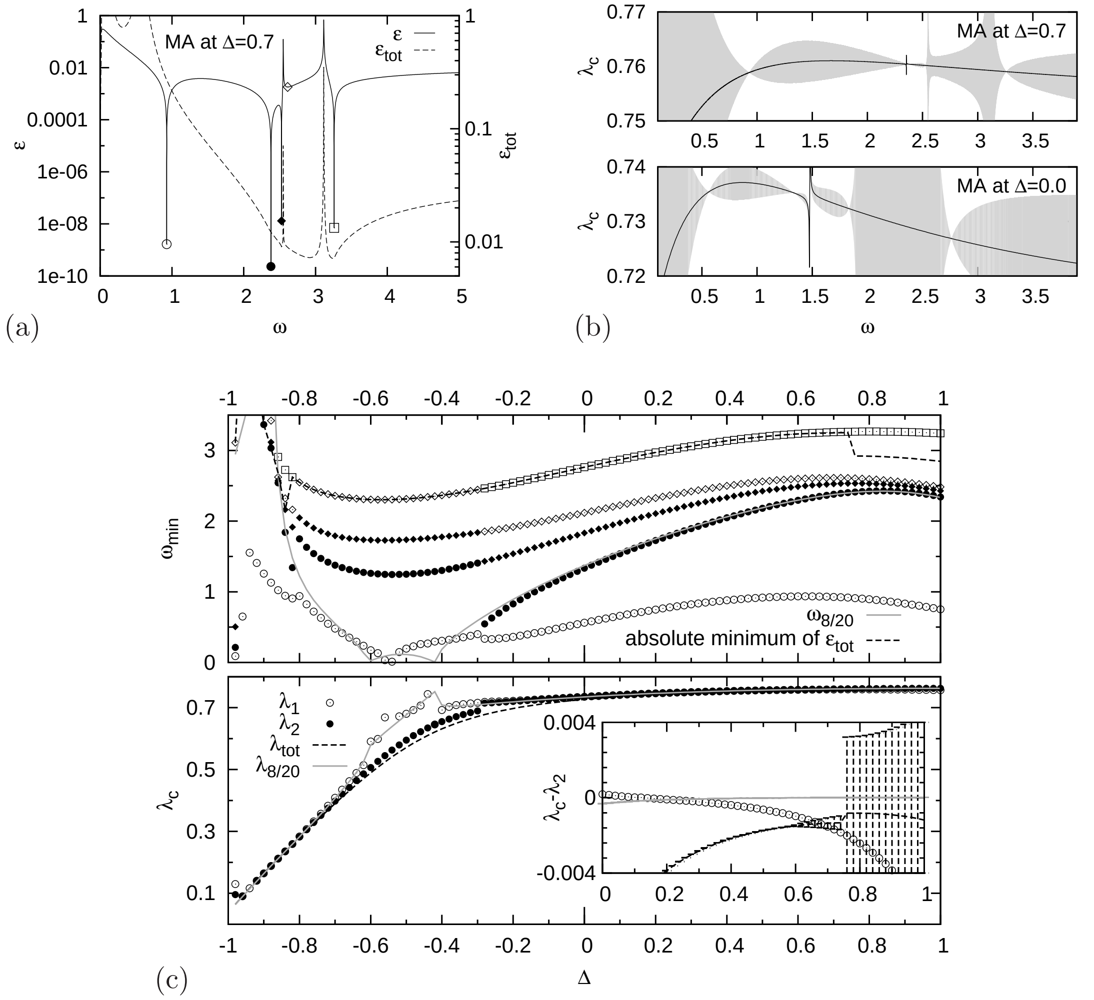

Figure 7.1: MA, extrapolation of exact data. (**a**) Contrary to ε_{tot} (right scale), the error estimate ε (left scale) does not permit to identify an absolute minimum in ω. The minima that look sharp on the logarithmic scale can be arbitrarily lowered by fine-tuning ω. (**b**) The final estimate λ_{c}, varies with the choice of ω. The variation tends to be smaller for larger values of Δ. The grey region indicates the error estimate ε. (**c**) Top: Locations of minima of ε vary continuously with Δ. The symbols identify each minimum as indicated in (**a**). The absolute minimum of ε_{tot} (dashed line) largely coincides with the highest minimum of ε. Skipping $L = 4$, leads to a single minimum that coincides with the second minimum of ε. The second minimum merges with the first minimum at $\Delta \approx 0.3$. Bottom: The final estimate at various significant values of ω: $\lambda_{1(2)} \ldots$ at the first (second) minimum, $\lambda_{8/20} \ldots$ at the single minimum of the shortened series $L \neq 4$, $\lambda_{\text{tot}} \ldots$ at the absolute minimum of ε_{tot}. The agreement is good for $\Delta \geq 0$, but not perfect (see inset, which shows the difference between λ_2 and other final estimates). At $\Delta \approx 0.74$, the absolute minimum of ε_{tot} jumps to a value (of ω) that does not minimize ε, which is shown by the dashed errorbars in the inset.

We have performed yet another test. Considering the fact, that MA of length $L = 4$ consists of a single basecell only, which is effectively very small indeed, we discarded the corresponding value from our series of exact finite-size estimates of the critical point. The analysis of the remaining series of four estimates for chains of length $L = 8, 12, 16$ and 20, yields a single minimum of ε. This is included in Fig. 7.1c as full grey line and denoted $\omega_{8/20}$. Roughly in the region $0 \leq \Delta \leq 1$, this single minimum very closely follows the second minimum of ε of the full series, that includes the smallest chain with $L = 4$. We take this as sign that the second minimum of the full series does indeed bear some significance. In the vicinity of the point where the two lowest minima of ε merge, $\omega_{8/20}$ deviates visibly and meets the abscissa twice at $\Delta \approx -0.42$ and -0.6.

Considering the final estimate λ_c at the different minima, we note that, at first sight, there is relatively good agreement in the region $0 \leq \Delta \leq 1$, but the inset in the bottom of Fig. 7.1c shows that the agreement is at most up to two digits. Only the difference between λ_2 and $\lambda_{8/20}$ (grey line in the bottom of Fig. 7.1c), the final estimate at the second minimum of the full series and the final estimate at the single minimum of the reduced series, respectively, is smaller than 10^{-3}. Taking into account that the choice of ω is almost the same in both cases, this is, in fact, no big surprise. But the fact that inclusion or omission of the smallest chain does not make too much of a difference in the region $0 \leq \Delta \leq 1$ is worthwhile to be noted. It does, however, make a difference for anisotropies smaller than $\Delta \approx 0$. Below this point, the range of final estimates begins to spread out. At $\Delta \approx -0.30$, where the second minimum of the full series "vanishes", the first minimum takes over, and the line of final estimates is smoothly continued down to $\Delta \approx -0.4$, where a discontinuous variation of final estimates λ_1 (open circles), but also of final estimates $\lambda_{8/20}$, sets in. The region of uncontrolled behaviour of final estimates λ_1 and $\lambda_{8/20}$, seems to coincide with the region between the two points where $\omega_{8/20} \approx 0$. Quite in contrast, the absolute minimum of $\varepsilon_{\mathrm{tot}}$ consistently produces a (dashed) continuous line of final estimates, which mark a lower boundary for λ_c in the present analysis. The higher minima of ε of the full series produce similar final estimates at slightly higher values. At $\Delta \approx -0.62$, the range of final estimates decreases and the different estimates seem to fall on a continuous line again.

Finite-size series and final extrapolated estimates of the critical bond alternation λ_c are listed in Table 7.2 for selected values of the exchange anisotropy Δ, the values that our QMC simulations targeted at. Each value included in Table 7.2, represents an arguably justified final estimate of the critical point. From a look at table Table 7.2, it can be seen that in the region $0 \leq \Delta \leq 1$ we could objectively conclude with an accuracy of two to three digits (not counting the leading zero). The test application presented in Sect. 6.1.4, however, showed that there may be even better agreement with a known exact results than can be deduced from the extrapolation. Here, we do not have exact results to compare with, but we have simulation data which will be presented in the next section. Comparison with our results obtained from QMC simulations (Sect. 7.2) does indeed single out the final estimates at the second minimum of the full series (or equally the final estimates at the single minimum of the reduced series) as the optimal estimate of the critical point.

Comparing the dependency of ω_2 on Δ with the exponent $1/\nu$, which is known exactly for the spin-$\frac{1}{2}$ XXZ chain and shown in Fig. 5.6 and estimated in this work

Table 7.2: Selected extrapolation results of MA. The final estimates λ_i correspond to the following choices of ω: $\lambda_1 \ldots$ first minimum, $\lambda_2 \ldots$ second minimum, $\lambda_{\text{tot}} \ldots$ absolute minimum of the overall error, $\lambda_{8/20} \ldots$ without data from $L = 4$.

L	$\Delta = 0$	$\Delta = 0.1$	$\Delta = 0.2$	$\Delta = 0.3$	$\Delta = 0.4$
4	0.46440838	0.47590904	0.48378987	0.48813585	0.48900829
8	0.65133708	0.66810161	0.68096028	0.69056115	0.69737082
12	0.68977526	0.70444722	0.71555596	0.72391699	0.73009323
16	0.70525010	0.71825100	0.72800886	0.73536293	0.74087233
20	0.71336510	0.72517855	0.73400921	0.74067735	0.74571463
λ_1	0.73542	0.74132	0.74628	0.75033	0.75356
λ_2	0.73524	0.74130	0.74637	0.75055	0.75395
λ_{tot}	0.72686	0.73575	0.74250	0.74772	0.75178
$\lambda_{8/20}$	0.73492	0.74112	0.74626	0.75048	0.75391

L	$\Delta = 0.5$	$\Delta = 0.6$	$\Delta = 0.7$	$\Delta = 0.8$	$\Delta = 0.9$	$\Delta = 1$
4	0.48645142	0.48050514	0.47121815	0.45866525	0.44296368	0.42428616
8	0.70169549	0.70369748	0.70340390	0.70070805	0.69536595	0.68699741
12	0.73445775	0.73723389	0.73851463	0.73826067	0.73627506	0.73215083
16	0.74490380	0.74768631	0.74933809	0.74986956	0.74915703	0.74687241
20	0.74946576	0.75214996	0.75389171	0.75472854	0.75458953	0.75322470
λ_1	0.75605	0.75783	0.75888	0.75912	0.75842	0.75662
λ_2	0.75668	0.75881	0.76041	0.7616	0.76228	0.76262
λ_{tot}	0.75493	0.75732(4)	0.7591(3)	0.761(4)	0.761(5)	0.761(6)
$\lambda_{8/20}$	0.75666	0.75880	0.76041	0.76156	0.76229	0.76264

for MA (and MB) in Sect. 8.2, one recognizes qualitatively similar behaviour. The exponent $1/\nu$ is supposed to be responsible for the finite-size shift of pseudocritical values, which are the locations of minima in the energy gap. It starts out at some value ($1/\nu = 2/3$, to be precise) at $\Delta = 1$ and decreases with decreasing Δ, until it becomes zero at another value (at $\Delta = -1/\sqrt{2} \approx 0.707$, in the spin-$\frac{1}{2}$ chain). The point where the exponent $1/\nu$ becomes zero, marks the onset of a critical region in the spin-$\frac{1}{2}$ chain. Our results plotted in Fig. 7.1c suggest that the equivalent point of MA is located roughly in the region $0.6 \leq \Delta \leq -0.3$, or more tentatively in the vicinity of $\Delta \approx -0.42$. The problem, here, is that we cannot interpret the fact that the first and second minima merge at $\Delta \approx -0.3$, or the fact that $\omega_{8/20}$ meets the abscissa twice. This puts the amount of insecurity into our guess of where the point, that is equivalent to $\Delta = -1/\sqrt{2}$ of the spin-$\frac{1}{2}$ chain, is located.

We have yet ignored the fact that in the spin-$\frac{1}{2}$ chain there are logarithmic corrections at the antiferromagnetic isotropic point $\Delta = 1$. If this also the case in MA (and MB), the BST extrapolation is prone to yield systematically wrong results. Close to the isotropic point, power-law corrections with small exponents may also lead to systematic deviations of final estimates from the true critical value. The change of shift of the minima of ε, but also the clear and growing discrepancy between λ_1 and λ_2, that set in when approaching the isotropic point from below, might be a sign of small power-law corrections in the shift of pseudocritical values, that ultimately become logarithmic at $\Delta = 1$. Without detailed investigation of the mechanisms underlying the BST algorithm this, however, remains speculative.

7.1.2 MB with basecell $\frac{1}{2} - \frac{1}{2} - \frac{3}{2} - \frac{3}{2}$

For MB, we have only four exact finite-size estimates of the critical point. The shortness of the series leads, compared to MA, to less accurate estimates of the critical point, but also to an analysis that is less involved. Both, the error ε of the final estimate and the overall error ε_{tot} exhibit, as functions of the BST parameter ω, unique minima, the localization of which does not present a challenge. Again, we find a smooth shift of the minima's locations with varying exchange anisotropy Δ, depicted in the top of Fig. 7.2, this time without any irregularities.

The minimum of ε shifts, similarly to the second minimum of ε in MA, to smaller values with deceasing Δ in the region $-0.44 \leq \Delta \leq 0.74$. The inversion of the shift when approaching the AF isotropic point is more pronounced than for MA. Furthermore, the location of the minimum of ε does never become zero, as before in MA, but shows a minimum at $\Delta \approx -0.44$, which remains our only indication of the possible onset of a critical region. The minimum of ε_{tot} is located at higher values of ω, values that, obviously, do not minimize ε.

The final estimates of the critical point λ_c, at both, the minimum of ε and the minimum ε_{tot}, denoted λ_1 and λ_{tot}, respectively, are equally well justifiable. They are displayed in the bottom of Fig. 7.2 and listed in Table 7.3 for selected values of the exchange anisotropy Δ, along with the corresponding series for finite-size pseudocritical points. The difference between the two final estimates of the extrapolation procedure, which we might take as indicator for the uncertainty of a proper final estimate, is smallest in a region roughly centered at $\Delta \approx 0.6$ (see the inset in the bottom of Fig. 7.2), and largest around $\Delta \approx -0.4$. Again, we anticipate our QMC results, that now single out the minimum of ε as the optimal criterion to set the BST parameter ω.

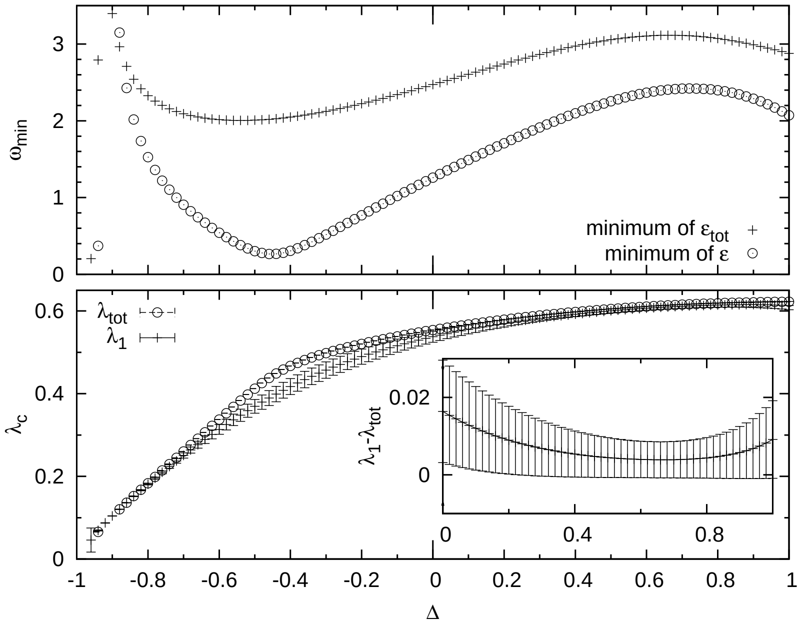

Figure 7.2: MB, extrapolation of exact data. Top: Locations of minima of ε and $\varepsilon_{\mathrm{tot}}$ for MB. Bottom: The final estimate of the critical point λ_{c}: $\lambda_1 \ldots$ at the minimum of ε, $\lambda_{\mathrm{tot}} \ldots$ at the minimum of $\varepsilon_{\mathrm{tot}}$.

Table 7.3: Selected extrapolation results of MB. The final estimates λ_i correspond to the following choices of ω: $\lambda_1 \ldots$ first minimum of ε, $\lambda_{\mathrm{tot}} \ldots$ absolute minimum of $\varepsilon_{\mathrm{tot}}$.

L	$\Delta = 0$	$\Delta = 0.1$	$\Delta = 0.2$	$\Delta = 0.3$	$\Delta = 0.4$
4	0.36598988	0.38314169	0.39774473	0.40941572	0.41770277
8	0.49569362	0.51716062	0.53529063	0.55028648	0.56228339
12	0.52141978	0.54144000	0.55808649	0.57180198	0.58291353
16	0.53201258	0.55085527	0.56640536	0.57920230	0.58963254
λ_1	0.55399	0.56735	0.57895	0.58899	0.59758
λ_{tot}	0.54(2)	0.56(2)	0.57(1)	0.582(8)	0.592(6)

L	$\Delta = 0.5$	$\Delta = 0.6$	$\Delta = 0.7$	$\Delta = 0.8$	$\Delta = 0.9$	$\Delta = 1$
4	0.42209548	0.42203833	0.41695660	0.40630291	0.38962793	0.36665709
8	0.57132580	0.57733706	0.58007326	0.57904619	0.57340358	0.56178398
12	0.59163507	0.59806584	0.60217114	0.60372245	0.60214731	0.59618827
16	0.59795399	0.60431532	0.60875715	0.61117963	0.61122311	0.60791049
λ_1	0.60479	0.61067	0.61528	0.61868	0.62097	0.62229
λ_{tot}	0.600(6)	0.607(5)	0.611(5)	0.614(6)	0.615(7)	0.61(1)

7.2 Finite-Size Scaling of Quantum Monte Carlo Data

In this section, the final QMC estimates of λ_{c} as function of the exchange anisotropy Δ of both mixed spin models shall be presented. Additionally, some effective shift exponents will be discussed.

Simulations have been run at eleven equidistant values of the exchange anisotropy in the range $0 \leq \Delta \leq 1$. For each Δ fixed, a small set of simulation points λ was spread equally-spaced according to the generic rule

$$|\lambda - \lambda_{\mathrm{c}}| L^{1/\nu} \leq r_0 \,,$$

with pre-determined estimates of λ_{c} and $1/\nu$, and the value r_0 fixed. For MA five points were chosen with $r_0 = 0.5$ and for MB seven points with $r_0 = 1$. This generic rule was abandoned were it seemed necessary. For large systems at small Δ, a finer spacing was chosen, and for small systems at large Δ, a few extra points were added in order to include the zeroes of the twist parameter, in the simulated range of the control parameter λ. In every simulation $2 \cdot 10^5$ measurements of various observables were recorded after discarding the first 10^4 updates for equilibration. An exception is MA at the isotropic point $\Delta = 1$, where $5 \cdot 10^5$ measurements ware taken in order to have a slightly improved dataset in anticipation of logarithmic corrections. To ensure that primarily groundstate properties were measured, the aspect ratio β/L, was set to an integer value such that the temporal extent β, of the system is at least six times larger than the imaginary time correlation length ξ. With a decreasing energy gap, the correlation length becomes large at small values of Δ. The largest chosen aspect ratio was 6 for MB at $\Delta = 0$.

Pseudocritical points $\lambda^*(L)$, were determined by multi-histogram reweighting.[1] For MA series of 29 different chain lengths (containing several geometric series) in the range $8 \leq L \leq 384$ have been simulated, and for MB series of 25 different chain lengths in the range $8 \leq L \leq 256$. Error estimates of each data point have been calculated via reweighting of jacknifed datasets. The binwidth was consistently set to 1000, in the final analysis. To extract the final estimates of critical points $\lambda_{\mathrm{c}}(\Delta)$, non-linear three-parameter fits to the standard FSS form of the shift of pseudocritical points,

$$\lambda^*(L) = \lambda_{\mathrm{c}} + \mathcal{A} L^{-\theta} \,, \tag{7.1}$$

with the effective shift exponent θ, and the leading amplitude of the shift $\mathcal{A}$, have been applied. The final estimate of the critical point λ_{c}, represents a “background” term in the power-law fit, it is pinned by estimates of $\lambda^*(L)$ at large system sizes. This is not the case for the shift exponent and the amplitude. The influence of the minimum and maximum chain length, $L_{\min}$ and $L_{\max}$, respectively, that enter in the fits, has been studied carefully. A consistent final estimate was chosen restrictively and individually for each observable in order to produce the smallest possible final error estimate. The influence of $L_{\min}$ and $L_{\max}$, is exemplary illustrated in Figs. 7.3 (MA) and 7.4 (MB) for the zeroes and crossing points of the twist parameter at selected values of Δ.

---

[1] Specific localization tasks have been accomplished using Numerical Recipe routines [218].

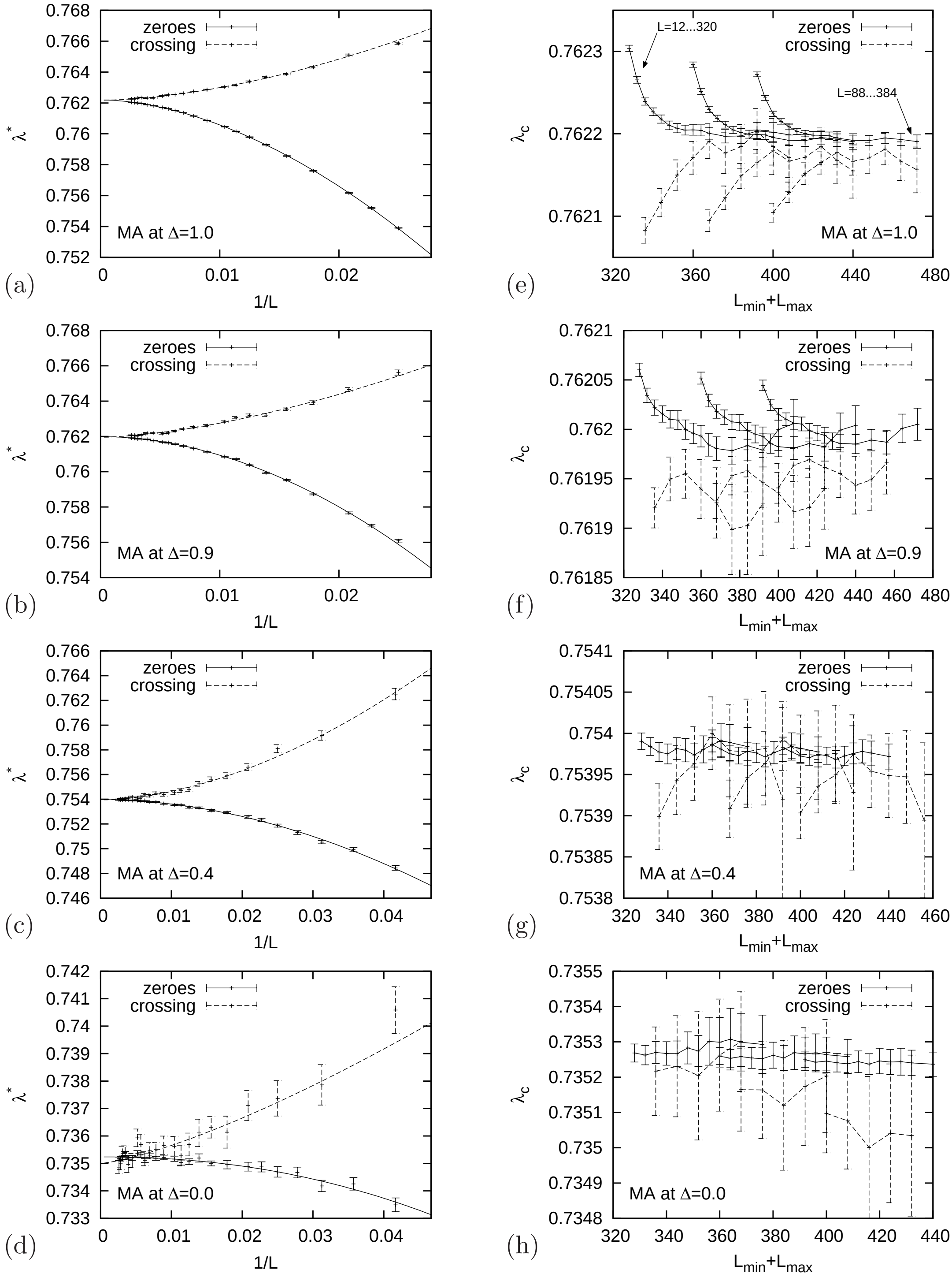

Figure 7.3: (**a**–**d**) Pseudocritical points λ^* (zeroes and crossing of data curves of two different chain lengths $L/2$ and L), obtained from the twist parameter of MA. (**e**–**h**) Influence of L_{min} and L_{max} on the estimate of λ_{c} in the fit to (7.1). Series of datapoints connected by lines all have the same L_{max}.

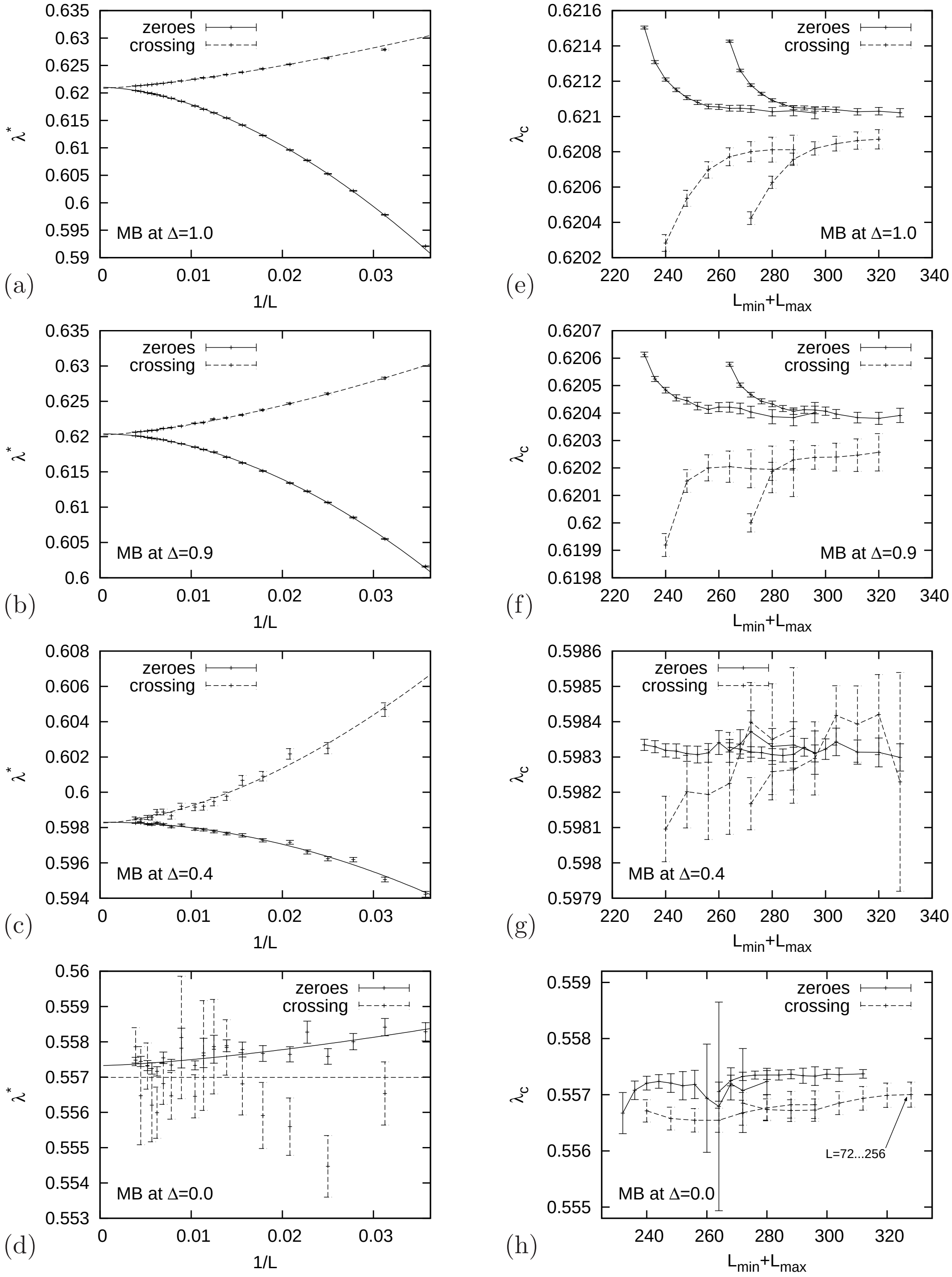

Figure 7.4: Same as Fig. 7.3, but for MB.

Table 7.4: Estimates of the critical values $\lambda_c(\Delta)$ of MA, obtained from series of pseudocritical points. Fits to (7.1): $z_0 \ldots$ zeroes of the twist parameter; $z_{\mathrm{cr}} \ldots$ crossing points of the twist parameter of two different chain lengths, $L/2$ and L; $\xi \ldots$ maxima of the second-moment estimator of the imaginary time correlation length; $\chi \ldots$ maxima of the susceptibility. Results of the fit of the twist parameter's zeroes to a 3^{rd}-order polynomial in L^{-2}, are denoted by $z_{0,\mathrm{poly}}$.

Δ	z_0	z_{cr}	$z_{0,\mathrm{poly}}$	ξ	χ
0.0	0.73524(3)	0.73500(21)	0.73525(3)	0.73554(51)	0.73510(17)
0.1	0.74138(2)	0.74122(10)	0.74137(2)	0.74137(21)	0.74158(9)
0.2	0.74645(2)	0.74640(6)	0.74645(2)	0.74652(10)	0.74656(4)
0.3	0.75061(2)	0.75062(4)	0.75060(1)	0.75074(6)	0.75072(3)
0.4	0.75397(1)	0.75395(6)	0.75397(1)	0.75401(3)	0.75403(2)
0.5	0.75668(1)	0.75670(4)	0.75667(1)	0.75666(2)	0.75670(1)
0.6	0.75878(1)	0.75878(4)	0.75877(1)	0.75879(2)	0.75879(1)
0.7	0.76033(1)	0.76034(3)	0.76032(1)	0.76032(2)	0.76033(1)
0.8	0.76140(1)	0.76142(3)	0.76138(1)	0.76138(1)	0.76139(1)
0.9	0.76200(1)	0.76195(4)	0.76198(1)	0.76199(1)	0.76199(1)
1.0	0.76220(1)	0.76218(2)	0.76217(1)	0.76218(1)	0.76218(1)

Generally, for all Δ and both models, the zeroes of the twist parameter (5.5), which serves as convenient indicator of transitions between different valence bond configurations [141], yielded the most accurate results. Two fits have been applied in that case, the standard FSS fit to (7.1), and a 3^{rd}-order polynomial fit in L^{-2} of the zeroes, as used in [141]. Finally, we compared against the crossing points of the twist parameter, and the maxima of the second-moment estimator (6.69) of the imaginary time correlation length ξ, and the transversal staggered magnetic susceptibility χ, the improved estimator of which is defined in (6.65).

The individual estimates of λ_c are listed in Tables 7.4 (MA) and 7.5 (MB). It has been discussed in Sect. 6.3 and it is clearly visible Figs. 7.3 and 7.4, that the quality of datasets becomes increasingly poor at small values of Δ. This is particularly severe for the crossing point of the twist parameter and those pseudocritical points that are defined via maxima of observables. In two extreme cases of MB no results could be obtained while in some others only the simple fit to a constant could be stably applied. The latter are marked specifically in Table 7.5. All values are quoted with five digit accuracy and errors rounded up. Numeric details of the individual fits can be found in the appendix (Tables B.1–B.10). Being restrictive in choosing the smallest possible consistent error of the final estimate, we consider this final rounding justified when taking into account several possible sources of systematic under-estimation of the error at different levels of the analysis. Using the squareroot of diagonal elements of the covariance matrix as error estimates, neglects the correlation between fit parameters [218]. Using a single leading power-law term in (7.1) completely neglects corrections to FSS. Even though we try to capture this fact by successively omitting small chain lengths, this may lead to slightly wrong estimates of λ_c and underestimated errors, in particular at the isotropic point where we expect logarithmic corrections.

Table 7.5: Same as Table 7.4, but for MB. Results from fitting to a constant are marked by *.

Δ	z_0	z_{cr}	$z_{0,\mathrm{poly}}$	ξ	χ
0.0	0.55745(6)	0.55726(20)*	0.55747(4)		
0.1	0.56976(4)	0.56971(15)*	0.56976(4)	0.57240(108)	0.57142(31)*
0.2	0.58063(3)	0.58074(13)	0.58063(3)	0.58015(37)	0.58152(23)*
0.3	0.59014(3)	0.58982(26)	0.59014(3)	0.59001(24)	0.58952(83)
0.4	0.59831(3)	0.59826(10)	0.59830(2)	0.59857(21)	0.59823(18)
0.5	0.60523(2)	0.60513(7)	0.60522(2)	0.60519(5)	0.60512(11)
0.6	0.61091(2)	0.61084(6)	0.61089(2)	0.61089(4)	0.61091(4)
0.7	0.61531(2)	0.61520(5)	0.61529(1)	0.61533(2)	0.61529(3)
0.8	0.61847(2)	0.61841(6)	0.61845(1)	0.61847(2)	0.61841(3)
0.9	0.62041(2)	0.62023(4)	0.62036(1)	0.62041(2)	0.62038(2)
1.0	0.62104(2)	0.62085(5)	0.62093(2)	0.62100(2)	0.62098(1)

The values quoted in Tables 7.4 and 7.5 were subsequently combined in an error-weighted average to give final estimates of λ_{c} as a function of Δ. The final estimates are shown in Table 7.6, in comparison to the extrapolated results of the previous section.

A graphical comparison of QMC results with the various different extrapolated estimates of the previous section is given in Fig. 7.5. It becomes immediately obvious that for MA the values labelled λ_2 and $\lambda_{\mathrm{f},8/20}$ match best with the QMC results. These are the values obtained from extrapolation of five exact points with the free parameter ω set to the *second* minimum and four exact points (omitting $L = 4$) which has only a single minimum in ω, respectively. This confirms our judgement from the previous section that λ_2 gives the most significant result for MA. Comparison of the corresponding values in Table 7.6 shows that the agreement holds for up to four in some cases even five digits. While this may seem to be an overwhelming success of the extrapolation method, we note, however, that an objective choice of the optimal ω, as well as an objective error estimate in the fourth or fifth digit solely based on exact data would have been difficult, if not impossible. That the extrapolation of only five points leads to such accuracy can be explained by the fact that the increment of L is the size of the basecell, i.e. 4. The fifth exact value is obtained from $L = 20$, which is already a rather large system to diagonalize exactly. The situation is slightly different for MB, because $L = 16$ is the largest chain that has been diagonlized and only four exact values have been extrapolated. Comparison shows agreement in roughly two to three digits between QMC and ED results, which would have been indeed possible to be deduced on the basis of the numbers shown in Table 7.3. As pictured in Fig. 7.5b, the value λ_1 agrees much better than λ_{tot}. Again the criterion to minimize only the final error instead of the overall error leads to better estimates.

For both, MA and MB, the agreement between ED and QMC data is best in an intermediate region of the Δ-interval of interest. The growing discrepancies at the boundaries of the Δ-interval of interest, may indicate a growing influence of corrections to scaling that would interfere in both, extrapolation and FSS, alike.

Table 7.6: Final estimates of the phase boundaries $\lambda_c(\Delta)$. Quantum Monte Carlo (QMC) results are error-weighted averages of the individual estimates listed in Tables 7.4 and 7.5. Representatives of exact diagonalization (ED) results are the values denoted λ_2 (MA) and λ_1 (MB) in the previous section, which turned out to be the best estimates when compared to the QMC results (see Fig. 7.5).

	MA			MB		
Δ	ED	QMC	$\frac{\beta}{L}$	ED	QMC	$\frac{\beta}{L}$
0.0	0.73524	0.73524(2)	5	0.5540	0.55746(3)	6
0.1	0.74130	0.74137(2)	5	0.5673	0.56977(7)	5
0.2	0.74637	0.74645(2)	4	0.5790	0.58064(5)	5
0.3	0.75055	0.75062(2)	4	0.5890	0.59014(2)	4
0.4	0.75395	0.75398(2)	3	0.5976	0.59831(1)	4
0.5	0.75668	0.75668(1)	3	0.6048	0.60522(1)	4
0.6	0.75881	0.75878(1)	3	0.6107	0.61090(1)	3
0.7	0.76041	0.76032(1)	3	0.6153	0.61530(1)	3
0.8	0.76155	0.76139(1)	3	0.6187	0.61846(1)	3
0.9	0.76228	0.76199(1)	3	0.6210	0.62038(2)	3
1.0	0.76262	0.76218(1)	3	0.6223	0.62098(2)	3

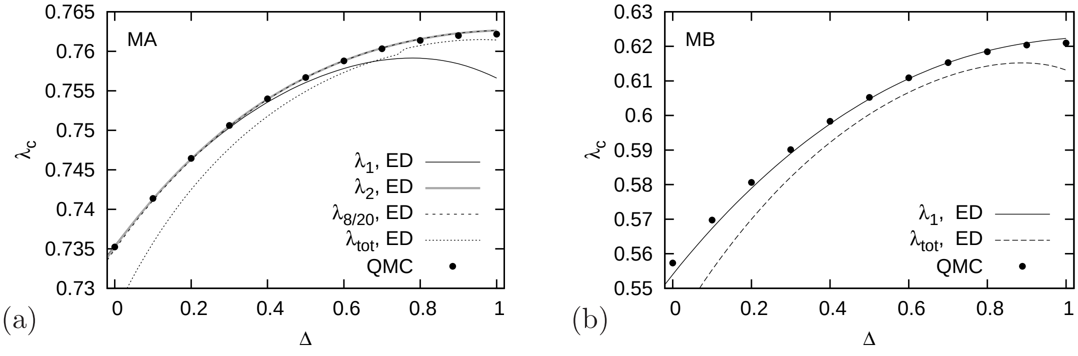

Figure 7.5: Comparison of final estimates of the critical points $\lambda_c(\Delta)$. QMC results clearly single out λ_2 and $\lambda_{8/20}$ as best ED estimates for MA (**a**), and λ_1 for MB (**b**).

Pre-determined estimates of λ_c To obtain first estimates of λ_c and $1/\nu$ we followed two very different strategies for the two models considered. For MA we performed a relatively widespread search for the critical point at a moderate aspect ratio $\beta/L = 2$. The error-weighted mean of λ_c from several quantities yielded an accurate first estimate serving as center in the final simulation run. The final estimate at modified aspect ratio confirmed, in fact, the first estimate in most cases. The first estimate of $1/\nu$ was calculated as the covariance-weighted mean of individual estimates from several moments and Binder cumulants of the transversal and longitudinal string observables. For MB we used the values obtained from extrapolation of exact data to simulate single points for various chain lengths at an aspect ratio $\beta/L = 3$. Using single-histogram reweighting we calculated the crossing points of the Binder cumulant of the transversal string observable which serves as order parameter. This turned out be suboptimal and we do not put much significance into these values, in particular the error estimates. They simply served as center to place the points of the final run. The exponent $1/\nu$ of MB was calculated directly at the ED values for several quantities (moments and Binder cumulants of the string observables) and combined in a covariance-weighted mean. Preliminary estimates of λ_c, for both models, are listed and compared to final estimates in Table B.11.

Effective shift exponents. Pseudocritical points are supposed to shift to leading order with $L^{-\theta}$ and the shift exponent is expected to be $\theta = 1/\nu$. The ratio $1/\nu$ will be determined independently in the Sect. 7.2. $1/\nu$ decreases from the value 1.5 at $\Delta = 1$ to roughly 0.6 and 0.5 at $\Delta = 0$ for MA and MB, respectively. In Fig. 7.6 we show the effective shift exponents as obtained from the power-law fits that yielded our final estimates of λ_c. At the isotropic point, the estimates obtained from the twist parameter and the correlation length agree with the ones obtained by the author in previous work [50, 51]. Apart from a few values of the maxima of χ in MB, however, the effective shift exponents are nowhere near the expected and confirmed behaviour of $1/\nu$, they even do not coincide at all (with a noted exception of zeroes and crossings of the twist parameter z for $\Delta \geq 0.3$ in MA). Primarily, this means that the various pseudocritical points shift with different effective exponents. As pointed in [244], non-analytic corrections to FSS can be responsible for effective shift exponents $\theta \neq 1/\nu$.

In Fig. 7.6 we also added the values of ω, the free parameter in the extrapolation algorithm, at the second minimum. It follows the effective shift exponent of the second-moment correlation length's maxima, in particular in MA, but also in MB, less convincingly however. The imaginary time correlation is an estimate of the inverse energy gap, the minima of which were used in the extrapolation of the previous section. This suggests that the optimal ω does indeed bear the physical significance of an effective shift exponent.

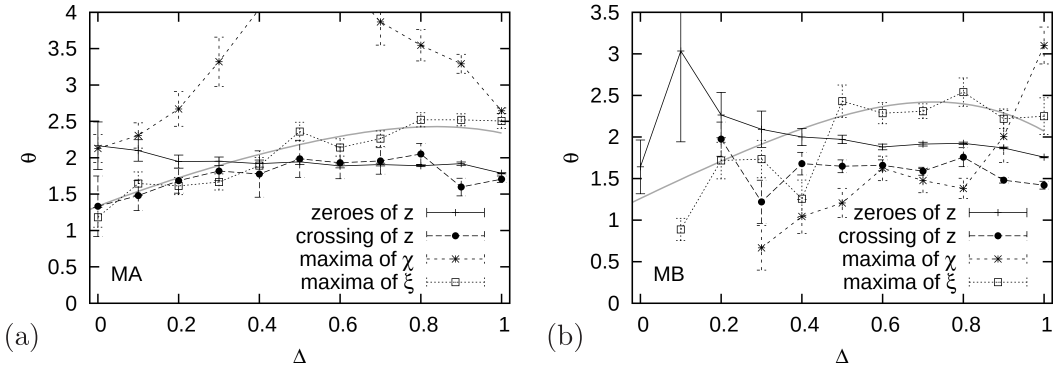

Figure 7.6: Effective shift exponents θ, as obtained from fitting pseudocritical points of the twist parameter z, the second-moment correlation length ξ, and the susceptibility χ, to (7.1). The curves without datapoints show the values of the BST parameter ω at the second minimum (see Sect. 7.1).

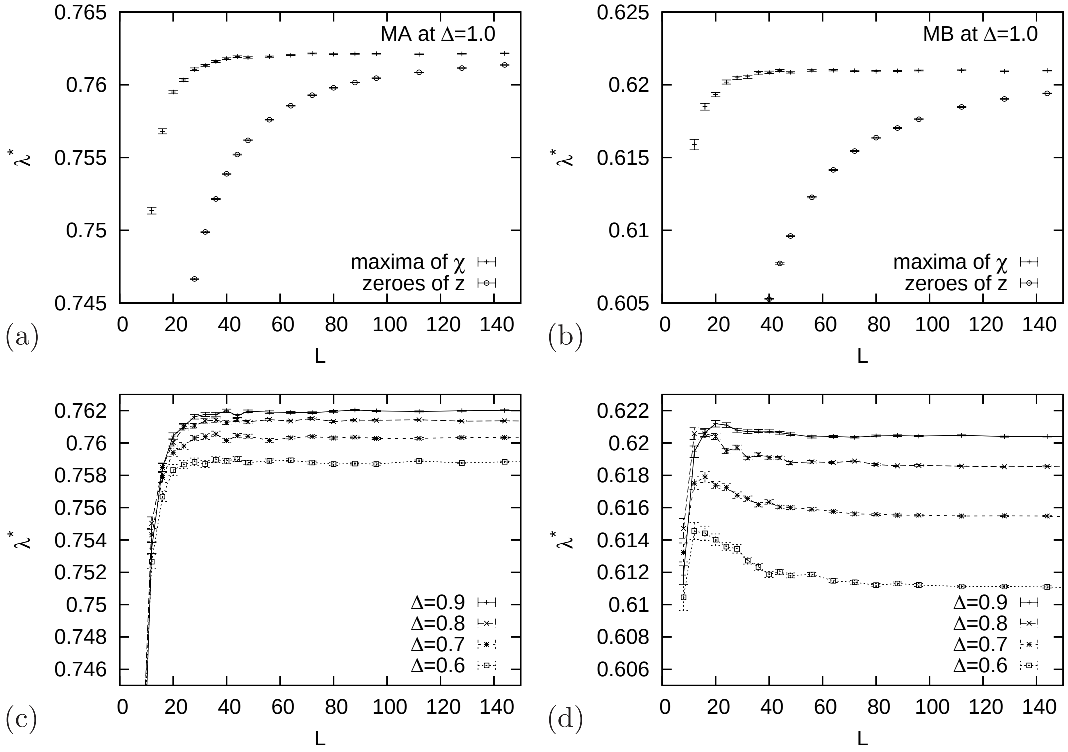

Figure 7.7: Shift of pseudocritical points λ^*, with the chain length L. (**a**,**b**) Comparison of the shift of the zeroes of the twist parameter z, to the shift of the maxima of the susceptibility χ. (**c**) Fast but monotonous shift of the susceptibility's maxima in MA. (**d**) Non-monotonous shift of the susceptibility's maxima in MB.

The maxima of the susceptibility show a particularly interesting shift behaviour, which is why we shall discuss them separately and in a bit more detail. If we compare, at $\Delta = 1$, the location of the maxima of the susceptibility with the location of the zeroes of the twist parameter, we see immediately that in both models the maxima converge much faster towards the final value. The sign of the shift amplitude is the same (negative) for both observables. In MA this fast convergence is present also for the other values of $\Delta < 1$, which results in remarkably large effective shift exponents $\theta_{\text{eff}} > 2$ ($\theta_{\text{eff}} \approx 5$ at $\Delta = 0.5$!). Quite in contrast, we observe in MB a manifestly non-monotonous shift for $\Delta < 1$. This indicates that in this case the amplitude of the leading term in the shift is positive rather than negative.

It is not possible to model non-monotonous shift behaviour with a single power-law, but it can be explained by an additive term with opposite sign. If a similar additive term with opposite sign is present also in MA, it is possible that it is strong enough to change the effective sign of the shift altogether. For large L it may then compensate the leading shift within the statistical accuracy, which is a possible explanation for the fast convergence in MA that we observe and the large effective shift exponents.

Modelling the non-monotonous shift by

$$\lambda^*(L) = \lambda_{\text{c}} + S_0 L^{-\theta} + S_1 L^{-\omega}\,, \tag{7.2}$$

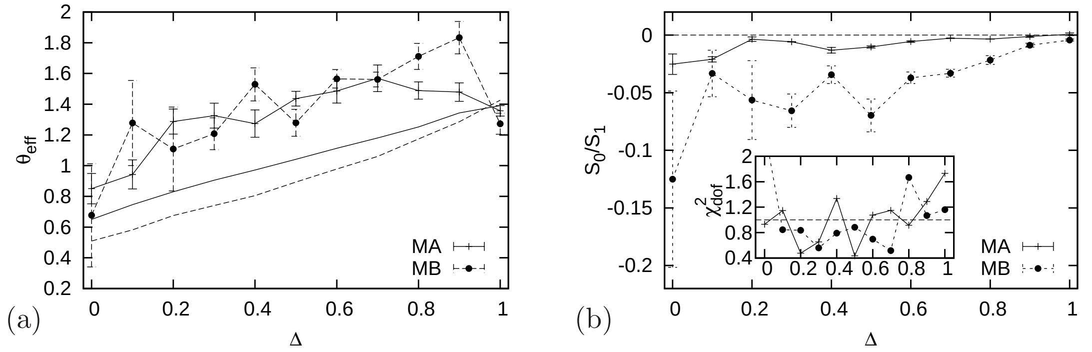

Figure 7.8: Result of fitting the location of the susceptibility's maxima to (7.3), with $1/\nu = \theta$ a free parameter. (**a**) The effective shift exponent θ takes approximately the same values in both models. It is generally larger than our estimates of the ratio $1/\nu$ (see next section), which are indicated by lines without datapoints. (**b**) The ratio of amplitudes S_0/S_1 takes negative values in both models.

we face the problem of a non-linear five-parameter fit. It is, in fact, extremely difficult to extract reasonable results from that kind of fit, and impossible on the basis of our data. If we fix $\theta = 2$, the value obtained from a fit using chain lengths $L = 20 \dots 256$, in MB at $\Delta = 0.9$ we get $\omega \approx 4 = 2\theta$. Even though this relation is not precisely reproduced throughout the smaller values of Δ, we took it as a starting point. In the presentation of FSS in Sect. 6.4, we stated that analytic corrections induce precisely this kind of subleading terms in $L^{-1/\nu}$, i.e.,

$$\lambda^*(L) = \lambda_c + S_0 L^{-1/\nu}\left(1 + \tilde{S}_1 L^{-1/\nu}\right) = \lambda_c + S_0 L^{-1/\nu} + S_1 L^{-2/\nu}\,. \qquad (7.3)$$

We let θ be a free parameter, used $\omega = 2\theta$, and fitted the location of the maxima of the susceptibility of both models, and thereby used all chain lengths $L \geq 8$. The result is shown in Fig. 7.8. We find remarkably similar values of θ for both models (Fig. 7.8a). Only for $\Delta \geq 0.8$ the results differ significantly. The ratio of the amplitudes S_0/S_1 is negative (Fig. 7.8b), and indeed smaller for MA. The large value of S_1 in MA is sufficient to effectively change the sign of the visible shift. We thus conjecture that in both models the same mechanism is responsible for the peculiar shift behaviour of the susceptibilities' maxima.

However, it is important to note, that the above discussion is based on effective values, and is only of qualitative significance. All chain lengths are included in the fits and $L = 8$ certainly is not large enough to be in the asymptotically dominant region. Various other correction effects are unnoticed and included in all our analysis. We also tried to fix θ to our estimates of $1/\nu$ presented in the next chapter. Then, ω can be either a free parameter or also fixed to $2/\nu$. We do not get reasonable values of χ^2_{dof} in the case of both exponents fixed, $\omega = 2\theta = 2/\nu$. However, the picture of competing amplitudes of opposite sign still holds in that case, as well as in the case of $\theta = 1/\nu$ fixed and ω free.

7.3 Summary

By combined effort of ED with extrapolation (Sect. 7.1) and QMC with FSS (Sect. 7.2), quantitative understanding of the phase boundaries of MA and MB has been gained in this section. The boundaries separate a dimerized from a quadrumerized phase, both of which can be understood in terms of different underlying valence bond configurations (see Sect. 5.2). They correspond to the boundary that separates two physically equivalent dimerized phases in the spin-$\frac{1}{2}$ chain (see Sect. 5.3), also known as self-dual Gaussian criticality line.

The focus of QMC has been laid on the positive XY-like region of the exchange anisotropy, $0 \leq \Delta \leq 1$. Exact data shows that a line of continuously varying critical points extends beyond $\Delta = 0$. The analysis of exact data further implied the existence of a significant region roughly located at $\Delta \approx 0.4$ in both models. Using the picture given by the phase diagram of the spin-$\frac{1}{2}$ chain (see Sect. 5.3), this region can be interpreted as the end of the critical line and the beginning of a critical region. In the critical region, bond alternation as controlled by the parameter λ, is not a relevant operator anymore [24]. Beyond the end of the critical line it is still possible to extrapolate exact finite size estimates of the minima of the energy gap, up to some limitations in choosing the optimal result. The values possibly represent a continuation of the Gaussian critical line into the critical region.

In Fig. 7.9 we embed our final results in a map of the “gradient” (the derivative with respect to λ, to be precise) of the energy gap of small systems ($L = 12$ for MA and $L = 8$ for MB). These finite-size “phase diagrams” visibly mimic the critical line and the onset of the critical region. The dark areas close to the ferromagnetic side ($\Delta = -1$) indicate small slopes of the energy gap in λ. The plots in Fig. 7.9 are to be compared to the corresponding sections of the phase diagrams of the spin-$\frac{1}{2}$ and spin-1 chains displayed in Sect. 5.3. The critical lines of the mixed spin chains shift to smaller values with decreasing Δ, a property shared, in fact, with spin-1 chain. The change in the critical value λ_c, is more pronounced in MB. While the spin-1 chain exhibits two transitions in λ, the subspin-topology of the mixed spin chains prohibits a second transition, which relates the mixed spin chains to the spin-$\frac{1}{2}$ chain. Our rough estimate of the end of the critical line $\Delta \approx 0.4$ is clearly smaller than the exactly known corresponding value of the spin-$\frac{1}{2}$ chain, $\Delta = -1/\sqrt{2} \approx -0.7$, but also significantly larger than the value of the spin-1 chain, $\Delta = 0$. The numerical values of the final result in this section, as shown in Fig. 7.9 and given in Table 7.6, serve as basis for the determination of certain critical exponent ratios ($1/\nu$, α/ν and $\beta_{z,x}/\nu$) discussed in Sect. 8, and the investigation of the operator content based on finite-size spectra in Sect. 10. At the isotropic point, the final estimates of λ_c agree with previously obtained estimates for both MA [48–51] and MB [50].

The comparison of ED and QMC results (see Fig. 7.5) provided a means to decide upon which of the ED candidate estimates of the critical line is indeed optimal. It has been found that the thus chosen values show, considering the shortness of finite-size series, remarkable agreement with the QMC results for MA and reasonable agreement for MB. Another comparison of ED and QMC data (included in Fig. 7.6) suggests the identification of the optimal choice of the BST parameter ω with the effective FSS shift exponent θ, of the inverse energy gap.

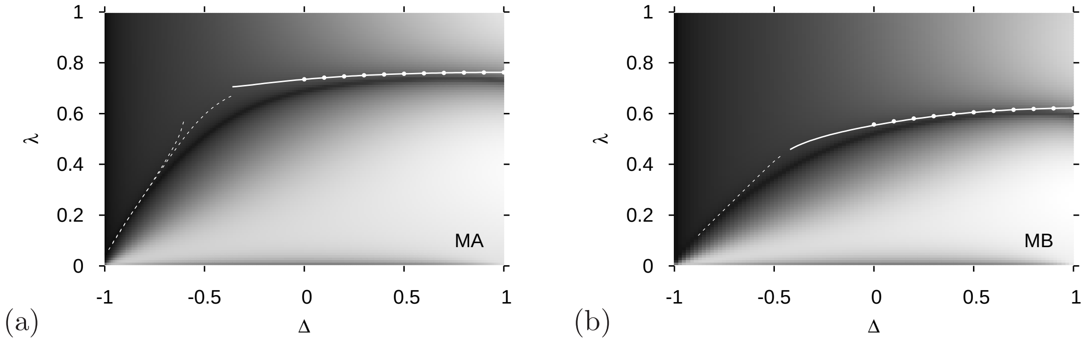

Figure 7.9: The phase boundaries $\lambda_c(\Delta)$, of the mixed spin models, MA and MB, in the space of bond-alternation λ, and XXZ exchange anisotropy Δ. White dots show the results of QMC (Sect. 7.2), while the lines those of ED (Sect. 7.1). Ends of the full lines mark our approximate estimates of the onset of a critical region. Dashed lines show results of extrapolation without the explicit significance of a phase boundary. The shaded background represents the derivative with respect to λ of the energy gap of small systems ($L = 12$ for MA and $L = 8$ for MB), with dark areas representing small (down to zero) slopes.

Considering the shift exponent θ, we state that pseudocritical points of different observables yielded different shift exponents. Furthermore, none of the obtained values matches with our estimates of $1/\nu$, which will be presented in Sect. 8.2. The presence and influence of one or more irrelevant scaling fields may generate effective shift exponents $\theta \neq 1/\nu$ [244], which then need not be the same for different definitions of pseudocritical points. As a particularly interesting showcase, the shift of the susceptibility's maxima has been presented and discussed in more detail (see Fig. 7.7). In leaving this section, we remark that we have not taken the possible presence of logarithmic corrections into account here. These certainly turn results concerning the shift exponent into effective ones. Our study of the dependence of λ_c at the isotropic point, $\Delta = 1$, on $L_{\min}$ and $L_{\max}$, the minimum and maximum chain length used in FSS power-law fits, respectively, showed that we obtained relatively stable estimates of λ_c (see Fig. 7.3e and Fig. 7.4e). But the slow nature of logarithmic corrections may turn our estimates of λ_c at the isotropic point into effective estimate that are, in fact, wrong. With the level of accuracy reached, this systematic error may not be hidden anymore by the statistical error. This issue shall be addressed again in Sect. 11.2.

8 Critical Exponents

In this section, ratios of thermodynamic critical exponents, as obtained from the FSS analysis of QMC data, shall be presented and discussed. The FSS method of analysis has been presented in detail in Sect. 6.4. The emphasis is put on final results of conventional FSS that considers the leading term only. The influence of corrections to FSS, however, will be discussed were it seems necessary and shall be readdressed again in Sect. 11.

The leading behaviour of finite-size estimates of physical observables $\mathcal{O}_L$, at the critical or pseudocritical points follows

$$\mathcal{O}_L = B + AL^{\rho/\nu} + \cdots \,, \tag{8.1}$$

with a background B, the leading amplitude A, and ρ the critical exponent of observable $\mathcal{O}$. Apart from the direct non-linear three-parameter fit to the above power-law, a standard method to extract the ratio ρ/ν, is the *double-log linear fit*, where

$$\ln \mathcal{O}_L = \ln A + \frac{\rho}{\nu} \ln L + \ln \left(1 + \frac{B}{A} L^{-\rho/\nu} \right) + \cdots \,, \tag{8.2}$$

is fitted to a straight line in $(\ln L)$, which yields ρ/ν as the slope. The presence of a background B spoils this linear fit and produces "corrections" to FSS that vanish asymptotically as $L^{-\rho/\nu}$ (if ρ is positive). In this case, the strength of the corrections depends crucially on the ratio B/A, and the suppressing factor $L^{-\rho/\nu}$. In addition to a possible background, also the presence of power-law (and of course logarithmic) corrections to FSS spoil the double-log linear fit. However, all corrections become unimportant if only sufficiently large systems are considered. In many favorable cases these sufficiently large systems are accessible in simulations. Alternative methods that incorporate sub-leading terms of FSS shall be introduced "on-the-fly" where appropriate in the course of the following presentation.

The choice of the individual final estimates of ρ/ν was a subtle task. By increasing $L_{\min}$, the minimum chain length used in the fits, step by step, we tried to exclude sub-leading finite-size effects induced by corrections to FSS. In some cases we had to go to rather large $L_{\min}$, where the statistical inaccuracy induced by the large systems set in, because we found a visible and strong dependence on $L_{\min}$. Most importantly, however, we set a high value on disentangling what we expect or hope to see from what we actually see. Knowing accurate estimates for γ/ν from Sect. 8.1, and knowing that by usual and extended [129–133] Gaussian scaling relations, we do actually need only one single exponent (or exponent ratio) to be able to calculate all other critical exponents. We can thus state values of the other ratios in the subsequent sections, that we expect to find. Our goal, however, was *not* to show what we want to see, but to *test* objectively if the mixed spin models satisfy standard and extended scaling relations. We note, that it would have been possible in almost all cases to "tune" results by deliberately choosing other optimal estimates that more optimally satisfy scaling relations, or simply to raise $L_{\min}$ sufficiently. In every case, our objective criteria were

- primarily the $L_{\min}$-dependence of ρ/ν, backed up by
- consideration of the dependence on $L_{\max}$, the maximum chain length used in FSS fits, which in a single case only lead to a reduced $L_{\max}$, as well as
- χ^2_{dof}, which already for moderate $L_{\min}$ usually lost decisive significance in many cases, and
- the $L_{\min}$- and $L_{\max}$-dependence of other fit parameters, i.e. background and amplitude (of leading and possibly subleading terms).

This section on critical exponents starts out in Sect. 8.1 with the critical exponent ratio γ/ν, where ν is the critical exponent of the correlation length and γ the critical exponent of the transversal staggered magnetic susceptibility χ. This represents our only estimate of a thermodynamic exponent ratio that has been determined independently from our estimates of critical points. We consider γ/ν the best estimate of this section. Section 8.2 is dedicated to $1/\nu$, which has been obtained from five different observables. The discussion will put a focus on the determination of a covariance-weighted mean to obtain a combined final estimate. The results of straightforward application of power-law fits in order to determine α/ν, with α the critical exponent of the specific heat, are the matter of Sect. 8.3. In Sects. 8.4 and 8.5 the exponent ratios of the longitudinal and transversal string observables, β_z/ν and β_x/ν, respectively, will be presented along with a discussion of corrections to FSS. All critical exponent ratios will be converted into a single scaling dimension x_λ, thereby testing standard and extended scaling relations in Sect. 8.6 (which, in fact, will also be done due course of this section). An important aspect of this central section, that all Δ-point of the mixed spin models correspond to different Δ-points of the spin-$\frac{1}{2}$ chain, will be pointed out in Sect. 8.7, followed by a summary in Sect. 8.8.

8.1 γ/ν

The exponent γ controls the critical divergence of the transversal staggered magnetic susceptibility χ, which has been measured by the improved estimator

$$\langle\chi\rangle = \left\langle \frac{1}{4L\beta} \sum_{\text{loops } \mathcal{L}} |\mathcal{L}|^2 \right\rangle , \tag{8.3}$$

where $|\mathcal{L}|^2$ is the squared size of a single loop, and the sum runs over all loops in a decorated configuration (see Sect. 6.2.4). L and β are the spatial and temporal extent of the 2D configurations, i.e. chain length and inverse temperature. Thanks to the novel application of reweighting methods to improved estimators, we were able to locate the maxima of the susceptibility with high precision, yet subject to the critical considerations at small Δ, discussed in Sect. 6.3. However, in contrast to the position of the maxima, the values at the maxima are much less affected, and we will present very accurate estimates of the ratio γ/ν in the following.

Figure 8.1 shows double-log plots of our data for both models. Apart from the lowest curves, the datasets at the isotropic point $\Delta = 1$, all datasets form, at first sight, excellent straight lines. We carefully studied the influence of the minimum chain length $L_{\min}$ used in the linear fits (and also of maximum chain length $L_{\max}$, which, however, had no significant influence). The result is shown in Figs. 8.2–8.4, where we plot the dependence of the estimate of γ/ν on $L_{\min}$.

The isotropic point $\Delta = 1$, is special. We expect $\gamma/\nu = 1$, but logarithmic corrections are supposed to be present and the finite-size growth of the maxima is considerably modified by a logarithmic factor, $\chi_{\max}(L) \sim L^{\gamma/\nu}(\ln L)^{\hat{\gamma}-\hat{\nu}\gamma/\nu}$ with $\hat{\nu} = 1/2$. Thus, the supposed linear growth of the maxima is, in fact, enhanced by the logarithmic factor and the neglect of this multiplicative correction leads to an effective overestimation of γ/ν. This is exactly what we see in Fig. 8.2. First of all, it is difficult to decide on a final estimate on the basis of these plots. Even for relatively large $L_{\min}$ the estimates do not seem to converge. Depending on the window of L's used in the fit the logarithmic factor is mimicked by a small effective exponent that adds to the true value of γ/ν. We shall treat this case in more detail in Sect. 11.2.

At large values of $\Delta \neq 1$, a visible dependence of the estimates of γ/ν on $L_{\min}$ can still be seen, but in general good convergence can be observed. The final estimates were chosen restrictively in order to assure the evidentiary value, such that reasonable and minimally possible error estimates were achieved. This was problematic at $\Delta = 0.9$ in both models. A look at Fig. 8.3a and Fig. 8.4a, reveals that there is still a strong dependence on $L_{\min}$. According to the not truly converged shift towards larger values we may face the threat of underestimating the true values of γ/ν. Comparing the scale, however, shows that the drift is far less pronounced than the drift at the isotropic point. We interpreted the visible drift at $\Delta = 0.9$ in both models, as a clear sign of subleading corrections to FSS. The quality of data at $\Delta = 0.9$ can safely be considered excellent and thus we tried to quantify the subleading effects and check the validity of the estimates of γ/ν obtained from single power-law FSS. We considered two mechanisms to explain the observed data, the presence of a background and the presence of power-law corrections to FSS.

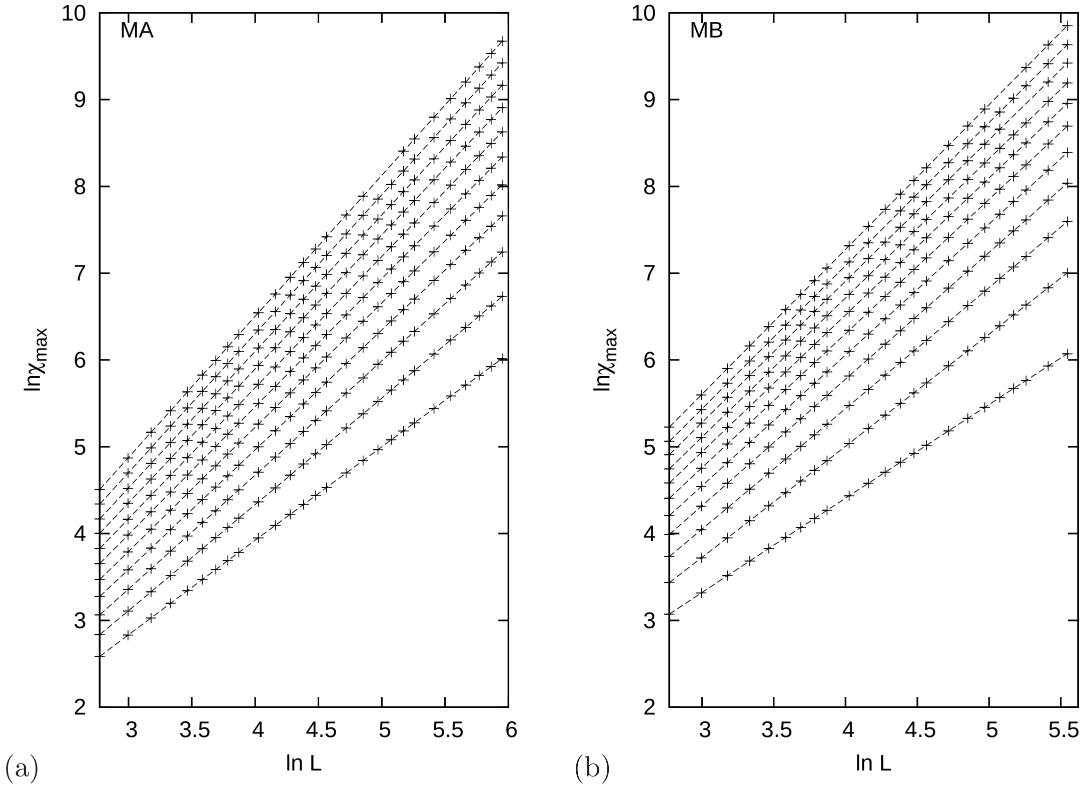

Figure 8.1: Finite-size growth of the maxima $\chi_{\max}$, of the transversal staggered magnetic susceptibility. Datasets correspond to $\Delta = 0 \ldots 1$, from top to bottom.

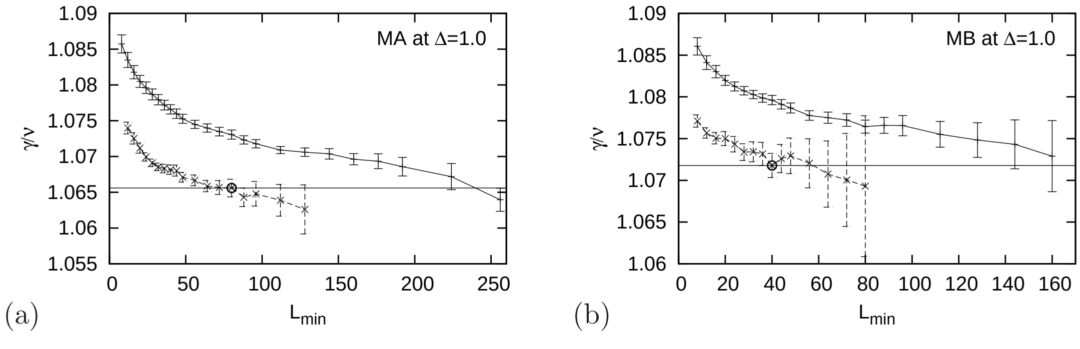

Figure 8.2: $L_{\min}$-dependence of the final estimate of γ/ν at the isotropic point $\Delta = 1$. Datapoints connected by full lines result from double-log linear fits, while those connected by dashed lines result from the subtraction method. Circles and full horizontal lines indicate our final optimal estimates.

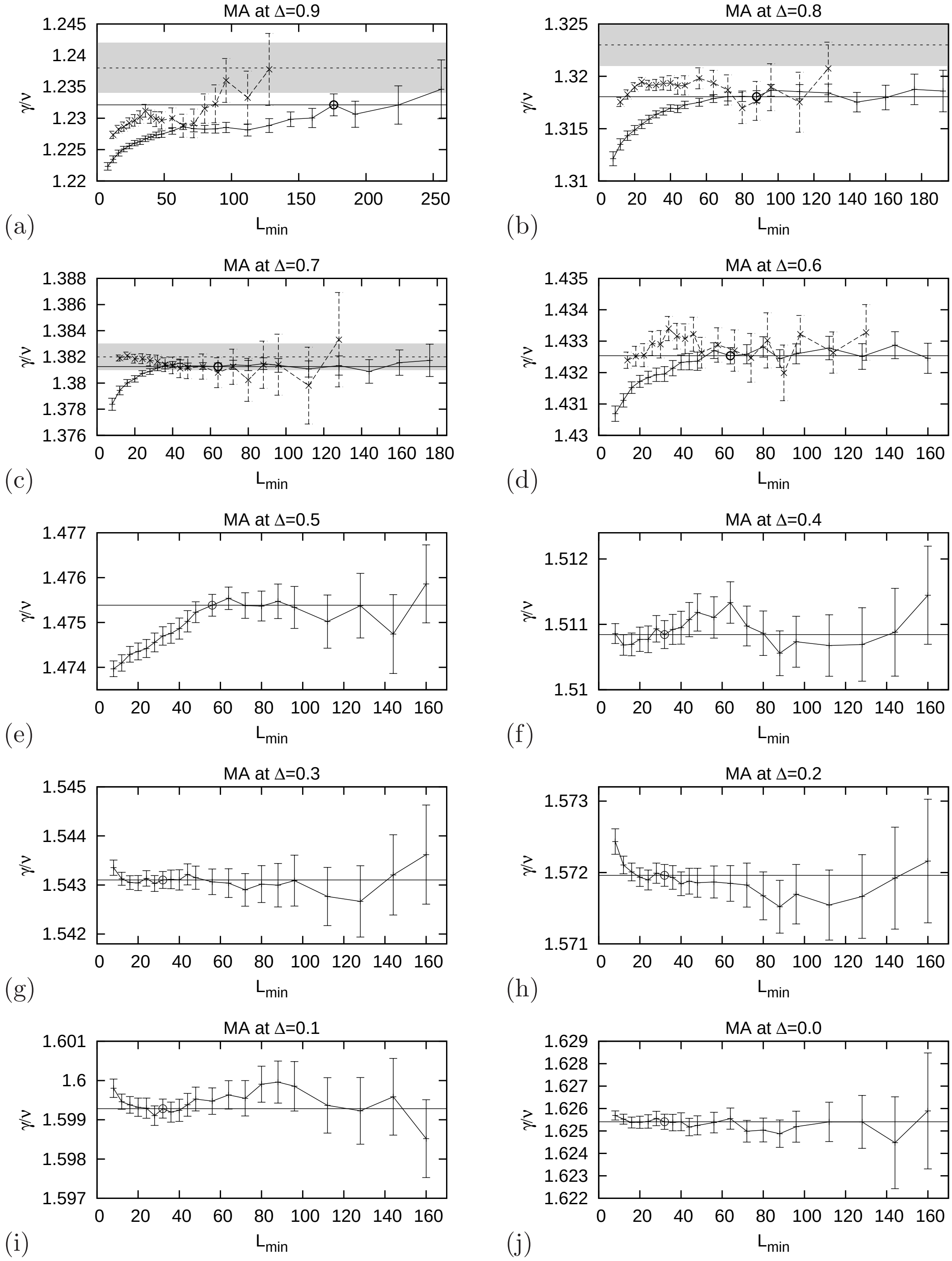

Figure 8.3: $L_{\min}$-dependence of the final estimate of γ/ν of MA. Full (dashed) lines connect datapoints resulting from double-log linear fits (the subtraction method). Circles and full horizontal lines indicate optimal final estimates. The horizontal line and the grey area show value and error of γ/ν, when taking an effective power-law correction into account.

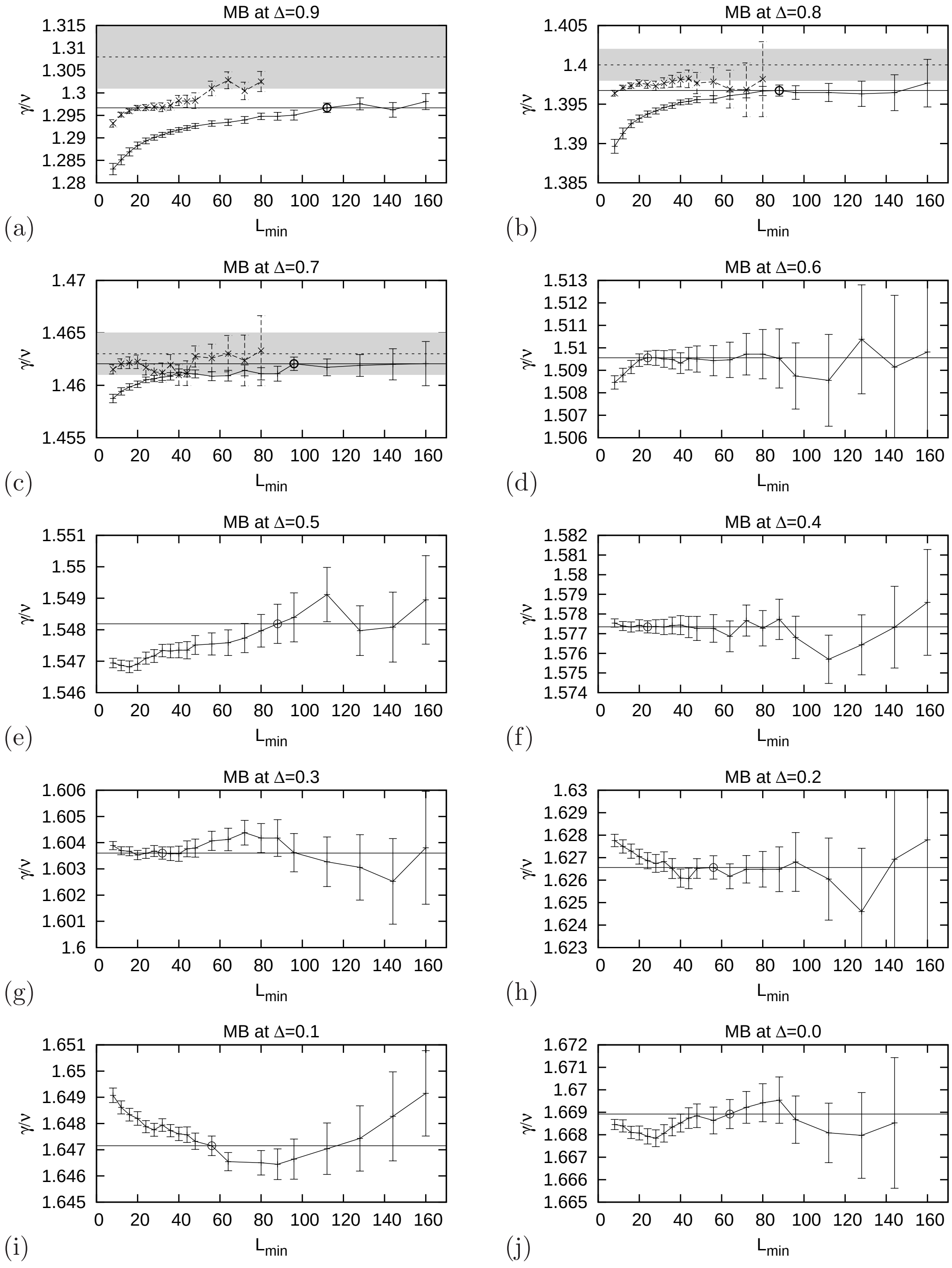

Figure 8.4: Same as Fig. 8.3 but for MB.

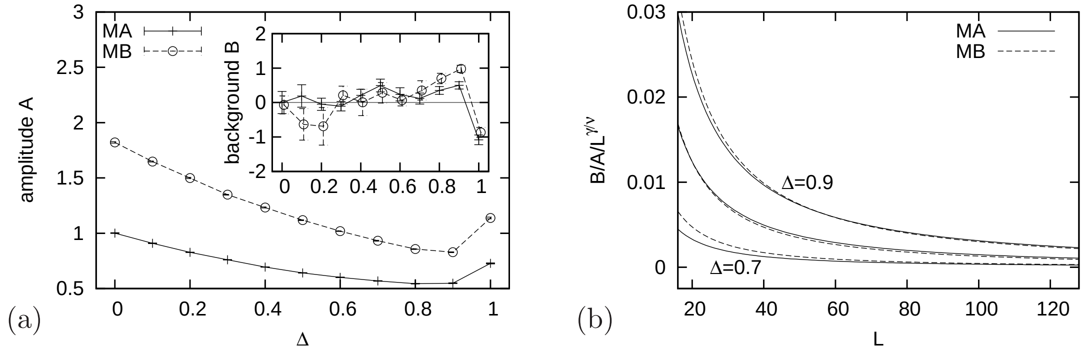

Figure 8.5: (**a**) (Effective) background B (inset) and amplitude A of the FSS behaviour of susceptibility's maxima, obtained from a direct fit to the power-law (8.1). (**b**) The factor $B/A/L^{\gamma/\nu}$ determines the "strength" of corrections induced by the presence of a background in the linear fit to (8.2) (the double-log linear fit). Curves shown are for $\Delta = 0.9, 0.8$ and 0.7, from top to bottom.

A background induces corrections in the double-log linear fit that vanish asymptotically as $\sim L^{-\gamma/\nu}$. With $\gamma/\nu > 1$, one may expect these corrections to vanish sufficiently fast, but one also needs to take the ratio of the background and the amplitude B/A into account. Only in combination with this ratio, the factor $L^{-\gamma/\nu}$ can be judged either significant or not. In Fig. 8.5 we show the results of power-law fits with L_{min} growing from 24 (12) at $\Delta = 0$ to 72 (40) at $\Delta = 1$ for MA (MB). We find indeed a significant background, that may be effective or true, for $\Delta \geq 0.8$ in both models. Yet more important is the fact that at precisely those values of Δ, the amplitudes are comparatively small. The relevant ratio $(B/A)L^{-\gamma/\nu}$ is plotted in Fig. 8.5b as a function of L, which nicely illustrates the weakening bias of a potential background with decreasing Δ. Qualitatively this is consistent with the decreasing drifts.

The *subtraction* method, that is to, instead of (8.2), fit

$$\ln(\mathcal{O}_{2L} - \mathcal{O}_L) \sim \ln(A(1 - 2^{\rho/\nu})) + \frac{\rho}{\nu} \ln L \tag{8.4}$$

to a straight line in $\ln L$, eliminates background terms at the cost of a reduced number of data points with enlarged error estimates leading to an overall increase of the final error estimate. We used the subtraction method to check for consistency, and the corresponding results are included in Figs. 8.3a–c and 8.4a–c as datapoints connected by dashed lines. Even at $\Delta = 0.9$, where for both models a slight discrepancy is obvious we consider the results of the two different methods consistent. At the isotropic point, we used the results of the subtraction method as our "final" estimates, because we can at least observe some kind of convergence within errorbars, which is not the case with the double-log linear fit.

The presence and neglect of power-law corrections to FSS may lead to systematically wrong estimates of critical exponent ratios, in particular, if the subleading exponents are small and the corresponding terms vanish slowly. The fact that one needs to estimate at least two unknown exponents from non-linear fits, turns the consideration of power-law corrections quite difficult [242]. Taking power-law corrections into account,

Table 8.1: Final estimates of the critical exponent ratio γ/ν, of the transversal staggered magnetic susceptibility χ, obtained from double-log linear fits. Columns headed by $(\gamma/\nu)_\omega$ list the results when a power-law correction, captured by an effective correction exponent ω, is taken into account.

		MA			MB	
Δ	γ/ν	$(\gamma/\nu)_\omega$	ω	γ/ν	$(\gamma/\nu)_\omega$	ω
0.0	1.6254(4)			1.6689(7)		
0.1	1.5993(3)			1.6472(4)		
0.2	1.5720(2)			1.6266(6)		
0.3	1.5431(2)			1.6036(3)		
0.4	1.5108(3)			1.5773(4)		
0.5	1.4754(3)			1.5482(7)		
0.6	1.4325(3)			1.5096(4)		
0.7	1.3813(3)	1.382(1)	1.20(10)	1.4621(7)	1.463(3)	0.82(11)
0.8	1.3181(6)	1.323(2)	0.60(5)	1.3967(8)	1.400(3)	0.84(11)
0.9	1.2321(18)	1.238(4)	0.40(8)	1.2967(11)	1.308(8)	0.54(12)
1.0	1.0656(13)			1.0718(15)		

we model the growth of the susceptibility at the maximum by [242]

$$\ln \chi_{\max}(L) = \ln A + \frac{\gamma}{\nu} L + \ln\left(1 + CL^{-\omega}\right) \approx \ln A + \frac{\gamma}{\nu} L + CL^{-\omega}\,, \tag{8.5}$$

where ω (C) is an *effective* correction exponent (amplitude) the value of which may be determined by several different exponents (and amplitudes) as well as by the presence of a background, which shall be ignored. Fixing ω, we fitted our data to both, the exact and approximate, of the above forms and searched for the minimum in the χ^2-deviation "by hand". We then studied the influence of $L_{\min}$ for a few small values and obtained a short series of $\omega_{\min}$. Looking for the points with a 1% increase in χ^2 gave a rough estimate of the error of $\omega_{\min}$. Variation of ω within the errorbars of the final value yielded an estimate of γ/ν and its error. The corresponding results are included in Table 8.1 which lists the final estimates γ/ν from the double-log linear fits, and in Figs. 8.3a–c and 8.4a–c as dashed horizontal lines embedded in grey areas that indicate the error estimate.

For, e.g., MA at $\Delta = 0.9$, we obtained in this way $\omega = 0.40(8)$, which is indeed relatively small as expected, and $(\gamma/\nu)_\omega = 1.238(4)$ which is slightly larger than our final estimate of double-log linear fit, $\gamma/\nu = 1.232(2)$. The two estimates are not really significantly inconsistent but they differ. In MA, our estimates of the correction exponent grow unambiguously with decreasing Δ, but this is not exactly reproduced in MB. Nonetheless, in order to interpret the correction exponent, we looked for a candidate that varies with the exchange anisotropy and compared it to some irrelevant RG eigenvalues of the Gaussian operator content (see also Fig. 6.11). Using our estimate of γ/ν, the absolute value of the RG eigenvalue $|y_{0,4}| = |2 - x_{0,4}|$, can be computed using (5.35) after converting γ/ν to $K = 1/(4 - 2\gamma/\nu)$. The numbers are listed in Table 8.2, and they grow with decreasing Δ but they do not match the estimates of the correction exponent ω. However, the scaling operator with RG eigenvalue $y_{0,4}$, is precisely the operator that generates logarithmic corrections at the isotropic point. Thus, if the same logarithmic corrections are indeed present in the mixed spin models, it seems reasonable to assume that the corresponding operator still exerts some influence also at smaller values of Δ. We have tried various fits including several terms with fixed exponents chosen among various candidates originating from non-analytic (see again Fig. 6.11) and/or analytic corrections to FSS, but it turned out impossible to disentangle the effect of different terms.

Table 8.2: Comparison of the effective correction exponent ω to the RG eigenvalue $|y_{0,4}|$, which is zero at the isotropic point, and thus known to be responsible for the presence of logarithmic correction in the spin-$\frac{1}{2}$ chain.

	MA		MB	
Δ	ω	$\lvert y_{0,4}\rvert$	ω	$\lvert y_{0,4}\rvert$
0.7	1.20(10)	1.236(6)	0.82(11)	1.724(14)
0.8	0.60(5)	0.954(9)	0.84(11)	1.333(12)
0.9	0.40(8)	0.625(14)	0.54(12)	0.890(30)

We conclude this section graphically with Fig. 8.6, where the estimates of the critical exponent ratio γ/ν, as listed in Table 8.1, are plotted in comparison to the exactly known values of the spin-$\frac{1}{2}$ chain. We consider the results of double-log linear fits, which assume a single power-law FSS behaviour of the susceptibility's maxima, our final results, which shall be used for further reference and comparison.

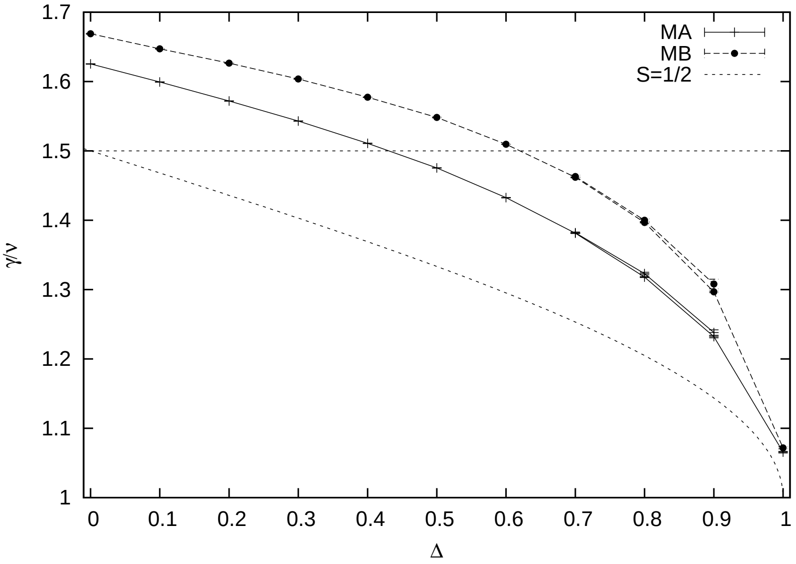

Figure 8.6: Final estimates of the critical exponent ratio γ/ν of the transversal staggered magnetic susceptibility χ, obtained from double-log linear fits. The dashed curve shows the exactly known γ/ν of spin-$\frac{1}{2}$ chain. The dashed horizontal line marks the pure XY-point of the spin-$\frac{1}{2}$ chain, where $\gamma/\nu = 3/2$. At $\Delta = 0.7, 0.8$ and 0.9, the extra points added show the results when an effective power-law correction is taken into account.

8.2 $1/\nu$

The critical exponent ν controls the divergence of the correlation length. It is a quantity of central importance. The theory of FSS implies that all other critical exponents can usually only be obtained as ratios over ν, and the ratio $1/\nu$ is supposed to control the leading shift of pseudocritical points. Our analysis of the shift in the previous section did not yield a conclusive value of $1/\nu$. We thus want an independent estimate which can be obtained by studying the size-dependence of logarithmic derivatives of moments of the order parameter(s), and the derivative of the Binder parameter [153, 240–242].

In Sect. 5.4 we adjusted the definition of string observables, that can be used as (dis)order parameters to distinguish the low-λ- from the high-λ-phase in the spin-$\frac{1}{2}$ chain, to mixed spin chains. The measurement of the longitudinal string observable D_z is straightforward and implemented via integrated estimators. The use of improved estimators also permits the measurement of a transversal version D_x. The λ-derivative of the expectation value of an observable can be calculated by

$$\frac{\mathrm{d}\langle\mathcal{O}\rangle}{\mathrm{d}\lambda} = \frac{\mathrm{d}}{\mathrm{d}\lambda}\frac{\oint \mathcal{D}[n(\tau)]\,\mathcal{O}[n(\tau)]\,W[n(\tau)]}{Z}\,, \tag{8.6}$$

with $\mathcal{O}[n(\tau)]$, the value of observable $\mathcal{O}$ in a configuration represented by the path $n(\tau)$. $\mathcal{D}$ is the measure and W the weight (6.32) of the configuration, respectively, and Z is the partition function (6.19) (see Sect. 6.2). Dividing by $\langle\mathcal{O}\rangle$ yields the logarithmic derivative, which reads here

$$\frac{\mathrm{d}\ln\langle\mathcal{O}\rangle}{\mathrm{d}\lambda} = \beta\Delta\langle E_\lambda\rangle - \langle n_\lambda\rangle/\lambda - \frac{\beta\Delta\langle E_\lambda\mathcal{O}\rangle - \langle n_\lambda\mathcal{O}\rangle/\lambda}{\langle\mathcal{O}\rangle}\,. \tag{8.7}$$

E_λ is the normalized and reduced, diagonal energy stored in λ-bonds (cf. (6.33) and (6.92)), and n_λ is the number of jumps or breakups on λ-bonds (see Sect. 6.2), that represents the off-diagonal contribution to the total energy on λ-bonds. By reweighting each observable and product of observables individually to the critical point we could calculate the critical point estimates of logarithmic derivatives. For improved estimators the above equation simplifies. There is no diagonal contribution, only the number of breakups on a decorated configuration. The estimator of the derivative of the Binder parameter follows from the quotient rule,

$$\frac{\mathrm{d}U_{\mathcal{O},4}}{\mathrm{d}\lambda} = \frac{\mathrm{d}}{\mathrm{d}\lambda}\frac{\langle\mathcal{O}^2\rangle^2}{\langle\mathcal{O}^4\rangle} = U_{\mathcal{O},4}\left(2\frac{\mathrm{d}\ln\langle\mathcal{O}^2\rangle}{\mathrm{d}\lambda} - \frac{\mathrm{d}\ln\langle\mathcal{O}^4\rangle}{\mathrm{d}\lambda}\right)\,. \tag{8.8}$$

We chose five observables to enter the final analysis. The logarithmic derivatives of

- the moments D_x and D_x^2, of the transversal string observable,
- the moments $|D_z|$ and D_z, of the longitudinal string observable,

and the derivative of

- the unnormalized and unshifted Binder parameter $U_{z,4} = \langle D_z^2\rangle^2/\langle D_z^4\rangle$, that combines the second and fourth moment of the longitudinal string observable.

For each of the five observables we chose an optimal estimate of $1/\nu$ individually and independently. Examples of datasets and the dependence of the FSS-estimate of $1/\nu$ on the minimum chain length, L_{min}, used in the double-log linear fits are shown in Figs. 8.7–8.10. The logarithmic derivative of $|D_z|$ is the exemplary representative of the longitudinal observables. The quality of the integrated estimator is significantly better than that of improved slice estimators. Yet the latter are not improved in the sense that they give better results than unimproved estimators. They are improved in the sense that they can be measured at all.

As for γ/ν, we found a strong dependence of the final estimate on L_{min}. This implies the presence of neglected corrections to FSS. Remarkably, the drift of $1/\nu$ in L_{min} seems to be, in both models, weakest at the isotropic points[1]. Yet first of all, $1/\nu$ is nowhere near the expected value 3/2, and, second, it also differs significantly from the effective value that can be calculated from our estimate of γ/ν. A possible explanation for the observed strong drifts in L_{min}, apart from power-law corrections to FSS, is the presence of a background term. To check for the presence of a background term we performed fits directly to a power-law in L. The results are shown in Fig. 8.11 for the logarithmic derivative of the longitudinal string observable, $\mathrm{d}\ln D_z/\mathrm{d}\lambda$. What we found is a sizeable negative (effective) background. The effect of the background is amplified by a small value of the amplitude A, in particular in MA *and* for large values of Δ. The exponent $1/\nu$ decreases with decreasing Δ leading to a weaker suppression of the correction term. Indeed, putting the pieces together, we find an enhanced influence of the background on the double-log linear fit at small values of Δ. Even for the relatively long chain with $L = 128$, in the more favorable case of MA, the correction term at $\Delta = 0$ still is $\approx \ln(1 - 0.07) \approx -0.07$.

We emphasize that we do not consider this as proof for the presence of background terms. We did not succeed in disentangling the effect of further – true – corrections to FSS. But the observed effective values of background and amplitude present an explanation for the strong drifts of the estimates of $1/\nu$ with L_{min} at small values of Δ. We have also applied the subtraction method to eliminate background terms and found overall good agreement with the results from double-log linear fits. The inclusion of power-law corrections made the analysis much more complicated, as no linear fits could be used anymore. We relied on purely linear fits in the analysis of crosscorrelations. Having found rather accurate and consistent results by the double-log linear fits, backed up by the above explanation for the observed drifts, we refrain from discussing our attempts to extract power-law corrections here.

To combine all five different estimates of $1/\nu$ into a final one we computed the error-weighted *and* the covariance-weighted mean. The covariance-weighted mean takes into account that all five different estimates of $1/\nu$ originate from the same set of data and are, hence, correlated. The covariance-weighted mean can be calculated by [251]

$$(1/\nu)_{\text{c}} = \sum_i \omega_i (1/\nu)_i \,, \tag{8.9}$$

---

[1] See also Sect. 8.4, where a similar behaviour appears in the analysis of the longitudinal string observable and β_z/ν.

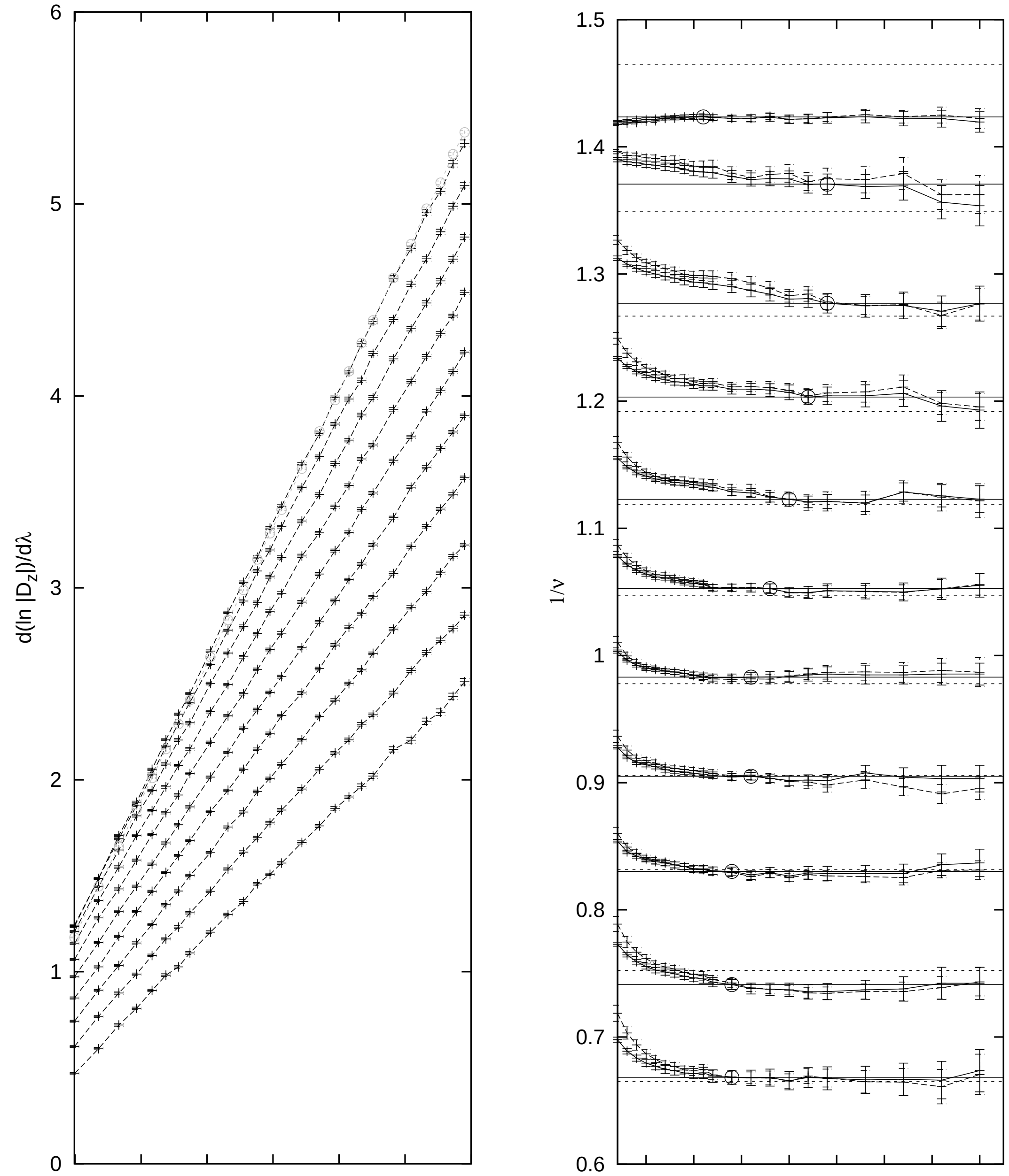

Figure 8.7: MA, logarithmic derivative of $|D_z|$. (**a**) FSS behaviour at the critical point $\lambda_c(\Delta)$. (**b**) $L_{\min}$-dependence of the final estimate of $1/\nu$ from double-log linear fits. For all Δ, $L_{\max} = 384$. Results of fitting with error-weighted datapoints (full lines) are compared to unweighted jacknifed fits (dashed lines). Circles and full horizontal lines indicate our final optimal estimates. Dashed horizontal lines show the estimate $1/\nu$ obtained from γ/ν by Gaussian scaling relations. Datasets correspond to $\Delta = 0 \ldots 1$ from bottom to top in both, (**a**) and (**b**). For better distinction the dataset of $\Delta = 1$ is grey with circles in (**a**).

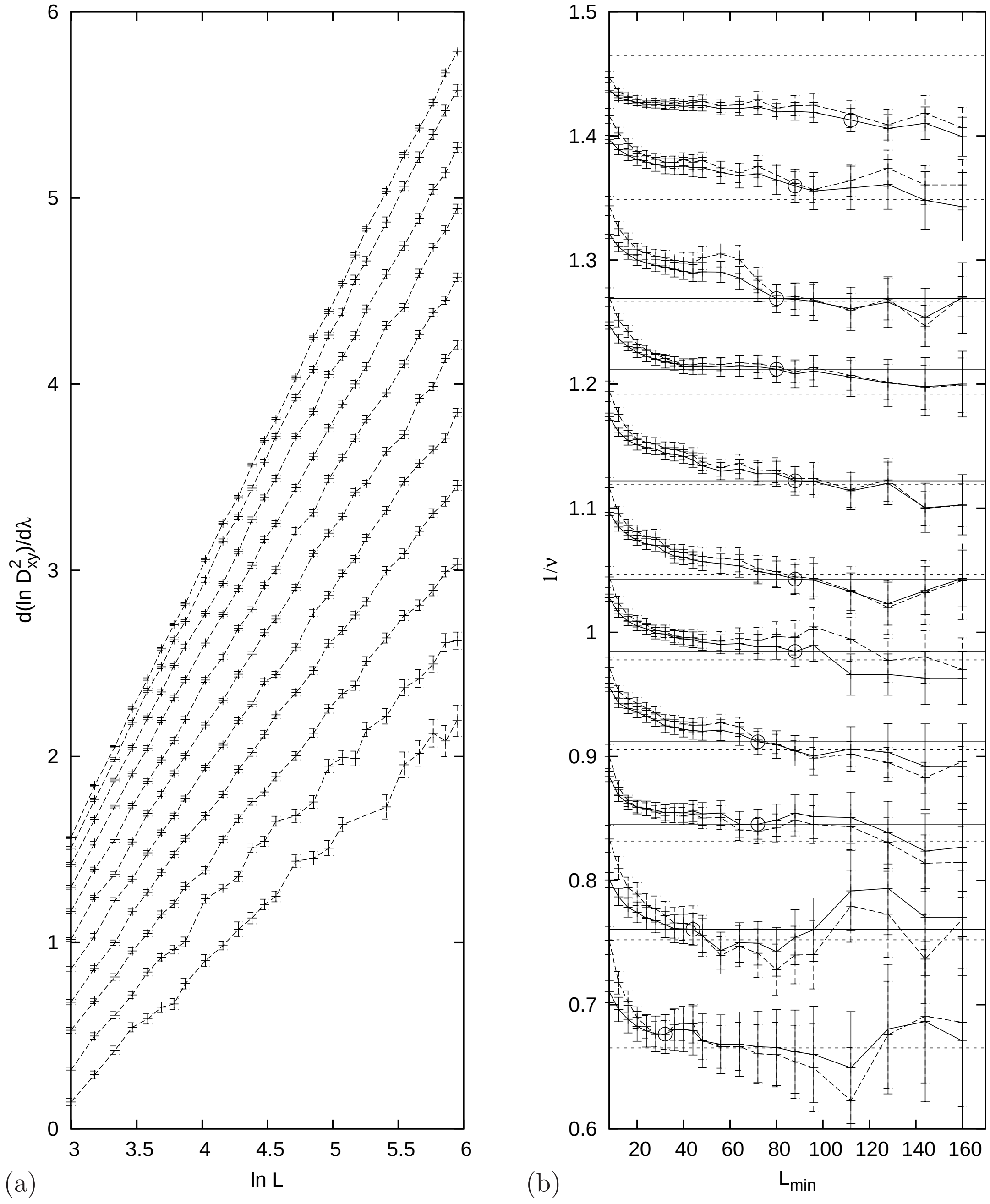

Figure 8.8: Same as Fig. 8.7, but for the logarithmic derivative of D_x^2.

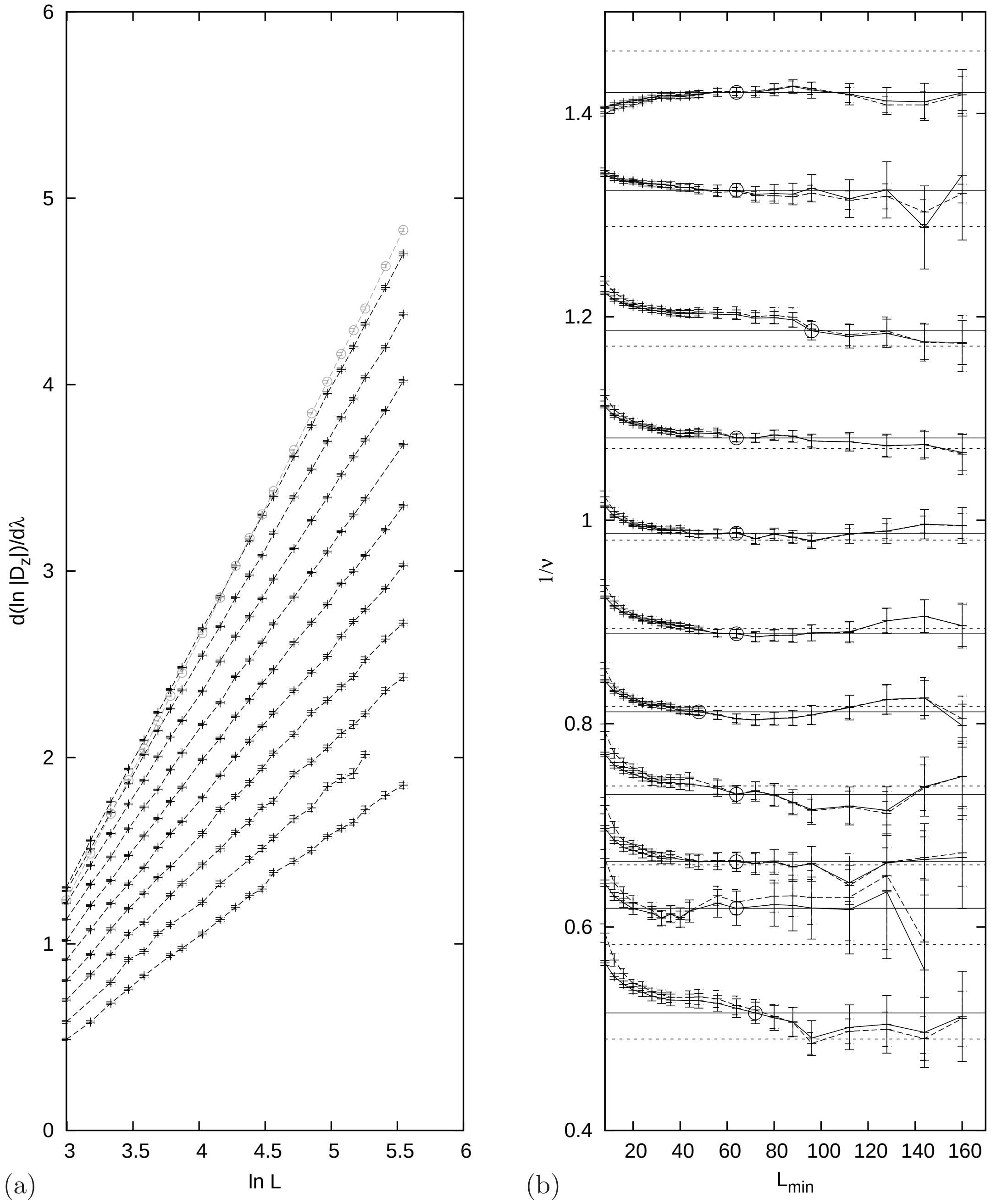

Figure 8.9: MB, logarithmic derivative of $|D_z|$. (**a**) FSS behaviour at the critical point $\lambda_c(\Delta)$. (**b**) $L_{\min}$-dependence of the final estimate of $1/\nu$ from double-log linear fits. $L_{\max} = 256$ for all Δ, apart from $\Delta = 0.1$ where $L_{\max} = 192$. Results of fitting with error-weighted datapoints (full lines) are compared to unweighted jacknifed fits (dashed lines). Circles and full horizontal lines indicate our final optimal estimates. Dashed horizontal lines show the estimate $1/\nu$ obtained from γ/ν by Gaussian scaling relations. Datasets correspond to $\Delta = 0 \ldots 1$ from bottom to top in both, (**a**) and (**b**). For better distinction the dataset of $\Delta = 1$ is grey with circles in (**a**).

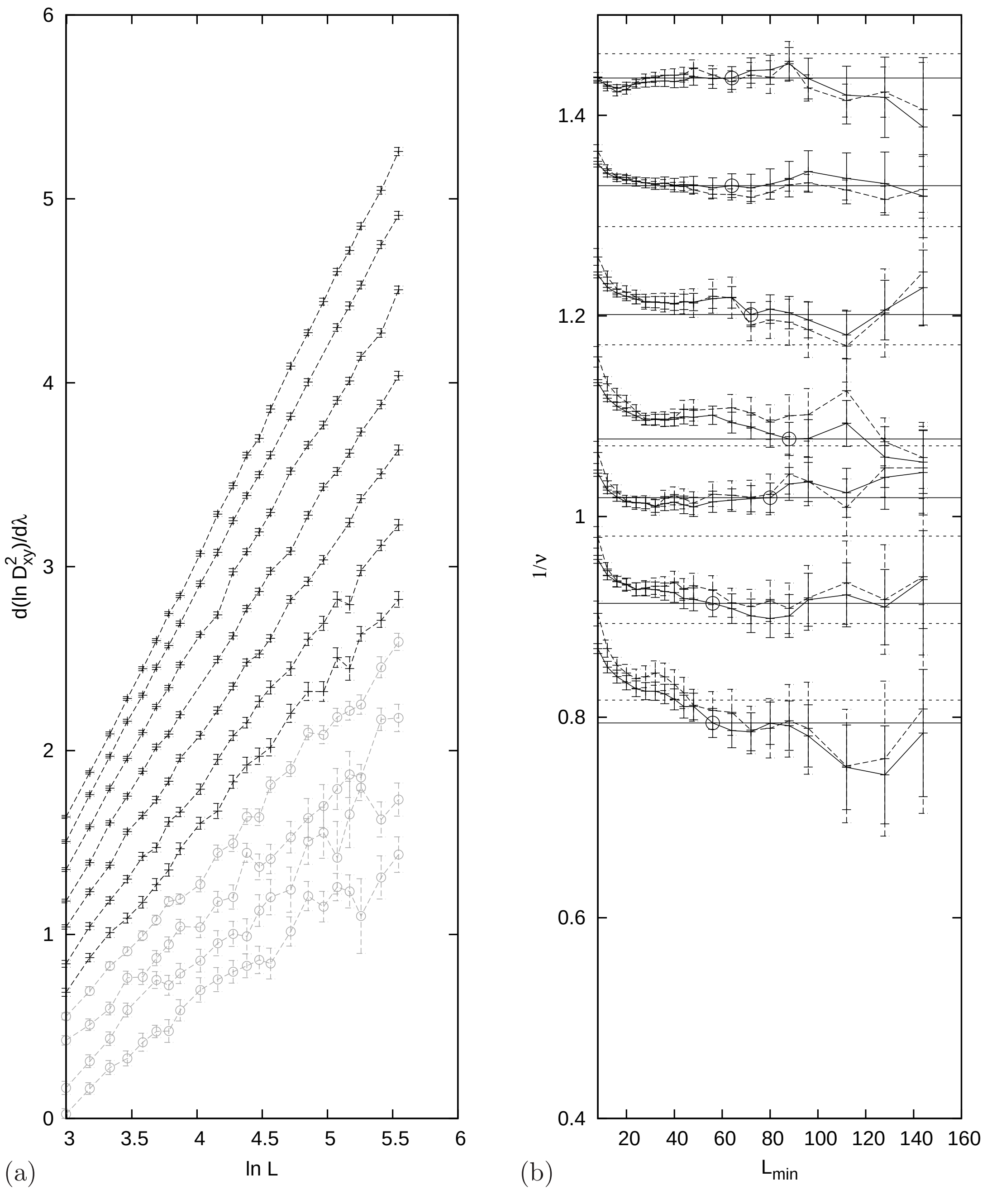

Figure 8.10: Same as Fig. 8.9, but for the logarithmic derivative of D_x^2. Datasets for $\Delta \leq 0.3$ (shown in grey with circles) proved particularly bad. They did not enter the final estimate of $1/\nu$ of MB.

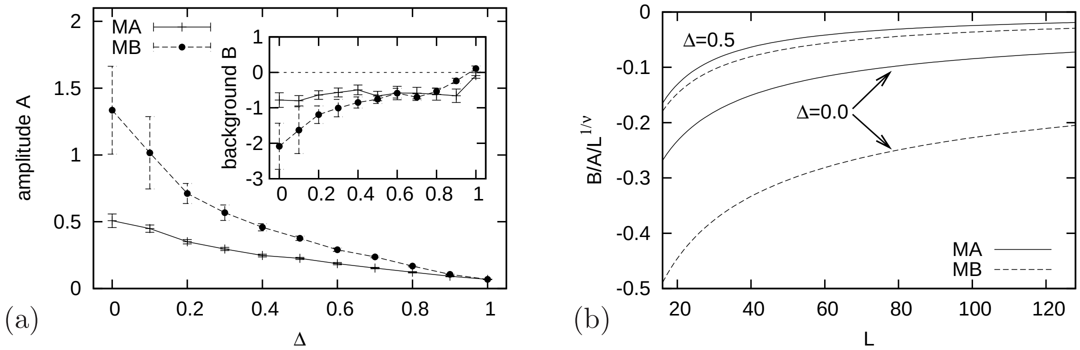

Figure 8.11: (**a**) (Effective) background B (inset) and amplitude A of the FSS of the logarithmic derivative of the longitudinal string observable, $\mathrm{d}\ln D_z/\mathrm{d}\lambda$, at the critical point, obtained from a direct fit to the power-law (8.1). (**b**) The "strength" of corrections due the presence of an (effective) background, given by the factor $B/A/L^{1/\nu}$, decreases with increasing Δ.

with weights

$$\omega_i = \frac{1}{Z}\sum_j [\Gamma^{-1}]_{ij}\,, \tag{8.10}$$

where $Z = \sum_{ij}[\Gamma^{-1}]_{ij}$, is a normalization factor and Γ^{-1}, the inverse of the covariance matrix $\Gamma_{ij} = \langle(1/\nu)_i(1/\nu)_j\rangle - \langle(1/\nu)_i\rangle\langle(1/\nu)_j\rangle$. The error estimate that takes crosscorrelations into account is [251]

$$\sigma = \sum_{ij}\omega_i\omega_j\Gamma_{ij}\,. \tag{8.11}$$

Using, instead of weights (8.10), $\omega_i = Z^{-1}/\sigma_i^2$, with σ_i^2 the variance of estimate $(1/\nu)_i$, yields error-weighted mean. The elements of the covariance matrix can be estimated by the jacknife method [251],

$$\Gamma_{ij} = \frac{n-1}{n}\sum_{l=1}^{n}\left[(1/\nu)_{i,l} - \overline{(1/\nu)}_i\right]\left[(1/\nu)_{j,l} - \overline{(1/\nu)}_j\right], \tag{8.12}$$

where n is the number of jacknife bins and $\overline{(1/\nu)}_i$ denotes the average over n jacknife estimates $(1/\nu)_{i,l}$. A numerical inversion of the estimated covariance matrix leads to the weights ω_i. In all of the following analysis, the width of jacknife bins has been set to 1000 giving $n = 200$, apart from MA at $\Delta = 1$, where $n = 500$.

An important issue is the jacknife method to estimate the covariance matrix. Every datapoint, shown for example in Fig. 8.7, and its corresponding error estimate are the result of jacknifed reweighting to the critical point. To extract the final estimates we have consistently chosen jacknife bins of size $l_\mathrm{b} = 1000$. With $2 \cdot 10^5$ measurements, this yielded $n_\mathrm{b} = 200$ jacknifed values $\mathcal{O}_{L,i}$, for every observable and chain length. A linear fit then was performed for every jacknife set with index i,

$$\ln\mathcal{O}_{L,i} = \ln A_i + (1/\nu)_{\mathcal{O},i}\ln L\,, \tag{8.13}$$

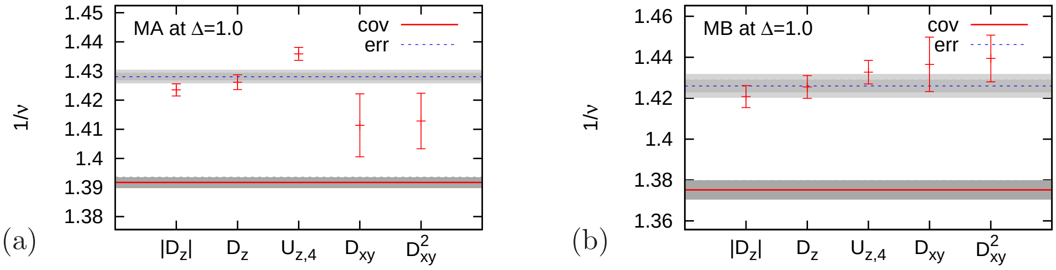

Figure 8.12: (Color online) Final estimates of $1/\nu$ at the isotropic point $\Delta = 1$. Individual optimal estimates of $1/\nu$ are shown as datapoints with errorbars. Symbols that show moments of $D_{z/xy}$, are used as shorthand for the logarithmic derivatives thereof, while $U_{z,4}$ represents the derivative of the Binder parameter of the longitudinal string observable D_z. The full red line gives the covariance-weighted mean (cov) and the dashed blue line the error-weighted mean (err). Grey areas represent the corresponding error estimates, with two shades of grey showing the error-weighted error (small area) and covariance-weighted error (large area) of the error-weighted mean.

resulting in n_b estimates $(1/\nu)_{\mathcal{O},i}$ for each observable $\mathcal{O}$. The error estimate of $(1/\nu)_{\mathcal{O}}$ then was calculated with the usual jacknife formula. In the fits to the above form, however, datapoints were not weighted, as usual, with the inverse of the squared error. Taking errors of $\mathcal{O}_L$ into account would need the calculation of the errors of each value in the jacknifed sets of estimates, i.e. a doubled jacknife. We did not try such a doubled jacknife as the number of reweighting procedures then would grow with the square of the number of jacknife bins. We compared the results of jacknifed unweighted linear fits to those of linear fits to weighted datapoints (see Figs. 8.7b and 8.8b–8.10b for examples) and generally found good agreement, as expected, in particular with the longitudinal observables. Discrepancies are more obvious in the transversal observables. Such a discrepancy indicates an underlying bias. If a bias of $(1/\nu)_{\mathcal{O}}$, calculated by the usual jacknife formal, was larger than 10% of the jacknife error estimate, we discarded the estimate and did not include it in the covariance-weighted mean. Figure 8.10a shows four datasets of MB in grey. Additionally to the poor quality, it was the biased estimate of $(1/\nu)$ that finally forced us to discard these series. Judging only the quality from a look at the plot, there would seem to be not much difference between the set of $\Delta = 0.4$ (the last set in black) and the set of $\Delta = 0.3$ (the first set in grey). In fact, we could have even included obviously biased estimates in the covariance-weighted mean. The error of the transversal estimates is generally large and they do contribute only very little to the covariance-weighted mean.

Figures 8.12–8.14 present all individual estimates of the ratio $1/\nu$ that enter in our final estimates. Covariance- and error-weighted mean are depicted as lines with a error bands (we use the same convenient way of presentation as in [251]). We find the surprising result that in many cases the covariance-weighted mean differs significantly from its error-weighted counterpart. Yet an unintuitive value of the covariance-weighted mean is not wrong [252]. It is, in fact, difficult to interpret these results and draw precise conclusions. Discrepancies between the covariance-weighted and the error-weighted mean seem to be stronger at large Δ, in particular at the isotropic point (Fig. 8.12)

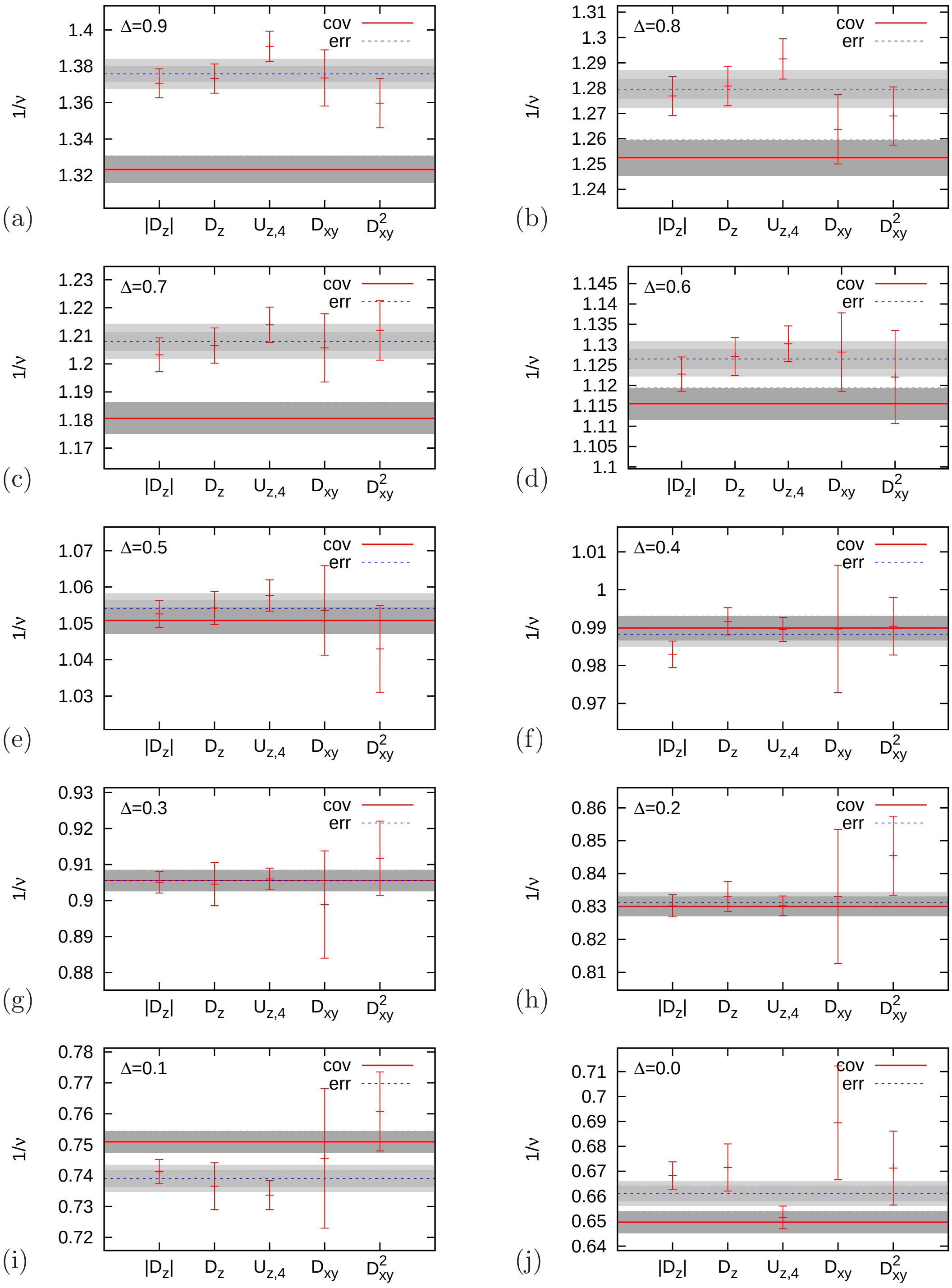

Figure 8.13: Same as Fig. 8.12, but for $\Delta < 1$ of MA.

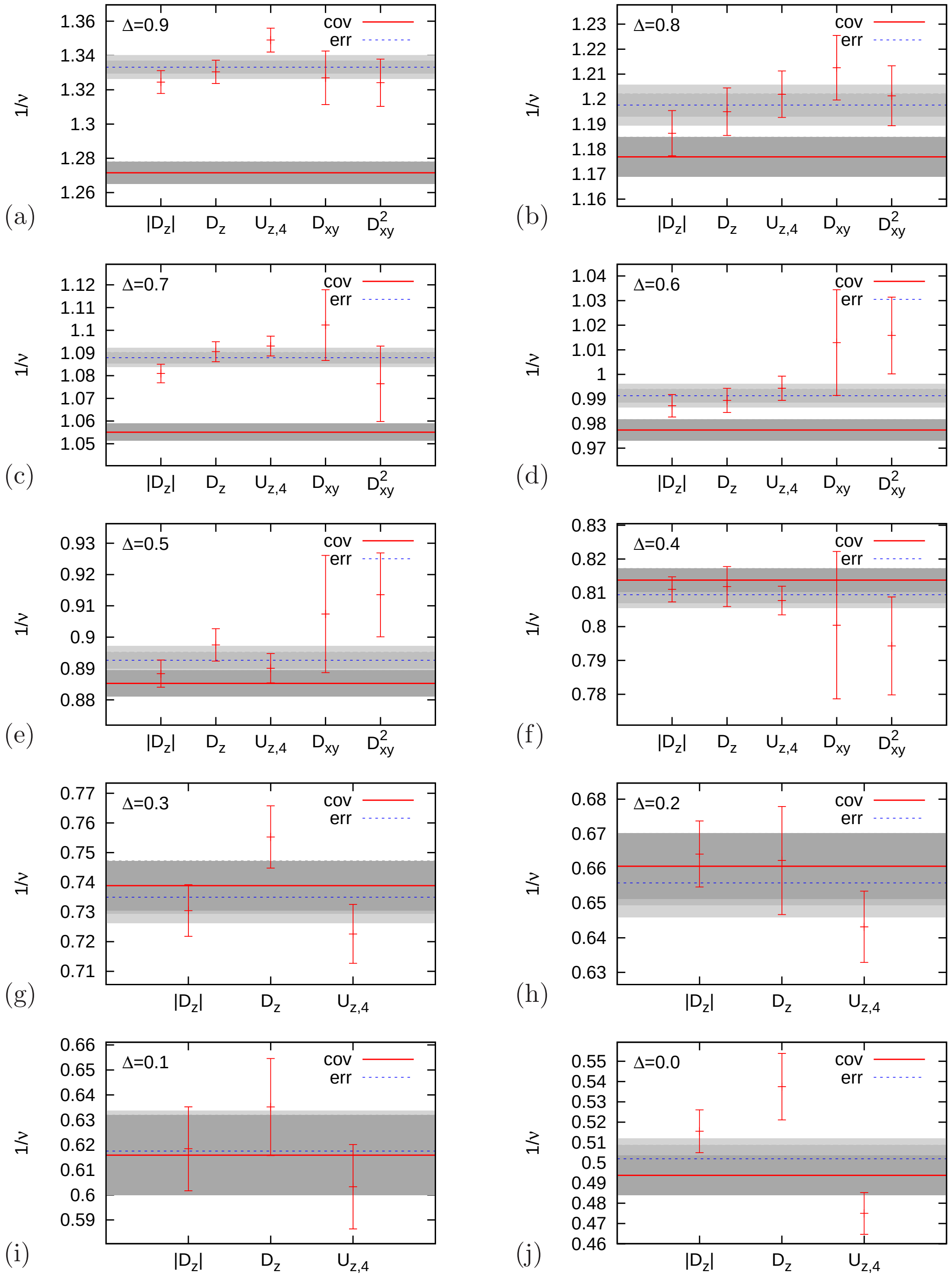

Figure 8.14: Same as Fig. 8.12, but for $\Delta < 1$ of MB.

Table 8.3: Normalized elements of the covariance matrix of MA at $\Delta = 1$. The elements represent the correlation between different estimates $(1/\nu)_{\mathcal{O}}$. Inversion yields the factors $\omega_{\mathcal{O}}$, the weights with which each individual estimate contributes to the covariance-weighted mean. The Δ-dependence of bold numbers is shown in Fig. 8.15.

	$\frac{\mathrm{d}\ln\langle\lvert D_z\rvert\rangle}{\mathrm{d}\lambda}$	$\frac{\mathrm{d}\ln\langle D_z\rangle}{\mathrm{d}\lambda}$	$\frac{\mathrm{d}\,U_{z,4}}{\mathrm{d}\lambda}$	$\frac{\mathrm{d}\ln\langle D_x\rangle}{\mathrm{d}\lambda}$	$\frac{\mathrm{d}\ \ln\langle D_x^2\rangle}{\mathrm{d}\lambda}$
$\frac{\mathrm{d}\ln\langle\lvert D_z\rvert\rangle}{\mathrm{d}\lambda}$	1	0.940	**0.994**	0.345	**0.376**
$\frac{\mathrm{d}\ln\langle D_z\rangle}{\mathrm{d}\lambda}$		1	0.931	0.387	0.406
$\frac{\mathrm{d}\,U_{z,4}}{\mathrm{d}\lambda}$			1	0.349	0.382
$\frac{\mathrm{d}\ln\langle D_x\rangle}{\mathrm{d}\lambda}$				1	**0.873**
$\frac{\mathrm{d}\ \ln\langle D_x^2\rangle}{\mathrm{d}\lambda}$					1
$\omega_{\mathcal{O}}$	4.138	−0.693	−2.430	0.002	−0.017

and at $\Delta = 0.9$ (Fig. 8.13a and Fig. 8.14a). However, this systematics cannot be conclusively deduced. It seems to be counteracted, for example, at $\Delta = 0.1$ and 0.0 in MA.

Non-overlapping errors can be generated by strong correlations between some of the individual estimates $(1/\nu)_{\mathcal{O}}$ [252]. The correlation coefficients are the normalized elements of the covariance matrix. We list an example of the normalized covariance matrix in Table 8.3 and plot the Δ-dependence of selected elements in Fig. 8.15. At the isotropic point and large Δ, the longitudinal observables are strongly correlated with coefficients ≈ 1 (at least > 0.9). These are the integrated estimators. The next relatively strong correlation is in between the transversal observables measured by improved estimators, while the correlation between the two different types of observables is relatively weak. However, the element between $|D_z|$ and $U_{z,4}$ remains strong down to $\Delta = 0.3$ in MB, while the overlap of the error estimate for $\Delta \leq 0.5$.

Questioning the reasons for the large and visible discrepancies, we propose the pres-

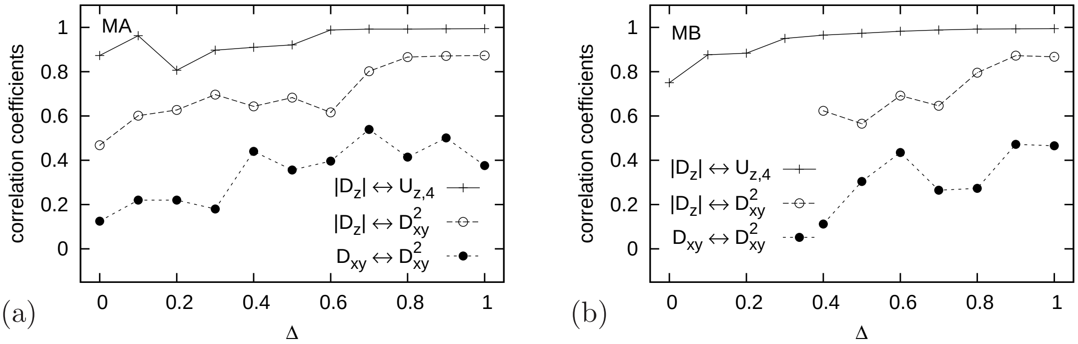

Figure 8.15: The estimate of $1/\nu$ obtained from, e.g., $|D_z|$, is correlated to that obtained from, e.g., $U_{z,4}$, because both observables are measured in one and the same simulation. The correlation coefficients tend to decrease with decreasing Δ.

ence of uncontrolled corrections to FSS (which includes the presence of a background term) and/or uncontrolled autocorrelations. Even though we tried to eliminate subleading FSS effects by a careful observation of the L_{min}-dependence, we cannot be sure that a convergence that we observe is to the true value of $/\nu$ or to an effective value. With the accuracy that we achieved, it is possible that systematic errors cannot be hidden be the statistical error anymore. This seems to be obvious at the isotropic point, where we observe convergence in L_{min}, but the final estimate of $1/\nu$ is far from the expected value 3/2. A deviation that can be explained by the presence of logarithmic corrections. Generally, the neglect of corrections to FSS will produce effective estimates of $(1/\nu)_{\mathcal{O}}$ and the effective estimates of the individual observables do not need to be the same. The attempt to squeeze potentially different effective values onto a single final estimate may fail, the failure being revealed by the covariance-weighted mean.

In most cases, we were able to eliminate the discrepancies by deliberately excluding more and more chain lengths that enter the crosscorrleation analysis. The increased error estimates ultimately lead to agreement between covariance-weighted and error-weighted mean. Similarly, we could achieve better agreement by using the subtraction method instead of double-log linear fits. Whatever we tried in that sense, amounted essentially to a blowup of errors until unintuitive discrepancies were removed.

Both, the error-weighted and the covariance-weighted final estimate of $1/\nu$ are shown in Fig. 8.16 as function of the anisotropy parameter Δ. The numbers, that represent the final result of this section, are listed in Table 8.4. Lists of individual estimates are put into the appendix (Tables B.13 and B.20). We compare to the known exact result of the spin-$\frac{1}{2}$ chain, and find a qualitatively similar behaviour, but quantitatively the decrease of $1/\nu$, i.e. the increase of ν, is enhanced in both mixed spin chains. Comparing to $1/\nu$ obtained from γ/ν by Gaussian scaling relations, we find a remarkable qualitative agreement. For MA we see that covariance-weighted and error-weighted mean embrace the value from γ/ν in the region $0.6 \leq \Delta \leq 0.9$, while for MB the covariance-weighted does satisfy the scaling relation indeed better than the error-weighted mean in the same Δ-region. However, a satisfaction of the Gaussian scaling relation,

$$\frac{1}{\nu} = 2 - \frac{1}{4 - 2\frac{\gamma}{\nu}}\,, \tag{8.14}$$

could not consistently be found within our statistical accuracy, in particular at larger values of Δ. In MB at $\Delta = 0.1$, the estimate lies visibly far off from what it is expected. We attribute this to the low quality of data. With MB at $\Delta = 0$ re-run, it is the point $\Delta = 0.1$ of MB, that sports the datasets of lowest quality used in the final analysis of this thesis.

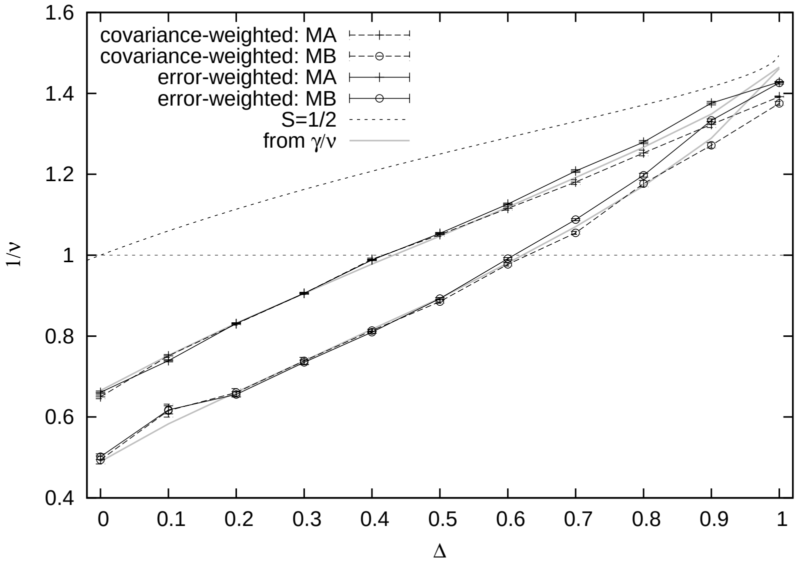

Figure 8.16: Final estimates of the critical exponent ratio $1/\nu$. The dashed curve shows the exactly known $1/\nu$ of spin-$\frac{1}{2}$ chain. The dashed horizontal line marks the pure XY-point of the spin-$\frac{1}{2}$ chain, where $1/\nu = 1$. The full grey line shows the values of $1/\nu$ as expected from conversion of γ/ν via (8.14).

Table 8.4: Final comparison of estimates of the critical exponent ratio $1/\nu$. The indices denote error-weighted (e) and covariance-weighted (c) mean.

	MA		MB	
Δ	$(1/\nu)_\mathrm{e}$	$(1/\nu)_\mathrm{c}$	$(1/\nu)_\mathrm{e}$	$(1/\nu)_\mathrm{c}$
0.0	0.661(4)	0.650(5)	0.502(7)	0.494(10)
0.1	0.739(3)	0.751(4)	0.618(11)	0.616(17)
0.2	0.831(2)	0.830(3)	0.656(7)	0.661(10)
0.3	0.906(2)	0.906(3)	0.735(6)	0.739(9)
0.4	0.988(2)	0.990(4)	0.809(3)	0.814(4)
0.5	1.054(3)	1.051(4)	0.893(3)	0.885(5)
0.6	1.126(3)	1.116(4)	0.991(3)	0.977(5)
0.7	1.208(4)	1.181(6)	1.088(3)	1.055(4)
0.8	1.280(5)	1.253(8)	1.198(5)	1.177(8)
0.9	1.376(5)	1.323(8)	1.333(4)	1.272(7)
1.0	1.428(2)	1.392(2)	1.426(4)	1.375(5)

8.3 α/ν

The specific heat is usually defined via the change of the internal energy with the temperature. Here, in the finite-size simulation of a quantum phase transition, the total energy stored in λ-bonds, given by the λ-derivative of the free energy F, i.e. $\lambda\,\mathrm{d}F/\mathrm{d}\lambda = \lambda\Delta\langle E_\lambda\rangle + \langle n_\lambda\rangle/\beta$, can be interpreted as "internal energy" with respect to the "thermal" control parameter λ. Thus, a suitable volume specific heat c_λ, of a chain of length L at finite inverse temperature β, can be defined and measured via

$$
\begin{aligned}
-Lc_\lambda &= \frac{\mathrm{d}}{\mathrm{d}\lambda}\left[\lambda\frac{\mathrm{d}F}{\mathrm{d}\lambda}\right] \\
&= \langle\tilde{E}_\lambda\rangle + \lambda\beta(\langle\tilde{E}_\lambda\rangle^2 - \langle\tilde{E}_\lambda^2\rangle) - 2(\langle n_\lambda\rangle\langle\tilde{E}_\lambda\rangle - \langle n_\lambda\tilde{E}_\lambda\rangle) + \frac{\langle n_\lambda\rangle^2 - \langle n_\lambda^2\rangle}{\lambda\beta}\,, \qquad (8.15)
\end{aligned}
$$

where $\tilde{E}_\lambda = \lambda\Delta E_\lambda$, is the diagonal energy stored in λ-bonds, and n_λ is the number of jumps on λ-bonds (see Sect. 6.2). Equation (8.15) combines the exepctation values of several observables. Each estimator thereof contributes its share to the statistical error estimate of c_λ. In order to perform a FSS analysis that permits to extract the exponent α/ν, we reweighted the specific heat to our estimates of critical points $\lambda_\mathrm{c}(\Delta)$.

The finite-size behaviour of the specific heat, reweighted to the critical point, is shown in Figs. 8.17a and 8.18a for MA and MB, respectively. In both models, clearly divergent datasets appear for large Δ, while for small Δ datasets *converge*. This means that α/ν is negative in those cases. This is in perfect qualitative agreement with hyperscaling, which predicts that $\alpha/\nu = 2/\nu - 2$. With $1/\nu$ decreasing from $1/\nu \approx 3/2$ at the isotropic point to some $1/\nu \approx 0.6$ at $\Delta = 0$, α/ν must change sign at some value of Δ. Converging datasets converge to the background B, and we must assume a sizeable background also in the diverging datasets. A weak signal in combination with a significant background is a common feature of the specific heat in many models.

We exclusively present results of non-linear three-parameter fits to a single power-law with background in this section. The output is listed in Tables B.14 and B.21 in the appendix, and a compressed version is shown in Table 8.7 at the end of this section. Where possible, we compared results to the output of the subtraction method and found no significant differences, with, however, the significant difference that the background is not computed. Furthermore, it should be obvious from the datasets that subtracting $c_{\lambda,L}$ from $c_{\lambda,2L}$ substantially increases the error at small Δ.

Due to the weak signal at small Δ we did not enjoy the luxury to arbitrarily raise L_min (see Figs. 8.17b and 8.18b). Corresponding fits quickly produce extremely large errors. For MB at $\Delta = 0$, for example, this means that we had to use *all* ($L = 8, \ldots, 256$) datapoints to estimate α/ν. Remarkably the value is in good agreement with the expectation from calculating α/ν from γ/ν obtained in Sect. 8.1. The "optimal" estimate of α/ν for MB at $\Delta = 0$ thus strongly depends on the finite-size value of the specific heat in the particularly short chain with $L = 8$. The long chains essentially and merely fix the background. To resolve the small range of values we would have to at least have doubled accuracy, implying roughly four times longer data series. Similar but not as limiting considerations apply to the other converging datasets in both models.

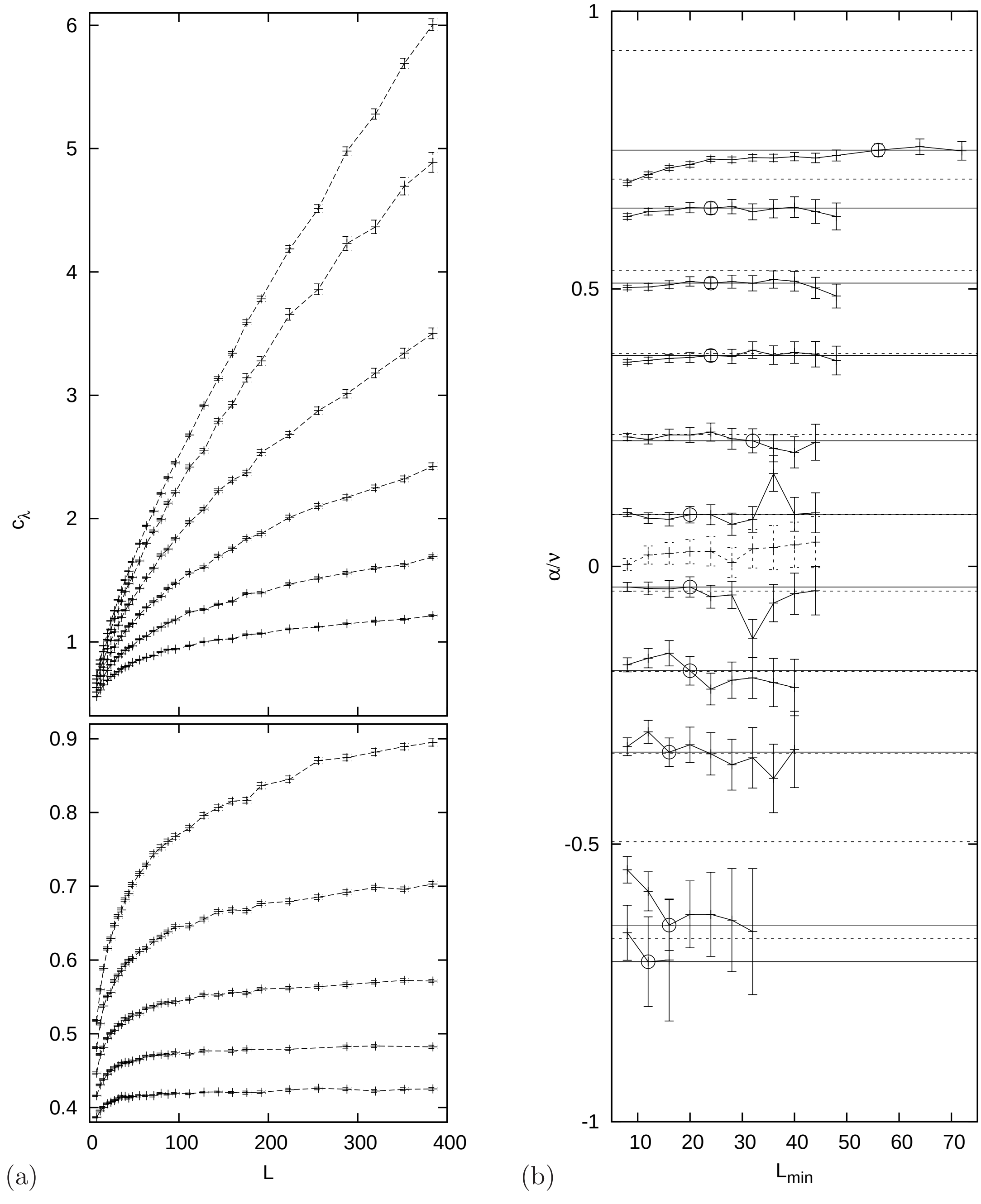

Figure 8.17: MA, FSS analysis of the volume specific heat, c_λ. (**a**) FSS behaviour at the critical point $\lambda_c(\Delta)$. (**b**) $L_{\min}$-dependence of the final estimate of β_z/ν from power-law fits. For all Δ, $L_{\max} = 384$. An extra dataset (connected by dashed lines shows the results of power-law fits with the exponent initially set to a positive value. Datasets correspond to $\Delta = 0 \ldots 1$ from bottom to top.

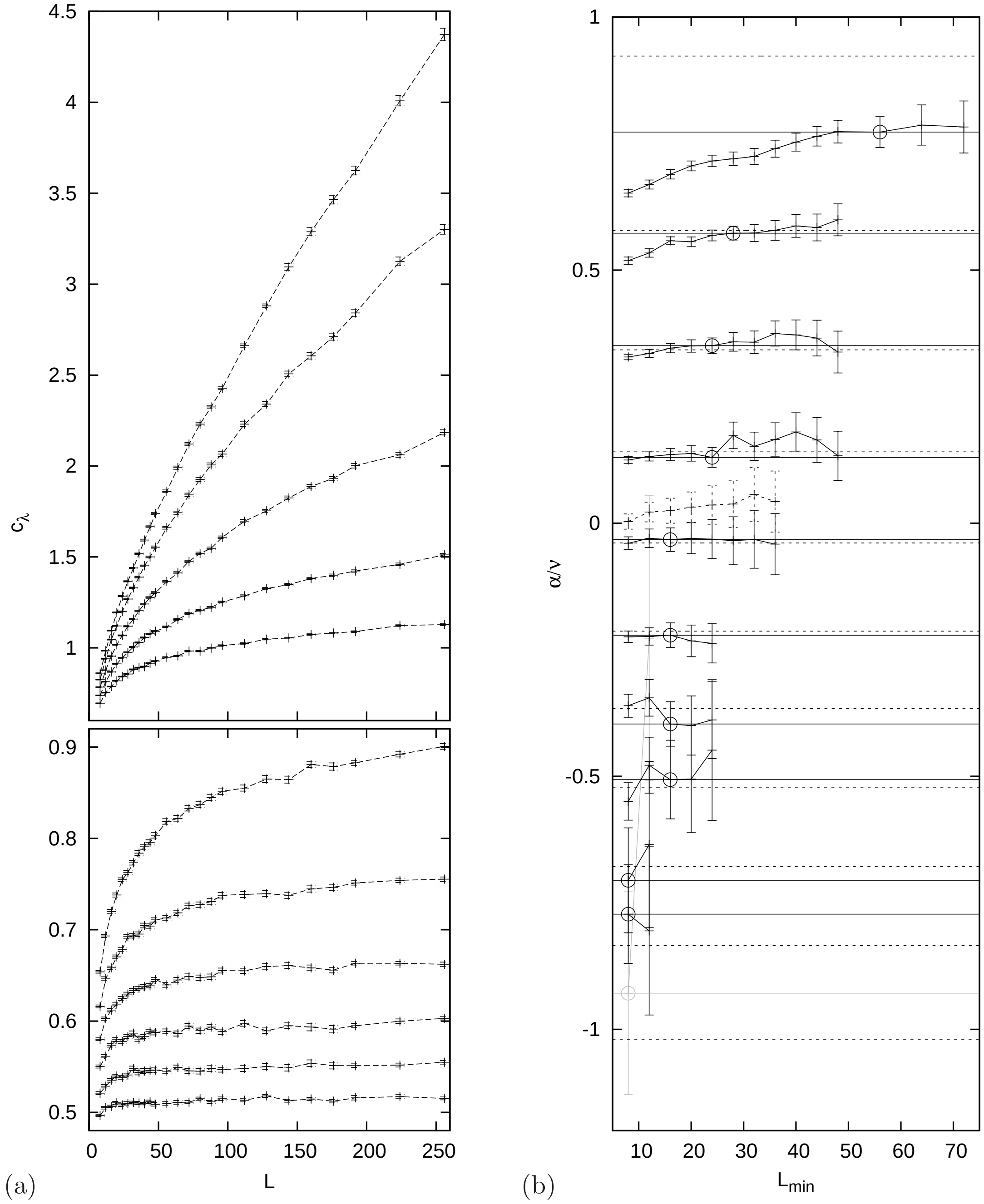

Figure 8.18: Same as Fig. 8.17 but for MB. Two datapoints for $\Delta = 0$ in (**b**) are plotted in grey for better visibility against the neighbouring datasets. $L_{\max} = 256$ for all Δ.

Table 8.5: MA at $\Delta = 0.4$. Comparison of different fits. A fit to a power-law with the initial value of α/ν negative and positive, symbolized by $B + AL^{\pm|\alpha/\nu|}$, and a fit to a logarithmic divergence, $B + A \ln L$.

fit to	Δ	L_{min}	B	A	α/ν	dof	χ^2/dof
$B+AL^{-\lvert\alpha/\nu\rvert}$	0.4	20	3.4(1.3)	−3.08(1.3)	−0.04(2)	23	0.96
$B+A\ln L$	0.4	20	0.324(4)	0.097(1)		24	1.03
$B+A\ln L$	0.4	44	0.334(6)	0.095(2)		18	0.92
$B+AL^{+\lvert\alpha/\nu\rvert}$	0.4	20	−2.9(3.0)	3.26(3.0)	0.027(22)	23	1.37

Table 8.6: Same as Table 8.5 but for MB at $\Delta = 0.6$.

fit to	Δ	L_{min}	B	A	α/ν	dof	χ^2/dof
$B+AL^{-\lvert\alpha/\nu\rvert}$	0.6	16	4.7(2.8)	−4.3(2.7)	−0.032(24)	20	1.84
$B+A\ln L$	0.6	16	0.450(5)	0.123(2)		21	1.74
$B+A\ln L$	0.6	44	0.458(10)	0.121(3)		14	1.49
$B+AL^{+\lvert\alpha/\nu\rvert}$	0.6	16	−4.0(4.9)	4.5(4.9)	0.025(25)	20	2.06

At some Δ the exponent ratio α/ν must become zero. We identify this point to be roughly $\Delta = 0.4$ in MA and $\Delta = 0.6$ in MB. There, α/ν assumes very small negative values if the initial value of α/ν in the fits is set negative, which is consistent with the expectation. The power-law fits depend crucially on the sign of the initial value given to α/ν, and if we choose the initial value to be positive we obtain a very small but positive estimate. By objective criteria it would difficult to decide which estimate is better or more correct. The absolute value of α/ν certainly is very small. If $\alpha/\nu = 0$, finite-size series should diverge logarithmically. Both, the data series of MA at $\Delta = 0.4$ and MB at $\Delta = 0.6$ are consistent with a logarithmic divergence, which we tested by a fit to

$$c_{\lambda,L} = B + A \ln L\,. \tag{8.16}$$

Results of the different fits, are listed in Tables 8.5 and 8.6 for comparison. The logarithmic fit is linear in its two fit parameters B and A and we can study the L_{min}-dependence up to larger values than in the power-law case, where we used $L_{\mathrm{min}} = 20(16)$ for MA (MB). For both models we found $L_{\mathrm{min}} = 44$, to give optimal final result which is why these values are added in Tables 8.5 and 8.6.

We conclude this section by plotting our final results in Fig. 8.19. Table 8.7 includes estimates that verify the hyperscaling relation $\alpha = 2-2\nu$, in almost all cases, with the notable exception of MA at $\Delta = 0.1$. Comparison to the value converted from γ/ν,

$$\frac{\alpha}{\nu} = 2 - \frac{2}{4-2\frac{\gamma}{\nu}}\,, \tag{8.17}$$

is included in Fig. 8.19. It shows good to excellent agreement in a central region of Δ-values, with, however, clearly visible discrepancies close to the isotropic point and rather low quality results at the other end of the region of interest.

Table 8.7: Final estimates of the critical exponent ratio α/ν of the volume specific heat c_λ, obtained from non-linear fits to a single power-law, and compared to the prediction from hyperscaling.

	MA		MB	
Δ	α/ν	$2((1/\nu)_\mathrm{c}-1)$	α/ν	$2((1/\nu)_\mathrm{c}-1)$
0.0	−0.71(9)	−0.701(9)	−0.9(3)	−1.013(20)
0.1	−0.65(5)	−0.498(8)	−0.77(10)	−0.768(33)
0.2	−0.33(3)	−0.340(6)	−0.71(11)	−0.679(19)
0.3	−0.19(3)	−0.189(6)	−0.51(8)	−0.522(17)
0.4	−0.04(2)	−0.020(7)	−0.40(5)	−0.373(7)
0.5	0.09(2)	0.102(8)	−0.22(3)	−0.230(9)
0.6	0.23(3)	0.231(8)	−0.032(24)	−0.045(9)
0.7	0.38(2)	0.361(12)	0.13(2)	0.110(8)
0.8	0.510(10)	0.505(15)	0.35(2)	0.354(16)
0.9	0.65(2)	0.646(16)	0.57(2)	0.543(13)
1.0	0.75(2)	0.783(4)	0.77(4)	0.750(10)

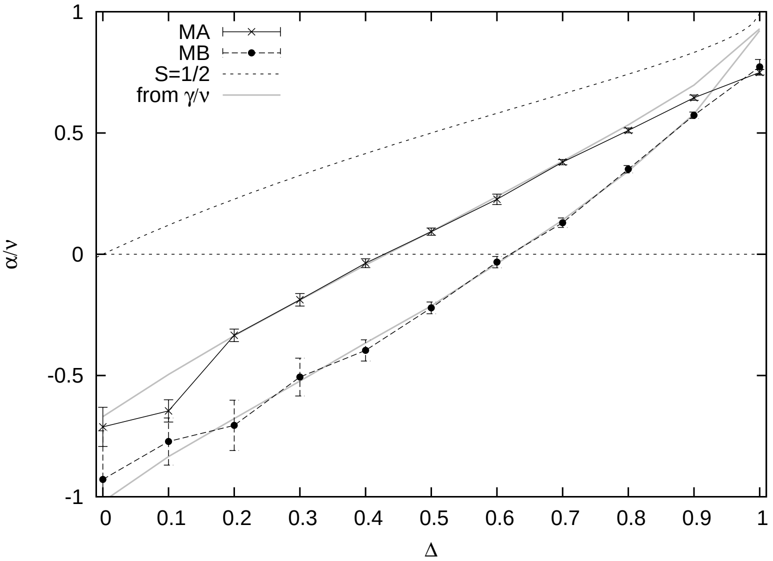

Figure 8.19: Final estimates of the critical exponent ratio α/ν of the volume specific heat c_λ, obtained from non-linear fits to a single power-law. The dashed curves show the exactly known value of α/ν for spin-$\frac{1}{2}$ chain. The dashed horizontal line marks the pure XY-point of the spin-$\frac{1}{2}$ chain, where $\alpha/\nu=0$, for comparison.

8.4 β_z/ν

We interpret the string observables, D_z and D_x, as defined in Sect. 5.4, as order parameters, or depending on the point of view disorder parameters. At the critical point they decrease with the chain length following a power-law behaviour, which results in a corresponding decreasing FSS behaviour $\sim L^{-\beta_{z/x}/\nu}$. Longitudinal and transversal string observables are supposed to have different exponents at $\Delta \neq 1$. In this section, we present the critical exponent ratios β_z/ν of the longitudinal string observable D_z, and some of its moments.

The definition of the observable D_z is a based upon an observable defined for the spin-$\frac{1}{2}$ chain, that itself relates to the polarization of the quantum Ashkin–Teller model (see Sect. 5.4). The polarization of the qAT model has a critical exponent that varies continuously on the Gaussian critical line, which can expressed via the fundamental scaling dimension x_λ, as

$$\frac{\beta_z}{\nu} = \frac{x_\lambda}{4} \,. \tag{8.18}$$

This gives the value to which our results are to be compared.

For a spin chain of length L, the string observable D_z is defined as the average of multi-point functions

$$D_z = \frac{2}{L}\sum_{i=1}^{L/2} D_{z,2i} = \frac{2}{L}\sum_{i=1}^{L/2}\prod_{k=0}^{2i-1}\Sigma_k^z = \frac{2}{L}\sum_{i=1}^{L/2}\prod_{k=0}^{2i-1}\prod_{j=1}^{2S_k}\mathrm{i}\sigma_{k,j}^z \,. \tag{8.19}$$

$D_{z,i}$ is a special multi-point function defined in terms of subspins, which has been expanded above for reference, and the $\sigma_{i,j}^z$ represent the Pauli matrices of subspins, or normalized subspin-variables that take the values ±1 (see (5.30) in Sect. 5.4). Our final estimates of critical exponent ratios β_z/ν, result from the integrated estimator of D_z (see Sect. 6.2.4). In contrast to the slice estimator, moments of an integrated estimator need to be measured and their time series stored individually. In the following we shall discuss the critical exponents of four different “moments”, that of the absolute value $|D_z|$ as well as that of D_z itself, D_z^2 and D_z^4. The critical exponents are labelled by superscripts $\beta_z^{(0)}$, $\beta_z^{(1)} \equiv \beta_z$, $\beta_z^{(2)}$ and $\beta_z^{(4)}$, respectively.

We made two interesting observations in the analysis of D_z and its moments:

1. Presence of seriously strong subleading corrections to FSS in both models, in particular for $\Delta \leq 0.8$. It turned out that most of the datasets could be very well modelled using an additive correction term in L^{-1}, i.e. fitting, instead of (8.1), to

$$\mathcal{O}_L = AL^{\rho/\nu} + CL^{-1} \,, \tag{8.20}$$

with C the amplitude of the L^{-1}-correction. Due to larger errors we could have easily overlooked these effects if we had used the slice estimator of the string observables in the following analysis.

2. Our data strongly suggests that

   $$\beta_z = \beta_z^{(2)}\,, \tag{8.21}$$

   but β_z comes out twice as large as expected, which is in disagreement with what has been found for the spin-$\frac{1}{2}$ chain [132, 147, 148]. It is the critical exponent ratio $\beta_z^{(0)}/\nu$, of the absolute value of the order parameter, that is closest to the expected value. Moreover, our analysis suggests that $\beta_z^{(4)} \approx 2\beta_z$.

Two examples of the observables' datasets (the values at our estimates of the critical point) are shown in Fig. 8.20a and Fig. 8.21a. Results of double-log linear fits exhibited a strong dependence on the minimum chain length L_{min}, which is shown by the datapoints connected by full lines in Figs. 8.20b and 8.21b. First of all, unlike in the previous analyses of the other exponent ratios, we would not have been able to deliberately choose "optimal" estimates that match our expectation, in most cases. A fact, that is particularly obvious and severe at $\Delta = 0$ in both models. Second, we faced a serious difficulty in choosing a final optimal estimate of $\beta_z^{(i)}/\nu$ at all. In many cases the drift with L_{min} cannot be seen to have come to an end even at $L_{\text{min}} = 160$, where the estimates of MA were obtained from linear fits to a total of nine datapoints, and those of MB from fits to five datapoints. We thus concluded that the leading power-law behaviour must be modified by a significant correction term. But already in the results of simple double-log linear fits, we observed the following relations

$$2\beta_z^{(0)} \approx \beta_z \approx \beta_z^{(2)} \approx \beta_z^{(4)}/2\,, \tag{8.22}$$

where the central part was matched best in our data, while the outer approximate relations remained conjectures at this stage.

We shall briefly comment on our first attempts to treat the strong corrections to FSS before discussing and interpreting our final results from fits to (8.20). A more detailed account of the "alternative" methods is given in Sect. C in the appendix. In addition to the usual suspects, background and subleading corrections, that subvert standard double-log linear fits we faced here yet another candidate, a slightly wrong estimate of the critical point.[2] Underestimation of the critical point would lead to a small and positive background, however, an effective background that we could extract from simple power-law fits to (8.1) turned out to be small but *negative*. To consider subleading power-law corrections to FSS, controlled by an (effective) correction exponent ω, we fitted our data to $AL^{-\beta_z/\nu}(1+CL^{-\omega})$, which indeed lead to significantly better match of results and expected values and, furthermore, to an improved satisfaction of (8.22) for all moments of the observable. Application of the *quotients* method [253] lead to our estimates of ω. Figure 8.22 shows these estimates and illustrates our attempt to associate the values with a source, either analytic or non-analytic corrections to FSS. Surprisingly, we found that ω roughly seems to follow $-1/(2\nu)$. Another candidate that seems to fit even better and is included in Fig. 8.22, is $2(y_{1,0} - 2) = -1/(2x_{0,2})$, which is twice the correction exponent that could be generated by a descendant of level 2 of the relevant primary scaling operator with RG eigenvalue $y_{1,0}$ (see Sects. 4

---

[2] Which is, of course, also a source of errors in our determination of $1/\nu$ and α/ν, where we have checked that it is not of significance.

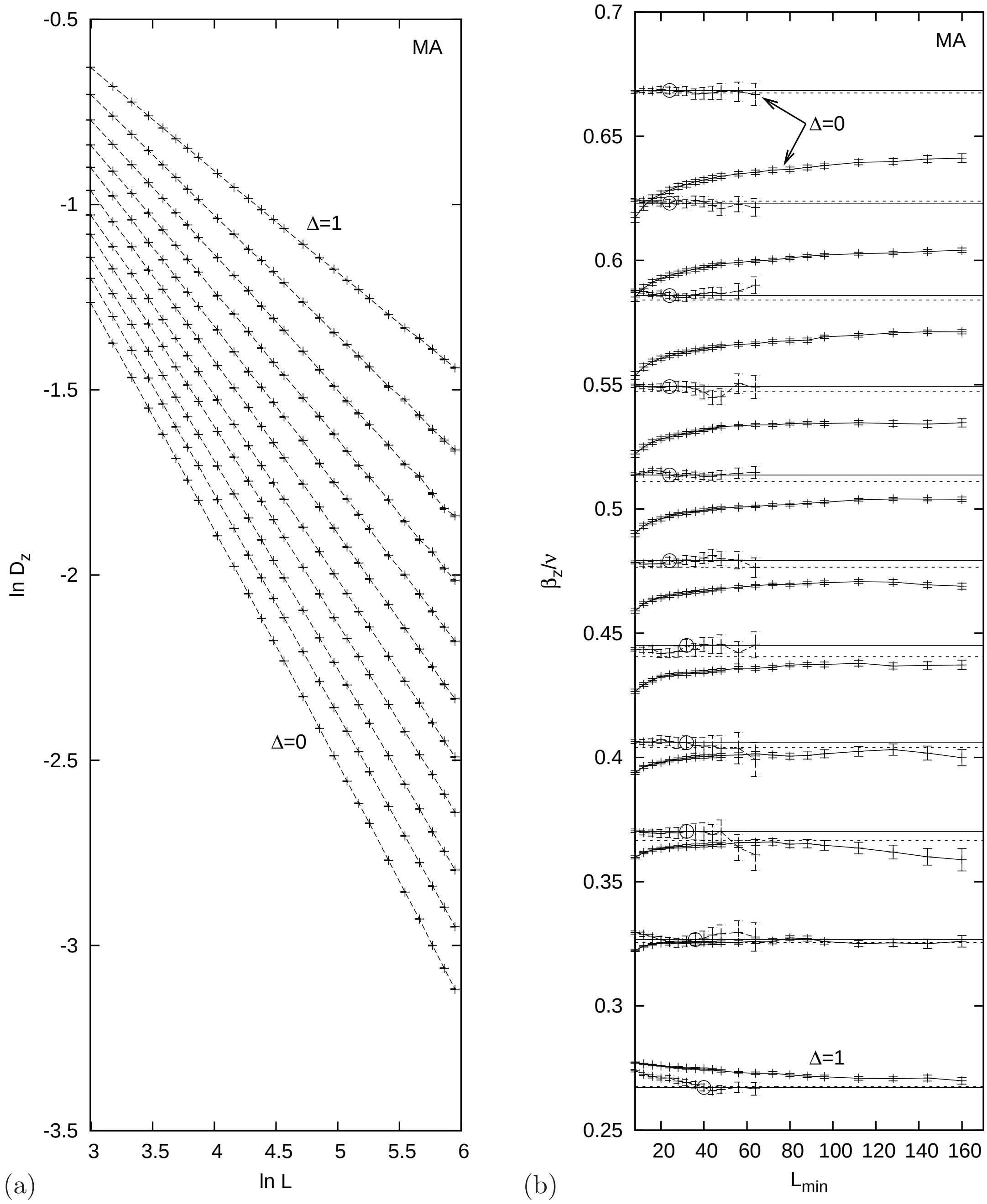

Figure 8.20: MA, FSS analysis of D_z. (**a**) FSS behaviour at the critical point $\lambda_c(\Delta)$. (**b**) $L_{\min}$-dependence of the final estimate of β_z/ν from double-log linear fits. For all Δ, $L_{\max} = 384$. Results of double-log linear fits (datapoints connected by full lines) are compared to results of fits to (8.20), which includes an additive correction in L^{-1}.

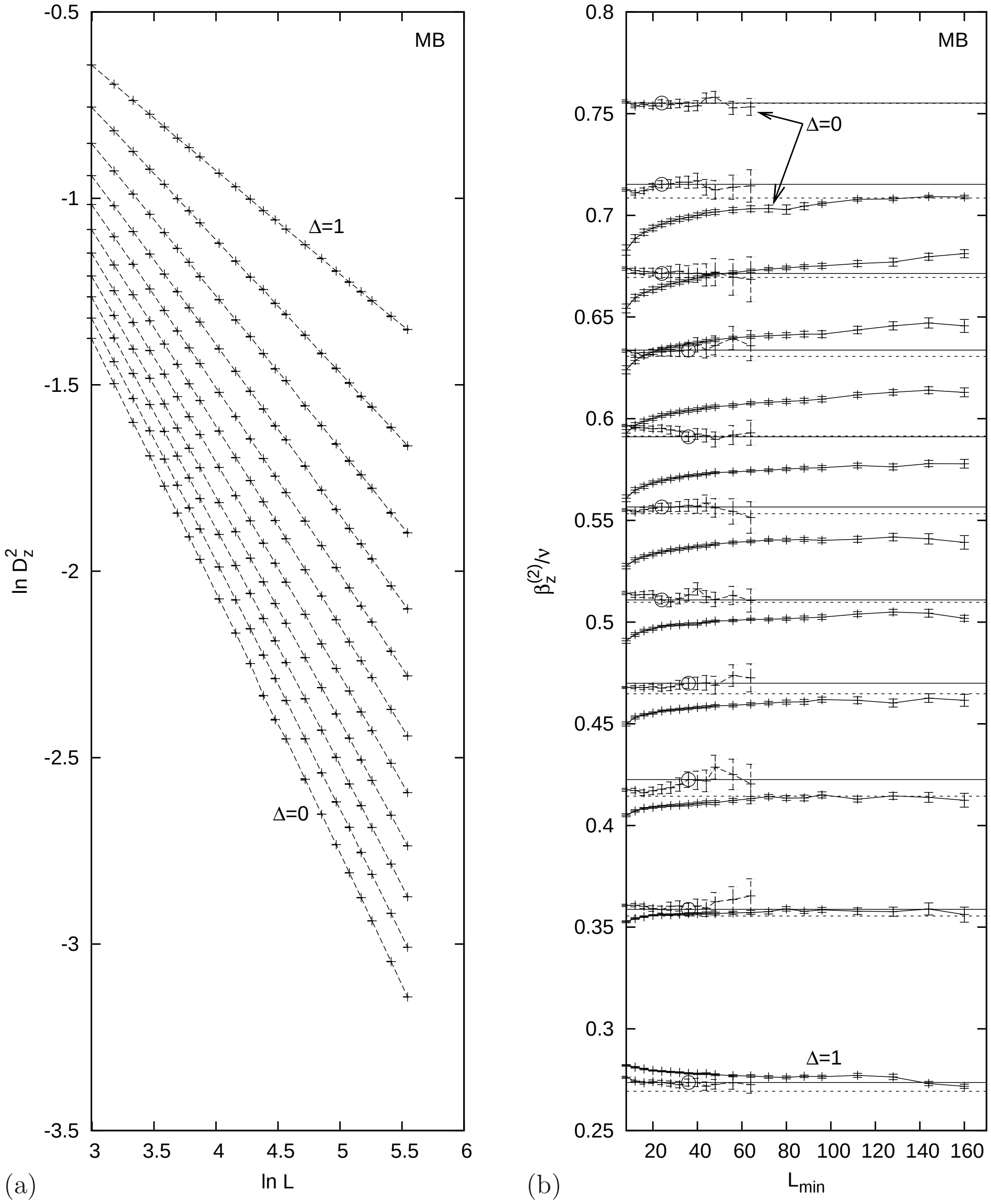

Figure 8.21: Same as Fig. 8.20, but for D_z^2 of MB.

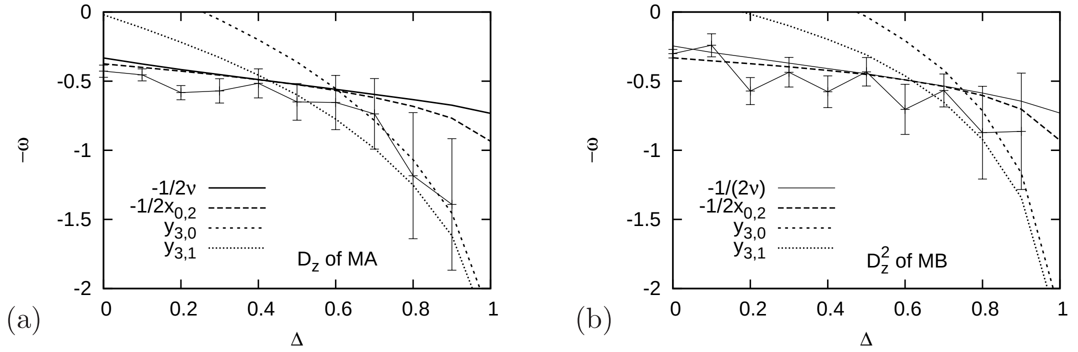

Figure 8.22: The effective correction exponent ω of D_z in comparison to some irrelevant RG eigenvalues (calculated using the estimates of γ/ν from Sect. 8.1) that lead to non-analytic corrections, $-1/(2\nu)$, and $2(y_{1,0}-2) = -1/(2x_{0,2})$.

and 6.4). Any other candidates are nowhere near our estimates. We are not aware of a mechanism that would generate the former, i.e. power-law corrections in $L^{-1/(2\nu)}$, but with $1/\nu = 2 - x_\lambda$, and $\beta_z/\nu = x_\lambda/2$, it follows that

$$-\frac{1}{2\nu} - \frac{\beta_z}{\nu} = -1\,, \tag{8.23}$$

which lead us to try fits to the above stated form (8.20).

The fits to (8.20) give reasonable values of χ^2 for all datasets and the results for β_z/ν included in Figs. 8.20b and 8.21b, as datapoints connected by dashed lines. The strong L_{min}-dependence, that was present in double-log linear fits, is almost completely removed, but even more striking is the "miraculous jump" of the outcome to values that match the expected ones (shown as dashed horizontal lines in Figs. 8.20b and 8.21b), in particular for the smaller values of Δ, where the mismatch was the worst. The improvement in matching scaling relations, however, is not consistent throughout all values of Δ. For MB at $\Delta = 0.7, 0.8$ and 0.9, results of double-log linear fits would be compatible with was is expected and at $\Delta = 0.8$ (third set from below in Fig. 8.21b) even better. Certainly, the corresponding datasets of MB (but also of MA) would deserve more attention. Nonetheless, we consider the success of fits to (8.20) remarkable and significant. A special point is $\Delta = 1$, where convergence in L_{min} could be, up to some minor discrepancies, concluded for both methods and models. But results are still far off from our modified expectation, $\beta_z/\nu = 1/4$. We blame, again, the possible presence of logarithmic corrections for this mismatch and consider the convergence as pseudo-convergence to some effective value. The exponent of the logarithmic modification in the FSS scaling behaviour of the qAT polarization is negative. Assuming a pure power-law would result in slightly overestimated values of β_z/ν, which is in agreement with our result that $\beta_z/\nu \approx 0.27$, in both models.

What our results show, in fact, is that it is possible to perform reasonable fits to (8.20) and to obtain results matching our expectations thereby. We remark here, that using $\omega = -1/(2x_{0,2})$, instead of $\omega = -1/(2\nu)$, would, of course, lead to very similar "improvement" of results, however, in order to fix the value $\omega = -1/(2x_{0,2})$, we would have to use our own estimates converted, e.g., from γ/ν, whereas fixing

$\omega = -1/(2\nu)$ automatically leads to the additive L^{-1}-correction. For our attempt to numerically prove the Gaussian nature of mixed spin models, MA and MB, and to associate the critical behaviour to the breaking of a hidden $Z_2 \times Z_2$ symmetry, this is unsatisfactory. Based on the data shown in Fig. 8.22, it may seem adventurous to conclude upon the correction exponent to be $\omega = 1/(2\nu)$. But, as mentioned in other parts of this thesis, the treatment of corrections to FSS is difficult [242]. The subleading effects need considerably more accurate data (or *a priori* knowledge) in order to be resolved unambiguously. It is very likely that, from the large set of candidates, other correction terms are also present and modify the single correction exponent ω to become an effective one. It is the data contained in Figs. 8.20b and 8.21b that we relied upon. In large parts of the Δ-region it was impossible to obtain final estimates of β_z/ν from double-log linear fits, we thus were forced to invoke the effective correction exponent ω, which was first treated as a free parameter and then set to a fixed value, the results of the latter treatment being our "optimal" final results.

We cannot come up with a conclusive explanation for the presence of the $L^{-1/(2\nu)}$-correction. Analytic corrections to FSS generate integer powers of $L^{-1/(2\nu)}$, but not half-integer ones. We have checked that the Gaussian operator content, of which a part is shown in Fig. 8.22, does not provide further candidates, neither primary nor secondary operators, with a suitable RG eigenvalue, other than the aforementioned one. Remains the non-Gaussian part of the operator content of the qAT model with constant RG eigenvalues. It is also known exactly [25, 159] and we explored it rather superficially without success. Furthermore, the inspection of finite-size spectra (see Sect. 10) did not not reveal the presence of constant levels in the appropriate energy range. Triggered by the second main observation, that $\beta_z = \beta_z^{(2)}$, however, we questioned the very definition of string observable D_z, itself. We found indeed a sub-optimal feature, that does generate an additive term in L^{-1}. In Sect. C we yet argue in detail, why this does not explain our observations either. The argument shall be briefly outlined in the following.

Our definition of string observables as stated in (5.31) and (8.19) includes the term $D_{z,L}$, which by (5.31) is a string consisting of all (sub)spins the chain has to offer. The groundstate of our models are singlets and located in the sector of zero magnetization. It is easy to calculate that in this case $\langle D_{z,L} \rangle = 1$, always. Thus, in every measurement according to (8.19), the constant 1 is added. With the normalizing factor $2/L$ in (8.19), the "constant" becomes size dependent and generates an additive term $\sim L^{-1}$, in every measurement. While this seems like a rather complicated backdoor to identifying sub-optimal, or even wrong definition, of the string observable, this term, that is present by definition, cannot explain our data on its own. Adding $1/L$ in every measurement can only lead to an additive "correction" in FSS with a positive amplitude C. The amplitude that we estimated, however, on the basis of fits to (8.20) is *negative* for all datasets. And even though, our argument is a bit more involved as presented in Sect. C, this main implication holds. The origin of the strong correction, be it of standard form in $L^{-1/(2\nu)}$ or in the completely equivalent additive form in L^{-1}, remains as yet unexplained.

An interesting aspect of the second observation is that it is possible to directly measure the string observable D_z, which we wish to interpret as (dis)order parameter. Compared to the paradigmatic example of an order parameter, the magnetization

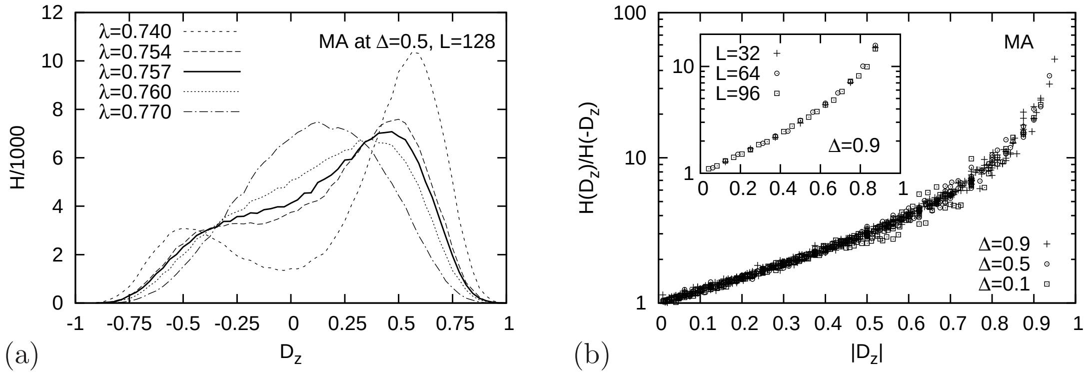

Figure 8.23: (**a**) Asymmetric distribution $H(D_z)$, of the transversal string observable D_z, for MA at $\Delta = 0.5$ and a chain length $L = 128$. Shown are distributions at different values of the bond alternation parameter λ. Our corresponding estimate of the critical point is $\lambda_c(0.5) = 0.76558(1)$. Below the critical point, the distribution becomes symmetrically double-peaked. (**b**) The ratio of histogram entries $H(D_z)/H(-D_z)$, does not seem to depend on Δ or the chain length L. The ratio is plotted for the indicated values of Δ but for all simulated chain lengths L. The inset shows a "diluted" version the main plot containing only a few chain lengths.

of a ferromagnet, this is worth to be noted. In finite-size MC simulations in zero magnetic field it is not possible to measure the spontaneous magnetization of the ordered phase directly. The distribution of measured values is symmetric and results in a zero mean. In the ordered phase, however, the distribution is double-peaked, which is the finite-size relict of the Z_2 symmetry breaking. Consequently, one has to measure the absolute value of the finite-size magnetization in order to study critical properties. The distribution of measured values is *asymmetric*, as shown in Fig. 8.23a. The asymmetric distribution is less surprising, if one considers the extreme limit $\lambda = 0$, where the spin chains decouple into isolated dimers, which are made up of like spins in our parameterization (λ controls the coupling between spins of different size). The terms in the sum of D_z contain, in fact, only complete dimers. In the groundstate each dimer is in a singlet state. The groundstate of the total chain is a direct product of local singlets and only those basis state that satisfy the local singlet constraint contribute. It follows immediately that in that case $D_z = 1$, in every basis state that contributes. Thus, at $\lambda = 0$, the distribution is extremely asymmetric and "sharply" peaked, permitting only one single value to be measured in the groundstate. Introducing a small $\lambda \neq 0$, the local singlet constraint is relaxed and further basis states, that still must have zero total magnetization but do not necessarily deliver $D_z = 1$ in a measurement, contribute to the groundstate. The extreme single-valued distribution deforms smoothly to become the asymmetric distribution shown in Fig. 8.23a.

In the low-λ region, where in the thermodynamic limit $D_z \neq 0$ (which is why we consider it the ordered region with respect to D_z), the distribution is double-peaked but still asymmetric. This can be clearly seen in Fig. 8.23. This is the reason why it is possible to measure and analyse D_z directly. Technically, we also consider this to be closely related to observation 2, that $\beta_z = \beta_z^{(2)}$. Our data, however, not only suggests equality of critical exponents, but also of the corresponding observables themselves, i.e. we found that $\langle D_z \rangle \approx \langle D_z^2 \rangle$ in QMC simulations. We have tested this feature for $L = 16$ in the spin-$\frac{1}{2}$ chain, $L = 12$ in MA, and $L = 8$ in MB, by ED calculations, which perfectly confirm that $\langle D_z \rangle = \langle D_z^2 \rangle$. The analysis further showed, that the ratio of histogram entries $H(D_z)/H(-D_z)$, assumes values that are independent of the the control parameters λ and Δ, and the chain length L (see Fig. 8.23). The reasons for this can be found in the peculiar asymmetric accumulation of strings in the definition of D_z, the translational symmetry of the models, and, most fundamentally, in the combinatorics of what measurement the basis states do actually contribute to the expectation value of D_z. While it is straightforward to verify, that for example there are $(L/2 - 1)$ times more basis states of the spin-$\frac{1}{2}$ chain that deliver $D_z = (L/2 - 2)$, than basis states that deliver $D_z = -(L/2 - 2)$, the combinatorics involved is considerably more complicated in the mixed spin models, and in particular for other possible values of D_z in a basis state. The observation, that the ratio $H(D_z)/H(-D_z)$ is independent of the control parameters, indicates, that it is, in fact, independent of the coefficients of basis states in the groundstate. It is further simple to show, that the value of $|D_z|$ that a basis state delivers is invariant under translation. In the groundstate the momentum is zero, and, consequently all basis states that can be translated into each other contribute with to the groundstate with same amplitude. Following this discussion further would put severe restrictions on the distribution which could be exploited in further analyses. We shall leave this subject to future work.

The main results of this section on the exponent ratio β_z/ν, are summarized in Table 8.8 and Fig. 8.24. For a more detailed exposition of some of the points made in this section, the reader shall be referred to Sect. C. Table 8.8 compares the values of β_z and $\beta_z^{(2)}$, while Fig. 8.24 compares the final results to the values expected via conversion from γ/ν and the corresponding exactly known values of the qAT model, respectively the spin-$\frac{1}{2}$ chain. The grey shaded regions indicate the variation of results when our estimates of the critical points are varied by one and three error bars. The influence of the precise value of the critical point is visibly stronger at the larger values of Δ. The insets in Fig. 8.24 account for our observation that $\beta_z = \beta_z^{(2)}$ and its extended form given in (8.22), which seems to be satisfied by our results within 2–3%. The exponent ratio $\beta_z^{(0)}/\nu$ of $|D_z|$ has been obtained exactly along the same lines as β_z/ν and $\beta_z^{(0)}/\nu$. However, it is very likely that, even though results are reasonable, the fit to (8.20) is not appropriate for the finite-size behaviour of the absolute value of D_z. Quite in contrast, the exponent ratio $\beta_z^{(0)}/\nu$ of D_z^4 could not be obtained from fits to (8.20), which did not yield reasonable results, but to the *square* of (8.20). It is shown in Sect. C, that by use of the quotients method, the outer parts of (8.22), i.e. that $2\beta_z^{(0)} = \beta_z$ and $\beta_z^{(4)}/2 = \beta_z$, hold even slightly better (see Figs. C.5b and C.5b in the appendix). However, considering the difficulties discussed in this section we consider (8.22) to hold as exact equalities a *conjecture*.

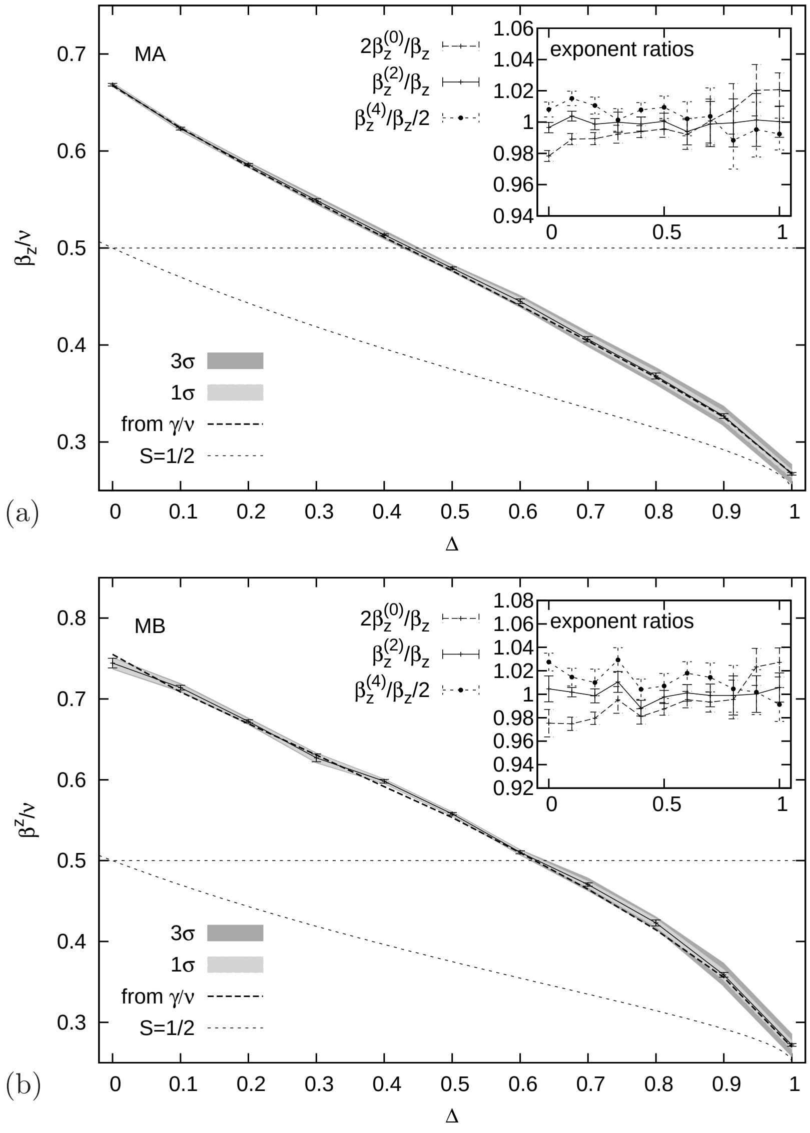

Figure 8.24: Final estimates of the critical exponent ratio β_z/ν of the longitudinal string observable D_z. Dashed curves show the exact value of β_z/ν for spin-$\frac{1}{2}$ chain (see main text). Dashed horizontal lines mark the pure XY-point of the spin-$\frac{1}{2}$ chain for comparison. The insets compare the exponents of the moments $|D_z|$, D_z^2 and D_z^4 to that of D_z itself.

Table 8.8: Final results of the critical exponent ratios of the transversal string observable D_z and D_z^2. Results are obtained from fits to (8.20).

	MA		MB	
Δ	β_z/ν	$\beta_z^{(2)}/\nu$	β_z/ν	$\beta_z^{(2)}/\nu$
0.0	0.6684(15)	0.6661(13)	0.7443(60)	0.7477(53)
0.1	0.6231(15)	0.6254(12)	0.7140(30)	0.7153(18)
0.2	0.5859(12)	0.5851(10)	0.6723(20)	0.6714(24)
0.3	0.5492(17)	0.5492(20)	0.6271(49)	0.6338(32)
0.4	0.5137(10)	0.5131(14)	0.5982(24)	0.5911(24)
0.5	0.4792(15)	0.4794(13)	0.5579(17)	0.5566(18)
0.6	0.4451(25)	0.4424(20)	0.5103(20)	0.5109(20)
0.7	0.4059(28)	0.4054(30)	0.4704(21)	0.4699(26)
0.8	0.3681(30)	0.3679(28)	0.4230(38)	0.4225(39)
0.9	0.3267(25)	0.3272(27)	0.3587(30)	0.3588(30)
1.0	0.2672(15)	0.2673(13)	0.2720(17)	0.2736(18)

8.5 β_x/ν

Qualitatively the behaviour of the transversal string observable D_x is very similar to that of its longitudinal counterpart D_z. In this section, we present our results for β_x/ν and $\beta_x^{(2)}/\nu$, where the latter denotes the corresponding ratio of the observable D_x^2.

The key to measure the expectation value of a transversal string observable like D_x, is the improved estimator for off-diagonal multi-point functions of n subspins (see Sect. 6.2.4),

$$\left(\sigma_1^x \cdots \sigma_n^x\right)_{\text{imp}} = \begin{cases} (-1)^{n_{\text{sbr}}} & \text{if no loop occurs an odd number of times,} \\ 0 & \text{otherwise,} \end{cases} \tag{8.24}$$

where the σ_i^x represent Pauli matrices of subspins with eigenvalues ±1, and n_{sbr} is the number of subspins affected by the sublattice basis rotation. We evaluate the improved estimator on a single time slice. The estimator of D_x is just the sum of $L/2$ improved estimators, but we cannot then simply take the square of it to get the estimator of D_x^2. The estimator of D_x^2 is the sum of $(L/2)^2$ improved estimators of $(L/2)^2$ multi-point functions. The workload to measure D_x^2 grows with L^2. Symmetries and combinatorics can be used to reduce the workload by a constant factor but the growth rate remains the same. Similarly, the workload to measure, e.g., the moment D_x^4, grows with L^4, which is why we have not measured it.

Our definition of the observable D_x is a based upon an observable defined for the spin-$\frac{1}{2}$ chain, that itself relates to the magnetization of the quantum Ashkin–Teller (qAT) model (see Sect. 5.4). The magnetization of the qAT model has a critical exponent that takes a constant value on the Gaussian critical line, $\beta = 1/12$, or $\beta/\nu = 1/8$ [132, 147, 148]. This is the value to which our results are to be compared. If we look at Fig. 8.25, where we plot the finite-size behaviour of D_x reweighted to our estimates of the critical points, we see on the double-log scale that all data sets have almost the same slope. Moreover, for $\Delta \leq 0.8$ datasets becomes nearly identical on the plotted scale. This is, so far, in perfect agreement with the expectation.

We did not face the the presence of a strong correction in the FSS analysis of D_x and D_x^2, as before for D_z and its moments. However, the improved estimators of transversal string observables were evaluated on a single time slice. Consequently the statistical errors are significantly larger than those of the integrated (unimproved) estimators of longitudinal string observables. The quality of underlying datasets at the smaller values of Δ is not overwhelming, in fact, as was discussed in Sect. 6.3, and it might as well be that the presence of a similar correction term with exponent $1/(2\nu)$ can simply be not resolved. In any case, our results are, apart from MA at $\Delta = 1$ (and $\Delta = 0.9$, in a strict sense) consistent with the assumption of a constant exponent ratio $\beta_x = 1/4$, which is however, again, twice as large as expected. Thus, even if the $L^{-1/(2\nu)}$-correction were present here, it would not be of relevance within the accuracy of the analysis. Conversely, the absence of $L^{-1/(2\nu)}$-corrections would support our argument from above, that the sub-optimal definition of the string observables *cannot be the only* explanation for the strong corrections, because the constant term is also present in measurements of D_x.

An exemplary set of our FSS analyses is shown in Fig. 8.26. As in the case of the longitudinal string observable D_z, the value of the critical exponent ratio β_x/ν that we measure is two times the expected value, i.e. $\beta_x/\nu \approx 1/4$ instead of 1/8. Again, similar to the analysis in the previous section, we find the relation

$$\frac{\beta_x}{\nu} \approx \frac{\beta_x^{(2)}}{\nu}\,, \tag{8.25}$$

to be almost perfectly satisfied, which is why we conjecture it to be an exact equality. This can be seen in Fig. 8.26a–d and in a different way in the insets of Fig. 8.27. The influence of the value of the critical point is exemplary shown in Fig. 8.26e–h and included in the final picture in Fig. 8.27 as errorband in two shades of grey, that indicate the variation of final estimates of β_x/ν, when the estimates of λ_c are varied with one and three errorbars. Numbers that correspond to the final results of Fig. 8.27 are listed in Table 8.9. Further numbers of interest can be found in the appendix.

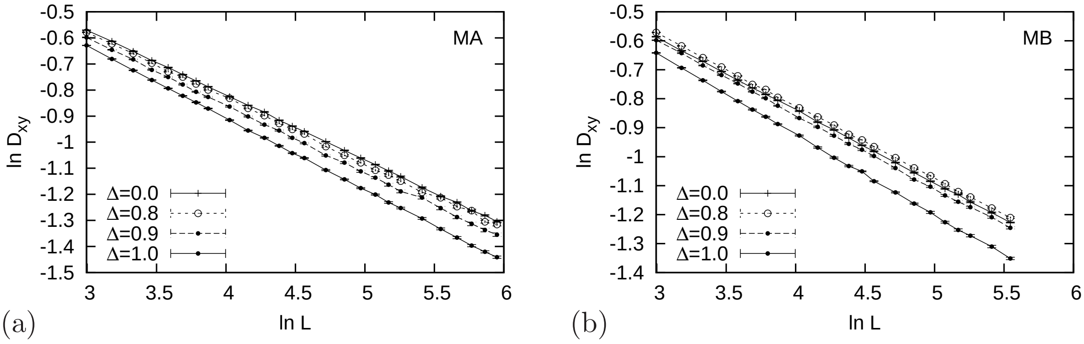

Figure 8.25: Selected examples of datasets that show the finite-size dependence of the transversal string observable D_x at our estimates of the critical points.

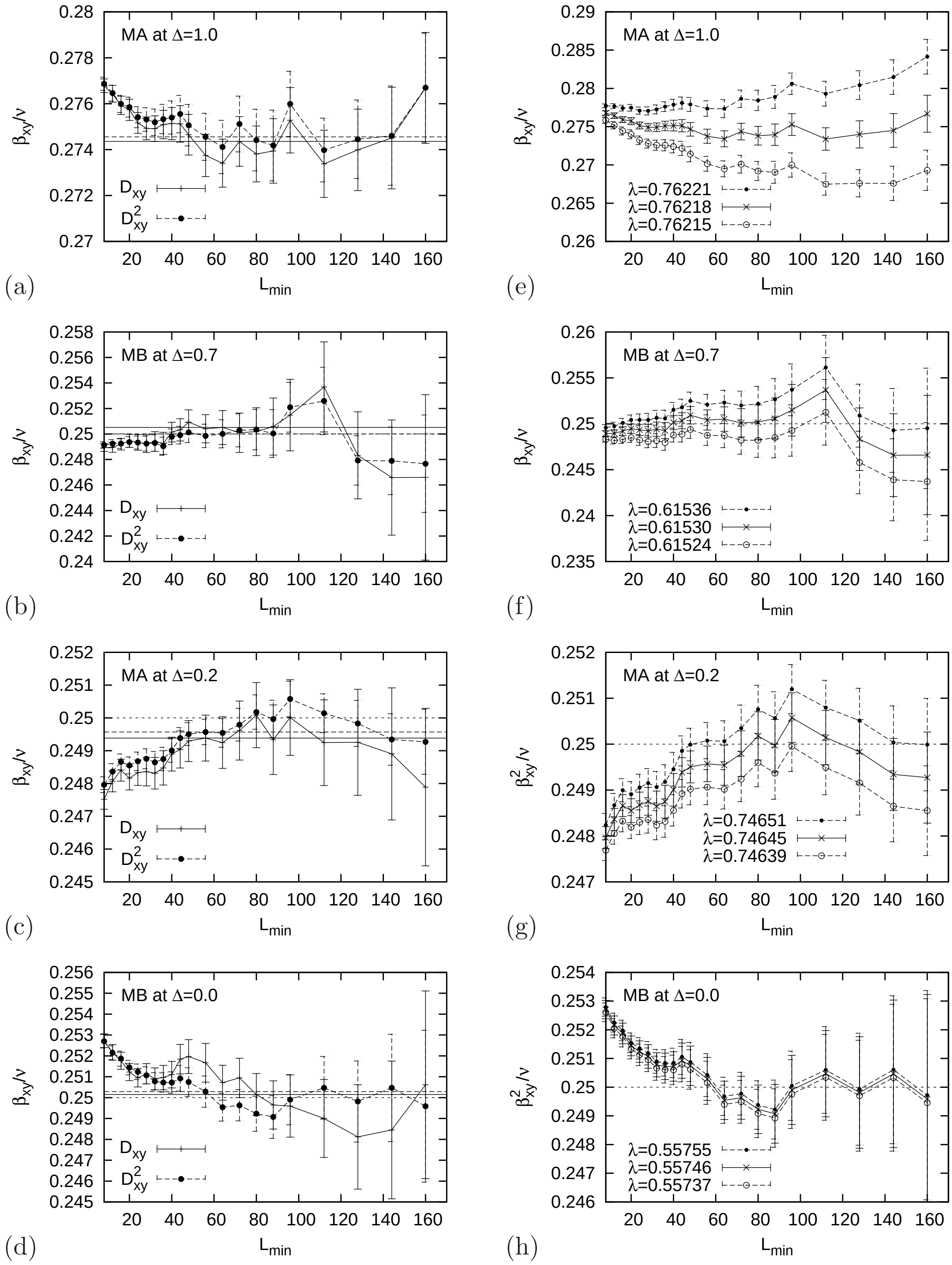

Figure 8.26: Selected examples of the dependence of results on the minimum chain length $L_{\min}$, used in double-log linear FSS fits. (**a**–**d**) Comparison of FSS results of the moments D_x and D_x^2. (**e**–**h**) Comparison of results at different estimates of the critical points, $\lambda = \lambda_c$ and $\lambda = \lambda_c \pm 3\sigma$.

Table 8.9: Final results of the critical exponent ratios β_x/ν and $\beta_x^{(2)}/\nu$, of the transversal string observable D_x and the moment D_x^2, respectively.

	MA		MB	
Δ	β_x/ν	$\beta_x^{(2)}/\nu$	β_x/ν	$\beta_x^{(2)}/\nu$
0.0	0.2494(5)	0.2494(4)	0.2501(11)	0.2503(8)
0.1	0.2499(11)	0.2496(6)	0.2500(9)	0.2506(4)
0.2	0.2494(7)	0.2496(4)	0.2505(11)	0.2501(7)
0.3	0.2506(5)	0.2495(4)	0.2501(6)	0.2495(4)
0.4	0.2494(7)	0.2495(12)	0.2504(6)	0.2500(4)
0.5	0.2496(9)	0.2510(10)	0.2499(9)	0.2494(9)
0.6	0.2469(11)	0.2469(11)	0.2480(13)	0.2487(11)
0.7	0.2502(9)	0.2500(9)	0.2505(14)	0.2500(11)
0.8	0.2515(25)	0.2515(20)	0.2513(13)	0.2510(13)
0.9	0.2559(23)	0.2561(27)	0.2452(43)	0.2498(41)
1.0	0.2744(11)	0.2746(11)	0.2606(73)	0.2631(56)

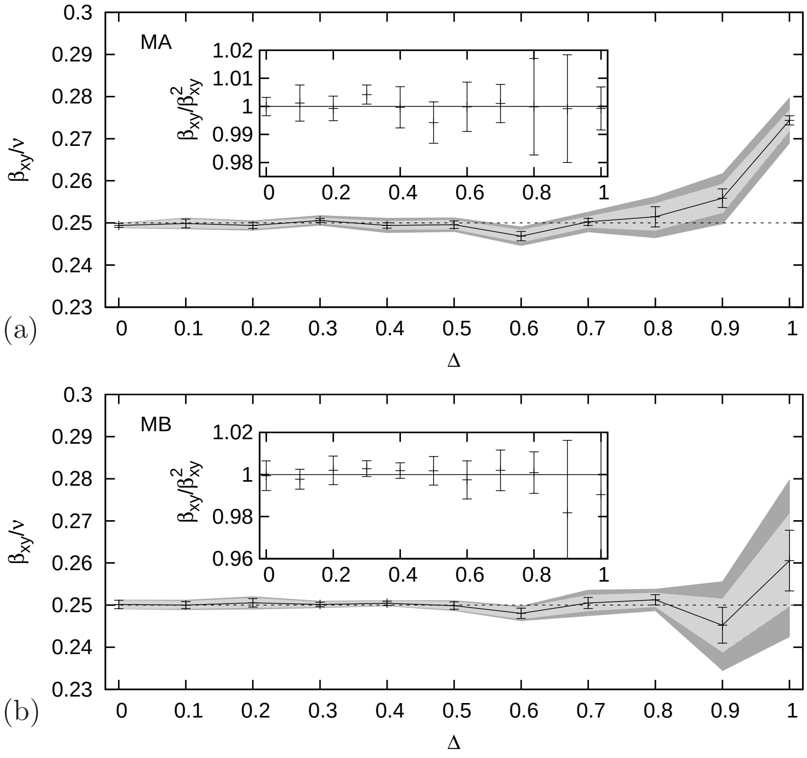

Figure 8.27: Final estimates of the critical exponent ratio β_x/ν of the transversal string observable D_x. Grey regions mark the variation, if our estimates of the critical points are varied by $\pm 1\sigma$ (light-grey) and $\pm 3\sigma$ (dark-grey). Dashed horizontal lines show the exactly known value of the spin-$\frac{1}{2}$ chain, $\beta_x/\nu = 1/4$ (see main text).

8.6 x_λ

We shall check conventional and extended scaling relations by converting all critical exponent ratios measured into the fundamental scaling dimension, x_λ, by

$$x_\lambda = \left(4 - 2\frac{\gamma}{\nu}\right)^{-1} = 2 - \frac{1}{\nu} = 1 - \frac{\alpha}{2\nu} = 2\frac{\beta_z}{\nu}\,. \tag{8.26}$$

This has already been done on-the-fly in the previous sections, therefore the brief but unified presentation in this section can be considered a preliminary summary. Note, that the last equation in (8.26) is not what would be expected from the scaling dimension of the polarization in the qAT model (which would be $x_\lambda = 4\beta_z/\nu$), but what we empirically had to accept in Sect. 8.4. Numerical values that follow from relations (8.26) are listed for a comparison in Tables 8.10 and 8.11, and the result of the first equation in (8.26) is plotted in Fig. 8.28a.

Leaving out the isotropic point we state rough agreement of the different estimates of x_λ within $\approx \pm 5\%$ in both models. Leaving further out $\Delta = 0.9$ in both models (and α/ν of MA at $\Delta = 0.1$), we observe better agreement within ≈ 2 (see the insets of Fig. 8.28b,c). Comparing the estimates of x_λ that are converted from $(1/\nu)_\mathrm{e}$ and $(1/\nu)_\mathrm{c}$, the error-weighted and covariance-weighted mean of our estimates of $1/\nu$, respectively, from Sect. 8.2, we find only a particularly small Δ-region of consistent agreement (see left insets of Fig. 8.28b,c). Even though not being perfectly consistent within errorbars, the estimates obtained from γ/ν and β_z/ν agree to within 1% in MA and 2% in MB (see right insets in Fig. 8.28a,b). This is truly remarkable, considering the fact that we had to treat strong corrections to FSS in that case, as discussed in Sect. 8.4.

In essence, this section illustrates the fact that we have calculated one and the same quantity several times.[3] In Sect. 8.2 we have used the covariance-weighting method to combine five different estimates of the exponent ratio $1/\nu$ and compared it to the error-weighted mean. Strictly speaking, this is what would have to be done also in the case of the scaling dimension x_λ. However, we face a problem here. Our jacknifed implementation of the covariance-weighted mean relies on unweighted fits and works reliably, in fact, only for linear fits. For the performance of non-linear fits, to treat corrections to FSS or even simply include the background, error-weighting is an important ingredient. This has been discussed in Sect. 8.2. It is certainly possible, to weight datapoints in jacknifed fits with the inverse of the squared error by a doubled jacknife procedure. The necessary squared amount of reweighting procedures needed in our analysis, made the workload increase dramatically, which is why we have not implemented the doubled jacknife. Nonetheless, we have indeed estimated the covariance matrix from unweighted linear fits and found that the covariance-weighted estimate of x_λ is largely dominated by value converted from γ/ν. This is no surprise, considering the fact that corresponding individual estimate of x_λ is indeed the most precise one. The error estimates of x_λ converted from the other exponent ratios are at least twice as large as the corresponding estimates from conversion of γ/ν. In many cases, in particular in MA, this ratio is even significantly larger, which is why we refrain from further presenting any covariance-weighted mean, here.

---

[3] And we shall meet two more ways to do so in Sects. 9 and 10.

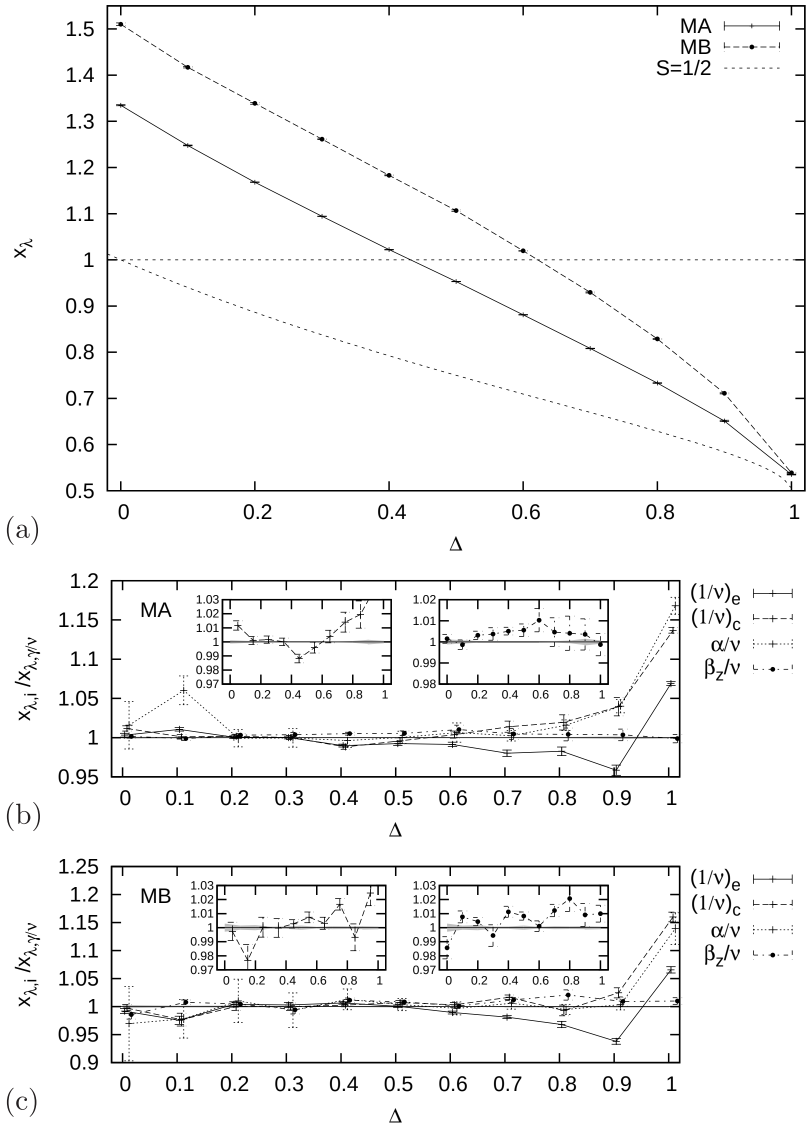

Figure 8.28: (**a**) Best estimates of the fundamental scaling dimension x_λ. (**b**,**c**) Comparison of different estimates if x_λ. Plotted is the ratio of $x_{\lambda,i}$ over the reference value $x_{\lambda,\gamma/\nu}$. The index i is a placeholder for the exponent ratio from which x_λ is converted by the scaling relations (8.26). The barely visible grey region centered at 1, is the error of $x_{\lambda,\gamma/\nu}$. Insets show close-ups of selected results.

Table 8.10: MA, comparison of x_λ. The fundamental scaling dimension x_λ, can be obtained from different scaling relations (8.26). Indices e and c denote error-weighted and covariance-weighted mean of $1/\nu$, respectively.

Δ	$\frac{1}{4-2\gamma/\nu}$	$2-\left(\frac{1}{\nu}\right)_\mathrm{e}$	$2-\left(\frac{1}{\nu}\right)_\mathrm{c}$	$1-\frac{\alpha}{2\nu}$	$2\frac{\beta_z}{\nu}$
0.0	1.3348(13)	1.339(4)	1.350(5)	1.356(41)	1.337(3)
0.1	1.2478(8)	1.261(3)	1.249(4)	1.323(23)	1.246(3)
0.2	1.1681(5)	1.169(2)	1.170(3)	1.167(13)	1.172(3)
0.3	1.0943(5)	1.094(2)	1.094(3)	1.094(13)	1.098(4)
0.4	1.0222(5)	1.012(2)	1.010(4)	1.018(10)	1.027(2)
0.5	0.9531(5)	0.946(3)	0.949(4)	0.953(8)	0.958(3)
0.6	0.8811(5)	0.874(3)	0.884(4)	0.887(11)	0.890(5)
0.7	0.8081(4)	0.792(4)	0.819(6)	0.810(6)	0.812(6)
0.8	0.7332(7)	0.720(5)	0.747(8)	0.745(5)	0.736(6)
0.9	0.6511(15)	0.624(5)	0.677(8)	0.677(6)	0.653(5)
1.0	0.5351(8)	0.572(2)	0.608(2)	0.625(6)	0.534(3)

Table 8.11: Same as Table 8.10, but for MB.

Δ	$\frac{1}{4-2\gamma/\nu}$	$2-\left(\frac{1}{\nu}\right)_\mathrm{e}$	$2-\left(\frac{1}{\nu}\right)_\mathrm{c}$	$1-\frac{\alpha}{2\nu}$	$2\frac{\beta_z}{\nu}$
0.0	1.5102(30)	1.498(7)	1.506(10)	1.464(101)	1.489(12)
0.1	1.4170(15)	1.382(11)	1.384(17)	1.386(49)	1.428(6)
0.2	1.3389(19)	1.344(7)	1.339(10)	1.353(52)	1.345(4)
0.3	1.2614(8)	1.265(6)	1.261(9)	1.253(39)	1.254(10)
0.4	1.1830(9)	1.191(3)	1.186(4)	1.198(22)	1.196(5)
0.5	1.1067(16)	1.107(3)	1.115(5)	1.111(13)	1.116(4)
0.6	1.0195(7)	1.009(3)	1.023(5)	1.016(12)	1.021(4)
0.7	0.9295(11)	0.912(3)	0.945(4)	0.935(10)	0.941(5)
0.8	0.8288(10)	0.802(5)	0.823(8)	0.825(8)	0.846(8)
0.9	0.7109(11)	0.667(4)	0.728(7)	0.713(7)	0.717(6)
1.0	0.5387(9)	0.574(4)	0.625(5)	0.614(16)	0.544(4)

8.7 Matching Universality Classes

In all final plots of results on critical exponent ratios in the preceding sections, we indicated values of the spin-$\frac{1}{2}$ chain at the special point $\Delta = 0$. The spin-$\frac{1}{2}$ chain at $\Delta = 0$ is the pure quantum XY model. In terms of the quantum Ashkin–Teller model this point corresponds to the decoupling of the two constituent quantum Ising chains, while in fermionic language it is the point of free, non-interacting fermions. It is signalled, for example, by $\alpha = 0$ or $x_\lambda = 1$. Clearly, our data suggests that the corresponding point is located in the vicinity of $\Delta = 0.4$ in MA, while for MB it is very close to $\Delta = 0.6$. With standard and extended [129, 131–133] scaling relations approximately fulfilled, in fact, every Δ-point in the mixed spin models corresponds to a particular Δ-point of the spin-$\frac{1}{2}$ chain. Another special point of interest would certainly be the end of the critical line. In the spin-$\frac{1}{2}$ chain the line ends precisely at $\Delta = -1/\sqrt{2}$, and the ED analysis of Sect. 7.1 suggests it to be roughly placed around $\Delta = -0.4$ in both mixed spin models. This point has not been studied in this section on QMC results.

Nonetheless, we wish to completely map the line of "universality classes" obtained for the mixed spin models onto that of the spin-$\frac{1}{2}$ chain. The relation that connects Δ with x_λ in the spin-$\frac{1}{2}$ chain is (5.44), which we simply rewrite as

$$\Delta = -\cos(\pi/2x_\lambda) =: \eta(x_\lambda)\,. \tag{8.27}$$

We assume that this relation can be modified appropriately to yield the correct relation between Δ and x_λ for MA and MB. However, in the utter lack of any theoretical backup for a decent ansatz we take refuge in polynomials. We used a polynomial to fit the difference between $\Delta(\eta)$ for the spin-$\frac{1}{2}$ chain (obviously the straight line $\Delta(\eta) = \eta$) and $\Delta_{\mathrm{MA/MB}}(\eta)$ for MA, respectively MB. The values of x_λ from conversion of our estimates of γ/ν were fed into $\eta(x_\lambda)$, and supplemented by two further reasonable assumptions concerning the shape of the polynomial. We demanded that at the isotropic points $|\Delta| = 1$, the difference $\Delta_{\mathrm{MA/MB}}(\eta) - \Delta(\eta)$, is zero. We tried various different ways to incorporate this demand, as well as different orders of polynomials. The best result we achieved by the following sixth-order polynomial ansatz,

$$p(\eta) = \left(a - b(\eta - m)^2 - c(\eta - m)^3\right)\left(1 - \eta^2\right)\,, \tag{8.28}$$

which left four free parameters in the fit.

Figure 8.29a shows Δ, plotted as a function of $\eta(x_\lambda)$, for both mixed spin models in comparison to the straight line of the spin-$\frac{1}{2}$ chain, while the inset shows the actual data that was fitted. At least visually, the curves appear reasonable. Even more so, if we consider that there is no reason to expect a dramatic change in the behaviour of the difference $\Delta_{\mathrm{MA/MB}}(\eta)$, at least until the end of the critical line. An this is exactly what we can deduce from the polynomial fits. According to the fitted polynomials shown in Fig. 8.29a, the end of the critical line occurs at $\Delta = -0.497$ in MA and $\Delta = -0.405$ in MB. A problem is, of course a meaningful error estimate. To this end, we also used the estimates of x_λ converted from the other exponent ratios, varied the values of x_λ within their own error estimates and compared results to different non-polynomial variations of (8.28), which, all in all, is reflected in the estimates $\Delta = -0.49(2)$ for MA,

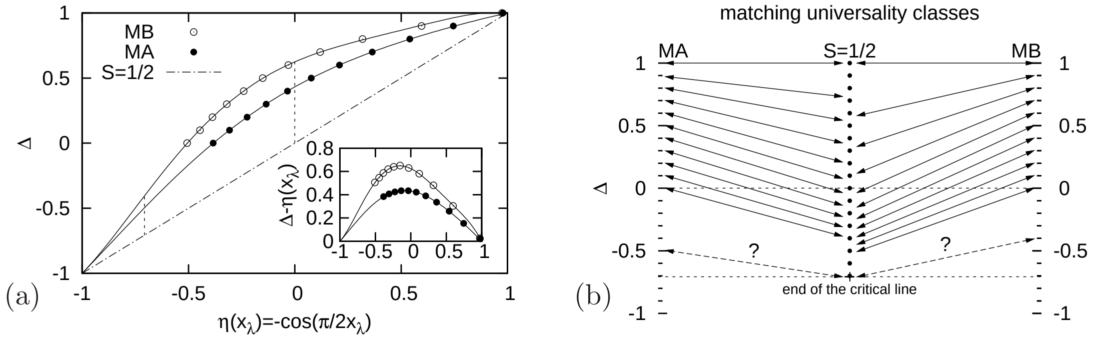

Figure 8.29: (**a**) Plotting Δ as a function of $-\cos(\pi/2x_\lambda)$ visualizes the difference between the mixed spin models and the spin-$\frac{1}{2}$ chain, for which the plotted function is an identity. Full curves show the polynomials (8.28) fitted to the difference $\Delta_{\mathrm{MA/MB}} - \eta$, which is plotted in the inset. The dashed vertical lines indicate the location of the pure quantum XY model ($eta = 0$) and the end of the Gaussian critical line ($\eta = -1/\sqrt{2}$). (*b*) Matching universality classes. The central vertical line of dots represents the ($\eta = -1/\sqrt{2}$) Gaussian critical line of the spin-$\frac{1}{2}$ chain, while at the borders the mixed spin models "reside". Arrows indicate where the simulated Δ-points of the mixed spin models would be located on spin-$\frac{1}{2}$ Gaussian critical line.

and $\Delta = -0.38(3)$ for MB. However, the error estimates just quoted, are naturally deprived from any statistical meaning. To test their significance and correctness, and thus the predictive power of this phenomenological inter- and extrapolation, shall be subject to future projects.

8.8 Summary

The major part of our numerical effort, both in data production and data analysis, has flowed into the results presented in this section. For eleven equally spaced values $\Delta = 0.0, 0.1, \ldots, 1.0$, we calculated the the critical exponent ratios γ/ν, $1/\nu$, α/ν and $\beta_{z,xy}/\nu$. Apart from the exception of β_{xy}/ν, we found all critical exponent ratios to vary significantly and continuously with the exchange anisotropy Δ.

Qualitatively, the variation with Δ is in very good agreement with the predictions (8.26) obtained from the Gaussian model. Furthermore, regular comparison with the exactly known values of the spin-$\frac{1}{2}$ chain showed, that the Δ-dependence of critical exponents is similar, yet numbers differ. At $\Delta = 1$, results of all three models come closest to each other. The enhanced symmetry at this point fixes the values of all critical exponents of the spin-$\frac{1}{2}$ chain to specific universal values, eg. $\alpha/\nu = \gamma/\nu = 1$, and generates multiplicative and additive logarithmic corrections. Our results permit the conclusion that precisely the same happens in our mixed-spin models, if we assume the presence of logarithmic corrections to be responsible for estimates that differ from what may be expected and the most obvious violation of extended scaling relations [129–133] at $\Delta = 1$.

Quantitatively, satisfaction of scaling relations (8.26) can be checked by inspection of Tables 8.10 and 8.11, while Fig. 8.28b,c shows the test graphically. Our best estimate of a critical exponent ratio arguably is γ/ν. It is the only estimate that we obtained independently from the precise location of the critical points, and its signal is large enough to dominate clearly over a possible background. We chose x_λ, converted from γ/ν, for which we exclusively used the results of the double-log linear fit and not those of any of the alternative methods, that might blow up the error estimate, as reference value to check scaling relations on-the-fly. In Fig. 8.28b,c the ratios of x_λ converted from the other exponents to the reference value are plotted.

Strictly speaking, our results do not consistently satisfy the scaling relations (8.26). We are thus not in the possession of a numerical proof of the Gaussian nature of our mixed spin chains. However, it is yet time to remember that we followed a restrictive way in choosing our optimal estimates of critical exponent ratios. In the urgent need to disentangle our expectations from the objective results, we judged every observable independently and tried to choose a final optimal estimate with smallest possible error. We emphasize, that, in almost all cases, we would have been able to deliberately choose different "optimal" estimate that better satisfy the scaling relations (8.26) and thereby prove what we want to see.

The universality class of a phase transition is determined by a few macroscopic properties of the model, most importantly, here, the symmetry of the order parameter. By extension of disorder parameters of the spin-$\frac{1}{2}$ chain, we presented quantities that behaved like (dis)order parameters, D_z and D_x. The longitudinal version, D_z, and its moments delivered, up to some serious points of critique and interest, the "correct" critical exponents. In Sect. 8.5 we found the critical exponent of D_x to be consistent with constant value $\beta_{xy} = 1/4$ for $\Delta \leq 0.8$ in both models. This indicates the presence of constant, i.e. *non*-Gaussian scaling dimensions, as in the quantum Ashkin–Teller model. Our definitions of the string observables are based on quantities that signal the spontaneous breaking of a hidden $Z_2 \times Z_2$-symmetry. We have no analytical proof to show that our definitions equally show such a breaking, but putting all pieces together, we conclude, that if our above stated result is true in the strict sense, then we have observed the breaking of the same hidden symmetry in this thesis, and newly defined order parameters that signal the transition, applicable, in principle to arbitrary mixed spin chains (see Sect. 5.4).

Points of critique are the pathological finite-size behaviour of D_z at the critical point, presumably hampered by the influence of corrections to scaling, and the peculiar (conjectured) relation of critical exponents of its moments,

$$2\beta_z^0 = \beta_z = \beta_z^2 = \beta_z^4/2\,. \tag{8.29}$$

We found the central part also to be fulfilled by the D_x, i.e. $\beta_{xy} = \beta_{xy}^2$. Furthermore, the observable itself yields a critical exponent that is two times larger than the value needed to satisfy expectations.

With the longitudinal string observable a notable exception, the general observation is that corrections to FSS grow in influence upon approaching the isotropic point, being visibly strongest precisely at $\Delta = 1$ (see also the data shown in Sect. 11.2). We remark, that this is, in fact, not inconsistent with our main hypothesis, which implies the presence of logarithmic corrections at the isotropic point. Turning the argument around, qualitative evidence for pronounced "slow" corrections to FSS at the isotropic point (as shall be presented in Sect. 11.2), suggest the corrections being of logarithmic type and thus support our main conclusion.

9 Gaussian Parameters and Central Charge

The main conclusion of the previous section is that the critical properties of the models studied can be explained in terms of the sine-Gordon model, a Gaussian model with extra irrelevant term that becomes marginal at the isotropic point and generates logarithmic corrections. Bond alternation, tuned by the control parameter λ, adds another relevant term and we have [24]

$$\mathrm{H} = \frac{v}{2\pi} \int \mathrm{d}x \left[\frac{1}{K} (\partial_x \Phi)^2 + K (\partial_x \Theta)^2 - u \cos(4\Phi) + t \sin(2\Phi) \right] . \tag{9.1}$$

The coupling constant $t(\lambda)$ is an unknown function of λ, such that $t(\lambda_\mathrm{c}) = 0$, and sufficiently close to the critical point $t \sim |\lambda - \lambda_\mathrm{c}|$. The Gaussian parameters that determine the properties of the model are the characteristic velocity v, a scale factor, and the coupling constant K. It is one of the most important features of the Gaussian model that scaling dimensions of primary scaling operators are known functions of the coupling constant K, which are given in (5.35). The scaling dimension of the operator induced by bond alternation is $x_\lambda = x_{0,2} = K$. We have become used to call x_λ it the *fundamental* scaling dimension, it is, of course, identical to K. We sticked to a different notation, however, depending on the context, with K emphasizing the significance as a scaling dimension of the Gaussian model, while x_λ reminds of the relation to the bond alternation parameter in the the mixed spin models.

Giamarchi [8, pp. 148 and 226] points out that the product vK relates to the response of the spin model to twisted boundary conditions and the observable ρ, that measures this response is called spin stiffness [20, 24, 194, 195],

$$vK = \pi L \rho \, , \tag{9.2}$$

where L is the length of the spin chain. With the improved estimator [195, 254, 255]

$$\rho_{\mathrm{imp}} = \frac{1}{4} \left\langle \sum_{\mathrm{loops}\ \mathcal{L}} (w_\mathrm{s}(\mathcal{L}))^2 \right\rangle , \tag{9.3}$$

where $w_\mathrm{s}(\mathcal{L})$ denotes the spatial winding number of loop $\mathcal{L}$, we have an estimator at hand to directly measure vK. Using the conformal symmetry of the Gaussian model it is possible to directly measure also v/K. From conformal invariance, we know that the normalized gap between groundstate and lowest excited state of a finite model is

$$\frac{E_1 - E_0}{v} = 2\pi x L^{-1} \, . \tag{9.4}$$

The proper conformal normalization is the velocity parameter v, and the energy gap is the inverse temporal correlation length ξ. We used moments of the transversal spin–spin correlation function $\langle \mathrm{S}_i^+ \mathrm{S}_{i+r}^- \rangle$ to estimate the correlation length. The scaling dimension x to be used above, is the scaling dimension of the operator S^+, that is $x_{0,1} = 1/(4K)$ [8, 24]. We thus have,

$$\frac{v}{K} = \frac{2L}{\pi\xi} \,. \tag{9.5}$$

Putting the pieces together we get the following expressions for the Gaussian parameters K and v,

$$K = \pi\sqrt{\xi\rho/2} \,, \tag{9.6}$$

$$v = L\sqrt{2\rho/\xi} \,, \tag{9.7}$$

in terms of the correlation length ξ and the spin stiffness ρ. Both quantities are measurable in the loop algorithm using fundamental loop properties, size and spatial winding number.

We used the values at the maxima of the of the spin stiffness and the fourth-moment estimator $\xi^{(4)}$, of the correlation length in the following analysis. We had to use $\xi^{(4)}$, simply because the second-moment estimator $\xi^{(2)}$, did not work, $\xi^{(2)} \neq \xi^{(4)}$. In Sect. 7.2, where used $\xi^{(2)}$ to locate the critical point, this did not matter because we were only interested in the location of the maxima, which coincide in both versions.

Figure 9.1a,b shows the finite-size estimates of K, which clearly converge to a constant value. The deviations from a constant value at small chain lengths are finite-size corrections, most likely induced by the usual suspects, analytic and non-analytic corrections to FSS. Equations (9.2) and (9.4) hold, in fact, only asymptotically. The slowest convergence can clearly be seen at the isotropic point $\Delta = 1$. We take this, again, as a strong sign for the presence of logarithmic corrections. We tried to capture the finite-size corrections, where possible, by a fit to

$$K(L) = K + CL^{-\omega} \,. \tag{9.8}$$

At small values of Δ, finite-size corrections quickly drown in the statistical inaccuracy of our data, and we extracted K simply by a fit to a constant of a few large-L datapoints. The comparison to our best estimates $x_{\lambda,\gamma/\nu}$, from Sect. 8.1, is shown in Fig. 9.1c,d. First of all, we note that, apart from at $\Delta = 1$, the two different estimates agree to within less than 0.4% in MA (5.2) and less than 0.2% in MB (5.3). But, including our error estimates in the judgement, we found some inconsistent values, in particular at $\Delta \geq 0.6$. The estimate $x_{\lambda,K}$ is larger than $x_{\lambda,\gamma/\nu}$. In Sect. 8.1, we observed that for $\Delta = 0.9$ we might have faced the threat of underestimating γ/ν and consequently also $x_{\lambda,\gamma/\nu}$, and tried to capture this by including an effective power-law correction to FSS. This lead to slightly larger estimates $(\gamma/\nu)_\omega$, which is qualitatively in agreement with $x_{\lambda,K}$ being larger than $x_{\lambda,\gamma/\nu}$ as shown in Fig. 9.1c,d. But the estimates $x_{\lambda,(\gamma/\nu)_\omega}$, are also shown, and it can be seen that the disagreement is even worse at $\Delta = 0.9$ and 0.8, and comparable at $\Delta = 0.7$, in both models.

Certainly, the estimates $x_{\lambda,K}$ and $x_{\lambda,\gamma/\nu}$, are correlated as they origin from the same sets of simulations. We estimated the covariance matrix on the basis of unweighted fits

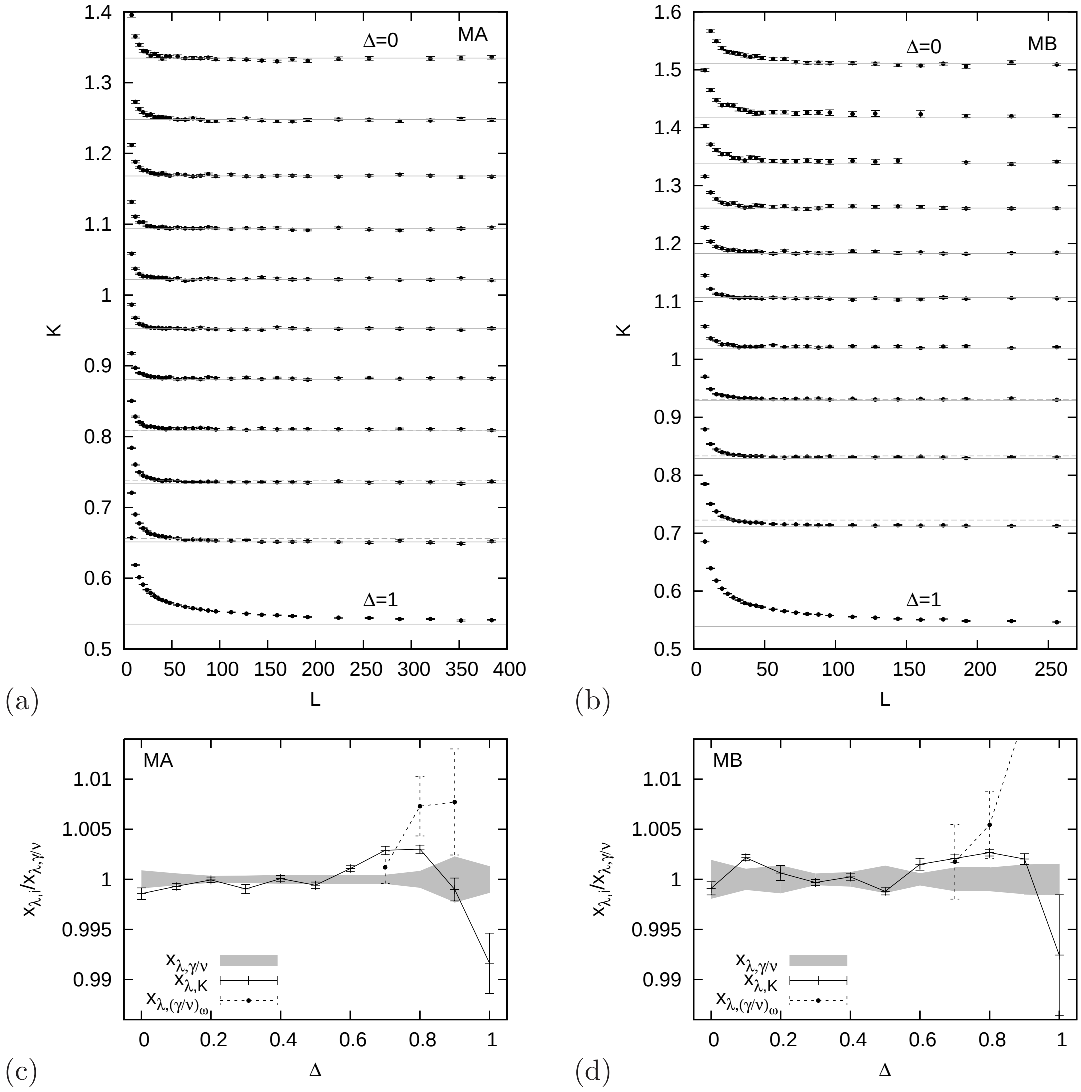

Figure 9.1: Direct estimate of the Gaussian parameter K which is identical to the scaling dimension x_λ, i.e. $K = x_\lambda = \pi\sqrt{\xi\rho/2}$. (**a**,**b**) L-dependence of finite-size estimates of K. Full horizontal lines indicate the estimates $x_{\lambda,\gamma/\nu}$ of Sect. 8.1, and dashed horizontal lines $x_{\lambda,(\gamma/\nu)_\omega}$. Datasets correspond to $\Delta = 0 \ldots 1$, from top to bottom, as indicated. (**c**,**d**) Ratio of different estimates of x_λ over $x_{\lambda,\gamma/\nu}$. The grey region centered at 1, indicates the error of $x_{\lambda,\gamma/\nu}$.

with the jacknife method, which is easily possible when fitting to a constant, but was not implemented for fits to the power-law (9.8) (see also the corresponding discussion in Sect. 8.2. What we found, was a positive correlation between the estimates which was < 0.6 for all $\Delta < 1$. This lead to rather well (i.e. intuitively) behaved covariance-weighted means which did not differ much from the error-weighted counterparts.

As far as the results of x_λ are concerned, this section is not much different from Sect. 8. The direct estimate of K is just another estimate of x_λ. The technical details are yet different. While throughout Sect. 8, we have been interested in exponents, it is the background term here, that yields the results. The other background term of interest, here, is the velocity parameter v. The finite-size estimates are shown in Fig. 9.2a,b. Again, all deviations at small chain lengths from the constant background term, must be due to finite-size corrections. All final estimates of v were obtained from fits to a constant of a few datapoints of long chains, they are shown in Fig. 9.2c,d. The velocities of the mixed spin models are very similar, and the comparison to the exactly known values (5.46) show that they are larger than those of the spin-$\frac{1}{2}$ chain, with the difference, however, getting smaller with decreasing Δ.

There would be yet another indirect estimate of the velocity available. According to the theory of conformal invariance, the size-dependence of the finite-size energy density e_L, in the groundstate is (see Sect. 4.3)

$$e_L = e_\infty - \frac{\pi v c}{6} \frac{1}{L^2} \,, \tag{9.9}$$

which provides a direct estimate of the product cv, via the slope of a linear fit in L^2. Using the property of the Gaussian model, and the spin-$\frac{1}{2}$ XXZ chain, that the central charge $c = 1$ [164, 198, 256], this would yield another estimate of v. Turned around, however, with an estimate of v already at hand, the above equation provides access to the central charge, estimated purely from QMC data.[1] This is what is shown in the insets of Fig. 9.2c,d, where it is confirmed that we, indeed, measured $c = 1$ throughout, with a small discrepancy in MB at $\Delta = 1$.

We conclude this section by a unified listing of Gaussian parameters $K = x_\lambda$, and v, and central charge c, for both models, in Table 9.1. The scaling dimension x_λ, the velocity v, and the central charge c, are all quantities that can, of course, be also obtained from extrapolation of exact data. We have checked that ED data does confirm the results of this section as far as possible. For MA, this will be part of the next section, where several low-lying energy levels will be calculated from extrapolation and interpreted. For MB, ED results suffer from a severe limitation. The Gaussian velocity v gives the important conformal normalization of energy spectra. Thus, v is a necessary ingredient in the interpretation of finite-size energy spectra and also in the determination of the central charge.

---

[1] A very efficient concurrent way to estimate the central charge, is provided from measurement of the entanglement entropy in DMRG calculations [257].

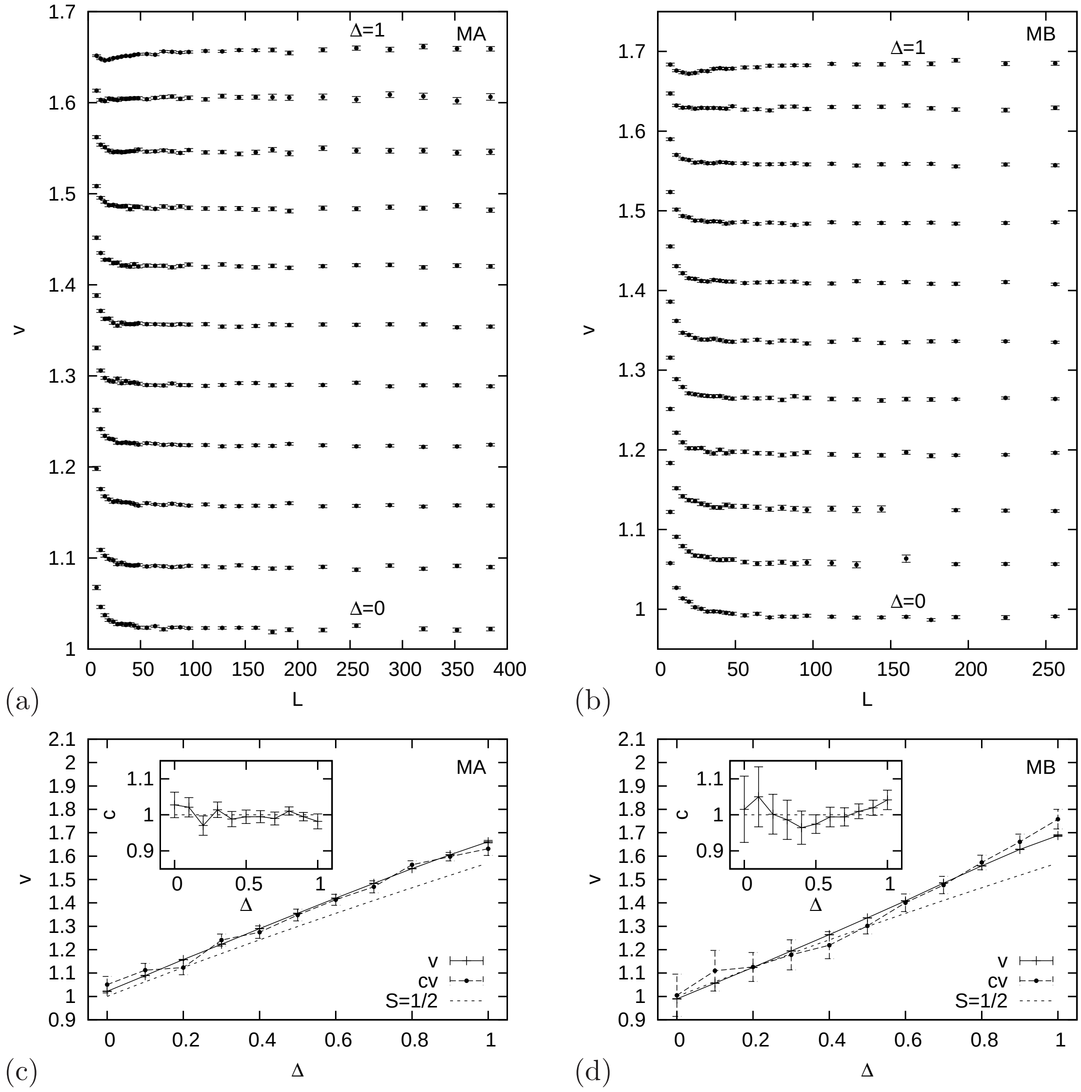

Figure 9.2: Estimate of the Gaussian velocity parameter $v = L\sqrt{2\rho/\xi}$. (**a**,**b**) L-dependence of finite-size estimates of v. Datasets correspond to $\Delta = 0 \ldots 1$, from bottom to top, as indicated. (**c**,**d**) Comparison of the velocity v and the product cv, obtained from fits to (9.9), and the exactly known velocity of the spin-$\frac{1}{2}$ chain [164, 196–198]. Insets show the central charge c.

Table 9.1: Gaussian parameters K and v, and central charge c, of MA and MB.

	MA			MB		
Δ	K	v	c	K	v	c
0.0	1.3329(8)	1.0221(8)	1.028(36)	1.5089(10)	0.9896(9)	1.015(93)
0.1	1.2469(4)	1.0894(5)	1.021(27)	1.4201(5)	1.0570(9)	1.050(84)
0.2	1.1681(4)	1.1576(4)	0.970(27)	1.3398(10)	1.1238(4)	1.002(56)
0.3	1.0933(5)	1.2234(4)	1.014(22)	1.2610(4)	1.1945(8)	0.986(55)
0.4	1.0222(4)	1.2900(5)	0.988(21)	1.1833(5)	1.2641(4)	0.964(46)
0.5	0.9525(3)	1.3556(5)	0.995(19)	1.1053(4)	1.3358(3)	0.974(26)
0.6	0.8821(3)	1.4203(4)	0.995(17)	1.0210(7)	1.4090(6)	0.994(28)
0.7	0.8104(4)	1.4835(6)	0.990(18)	0.9314(5)	1.4848(3)	0.994(26)
0.8	0.7354(3)	1.5468(6)	1.011(12)	0.8310(3)	1.5579(7)	1.010(21)
0.9	0.6505(8)	1.6058(7)	0.995(12)	0.7124(4)	1.6288(11)	1.020(22)
1.0	0.5306(17)	1.6619(54)	0.982(21)	0.5346(33)	1.6879(36)	1.041(28)

10 Finite-Size Spectra

Conformal theory tells us that primary scaling operators and their conformal towers generate the finite-size energy spectra [25]. For our spin chains with periodic boundary conditions this means that each of the finite-size energy levels is related to the scaling dimension of a scaling operator by [26, 136]

$$\frac{E_i(L) - E_0(L)}{2\pi v} = x_i L^{-1} + o(L^{-1}) \,. \tag{10.1}$$

We have calculated the (low-)energy spectra at $\Delta = 0.0, \ldots, 1.0$ for five different chain lengths $L = 4, 8, \ldots, 20$ of MA (5.2) (and four different chain lengths $L = 4, 8, \ldots, 16$ of MB (5.3)). The small systems, $L = 4$ and 8, have been fully diagonalized, while for the larger systems the Lanczos method with reorthogonalization has been used to get at most six levels in every symmetry sector (see Sect. 6.1). Exploitation of symmetries permits a block diagonalization of the Hamiltonian, with every block corresponding to an invariant symmetry sector. While on the one hand, symmetries are vital to reduce the dimension of a Hamiltonian that is to be diagonalized, block-diagonalization according to symmetries also permits, on the other hand, to assign energy levels to a specific symmetry sector and label them with a set of quantum numbers. Here, the Hamiltonian was split into sectors of constant magnetization $M = 0, 1, \ldots, M_{\text{max}}$, constant scaled momentum with respect to a basecell of size 4, $P = 0, 1, \ldots, L/4 - 1$, and constant parity $S = \pm 1$. We shall simply use the symbols $+$ and $-$ to label sectors that are even and odd, respectively, under spatial reflections. A triple MPS denotes the symmetry sector. "00+", for example, is the sector with $M = 0$, $P = 0$ and $S = +1$. The longest chain of MA with $L = 20$ consists of five basecells and the possible momenta are $p = 2\pi P/5$. This means that only for the sector with $P = 0$, real basis states can be constructed and be further be split into even and odd parity sectors. The other P-sectors have complex basis states and no parity sectors, we shall use $S = 0$, to label the complex P-sectors, indicating that we have no assignment of even or odd. However, symmetry under reflection in space means that the sector P is degenerate with the sector $P' = -P$. Out of five different P-sectors of the chain with $L = 20$, we thus only needed to treat the three sectors $P = 0, 1$ and 2.

We used the small-Δ spectra of $L = 20$ to, by comparison to values implied by our QMC analysis, associate Gaussian scaling dimensions to energy levels. The finite-size spectra can be normalized such that the energy of the lowest state in the sector $P = 1$, is unity [177]. We denote the energy of this state, the "norm"-state, by E_v, and the finite-size normalization v^* is

$$v^* = L \frac{E_v - E_0}{2\pi} \,. \tag{10.2}$$

In other words, plotting energy gaps $E_i - E_0$, in units of $E_v - E_0$, provides a way to identify the present scaling operators. The fact that the norm-state exists is not trivial, but fortunate. It cannot belong to the conformal tower of the identity and must therefore be a primary scaling operator [25]. It has already been used in the test application of Sect. 6.1.4, to calculate the norm of the spin-$\frac{1}{2}$ chain. For homogeneous spin chains the existence of the norm-state in the sector $P = 1$, is well known and confirmed [175].

Spectra of MA, $L = 20$, are particularly "beautiful" at $\Delta \leq 0.6$, in the sense that some states are already very close to the scaling dimensions that we can calculate from our estimates of γ/ν. This is illustrated in Fig. 10.1, where the spectrum of $\Delta = 0.3$ is shown. This is a finite-size spectrum, no extrapolation has been performed yet. The lowest states $E_{0,M}$, in the magnetization sectors $M \neq 0$, lie almost perfectly on a parabola in M (Fig. 10.1a), i.e. $(E_{0,M} - E_0)/(E_v - E_0) \approx M^2/(4x_\lambda) = x_{M,0}$, with $x_\lambda = x_{0,2}$, the fundamental scaling dimension inferred from our estimate of γ/ν. This strongly suggests to identify the magnetic quantum number M with the first index of the Gaussian scaling dimensions $x_{n,m}$, as in the case of the spin-$\frac{1}{2}$ chain [164]. The scaling dimension does not depend on the sign of the indices, which reflects the symmetry under spin inversion. We observe that the groundstates of the different M-sectors are alternatingly of odd (for M even) and odd (for M odd) parity, and they all lie in the sector $P = 0$.

Before proceeding with the identification of scaling operators in the spectrum of $\Delta = 0.3$ (Fig. 10.1), we note that coding the different symmetry sectors by color (assigned to different M-sectors) and symbols (assigned to different PS-sectors) proved extremely useful. Plotting the energy gaps in the momentum quantum number P, we can check for the conformal towers of primary scaling operators (see Fig. 10.1b). In sectors $P = \pm 1$, we find secondary scaling operators at level one for each the of M-sector groundstates in the close vicinity of the expected location $x_{M,0} + 1$. The lowest state in sector 010 is our norm-state. At level two, we find at least candidates of the same magnetization as the M-sector groundstates in sectors $P = 0, \pm 2$.

Two very important states are the second and third state of the sector with $M = 0$ and $P = 0$. One is in the even and the other in the odd parity sector. One is, in other words, the groundstate of sector 00+, and the other one the second state in sector 00−. Both states seem to be almost degenerate at $\Delta = 0.3$, and they both lie very close to scaling dimension $x_{0,2}$, which we know as the fundamental scaling dimension x_λ or the Gaussian parameter K. We have become used to calling the state in 00+ the *lower* K-state, and the state in 00− the *upper* K-state. At the isotropic point, the lower K-state, which has $M = 0$, is degenerate with two ($|M| = 1$)-states. They form the well-known elementary triplet excitation [210]. The upper K-state is the elementary singlet excitation, which becomes degenerate with the triplet in the thermodynamic limit, thus delivering the same scaling dimensions. Yet finite-size corrections are different, the amplitude of logarithmic corrections in the scaling dimension is negative for the triplet, and positive and three times larger for the singlet [206], which perfectly agrees with our observation, that the triplet state is the *lower* K-state. At $\Delta \neq 1$, exchange anisotropy splits up the triplet leaving behind a the degenerate doublet with $|M| = 1$.

Another branch of states can be found in close vicinity to values given by the parabola $x_{M,2} = M^2/(4x_\lambda) + x_\lambda$. We identify them with the corresponding primary scaling operators, but they do *not* belong to the sector $P = 0$. In perfect agreement with the conformal spin of Gaussian operators (5.36), level $x_{1,2}$ is found in sector $P = 1$, and level $x_{2,2}$, for example, in sector $P = 2$. With the $(P = 1)$-level in the vicinity of $x_{2,3}$ assigned to the conformal tower of $x_{3,0}$, there remains only another $(P = 2)$-candidate for $x_{2,3}$. Every non-zero momentum state in Fig. 10.1a is twofold degenerate. There are, thus, two primary scaling operators with scaling dimension $x_{M,2}$.

So far, in the spectrum at $\Delta = 0.3$, the states with $x_i < 1.5$ are exhausted and we note that there are *no* candidates in the vicinity of $x_{M,1}$. The significance of this observation lies in the fact that $x_{0,1}$ is the scaling dimension of the polarization of the quantum Ashkin–Teller model. It does, as it seems, not appear in the mixed spin models, at least not in the finite-size spectra with periodic boundary conditions. It would be interesting to check if this is also the case in the spin-$\frac{1}{2}$ chain which can be mapped onto the qAT model. We shall leave this, however, subject to future work, as well as a deeper investigation with modified boundary conditions to check if the corresponding scaling operator, AT-polarization density, belongs to the conformal operator content of the spin models at all. We can only conjecture that the parabola $x_{M,3}$ does not appear either. Finite-size corrections seem to become more apparent for large scaling dimensions and we cannot tell if the levels in the vicinity of $x_{M,3}$ belong to secondary or indeed primary scaling operators.

The region around $(E_i - E_0)/(E_v - E_0) = 2$ is of particular importance. It marks the marginal boundary between relevant and irrelevant scaling operators. In the spectrum of $\Delta = 0.3$, we observe several finite-size states in the vicinity of the marginal boundary. In Fig. 10.1, there are five visible levels close to the marginal value in the sector with $M = 0$. Only one of them belongs to $P = 0$. The other ones, for which $P \neq 0$, are each twofold degenerate, we thus have a total of nine levels to discuss. Two states of sector 020 must belong to the conformal tower of the identity, and according to [25] this should be the lowest levels in sector 020. The four states of sector 010 strongly seem to be secondary level-one states of the lower K-state and the upper K-state. There must be a scaling operator that is marginal on the entire critical line, it generates the motion along the critical line [132, 133]. In the spin-$\frac{1}{2}$ chain, the important marginal scaling operator belongs to the sector $P = 0$ [164], we thus identify x_{marg} as the third level in the sector 00−, and this leaves two levels, the second states of sector 020, to be precise, yet unexplained. As well as the groundstates of sector 120.[1]

This is already a lot information deduced from a single finite-size energy spectrum only. The next steps are to extend operator identification over the entire region $0 \leq \Delta \leq 1$, and to track the identities down to small chains in order to perform proper extrapolation. As far as the first step is concerned we note that for $\Delta > 0.6$ the above discussion would have been more complicated, because the finite-size levels deviate more strongly from the levels inferred from γ/ν. This does not make operator identification impossible, we could have used, e.g., the lower K-state as reference and tried to locate other scaling operators with respect to it. The point is, that the two variants make no big difference for $\Delta \leq 0.6$. It is clearly a remarkable feature of the small-Δ finite-size spectra, to exhibit small finite-size effects in the small scaling

---

[1] The remaining levels in the vicinity of the marginal region are the groundstates of sectors 220 and 30+, they have been already been identified with primary scaling operators with scaling dimensions $x_{2,2}$ and $x_{3,0}$, respectively.

dimensions already at the moderate chain length $L = 20$.[2] At the isotropic point the deviation is most severe, but this point exhibits another exceptionally "beautiful" aspect, its high degeneracy, which is why its finite-size spectrum is depicted in Fig. 10.2.

Figure 10.3a shows the Δ-dependence of the low-lying energy spectrum of $L = 20$, as obtained from the Lanczos method with reorthogonalization. Extrapolated results are shown in Fig. 10.3b in comparison to scaling dimensions calculated from the QMC estimate of γ/ν. We shall first discuss the production of and then comment on the extrapolated results.

Identification of $(x_{M,0})$-levels in the smaller systems is trivial. The groundstates of M-sectors, with M small, exist down to $L = 4$ and can be easily found. The situation is different with the non-zero momentum sectors. Obviously, for $L = 4$ there are none of these. This reduces the length of series to be extrapolated and we quickly end up in a situation where no reasonable extrapolation can be done. In the best case we have five values to extrapolate and in the worst three. Three points are clearly not enough to reasonably extrapolate with the BST algorithm, but in the special case of $x_{1,2}$ we find remarkable results.

We used the same strategy as in Sect. 7.1. We studied the dependence of the error estimate on the free parameter ω, located minima if possible and by comparison of, if possible, extrapolation of all five points with extrapolation of only four points (without $L = 4$, which is a single basecell only) tried to find a minimum of special significance. As in Sect. 7.1, we were able to reduce the error estimate to extremely – and unreasonably – small values by fine-tuning the search for minima in most, but not all, cases. Again we thus effectively lost control over the error estimates. There are many arbitrary criteria by which one can try to "choose" an error estimate. For convenience we arbitrarily chose to fix $\omega = 2$, throughout, and find this choice well justified for the following reasons. All optimal ω we found vary around the value 2. They are yet never constant, and the Δ-dependence varies within the different levels we extrapolated. The optimal ω of the norm-state, for example, starts at $\Delta = 0$ at a value ≈ 1.3, and remains roughly constant up to $\Delta = 0.5$, where it starts to rise quickly to a relatively large value ≈ 5.5, at the isotropic point. The estimate of x_v, however, remains nearly unchanged for values larger than $\omega \approx 2$. The optimal ω in the other cases is never smaller than 1, and apart from the just mentioned example and the notable exception of $x_{1,2}$ and $x_{1,0}{+}1$ at $\Delta = 0.5$, barely larger than 3. The combination of relatively stable estimates of the scaling dimensions in a region around $\omega = 2$, with reasonable error estimates that are not too large, we find our choice justified. Some selected values of extrapolated scaling dimensions are listed in Table 10.1

The scaling dimension $x_{1,2}$ is a particularly interesting case. Its energy level is located in the sector 110 for all $L \geq 8$ and it crosses at $\Delta \approx 0.4$ with a level of the same sector that we identified to correspond to a secondary operator with scaling dimension $x_{1,0} + 1$. The finite-size behaviour of the crossing is shown in Fig. 10.4a. While for $L = 12, 16$ and 20 the dependence on L is rather small and the location of the crossing is not really affected, for $L = 8$ the crossing shifts to larger Δ. Most notably, however, we find a remarkably small size dependence in the right branch of $x_{1,2}$. On the scale of Fig. 10.4a, the levels normalized with v^* of $L = 12, 16$ and 20 fall on top

---

[2] Which means, that $L = 20$ is not that moderate at all.

Table 10.1: Selected values of extrapolated scaling dimensions of MA. v is the characteristic velocity, or conformal normalization, such that $x_v = 1$. $x_{0,2(t)}$ and $x_{0,2(s)}$ denote the estimates of the scaling dimension $x_{0,2} = x_\lambda = K$, extrapolated from the lower K-state (triplet) and the upper K-state (singlet) (the elementary singlet excitation at $\Delta = 1$), respectively. At $\Delta = 1$, the lower K-state belong to a triplet, and delivers exactly the same extrapolated value as $x_{1,0}$. $x_{1,2(\mathrm{QMC})}$ denotes the estimate of $x_{1,2} = x_\lambda + 1/(4x_\lambda)$, calculated using γ/ν from our QMC simulations (see Sect. 8.1). The expected values at the isotropic point are $x_{1,0} = x_{0,2} = 1/2$ and $x_{1,2} = 1$.

Δ	v	$x_{1,0}$	$x_{0,2(t)}$	$x_{0,2(\mathrm{s})}$	$x_{1,2}$	$x_{1,2(\mathrm{QMC})}$
0.0	1.025(6)	0.1872(10)	1.328(8)	1.328(8)	1.515(2)	1.5221(14)
0.1	1.092(6)	0.2001(11)	1.244(7)	1.244(8)	1.444(6)	1.4481(9)
0.2	1.159(6)	0.2137(10)	1.167(7)	1.166(8)	1.380(8)	1.3821(5)
0.3	1.225(6)	0.2283(10)	1.092(7)	1.092(7)	1.321(9)	1.3228(5)
0.4	1.291(6)	0.2443(10)	1.022(5)	1.021(5)	1.266(9)	1.2667(6)
0.5	1.356(5)	0.2624(10)	0.950(7)	0.953(9)	1.214(18)	1.2154(6)
0.6	1.420(4)	0.2833(8)	0.875(13)	0.888(5)	1.163(4)	1.1648(6)
0.7	1.485(2)	0.3081(5)	0.792(21)	0.827(10)	1.116(6)	1.1175(6)
0.8	1.549(4)	0.3387(15)	0.694(29)	0.772(19)	1.072(5)	1.0742(10)
0.9	1.618(9)	0.3781(50)	0.575(30)	0.728(31)	1.033(3)	1.0351(24)
1.0	1.698(12)	0.431(14)	0.431(14)	0.702(36)	1.00000	1.0023(14)

of each other. Due to this observation, the final results of $x_{1,2}$, shown in Fig. 10.3 and listed in Table 10.1, are obtained from extrapolation of three normalized levels. This is the only case where we extrapolated normalized levels, i.e. $(E_i - E_0)/(E_v - E_0)$. In all other cases we extrapolated the unnormalized levels directly, i.e. $(E_i - E_0)L/(2\pi)$, and subsequently normalized them by v, which, in its own turn, was obtained from extrapolation (of four levels). Extrapolation of three values did not produce minima in ω at all, but neither did the extrapolation of four unnormalized levels in this case. A critical look at Fig. 10.4a, shows that the two branches of $L = 12$ that seem to form smooth lines, would form kinks if one tried to connect the datapoints such that the two lines cross. We have carefully checked our implementation of the Lanczos algorithm and have come to the conclusion that the numbers produced are correct and do give indeed the finite-size energy levels. We thus attribute the discussed behaviour to subtle finite-size effects in the vicinity of $\Delta = 0.5$[3], uncaptured by the BST extrapolation algorithm, and accept an error estimate that is relatively large compared to the errors of the neighbouring points (see Fig. 10.3b). The same discussion applies, in fact, to the crossing partner $x_{1,0} + 1$.

The most startling observation in $x_{1,2}$ is, however, the remarkable agreement with the values calculated from the QMC estimate of γ/ν *and* the extrapolated value $x_{1,2} = 1$, at the isotropic point $\Delta = 1$. The first observation can be checked in Table 10.1,

---

[3] In Sect. 8, we showed that MA at $\Delta = 0.5$ approximately corresponds to the pure XY spin-$\frac{1}{2}$ chain, at $\Delta = 0$. The pure XY point is known to generate its own, less apparent, type of logarithmic corrections [258–260], which are different from the ones at the isotropic point and mainly ignored in this thesis.

rather than by a mere look at Fig. 10.3, but the second observation is particularly impressive. From the extrapolation of three normalized levels ($L = 12, 16$ and 20) with $\omega = 2$ fixed, we obtain at the isotropic point $\Delta = 1$,

$$x_{1,2} = 1.0000000(8)\,. \tag{10.3}$$

Calculated from the QMC estimate of γ/ν, we get $x_{1,2} = 1.0023(14)$. The connection to $x_\lambda = x_{0,2}$ is given by

$$x_{1,2} = \frac{1}{4x_\lambda} + x_\lambda\,. \tag{10.4}$$

We find a strong deviation from the expected value of 1/2 in $x_{0,2}$, and all other scaling dimensions that we extrapolated, at the isotropic point, which we may assign to the presence of logarithmic corrections. The special form of $x_{1,2}$, and the extremely precise and "correct" result imply a cancellation of logarithmic corrections, and the agreement with the conversion from our QMC results implies a similar cancellation of significant power-law corrections at $\Delta < 1$.

Below we list and briefly discuss some further observations:

- The two different K-states do indeed approach each other after extrapolation. It is known that in the spin-$\frac{1}{2}$ chain, these levels are degenerate in the thermodynamic limit [210]. It is reasonable to expect that this should also be the case in mixed spin models, in particular in MA, the difference between the upper and lower K-state (both denoted $x_{0,2}$ in Fig. 10.3b) can be interpreted as a measure for the strength of corrections to scaling and FSS.

- The level which we suggestively identified with the exact marginal operator that generates the motion along the critical line, does get closer to the marginal boundary after extrapolation. At the isotropic point it is degenerate with the levels of $x_{2,0}$ and $x_{1,2} + 1$ which are both supposed to be equal to 2.

- In addition to the absence of scaling dimensions $x_{M,1}$ (and presumably $x_{M,m}$ with m odd), there are no obviously *constant* scaling dimensions in the relevant region, apart from unidentified states close to the marginal boundary. The magnetization of the quantum Ashkin–Teller model, for example, does have constant scaling dimension $x_M = 1/8$.

- The levels close to the marginal boundary which do not correspond to the exact marginal state are difficult to analyse. The identification of levels in the different chain lengths is not obvious (see Fig. 10.4b,c and d). Only the state in sector 220 can be tracked down to $L = 12$, giving three values to extrapolate, the result being included in Fig. 10.3. We shall leave the further clarification of these levels to future work.

For completeness we report here our estimates of the central charge c, as obtained from exact finite-size energy spectra (see Fig. 10.5). We applied the same analysis to MB also, with the problem that we had only three exact points in order to extrapolate the conformal normalization, which resulted in "error" estimates of roughly 10%. Within that accuracy, however, we conclude that $c = 1$ for MB, a conclusion also reached in the case of MA, but with considerably more certainty.

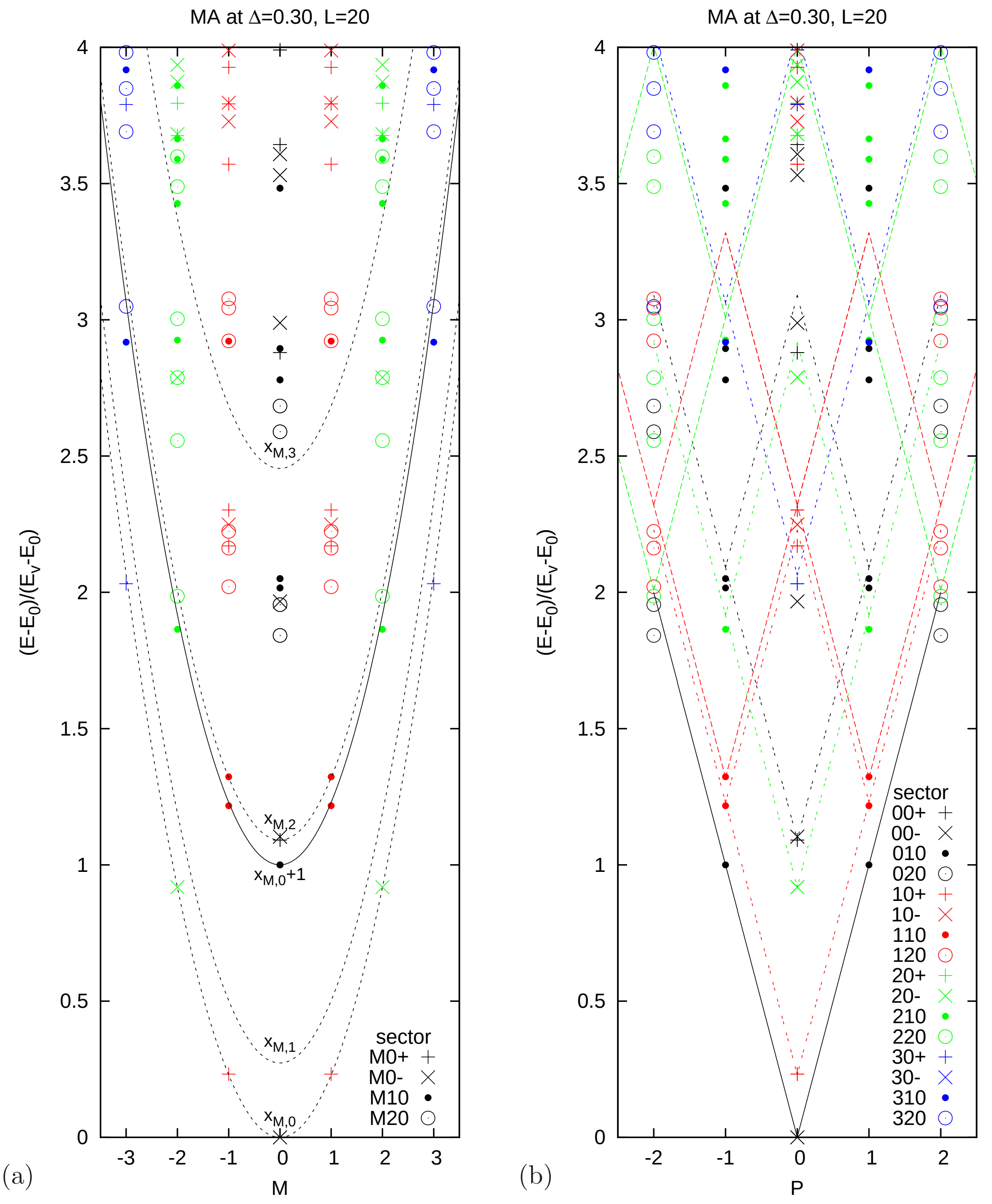

Figure 10.1: Exact finite-site spectrum of MA at $\Delta = 0.3$, $L = 20$. Levels are normalized such that the lowest state in the sector with $P = 1$, lies at 1. (**a**) Curves show the parabolae $x_{M,0} = M^2/(4x_\lambda)$. (**b**) Lines are drawn to facilitate the identification of conformal towers.

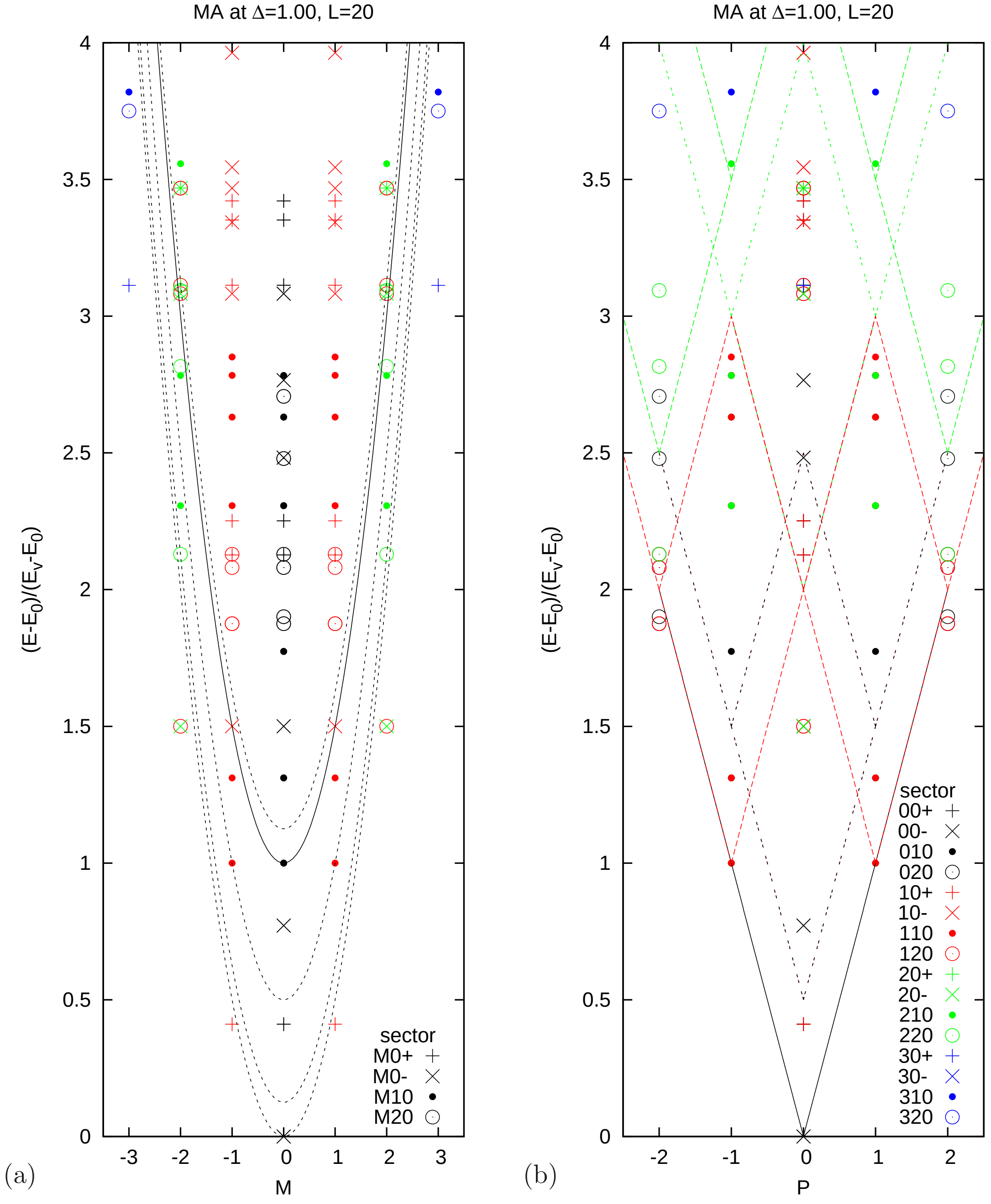

Figure 10.2: Same as Fig. 10.1, but for the isotropic point $\Delta = 1$.

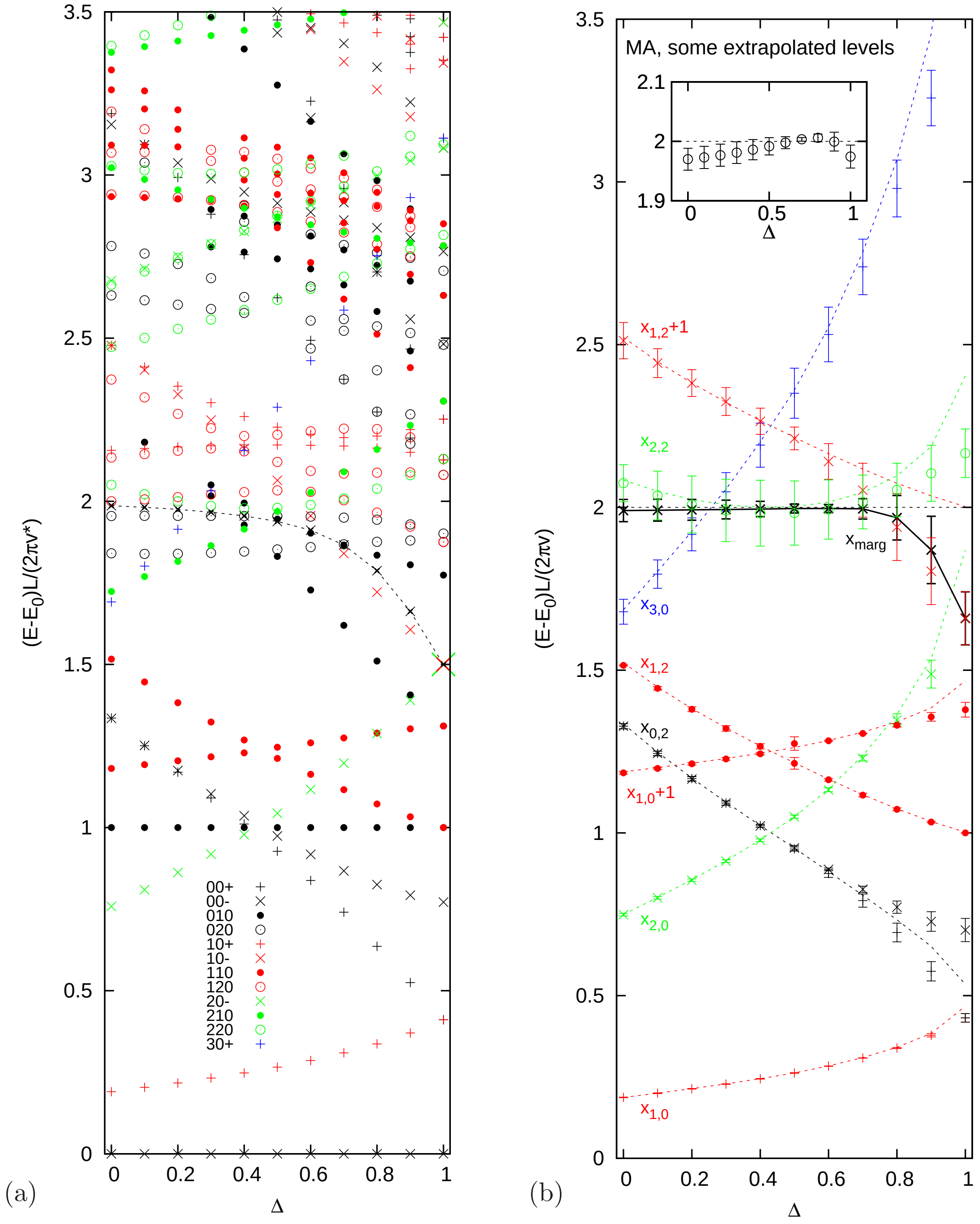

Figure 10.3: (**a**) Δ-dependence of low-lying energy levels of MA with $L = 20$. Levels are normalized such, that $x_v = 1$. The dashed curve indicates the level supposedly corresponding to the marginal operator. (**b**) Extrapolated scaling dimensions $x_{n,m}$, of some selected levels. Curves show the corresponding scaling dimensions calculated from our estimate of γ/ν of Sect. 8.1 via Gaussian scaling relations. The inset shows the scaling dimension $x = 2$, extrapolated from three energy levels in the sector with $P = 2$, it thus corresponds to a secondary state of the identity, which usually serves as normalization [25].

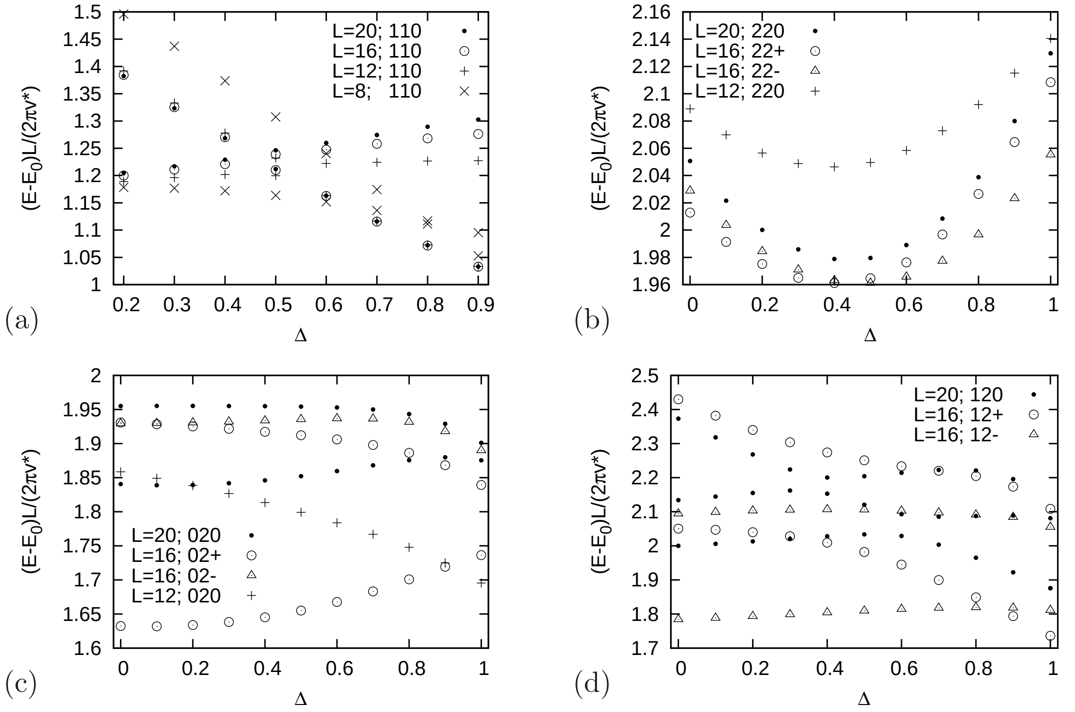

Figure 10.4: Finite-size behaviour of selected levels to illustrate the difficulty in identifying the levels of different chain lengths with the same scaling dimension. (**a**) Crossing of $x_{1,2}$ and $x_{1,0}+1$, discussed in detail in the main text. (**b**) Levels corresponding to $x_{2,2}$. For $L = 12$ and 20, the level belonging to sector 220 is twofold degenerate. For $L = 16$ the degeneracy is split into parity sectors, with a crossing at $\Delta \approx 0.4$. (**c**) Levels in the sector with $M = 0$ and $P = 2$ close to the marginal boundary. (**d**) Levels in the sector with $M = 1$ and $P = 2$ close to the marginal boundary.

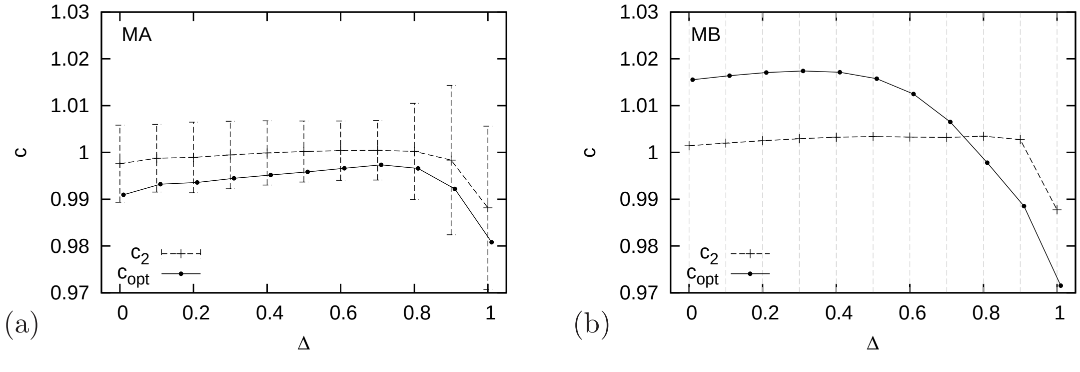

Figure 10.5: Results for the central charge c. c_2 denotes the result if the free parameter in the BST extrapolation is set fixed, $\omega = 2$, and c_{opt} the result if an optimal value is chosen such as to minimize the error estimate of c. Dashed vertical lines in (**b**) show are error estimates which do not fit on the chosen scale.

11 Corrections to Finite-Size Scaling

11.1 Power-Law Corrections

In virtually all observables studied in Sects. 8 and 9, we have observed corrections to FSS beyond the leading terms. In two cases only, we have tried to quantify the corrections, in terms of an effective correction exponent ω. In Sect. 8.1, the attempts targeted at three different values of Δ in both models, with the results that if the ω-term is included in (delicate) fits, the estimates of the leading exponent ratio γ/ν grew. However, comparison to the direct estimate of x_λ in Sect. 9, showed that this did not lead to a better agreement with the scaling relation $x_\lambda = 1/(4-2\gamma/\nu)$, quite in contrast, the values $x_{\lambda,(\gamma/\nu)_\omega}$ at $\Delta = 0.9$, where sub-leading finite-size corrections seemed to be especially pronounced, were quite far away from matching $x_{\lambda,K}$, in both models. In Sect. 8.4, after performing the analysis that included a power-law correction with an unknown effective exponent ω, we were lead to assume the presence of a yet unexplained additive L^{-1}-correction which, once included, yielded results in excellent agreement with our (modified) expectation. In both cases, however, the primary source of difficulties was the fact, that it is difficult to estimate *two* unknown exponents simultaneously.

There is, however, one quantity, the critical FSS exponent of which is unambiguously and well known, the correlation length. Finite-size estimates of the correlation length grow to leading order as $\sim L$. For the larger values of Δ, we found a clean and visible L-dependence of the ratio ξ/L, while at the smaller values of Δ, the L-dependence vanishes or drowns in the statistical inaccuracy of our data. Figure 11.1a,b shows some representatives at both ends of the Δ-range. We used the fourth-moment estimator of the imaginary time correlation length (see Sect. 6.2.4), which we denote ξ, and applied direct fits to

$$\frac{\xi}{L} = A + CL^{-\omega}\,, \tag{11.1}$$

with the output of not only the correction exponent ω, but also of the amplitude A, which, as explained in Sect. 4.3 and used already in Sect. 9, is related to the fundamental scaling dimension x_λ and the velocity parameter v. It becomes obvious from Fig. 11.1a, which shows ξ/L for MA (5.2) at the three smallest Δ's, that it was impossible fit the power-law (11.1) to the data in some cases. The situation is similar for MB (5.3). We thus tried to extract the effective values of ω, as long as possible, and used simple fits to a constant otherwise, to test that the relation $A = 2x_\lambda/\pi v$ was indeed satisfied.[1] We found that the second- and fourth-moment estimators of the imaginary time correlation length did not agree, with a growing discrepancy at larger values of Δ, which is why we used the fourth-moment estimator in this analysis.

---

[1] This is redundant, in fact, as $A = 2x_\lambda/\pi v$ was already used and implicitly tested in Sect. 9, which

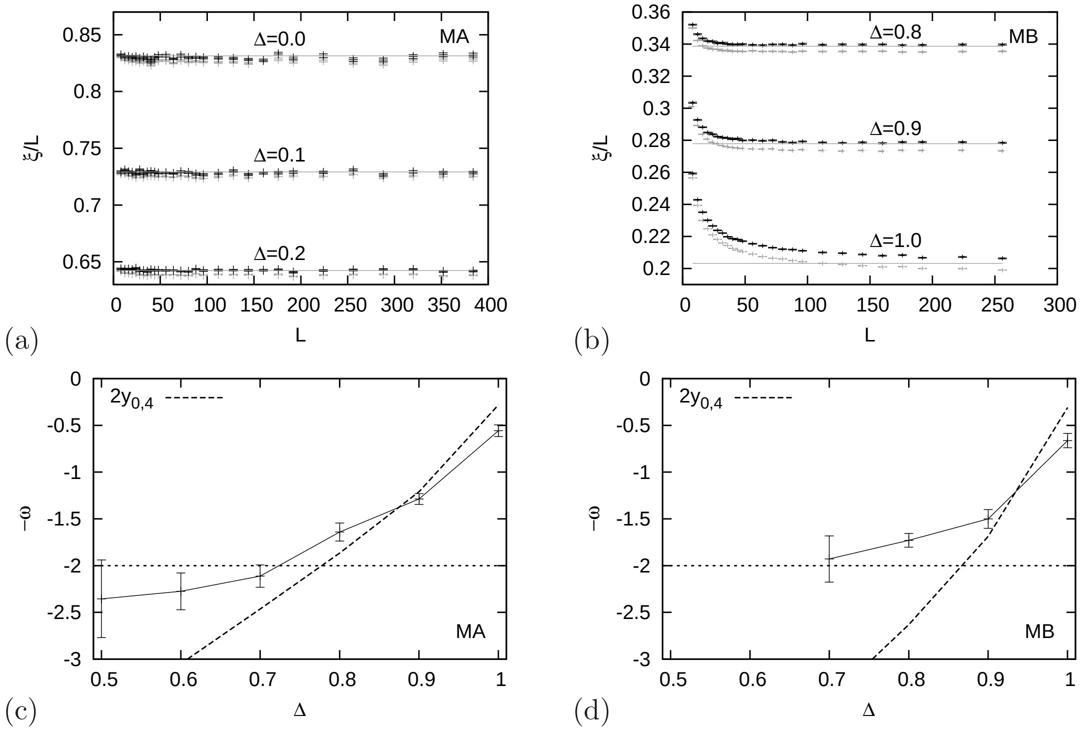

Figure 11.1: (**a**,**b**) To leading order in FSS, the ratio ξ/L is supposed to be constant. At larger values of Δ, sub-leading corrections are clearly visible and particularly "slow" at $\Delta = 1$. Black (grey) datasets show the fourth-(second-)moment estimator of the imaginary time correlation length. Horizontal lines indicate $2x_\lambda/\pi v$. (**c**,**d**) Effective correction exponent ω, as obtained from non-linear fits to (11.1), in comparison to the ingredients of (11.2), 2 and $2y_{0,4}$, calculated with $x_{\lambda,\gamma/\nu}$ and (5.35) (Sect. 8.1).

For the spin-$\frac{1}{2}$ chain, the leading correction exponent ω in (11.1) is [164, 244, 246, 247]

$$\omega = \begin{cases} 2|y_{0,4}|\,, & \text{if } \Delta > 0.5\,, \\ 2\,, & \text{if } \Delta \leq 0.5\,, \end{cases} \tag{11.2}$$

where $y_{0,4}$, is the RG eigenvalue of the scaling operator that generates the logarithmic corrections at the isotropic point, it is thus zero at $\Delta = 1$. Furthermore, precisely at $\Delta = 0.5$, multiplicative logarithmic corrections appear in the sub-leading power-law in (11.1) [164, 261], which are similar to but, obviously, of different origin than the logarithmic modifications of the leading behaviour at the isotropic point. From the matching of universality classes in Sect. 8, and in particular Sect. 8.7, we deduce that $\Delta = 0.5$ in the spin-$\frac{1}{2}$ chain, corresponds to $\Delta \approx 0.78$ in MA, and $\Delta \approx 0.86$ in MB.

Figure 11.1c,d shows, that our results for ω are, considering that sub-leading effects are treated, not really inconsistent with (11.2), if $y_{0,4} = 4x_{\lambda,\gamma/\nu} = 2/(2-\gamma/\nu)$ is used, and γ/ν is taken from our final results in Sect. 8.1. For completeness, the results for $\Delta = 1$ are also included, but with the presence of logarithmic corrections, further

---

is why we shall not go into further detail, here.

logarithmic terms mix into the effective value of ω. Even with the exact knowledge of the leading exponent, it would not be possible to unambiguously identify the dominant sub-leading exponent out of the large set of candidate exponents (see Sect. 6.4). However, the comparison to (11.2), at least suggests that the same form also applies to our mixed spin models, MA and MB. We did try to fix ω to a reasonable value and varyingly include further exponents from the Gaussian operator content, as well as as powers of $1/\nu$ (which result from analytic corrections to FSS). However, including two exponents, one fixed and one free, leads to four free parameters in the fit, and we found that these five parameters are sufficient to always generate reasonable fits, almost independent of the specific choice of exponents.

11.2 Logarithmic Corrections

In almost every plot in this thesis, that sports datasets of pseudocritical points, or values at our estimates of critical points, a pronounced slow finite-size behaviour is apparent in both mixed spin models at the isotropic point, $\Delta = 1$ (see Fig. 11.2 for two close-ups of examples). On the one hand, postulating this behaviour to be the result of logarithmic corrections would support our main hypothesis, because logarithmic corrections are a necessary feature of the Gaussian model that is supposed to describe the critical properties of MA (5.2) and MB (5.3). On the other hand, assuming our main hypothesis automatically leads to the conclusion, that the observed corrections to FSS at $\Delta = 1$, are indeed logarithmic. As described in Sect. 5.6, logarithmic corrections “spoil” the finite-size behaviour an virtually all length scales accessible in numerical methods and entails a chain of difficulties in a correct analysis.

In this section, we shall resume our numerical evidence for the presence of logarithmic corrections and explore the effective values of exponent ratios and the scaling dimension x_λ, obtained in Sects. 8 and 9. After this, we account for our attempts to quantify logarithmic corrections.

In the presence of logarithmic corrections, the size dependence of an observable $\mathcal{O}$ at the critical or pseudocritical points can be described by (see Sects. 5.6 and 6.4)

$$\mathcal{O}(L) = \mathcal{O}_0 + \mathcal{O}_1 L^{\rho/\nu} \mathcal{Z}^{\hat{\rho} - \rho\hat{\nu}/\nu} (1 + \cdots) \,. \tag{11.3}$$

The exponents ρ and $\hat{\rho}$ control the leading scaling behaviour of $\mathcal{O}$, $\mathcal{O}_0$ is a possible constant background term and the amplitude $\mathcal{O}_1$ is, in fact, only asymptotically constant. It is a function of the scaled variables r_u and r_l and thus generally depends itself on the system size L (see Sect. 6.4). The variable $\mathcal{Z}$ was introduced in Sect. 5.6 and shall be readdressed below. For the moment, it is important that asymptotically $\mathcal{Z} \sim \ln L$.

According to our main hypothesis, the exponent ratios relevant in FSS take the following values,

$$\frac{1}{\nu} = \frac{3}{2} \,, \quad \frac{\alpha}{\nu} = \frac{\gamma}{\nu} = 1 \,. \tag{11.4}$$

We empirically had to modify the corresponding ratio for the transversal string ob-

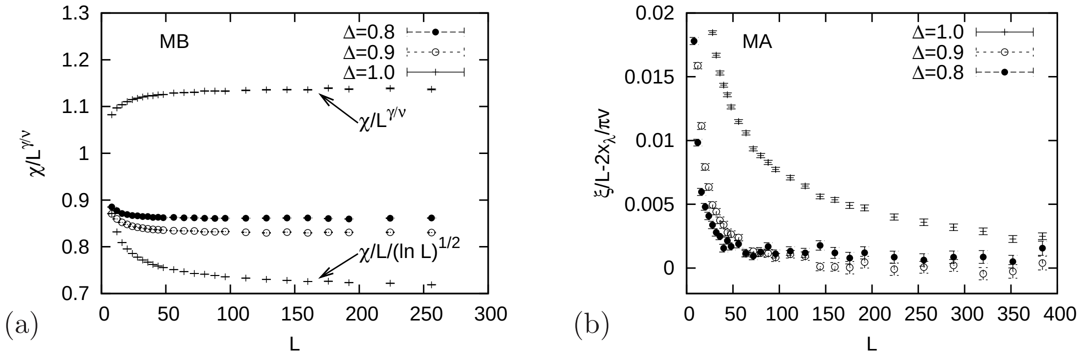

Figure 11.2: Pronounced slow convergence of the scaled susceptibility and the scaled correlation length at the isotropic point, $\Delta = 1$. (**a**) The effective amplitude of the leading correction changes sign, when the susceptibility χ is scaled with $L(\ln L)^{1/2}$ instead of $L^{\gamma/\nu}$, with the effective estimate for γ/ν from Sect. 8.1. (**b**) The scaled correlation length ξ/L is shifted by the leading amplitude $2x_\lambda/\pi v$, for better comparison.

servable D_z, which we expected to be $\beta_z/\nu = 1/8$, to

$$\frac{\beta_z}{\nu} = \frac{1}{4}\,. \tag{11.5}$$

The hatted log-exponents are universal. They are known exactly for the spin-$\frac{1}{2}$ chain,

$$\hat{\nu} = \frac{1}{2}\,, \quad \hat{\alpha} = -1\,, \quad \hat{\gamma} = 1 \quad \hat{\beta}_z = -\frac{1}{8}\,,\,, \tag{11.6}$$

where $\hat{\beta}_z$, actually denotes the exponent for the logarithmic corrections in the polarization of the quantum Ashkin–Teller model. This leads to the following combinations of exponents that are relevant in FSS,

$$\frac{\hat{\nu}}{\nu} = \frac{3}{4}\,, \quad \hat{\alpha} - \frac{\alpha}{\nu}\hat{\nu} = -\frac{3}{2}\,, \quad \hat{\gamma} - \frac{\gamma}{\nu}\hat{\nu} = \frac{1}{2}\,, \quad \hat{\beta}_z + \frac{\beta_z}{\nu}\hat{\nu} = -\frac{1}{16}\,, \tag{11.7}$$

where, again, we should separate the equation for β_z and $\hat{\beta}_z$, and rather state $\hat{\beta}_z + \frac{\beta_z}{\nu}\hat{\nu}$, to be unknown.

With this remark in mind, we assume the same hatted log-exponents for our mixed spin models. Thus, the expected leading finite-size behaviour of the susceptibility χ, and the specific head c_λ, at the isotropic point is

$$\chi(L) \sim L(\ln L)^{1/2}\,, \tag{11.8}$$

$$c_\lambda(L) \sim L(\ln L)^{-3/2}\,. \tag{11.9}$$

The effect of the logarithmic factor is particularly drastic in χ (see Fig. 11.2a), where the amplitude A, made a jump at $\Delta = 1$ in Sect. 8.1 (see Fig. 8.5a) against the general trend and the effective background came out negative, suddenly smoothly fits in the general trend. Neglecting the logarithmic modifications in a FSS analysis leads to effective estimates of the critical exponent ratios [204]. In Sect. 8.1, we estimated

$\gamma/\nu = 1.0656(13)$ for MA and 1.0718(15), which are slightly larger than the expected value, which is in very good agreement with imagining the logarithm being mimicked by an appropriate small power in L, the exponent of which depends on various factors, such as the window of chain lengths used in the fits. In Sect. 8.3, we estimated $\alpha/\nu = 0.75(2)$ for MA and 0.77(4), which are, in fact, significantly smaller than the expected value, but still in qualitative agreement with the image of the logarithm as a small power. The same happens with our estimates of $1/\nu$ (the covariance-weighted mean of MA at $\Delta = 1$ is $1/\nu = 1.392(2)$, and for MB $1/\nu = 1.375(5)$). The FSS exponent of the logarithm is $-\hat{\nu}/\nu = -3/4$, leading to effective exponent ratios that underestimate the true value $1/\nu = 3/2$, which is exactly what has been observed in Sect. 8.2, and at least in qualitative agreement with Affleck and Bonner [204], who calculated for the spin-$\frac{1}{2}$ chain the effective exponent $1/\nu = 1.28$. The estimate of exponent ratio β_z/ν, presented in Sect. 8.4, at the isotropic point is 0.2672(15) for MA and 0.2720(17) for MB, which is, again, in agreement with assuming the leading behaviour $L^{-\beta_z/\nu}$ being further suppressed by an additional small effective power (such as $-1/16$?).

Facing a difficult analysis, we have tested all methods applied in this section on the spin-$\frac{1}{2}$ chain, for which we simulated 30 different chain lengths between $L = 8$ and 512 precisely at the critical point $\lambda = 1$, with $5 \cdot 10^5$ measurements each.

We started our attempts to quantify the logarithmic corrections by testing if it was possible to extract the values of the hatted exponents if the exact critical exponent were fed into the analysis. We thus applied

$$\frac{\mathcal{O}(L)}{L^{\rho/\nu}} = Bx^{\hat{\theta}}\,, \tag{11.10}$$

with the free parameters B, an effective amplitude, and $\hat{\theta} = \hat{\rho} - \rho\hat{\nu}/\nu$. Having only two parameters to fit, we could raise $L_{\min}$, the minimum chain length used, to rather large values, reaching a roughly stable region of estimates of $\hat{\theta}$ at $L \approx 100$ in all three models. Table 11.1 lists all results that we consider to deliver good estimates as far as fits to (11.10) are concerned. In all three models we should get $\hat{\gamma} - \gamma\hat{\nu}/\nu = 1/2$ from the maxima of the susceptibility χ (respectively the values at $\lambda = 1$ in the spin-$\frac{1}{2}$ chain) and $\hat{\alpha} - \alpha\hat{\nu}/\nu = -3/4$ from the specific heat at the critical point. The former is clearly underestimated in all three models, while the latter is underestimating the spin-$\frac{1}{2}$ chain, and overestimated in the mixed spin models. Even if $L_{\min}$ is raised further, the exact values are not better produced. But, at least, the values are not completely and give at least the correct sign and approximate region of the exact value can be found. For $\hat{\beta}_z - \beta_z\hat{\nu}/\nu$ we found indeed a very small value which could indicate an exact value $\hat{\beta}_z - \beta_z\hat{\nu}/\nu = -1/16 = -0.0625$, but certainly also $-1/8 = -0.125$. This impossible to decide upon our numerical analysis.

In the next step, we tested if it was possible to see a linear behaviour in $\ln L$, which should appear when plotting

$$\left(\frac{\mathcal{O}_L}{L^{\rho/\nu}}\right)^{1/(\hat{\rho}-\rho\hat{\nu}/\nu)} \sim \mathcal{Z} \sim \ln L\,, \tag{11.11}$$

versus $\ln L$. That this indeed the case can be seen in Fig. 11.3 for the susceptibility χ (with $\gamma/\nu = 1$ and $\hat{\gamma} + \gamma\hat{\nu}/\nu = 1/2$) and for the specific heat c_λ (with $\alpha/\nu = 1$ and

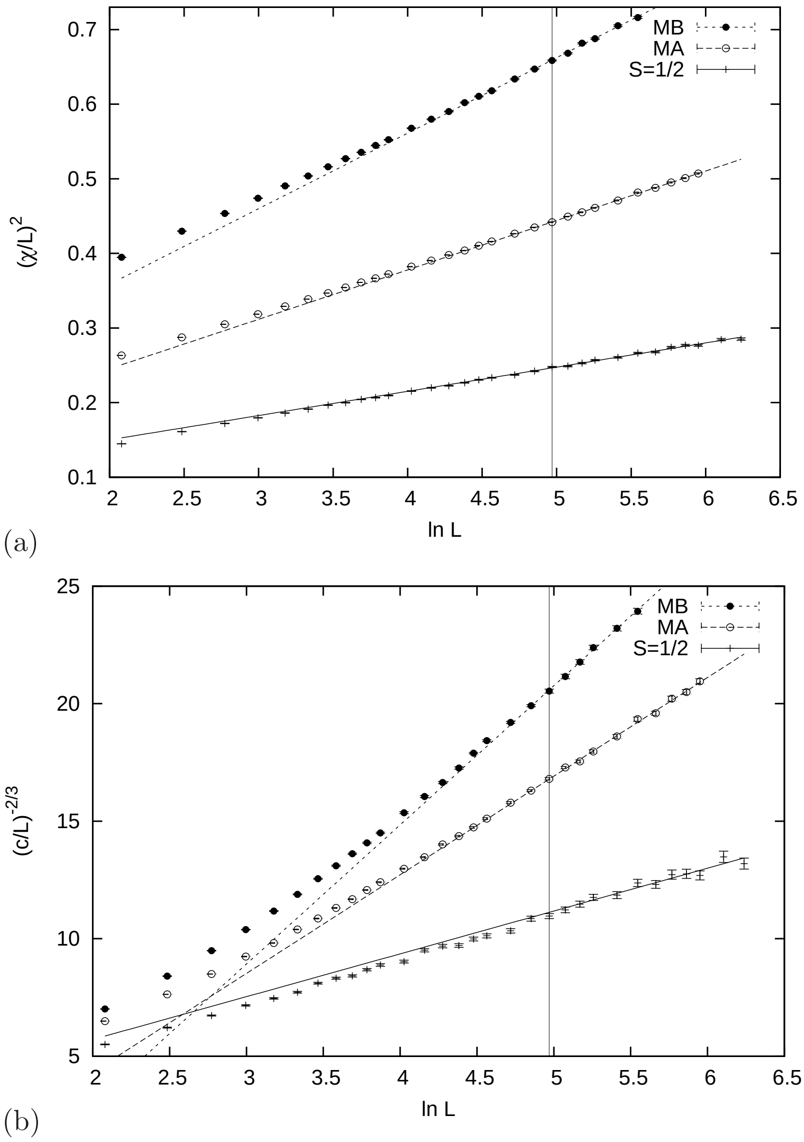

Figure 11.3: Asymptotic linear behaviour of the susceptibility χ (**a**) and the specific head c_λ (**b**). Vertical lines mark the smallest chain length used in the linear fit to (11.10). Mixed spin models, MA and MB, are compared to the spin-$\frac{1}{2}$ chain.

Table 11.1: Results of fits to (11.10).

		$L_{\rm min}$	$L_{\rm max}$	B	$\hat{\theta}$	dof	$\chi^2_{\rm dof}$
$S = 1/2$,	χ	160	512	0.29(1)	0.340(12)	9	1.19
MA,	χ	144	384	0.54(1)	0.381(3)	8	0.59
MB,	χ	112	256	0.88(1)	0.385(7)	6	1.69
$S = 1/2$,	c_λ	160	512	0.20(4)	−1.252(89)	9	0.87
MA,	c_λ	144	384	0.41(3)	−1.825(32)	8	0.97
MB,	c_λ	112	256	0.60(3)	−2.075(27)	6	0.50
$S = 1/2$,	D_z	160	512	1.25(11)	−0.080(49)	9	0.85
MA,	D_z	144	384	1.28(2)	−0.114(7)	8	0.83
MB,	D_z	112	256	1.30(1)	−0.135(5)	6	0.37

$\hat{\alpha} + \alpha\hat{\nu}/\nu = -3/2$). However, the drawback is that for the linear fits $L_{\rm min} = 160$ had to be used, in order to really see a linearity in $x = \ln L$. The variable x then ranges roughly from $x = 5$ to 6, and it could be argued that many functions look linear on such a short range. For both observables, compared to the spin-$\frac{1}{2}$ chain, a visibly stronger non-linear behaviour at small L can be seen in the mixed spin models. What is also apparent in Fig. 11.3, is that in the mixed spin models the datapoints at small L lie clearly above the "asymptotic" linearity, while in the spin-$\frac{1}{2}$ chain they lie slightly below. A technical difference in the data shown for χ, is that the maxima of the mixed spin models' susceptibility have been used, while for the spin-$\frac{1}{2}$ chain it was the values of χ at the critical point. Strictly speaking, these quantities behave slightly different, but we have checked this with the values of χ at our estimates of the critical points also for the mixed spin models and did not find a significant different. This relates to the observation of the fast shift of pseudocritical points, discussed in Sect. 7.2, which showed that for sufficiently large L, the pseudocritical points are essentially identical with the true critical point within the statistical accuracy.

We then focussed on the susceptibility only, representing our best data sets, to put the variable $\mathcal{Z}$ as given by virtue of (5.54), (5.55) and (5.60) with $l = \ln L$ in Sect. 5.6 (see also (6.117) in Sect. 6.4), to the test for the spin-$\frac{1}{2}$ chain. It reads in full, for reference,

$$\mathcal{Z} = \frac{u_0}{a_2 + a_3 u_0} \left(a_3 + \frac{a_2}{u_0} \frac{1 + a_2 u_0 \ln L}{1 - \frac{a_3}{a_2^2} \frac{\ln[\ln L + 1/(a_2 u_0) + a_3/a_2^2]}{\ln L + 1/(a_2 u_0)}} \right) , \tag{11.12}$$

with $a_2 u_0 = 1.753$. The susceptibility should behave as

$$\chi_L \sim A L \mathcal{Z}^{1/2} \left(1 + \frac{B}{A} L^{-1} \mathcal{Z}^{-1/2} \cdots \right) , \tag{11.13}$$

with B, a possible background, and A the leading amplitude. In the simplest fit, there is only the amplitude A that is a free parameter. We had to choose $L_{\rm min} = 224$ rather large, to be able to produce a reasonable fit. If (11.12) is indeed a good approximation

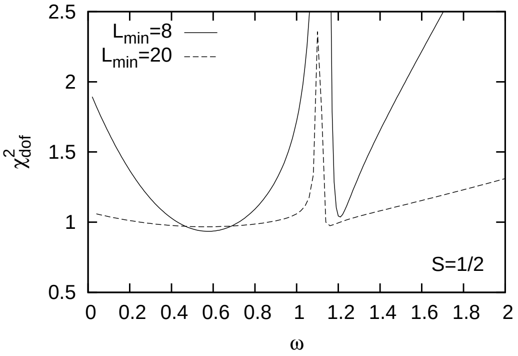

Figure 11.4: χ^2-deviation per degree of freedom (dof), for the fit of the susceptibility χ at the isotropic point of the spin-$\frac{1}{2}$ chain to (11.14). The effective correction exponent ω has been varied "by hand". We associate the first minimum to the presence of a power-law correction in $L^{-1/2}$ (see main text).

of the true behaviour of $\mathcal{Z}$ of the spin-$\frac{1}{2}$ chain – and the data in Fig. 1 of [210] confirm that it is –, this must be due to the terms in the brackets of (11.13), which could either be the background as indicated or neglected power-law corrections (indicated by the ellipses).

We tested for the presence of power-law corrections by varying the (effective) correction exponent ω, in a fit to

$$\chi_L = AL\mathcal{Z}^{1/2}\left(1 + CL^{-\omega}\right) , \tag{11.14}$$

"by hand", with the remarkable result shown in Fig. 11.4. The χ^2-deviation per degree of freedom shows two clear minima when the fit is performed with all datapoints ($L = 8 \ldots 512$). The first minimum resides at $\omega \approx 0.6$, and a second one appears at $\omega \approx 1.2$. Increasing $L_{\min}$ slightly, the first minimum becomes very shallow but the peculiar shape at the second minimum remains. Now there are two Gaussian scaling operators providing RG eigenvalues $|y_{2,2}| = |y_{1,4}| = 1/2$ at the isotropic point. In the view of Fig. 11.4 is is very likely that at least one of them does indeed generate significant non-analytic corrections to FSS. Fits to (11.14) with the exponent $\omega = 1/2$ fixed, give reasonable results. A sample of fit results to (11.14) with and without explicit background is given in Table 11.2. The essence is, that while it is reasonable to assume the presence of the $L^{-1/2}$-term, it is impossible to proof numerically. The second minimum shown in Fig. 11.4 might be the artefact of further powers of L being present, and there are plenty of candidates of primary and secondary operators, or the background incorporated as in (11.13), that deliver exponents $\omega = 1 \ldots 3/2$. Including either of them, fixed or as free parameter, induced enough degrees of freedom to perfectly fit our data. With this in mind, Table 11.2 with the aid of Fig. 11.4 can still be interpreted as a remarkable confirmation of the form (11.12), which is based on an approximate solution of the third order RG differential equation for the marginal field [210]. In particular, from Table 11.2 we can deduce a good estimate for the leading amplitude of the susceptibility of the spin-$\frac{1}{2}$ chain at the isotropic point:

$$A = 0.190(1)\,. \tag{11.15}$$

However, we must remark that as soon as we relax the ingredient $a_2u_0 = 1.753$, and consider it a free parameter, it drifts in fits to smaller values if $L_{\min} < 20$ is small, but for $L_{\min}$ larger, the minimum of χ^2_{dof} is particularly shallow and permits at most the conclusion $a_2u_0 > 0.5$. This way it would be rather difficult to get an estimate

Table 11.2: Results of various fits of the susceptibility of the spin-$\frac{1}{2}$ chain to (11.13) and (11.14). With $\mathcal{Z}$ given in (11.12), $a_2u_0 = 1.753$ [210] and $L_{\max} = 512$. The exponent ω, if given in the list, was fixed “by hand”.

$\chi L^{-1} = f(L)$	$L_{\min}$	ω	B	A	C	dof	χ^2_{dof}
$A\sqrt{\mathcal{Z}}$	224			0.1915(3)		5	1.54
$B{+}A\sqrt{\mathcal{Z}}$	128		0.8(2)	0.1905(4)		10	1.15
$B{+}A\sqrt{\mathcal{Z}}(1{+}CL^{-\omega})$	8	0.58	−0.12(2)	0.1894(2)	0.32(2)	30	0.93
	20	0.56	−0.14(4)	0.1892(4)	0.32(4)	27	0.97
$A\sqrt{\mathcal{Z}}(1{+}CL^{-1/2})$	56		0.1892(3)		0.21(2)	17	1.00
$B{+}A\sqrt{\mathcal{Z}}(1{+}CL^{-1/2})$	32		−0.03(9)	0.1892(6)	0.22(5)	21	1.04

of a_2u_0, if it was *a priori* unknown. This is yet, unfortunately, the case in the mixed spin models.

For the mixed spin chains, the situation is considerably different. We have no value to fix a_2u_0 to. Varying a_2u_0 and repeating the fits from above produced the disastrous output, that everything is possible. Minima of χ^2_{dof} are extremely shallow and essentially open towards large values of a_2u_0. But even worse, the fit parameters, in particular the leading amplitude, depend strongly on the value that a_2u_0 is set fixed to with no region of consistent results. We cannot even conclude, that (11.12) must be a bad approximation for the variable $\mathcal{Z}$, because of the additional power-law corrections, that are essentially out of control, as soon as a_2u_0 becomes a free parameter, even with exponents set to fixed values. We thus, for matters of completeness, comparison, and possibly future reference, applied fits to the asymptotic FSS forms derived by Salas and Sokal [211],

$$\frac{\mathcal{O}_L}{L^{\rho/\nu}(\ln L)^{\hat{\rho}-\rho\hat{\nu}/\nu}} = A\left(1 + (\hat{\rho} - \rho\hat{\nu}/\nu)\frac{a_3}{a_2^2}\frac{\ln\ln L}{\ln L} + \frac{K}{\ln L}\right) . \tag{11.16}$$

and, in slightly different form – by Shchur et al. [262], where the second term has a universal amplitude and is obtained using the approximation $(1-x)^{-n} \approx 1 + nx$, which holds for sufficiently small x. Shchur et al. [262] argued that $\ln\ln L/\ln L$, is not sufficiently small for this approximation to hold. The non-universal third term with amplitude K in (11.16) might effectively capture this. Results are listed in Table 11.3, for the susceptibility χ and the specific heat c_λ. Generally, the χ^2-deviation is reasonable. It is interesting to note that the (effective) amplitude of χ in the spin-$\frac{1}{2}$ is smaller than and, in fact, inconsistent with the value obtained above. It is largest in MB, while the amplitude of c_λ is smallest in MB, and largest in the spin-$\frac{1}{2}$ chain.

In contrast to observables such as the susceptibility, and the specific heat (or the string observable), the FSS behaviour of the correlation length ξ does not involve the variable $\mathcal{Z}$ if hyperscaling holds (see Sect. 5.6). Accepting the main hypothesis of this thesis, implies that hyperscaling is satisfied, and there is no need to assume multiplicative logarithmic modification in the FSS behaviour of the correlation length. We shall discuss our results on the basis of the fourth-moment estimator of the imaginary time correlation length, here. Scaled by L, the correlation length is supposed to converge

Table 11.3: Results of fits to (11.16).

model	obs	L_{min}	L_{max}	A	K	dof	χ^2_{dof}
$S = 1/2$,	χ	56	512	0.1767(7)	0.89(3)	18	1.00
MA,	χ	160	384	0.374(2)	0.57(2)	7	0.70
MB,	χ	96	256	0.612(4)	0.54(4)	7	1.46
$S = 1/2$,	c_λ	48	512	0.42(2)	−0.15(9)	19	1.36
MA,	c_λ	144	384	0.177(8)	3.1(3)	9	0.80
MB,	c_λ	80	256	0.120(7)	6.1(5)	10	1.48

Table 11.4: Results of fits of the correlation length ξ to three different ansatz functions.

model	fit	L_{min}	L_{max}	B	A	K	dof	χ^2_{dof}
$S = 1/2$	(11.18)	32	512	1.003(3)	0.095(3)		23	0.47
	(11.19)	32	512	0.973(2)	0.155(4)		22	0.43
	(11.20)	32	512	0.988(3)	0.125(4)		23	0.43
MA	(11.18)	80	384	0.924(2)	0.140(3)		13	0.33
	(11.19)	32	384	0.959(7)	0.0580(2)	0.163(24)	20	0.51
	(11.20)	80	384	0.793(4)	0.141(3)		13	0.33
MB	(11.18)	72	256	0.895(7)	0.162(7)		10	1.28
	(11.19)	32	256	0.958(20)	0.022(38)	0.269(61)	17	1.31
	(11.20)	72	256	0.875(8)	0.209(10)		10	1.32

to a “background” given by $B = 1/(2\pi v x_{1,0})$, which for the spin-$\frac{1}{2}$ chain takes the exactly known value $2/\pi^2$. Considering only the marginal field in a Taylor expansion of the scaling form of ξ, we fitted

$$\frac{\xi}{L} = B\frac{2}{\pi^2} + Au(\ln L)\,, \tag{11.17}$$

where the amplitude A has the meaning of a Taylor coefficient and B measures the deviation from $2/\pi^2$. We thus expect for the spin-$\frac{1}{2}$ chain to find $B = 1$.

As above, we tried different versions of $u(\ln L)$. Following [211], we used

$$\xi_L = B\frac{2}{\pi^2} + A\left(\frac{1}{\ln L} - \frac{a_3}{a_2^2}\frac{\ln\ln L}{(\ln L)^2}\right)\,, \tag{11.18}$$

and

$$\xi_L = B\frac{2}{\pi^2} + A\left(\frac{1}{\ln L} - \frac{a_3}{a_2^2}\frac{\ln\ln L}{(\ln L)^2}\right) + \frac{K}{(\ln L)^2}\,. \tag{11.19}$$

And following [210], we further used

$$\xi_L = B\frac{2}{\pi^2} + Au^{(2)}(\ln L) f_{\text{c}}^{(3)}(\ln L)\,, \tag{11.20}$$

with $f_c^{(3)}$ given in (5.61), for all three models. Results are listed in Table 11.4. Interestingly enough, the fit to (11.18) yields the best agreement with the expectation $B = 1$ in the spin-$\frac{1}{2}$ chain. Including the effective term $K/\ln L$, does not improve the result, neither does using Nomura's approximation (11.20). Quite obviously, the three different fits deliver inconsistent results within the mixed spin models. On the basis of χ^2_{dof}, it would not be possible to decide upon which result is better. A correct ansatz for the FSS behaviour would also include powers of L. Even though we considered our data at the isotropic point of good quality, we did not succeed incorporating even a single fixed correction exponent, in the sense that would yield illuminating results. This simply illustrates the difficulties in dealing with logarithmic corrections.

Remains to revisit our estimates of the critical points themselves, and to discuss the possible effect of logarithmic corrections thereon, before concluding this section, and, in fact, this thesis. In the presence of logarithmic corrections, the leading shift of pseudocritical points is supposed to follow,

$$\lambda^*(L) = \lambda_c + AL^{-3/2}\mathcal{Z}^{3/4} \,. \tag{11.21}$$

We have argued, that is not of much value to use $f_c^{(3)}$, in order to closedly express the variable $\mathcal{Z}$, when analyzing data of our mixed spin models. The replacement of $\mathcal{Z}$ by $\ln L$, is by no means justified, unless an effective term is introduced to capture thus generated correction terms. We ignored the logarithmic modification in Sect. 7.2, and judged the change with $L_{\min}$ of the final estimate of λ_c (see Figs. 7.3a and 7.4a for examples). However, ignoring logarithmic corrections inevitable leads to effective values of shift exponents. The zeros of the twist parameter provided our most accurate pseudocritical points. They converge to λ_c from below, thus presence of logarithmic corrections might lead to underestimated final values obtained from pure power-law fits, because a power, as small as it might be, will always asymptotically converge faster than a logarithm. This is why we have performed this final test. While using simply $\mathcal{Z}^{3/4} \sim (\ln L)^{3/4}$, did not lead to stable results when varying $L_{\min}$, the usage of

$$\mathcal{Z}^{3/4} \sim (\ln L)^{3/4} \left(1 + \frac{3}{8}\frac{\ln\ln L}{\ln L} + \frac{K}{\ln L}\right) , \tag{11.22}$$

did. We obtained for the latter $\lambda_c = 0.76223(1)$ in MA for $L_{\min} = 80$ with $\chi^2_{\text{dof}} = 1.00$, and $\lambda_c = 0.62114(3)$ in MB for $L_{\min} = 72$ with $\chi^2_{\text{dof}} = 1.57$. These values are to be compared to our final QMC estimates of Sect. 7.2, which are $\lambda_c = 0.76218(1)$ and $\lambda_c = 0.62098(2)$, respectively. For MA, the different estimates are almost consistent, indicating that we might have underestimated the error by a factor of two or three. For MB it is slightly worse, with a possible underestimation by a factor of four or five. Taking into account the high precision of estimates of $\lambda_c(\Delta)$ given in Table 7.6, we consider this acceptable. In the course of all of our analyses of critical exponent ratios, the results of which are presented in Sect. 8, we have checked the influence of the precise estimate of λ_c on the final estimate of exponents, by varying λ_c within up to six errorbars. Apart from the string observables (Sects. 8.4 and 8.5), we have not found any significant influence of more than just a few percent. Thus, we conclude the estimates of λ_c, given in Table 7.6, still to be worth quoted in their own right.

12 Summary, Conclusion and Outlook

Critical properties of two anisotropic mixed quantum spin chains, with a basecell structure $S^a - S^a - S^b - S^b$, that contains two different sizes of spin S^a, and S^b, have been the central topic of this thesis. In the basecells of the first model, denoted MA, $S^a = 1/2$, and $S^b = 1$, while in the second model, denoted MB, $S^a = 1/2$, and $S^b = 3/2$. The Hamiltonian, written in terms of the control parameters λ and Δ, which control the coupling between spin of different size, i.e. bond alternation, and the XXZ exchange anisotropy, has been introduced in Sect. 1 and stated in the precise form used in this thesis in Sect. 5.1. It has been placed into materials' context in Sect. 2.

Part I of this thesis contains an introduction into selected topics of theoretical background (Sects. 3–5) and an extensive description of the main computational methods of data production and analysis (Sect. 6). The most important quantities of interest in this thesis, critical exponents, have been introduced in Sect. 4, and highlighted from different points of view, that of renormalization and that of conformal invariance. An extensive knowledge of the critical properties of the spin-$\frac{1}{2}$ chain exists in the literature, part of which has been the topic of Sect. 5, along with some consideration of the spin-1 chain, but in particular the implications on mixed spin models of this thesis. In Sect. 5.4 we defined an observable based on strings of subspins, that we conjecture to be related to the hidden symmetry breaking in both, the spin-$\frac{1}{2}$ and the spin-1 chain, while Sect. 5.5, where the well-known Gaussian description of the spin-$\frac{1}{2}$ chain is introduced, sports the main hypothesis of this thesis. Section 6 describes in detail exact diagonalization (ED) and extrapolation, as well as the loop algorithm, reweighting and finite-size scaling (FSS). To the best of our knowledge, reweighting in combination with the loop algorithm has never been applied. In particular, we managed to apply the method to improved estimators of the loop algorithm, which, being a simple modification, has neither been described nor applied in the literature.

Part II contains the presentation and discussion of our final results, the phase boundary and critical exponent ratios of both mixed spin models, with a focus on the region of interest, $0 \leq \Delta \leq 1$, in Sects. 7 and 8, respectively. We further presented direct quantum Monte Carlo (QMC) estimates of Gaussian parameters and the central charge in Sect. 9. The best results obtained in Sect. 8, i.e. the exponent ratio γ/ν of the susceptibility, and the results of Sect. 9, relied crucially on the application of reweighting methods to improved estimators. A detailed technical discussion and interpretation of exact and extrapolated finite-size spectra of MA has been given in Sect. 10, and a final discussion of corrections to the leading finite-size scaling behaviour, which have also been considered due course, in Sect. 11, in particular of logarithmic corrections at the isotropic antiferromagnetic point, $\Delta = 1$.

The results part of this thesis presented massive numerical evidence in support of our main hypothesis, given in Sect. 5.5. This suggests to state the main hypothesis as the *main conclusion* of this thesis:

Mixed spin models, MA and MB, are Gaussian.

This implies that the critical phase transitions of bond-alternating XXZ anisotropic mixed spin models studied in this thesis are in the same universality class as the corresponding transitions in uniform spin chains, in particular the spin-$\frac{1}{2}$ chain. It is a specific property of the Gaussian model that knowledge of a single critical exponent is sufficient in order to calculate all other exponents. This leads to the existence of extended scaling relations. The values of critical exponents vary continuously with the Gaussian coupling constant K, which is itself equal to an exponent. At the isotropic point, $\Delta = 1$, SU(2) invariance of the XXZ Hamiltonian forces the Gaussian coupling constant to be $K = 1/2$.

The main computational effort has been focused on a limited region of the exchange isotropy, i.e. $0 \leq \Delta \leq 1$. In this region the numerical evidence leading to our main conclusion, consists in detail of the following:

- The estimates of critical exponent ratios, presented in Sect. 8, satisfy standard and extended scaling relations, which can be compactly written via their relation to the fundamental scaling dimension x_λ, i.e.

  $$x_\lambda = \left(4 - 2\frac{\gamma}{\nu}\right)^{-1} = 2 - \frac{1}{\nu} = 1 - \frac{\alpha}{2\nu} = 2\frac{\beta_z}{\nu}\,,$$

  to within 2% and better for $0.0 \leq \Delta \leq 0.8$, and to within 5% at $\Delta = 0.9$, in both mixed spin models (see Fig. 8.28). However, based on exact and numerical results for the spin-$\frac{1}{2}$ chain, the last of the above scaling relations should read $x_\lambda = 4\beta_z/\nu$ (discussed in Sects. 8.4 and 8.8).
- The direct estimates of Gaussian parameters in Sect. 9, i.e. the coupling K and the velocity v, are consistent with our main conclusion. In particular, the estimate of the Gaussian coupling $K = x_\lambda$, agrees with the estimates obtained in Sect. 8, within at least the same percentage as above (see Fig. 9.1c,d). Furthermore, the direct calculation of the velocity v, permitted to extract the central charge c, from estimates of the groundstate energy (see insets of Fig. 9.2c,d). The data is perfectly consistent with the known value $c = 1$, of the Gaussian model.
- Extrapolation of finite-size spectra of MA up to five basecells ($L = 20$), presented in Sect. 10, revealed several energy levels that could be uniquely identified with primary or secondary scaling operators of the conformal operator content of the Gaussian model (see Fig. 10.3b). It is worth noting, that this is a remarkable success of ED, when taking into account the reduced computational effort in comparison to QMC, but we emphasize that for MB we did not push ED beyond four basecells ($L = 16$), which prevented us from producing comparative results in that case.

A consequence of our main conclusion, was pointed out in Sect. 8.7. Every Δ-point of the mixed spin models, MA and MB, corresponds to a Δ-point of the spin-$\frac{1}{2}$ chain. As a summary, the most important main results of this thesis, the critical exponent ratios determined in Sect. 8, are plotted in Fig. 12.1, the scale of Δ chosen for the

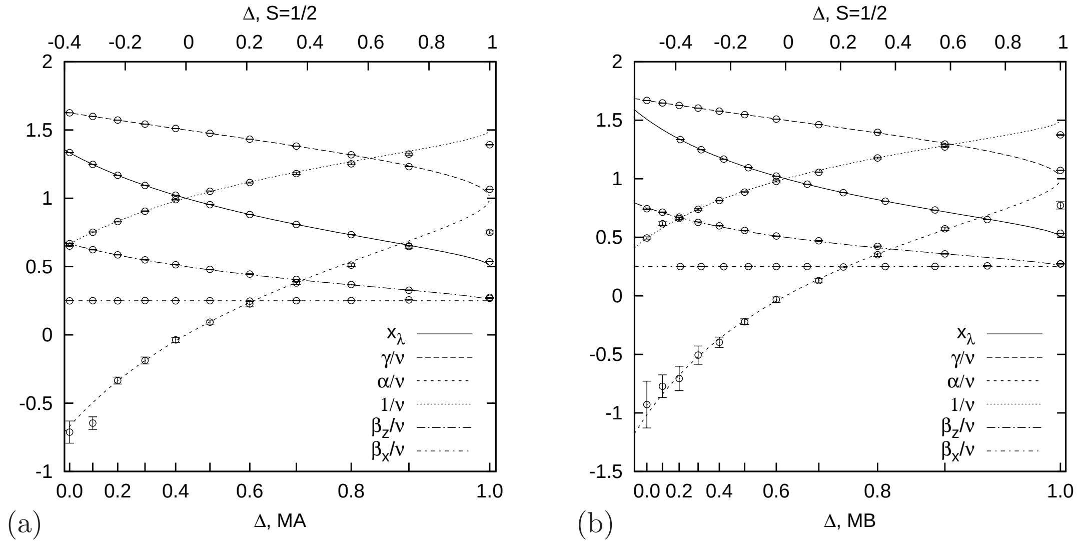

Figure 12.1: QMC results (datapoints) for the scaling dimension x_λ (Sect. 9) and all critical exponent ratios (Sect. 8). To every Δ in the mixed spin models, there corresponds a Δ of the spin-$\frac{1}{2}$ chain, which is shown by the adjusted bottom scale for the mixed spin models, MA and MB. Curves give the exactly known values of the spin-$\frac{1}{2}$ chain, with the exception of $\beta_{x/z}$, which are drawn twice as large (see Sects. 8.4 and 8.5).

mixed spin models such that a direct comparison to the exactly known values of the spin-$\frac{1}{2}$ chain is possible. Based on a phenomenologically motivated fit to a polynomial function, we "extrapolated" the results shown in Fig. 12.1, to determine the point where $1/\nu = 0$, which marks the point where the critical line fans out to become a critical region. In the spin-$\frac{1}{2}$ chain, this happens at $\Delta = -1/\sqrt{2}$, and we estimate the point to be $\Delta = -0.49(2)$ for MA and $\Delta = -0.38(3)$ for MB (see Sect. 8.7), which is not in disagreement with the rough estimate of $\Delta \approx -0.4$ in both models from the extrapolation analysis of exact pseudocritical points in Sect. 7.1. The validity of these predictions will have to be subject to future studies.

Both, the best estimate of an individual critical exponent ratio, i.e. γ/ν in Sect. 8.1, and the direct estimate of the Gaussian coupling constant $K = x_\lambda$, relied crucially on the measurement of improved QMC estimators. Due to the novel application of reweighting methods on improved QMC estimators, maxima of the quantities of interest, i.e. staggered transversal magnetic susceptibility, spin stiffness and imaginary time correlation length, could be evaluated with high precision. This lead to direct and indirect estimates of the fundamental scaling dimension x_λ, which were independent from the precise value of the critical points. We consider this thesis as proof-of-concept that improved estimators in the loop algorithm can be reweighted precisely as described in Sect. 6.3.

Prior to the determination of critical exponent ratios, the phase boundary $\lambda_c(\Delta)$, has been determined with high accuracy (see Sect. 7, and in particular Fig. 7.9). All final estimates of $\lambda_c(\Delta)$, have been determined with corrections to FSS neglected. If the observed general trend, that corrections to FSS decrease with decreasing Δ (see, e.g., Fig. 11.1), also applies to the finite-size behaviour of pseudocritical points, the isotropic point $\Delta = 1$, represents the worst case scenario with logarithmically vanishing corrections. It was shown in Sect. 11.2, that in that case we face the threat of having underestimated the true critical values by at most five errorbars.

Our attempt to generalize the definition of longitudinal and transversal string observables to mixed spin models (Sect. 5.4), raised several open questions, concerning the presence of strong corrections to scaling and the remarkable relation between exponent ratios of different moments of the observables. One of the main significances of the string observables is that the analysis of the transversal string observable D_x in Sect. 8.5, provided the only evidence in this thesis, for the presence of an exponent ratio that is constant in Δ, and consequently for the presence of a constant (non-integer) scaling dimension. Primary scaling operators with constant scaling dimension are part of the conformal operator content of the quantum Ashkin–Teller (qAT) model and, thus, the spin-$\frac{1}{2}$ chain, but do not belong to the Gaussian part of the operator content with varying scaling dimensions. A fractional scaling dimension $x_{\mathrm{P}} = 1/8$, and a scaling dimension x_{M}, that takes the same value at $\Delta = 1$ and grows continuously with decreasing Δ, are the signature of the qAT polarization and magnetization, respectively. These two observables are order parameters to detect the spontaneous breaking of a D_4-symmetry, that includes two $Z_2 \times Z_2$ sub-symmetries. Despite the, admittedly serious, conceptual problems discussed above and in Sects. 8.4, 8.5 and C, we conclude that our results for β_z/ν and β_x/ν exhibit the same signature. However, due to the mentioned difficulties, we refrain from claiming to have shown the breaking of a hidden $Z_\times Z_2$ symmetry and leave this aspect a conjecture. We remark, that extrapolation of finite-size spectra of MA (Sect. 10) showed complete absence of relevant non-integer scaling dimensions, which becomes apparent from a look at Fig. 10.3b. To determine the complete operator content of a critical model from ED and extrapolation, however, requires the consideration of general twisted boundary conditions.

The outlook on possible future projects can be divided into two complexes: work concering open questions and issues raised, and work extending the study presented in this thesis. Concerning the former we propose the following.

- Study alternative definitions of generalized string observables and measurements thereof. Instead of accumulating strings that contain an even number of sites, one could focus on strings containing an odd number, which would automatically result in a symmetric distribution of measured values. Furthermore, it could prove useful to avoid the accumulation of strings by focussing on the half-width string of length $L/2$, which corresponds to the correlation definition of the order parameter.

- Investigate the combinatorics of basis states that contribute to measurements of string observables, in order find an explanation for the observed relation between critical exponents of different moments.

- Extrapolate exact finite-size spectra of MA for different boundary conditions, in order find constant non-integer scaling dimensions.

- Invoke educated symmetry considerations, in order to gain a better control of corrections to scaling and finite-size scaling.

Projects that go beyond the present work could be the following.

- Determine the Kosterlitz–Thouless boundary, that borders the critical region, and, in particular, determine the end of the critical line, where we have presented a phenomenological estimate of.
- Use the understanding of the critical behaviour of *regular* mixed spin chains, to set out on an investigation of randomly disordered mixed spin models. In particular, the QMC algorithm implemented for this thesis is ready to go and applicable to basecells with arbitrary spin setup and a large variety of possible couplings. The field of randomly disordered spin systems includes site randomness [263, 264], which is inevitable in experimental realizations of mixed spin models, and bond randomness [265, 266], which is known to lead to Griffiths–McCoy singularities [24].
- Study the entanglement entropy of mixed spin models, where the DMRG algorithm [5] may be the optimal choice for simulations, because it implicitly calculates the block entanglement entropy as part of the algorithm. However, new methods, such as projector QMC [229], which can also be combined with the loop algorithm as used in this thesis [230], offer promising perspectives in that direction.

Part III

Appendix

A Plots

A.1 Quality of Reweighted Datasets

The plots on the following pages illustrate, as representative examples, the quality of reweighted data sets. Shown are, for both models, examples of a small system ($L = 36$ in MA, and $L = 32$ in MB) and a large system ($L = 384$ in MA, and $L = 256$ in MB), and examples of Δ with good, intermediate and bad quality data ($\Delta = 1, 0.2$ and 0 in MA, and $\Delta = 1, 0.4$ and 0 in MB).

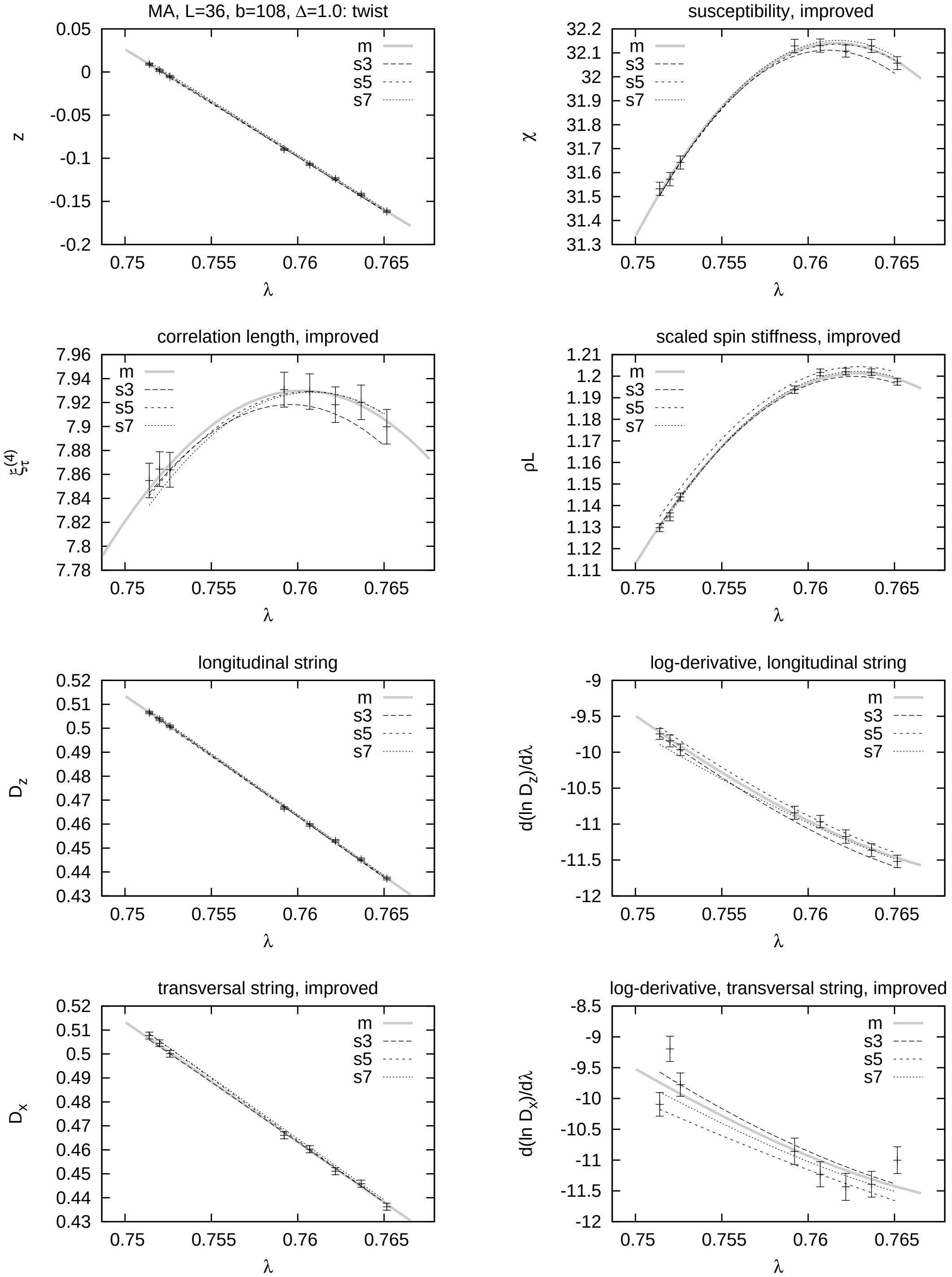

Figure A.1: Data of MA at $\Delta = 1$, $L = 36$ and $\beta = 108$. The label "si" (m) denotes data from single-(multi-)histogram reweigthing of the i-th (all) point(s).

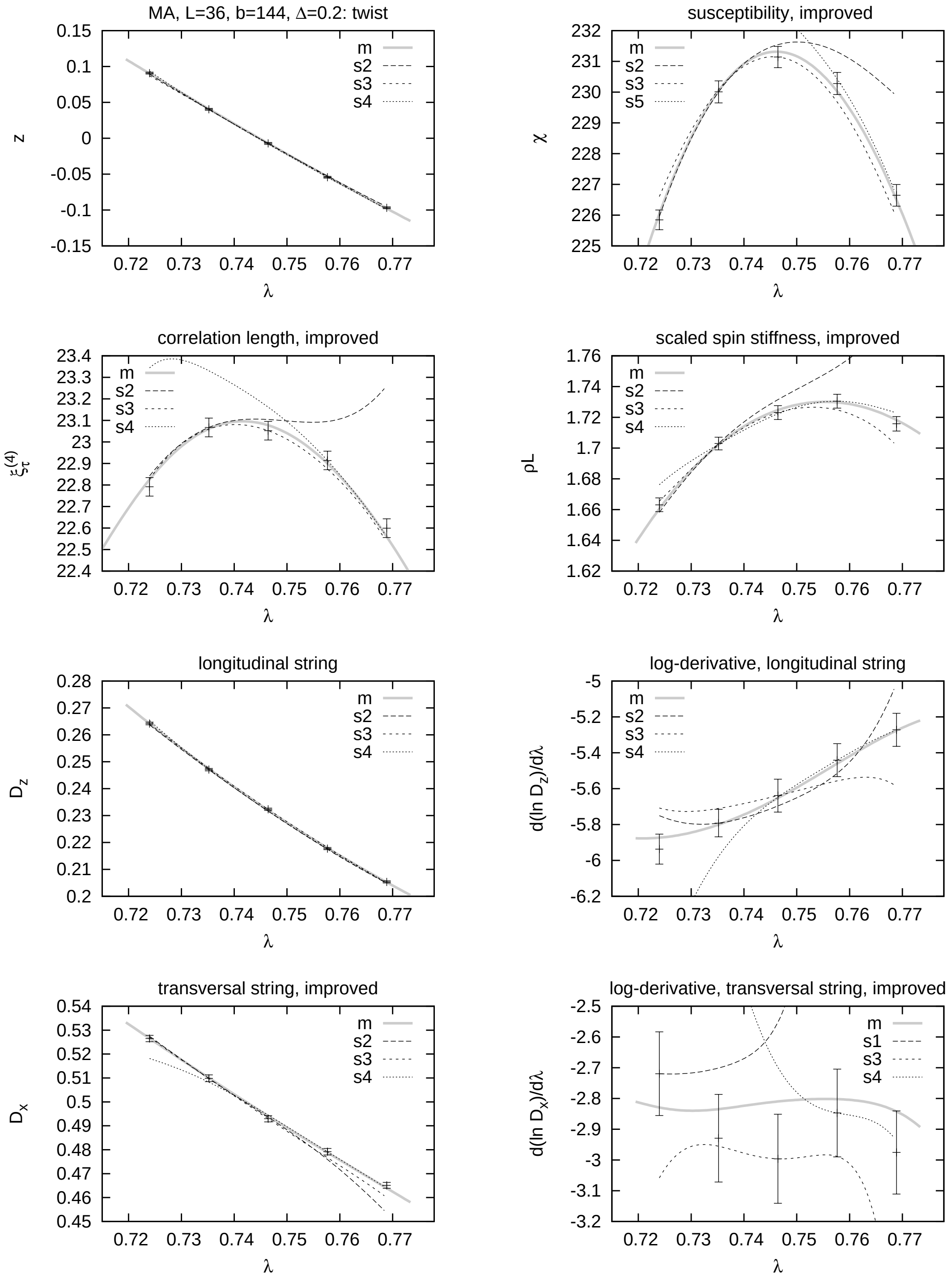

Figure A.2: Data of MA at $\Delta = 0.2$, $L = 36$ and $\beta = 144$. The label "si" (m) denotes data from single-(multi-)histogram reweigthing of the i-th (all) point(s).

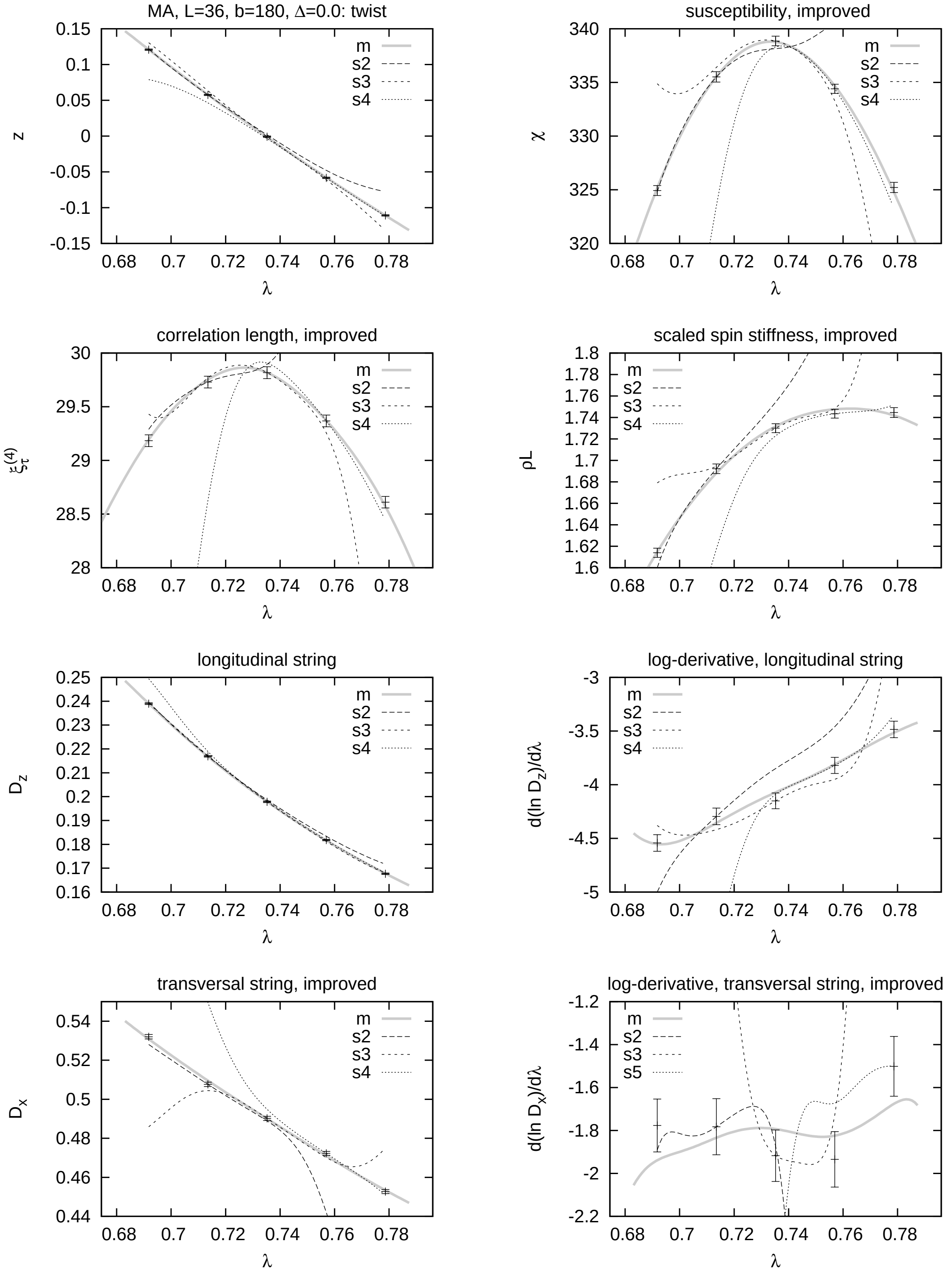

Figure A.3: Data of MA at $\Delta = 0.0$, $L = 36$ and $\beta = 180$. The label “si” (m) denotes data from single-(multi-)histogram reweigthing of the i-th (all) point(s).

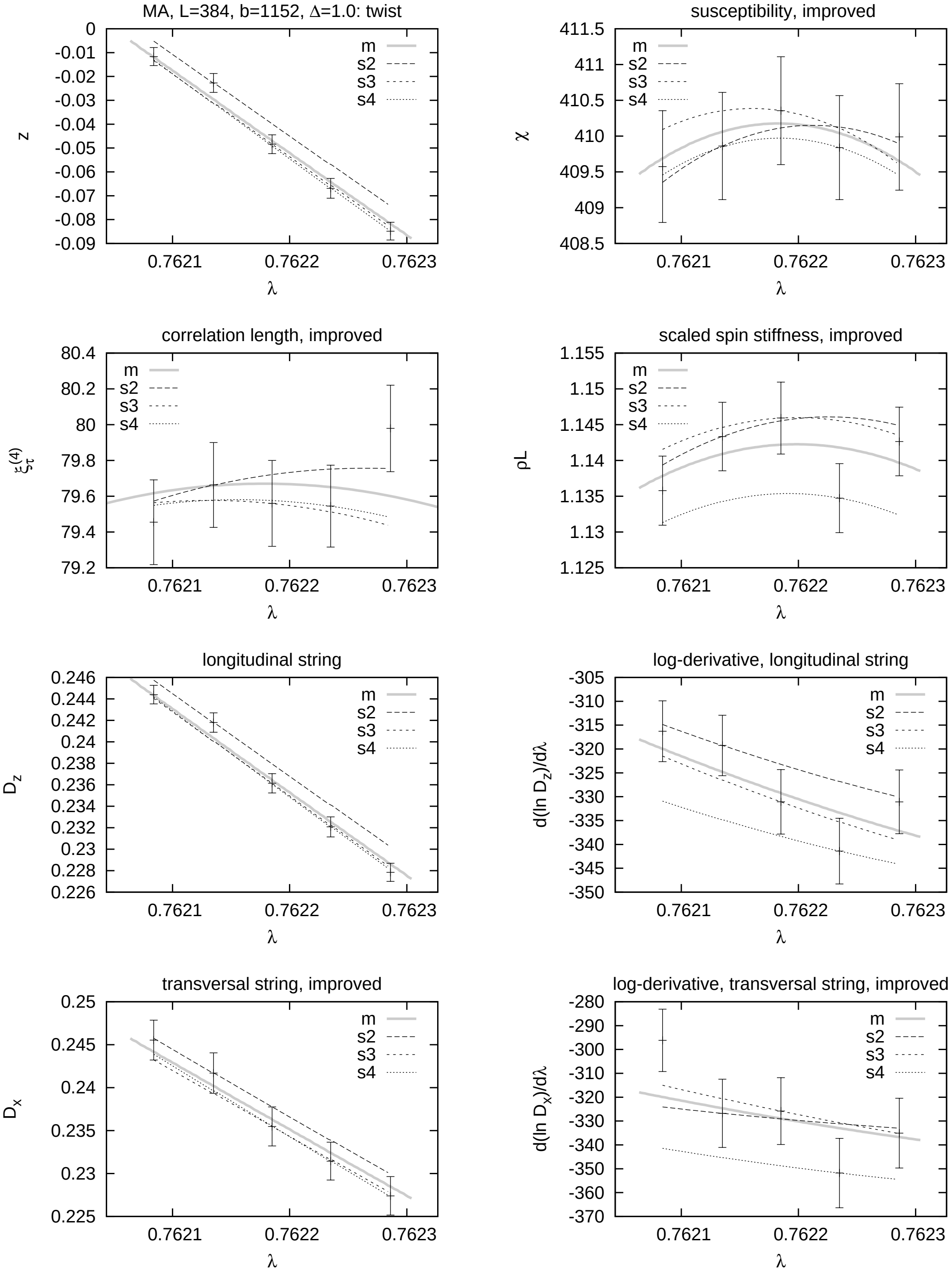

Figure A.4: Data of MA at $\Delta = 1.0$, $L = 384$ and $\beta = 1152$. The label "si" (m) denotes data from single-(multi-)histogram reweigthing of the i-th (all) point(s).

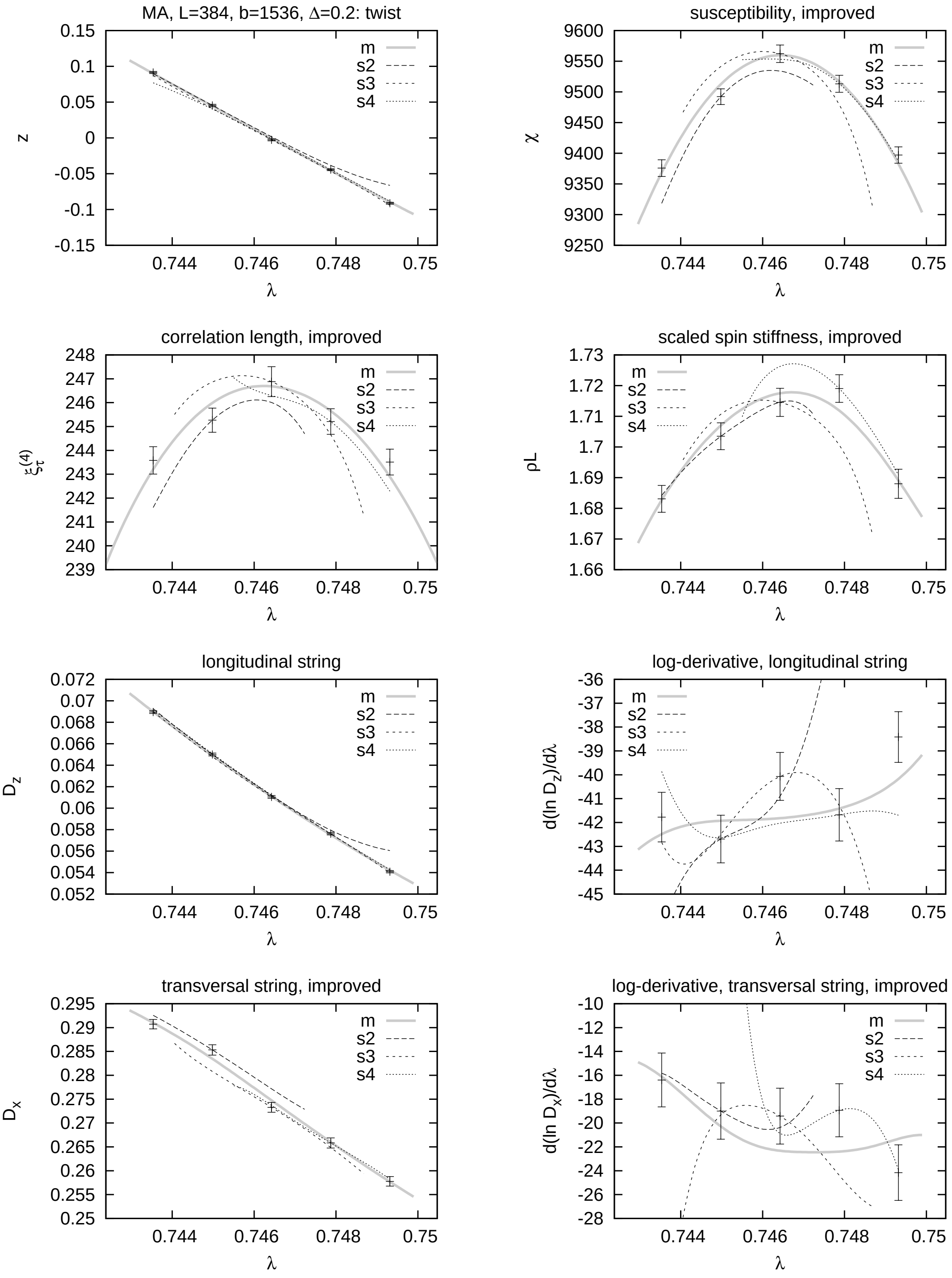

Figure A.5: Data of MA at $\Delta = 0.2$, $L = 384$ and $\beta = 1536$. The label "si" (m) denotes data from single-(multi-)histogram reweigthing of the i-th (all) point(s).

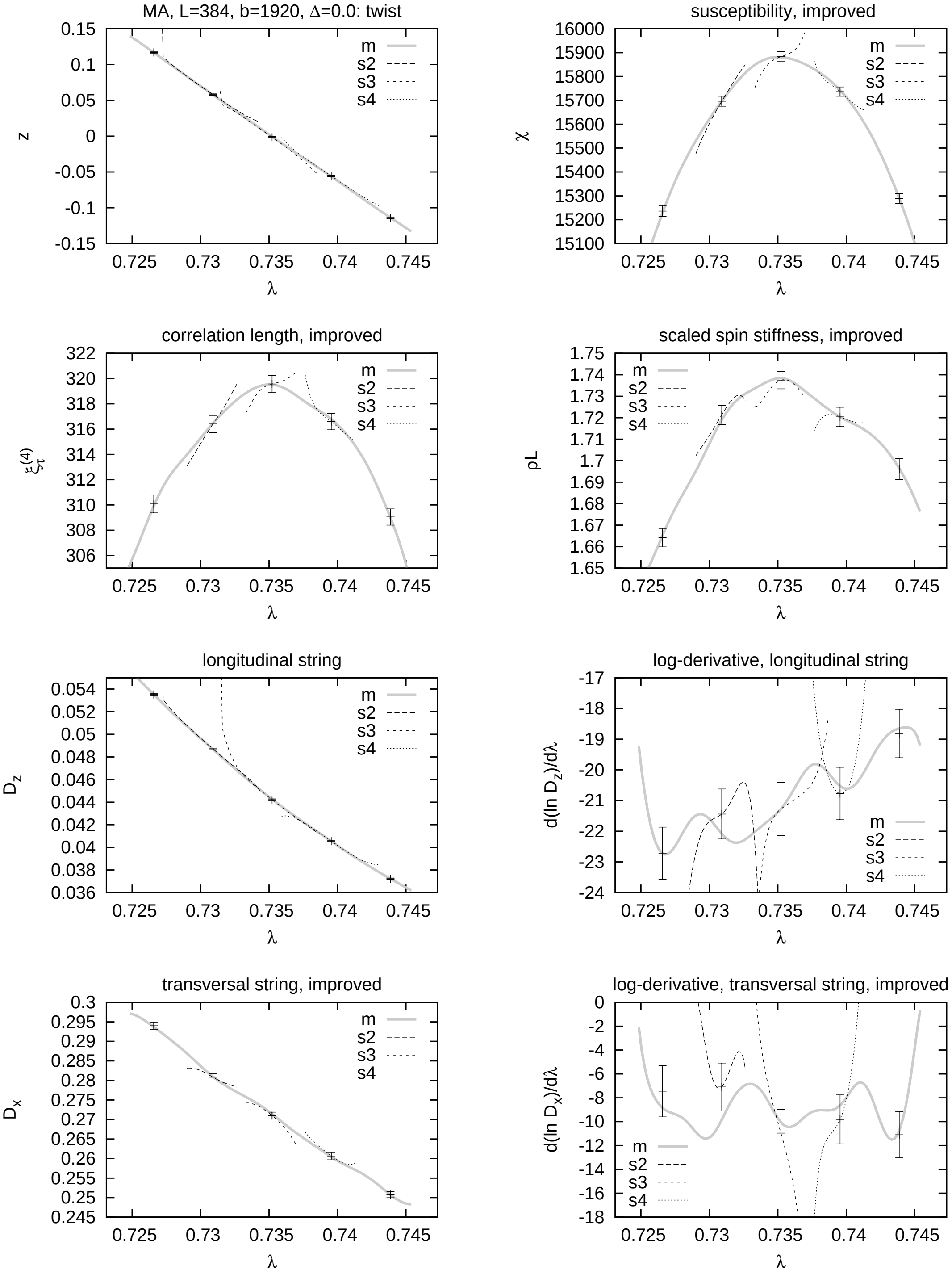

Figure A.6: Data of MA at $\Delta = 0.0$, $L = 384$ and $\beta = 1920$. The label "si" (m) denotes data from single-(multi-)histogram reweigthing of the i-th (all) point(s).

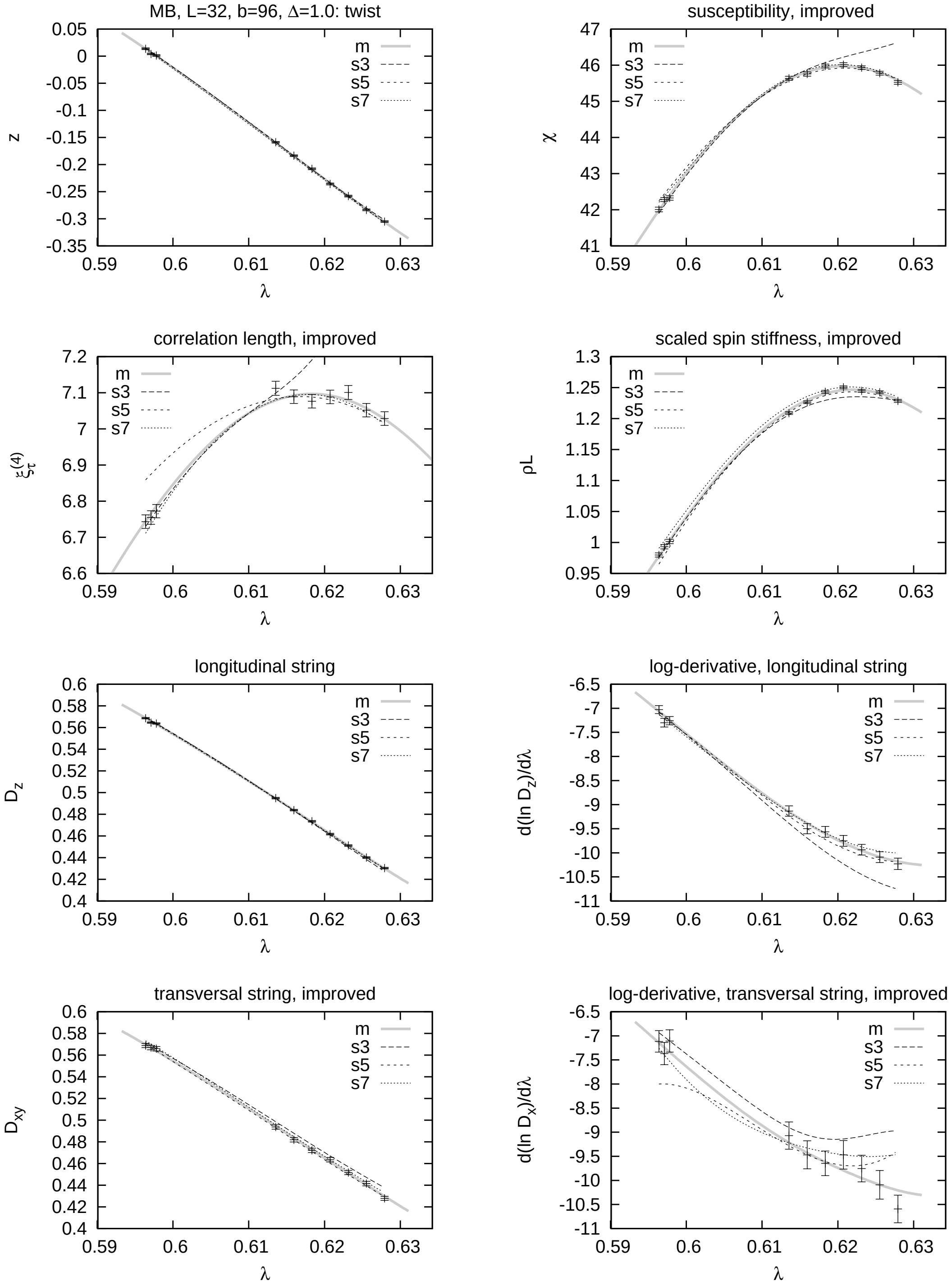

Figure A.7: Data of MB at $\Delta = 1.0$, $L = 32$ and $\beta = 96$. The label "si" (m) denotes data from single-(multi-)histogram reweigthing of the i-th (all) point(s).

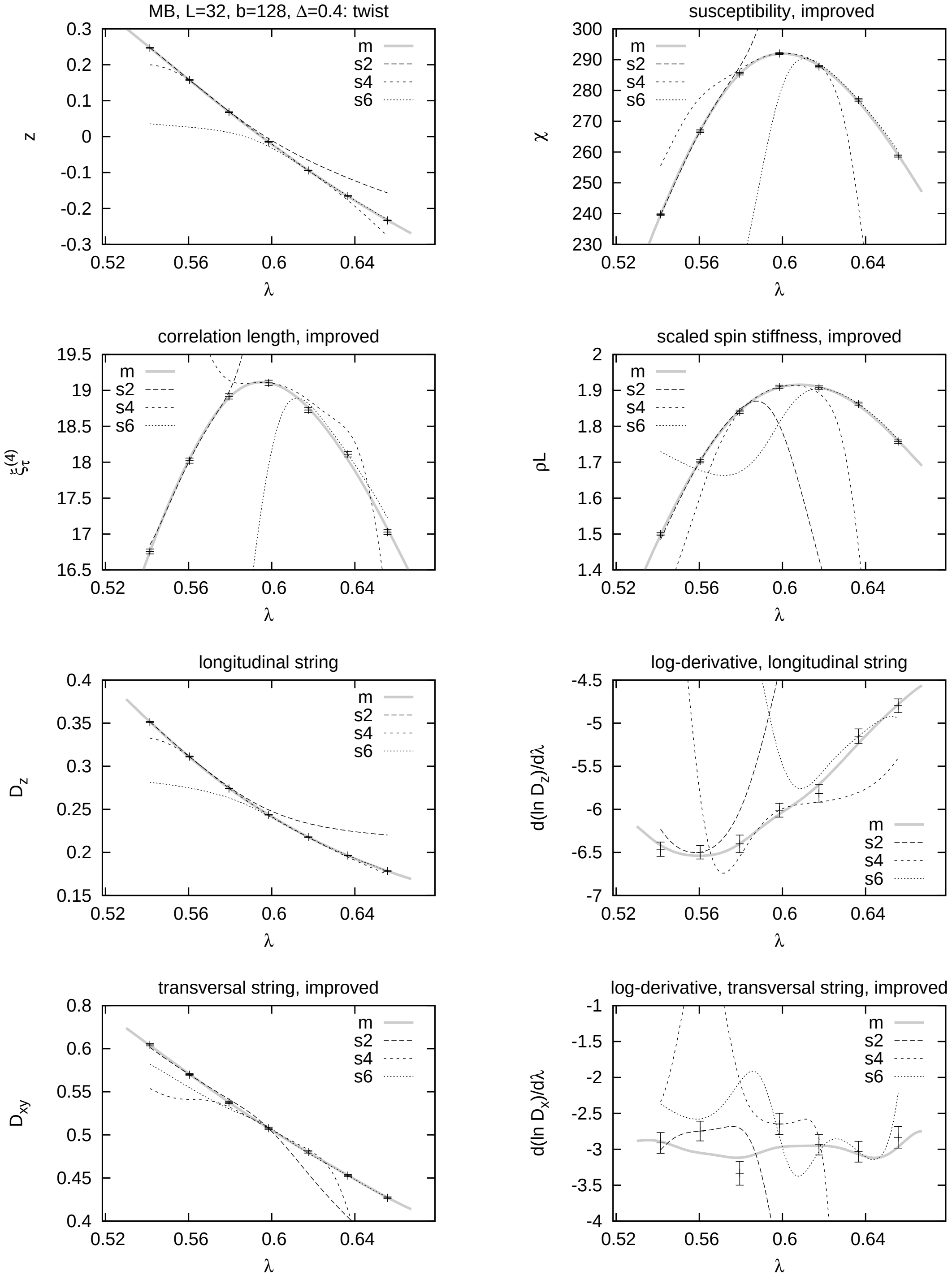

Figure A.8: Data of MB at $\Delta = 0.4$, $L = 32$ and $\beta = 128$. The label "si" (m) denotes data from single-(multi-)histogram reweigthing of the i-th (all) point(s).

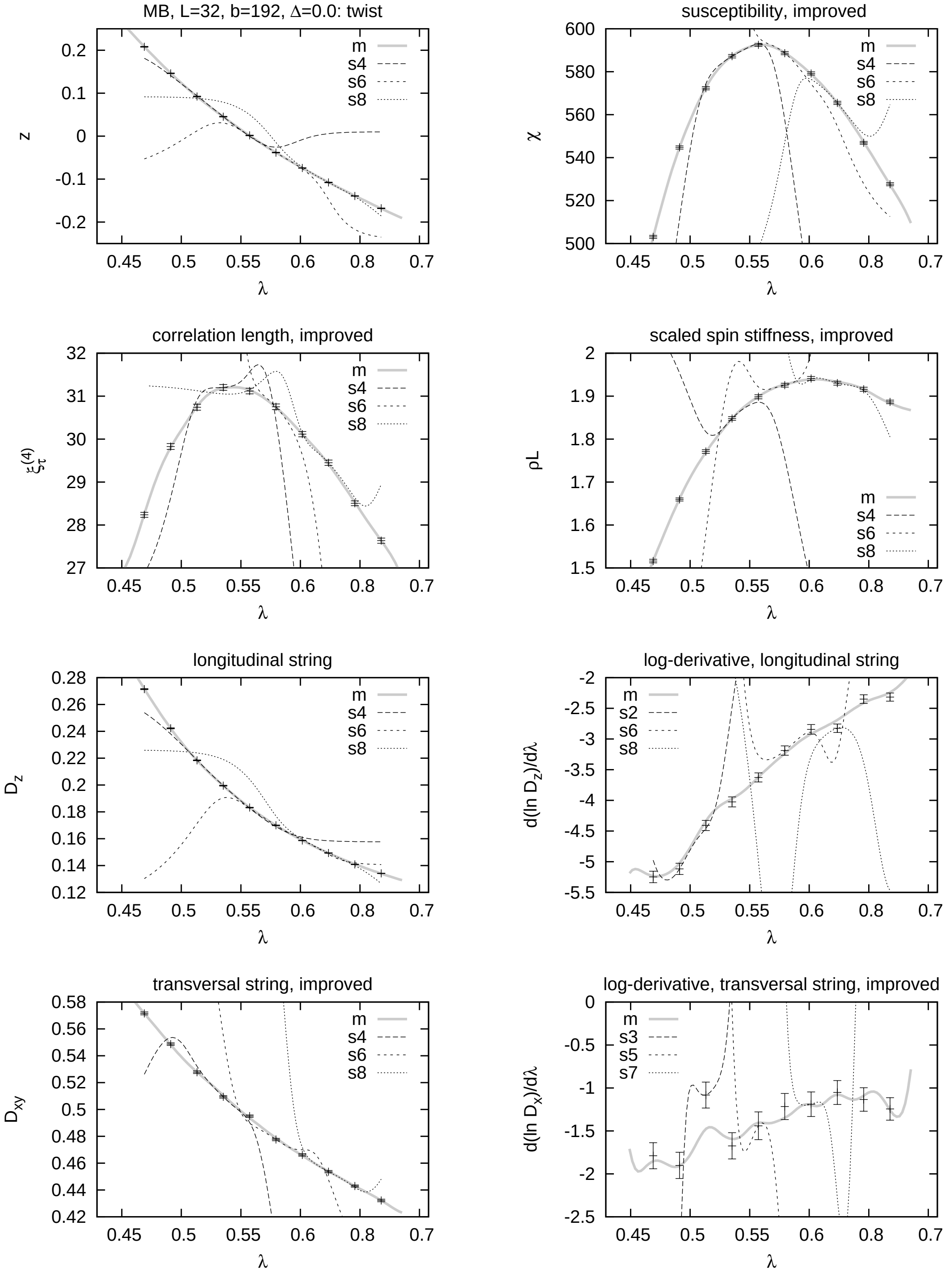

Figure A.9: Data of MB at $\Delta = 0.0$, $L = 32$ and $\beta = 192$. The label "si" (m) denotes data from single-(multi-)histogram reweigthing of the i-th (all) point(s).

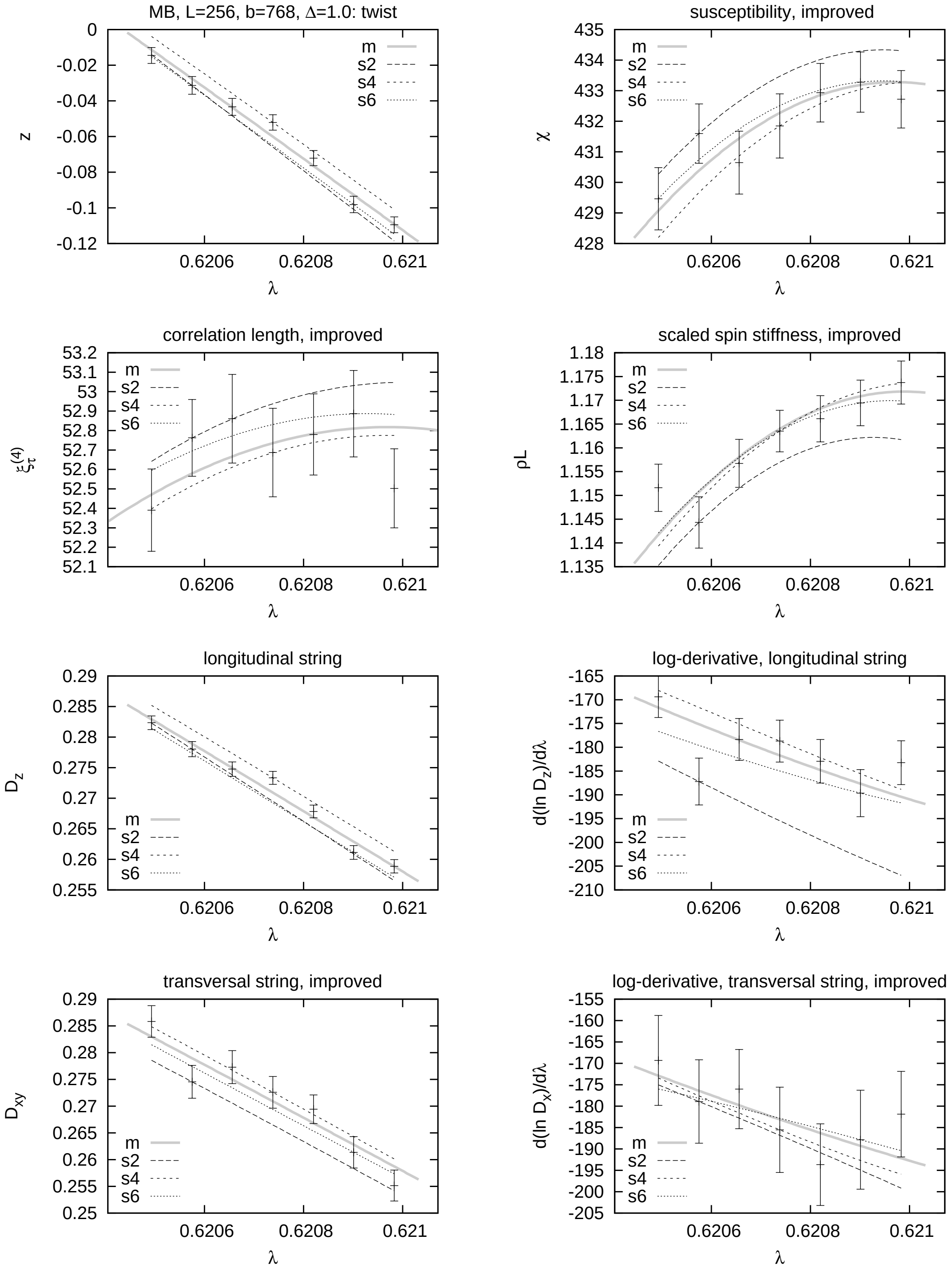

Figure A.10: Data of MB at $\Delta = 1.0$, $L = 256$ and $\beta = 768$. The label "si" (m) denotes data from single-(multi-)histogram reweigthing of the i-th (all) point(s).

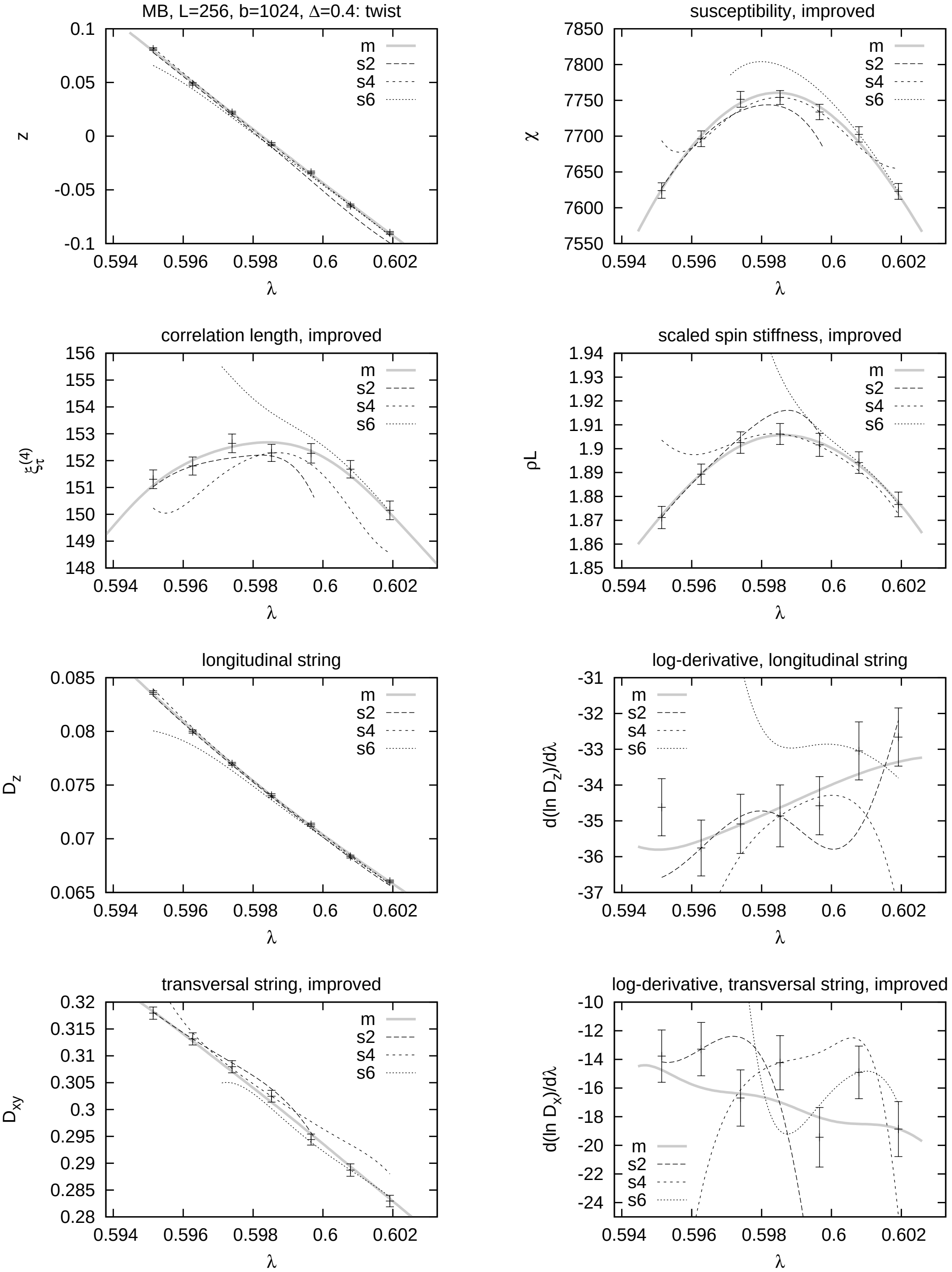

Figure A.11: Data of MB at $\Delta = 0.4$, $L = 256$ and $\beta = 1024$. The label "si" (m) denotes data from single-(multi-)histogram reweigthing of the i-th (all) point(s).

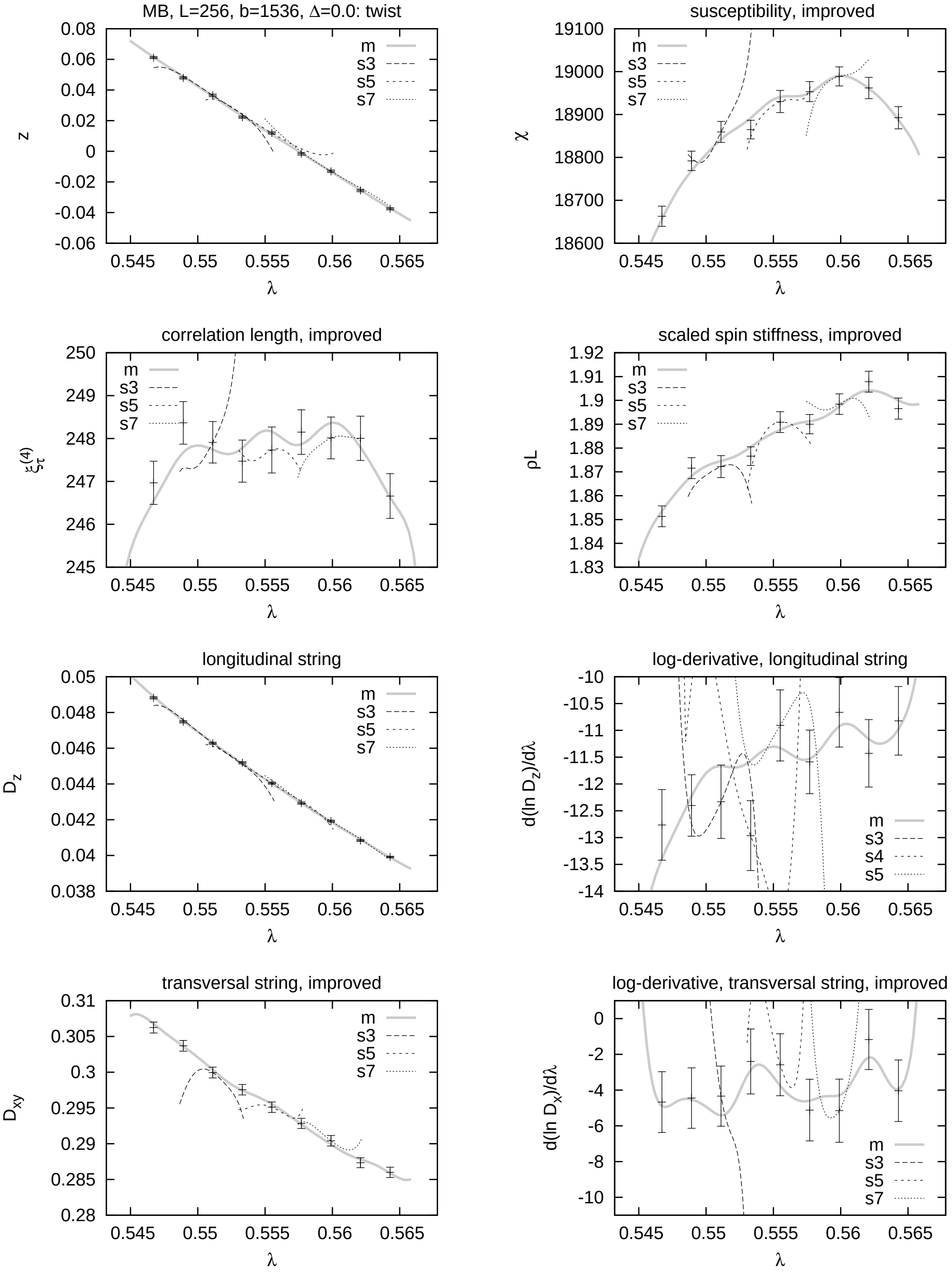

Figure A.12: Data of MB at $\Delta = 0.0$, $L = 256$ and $\beta = 1536$. The label "si" (m) denotes data from single-(multi-)histogram reweigthing of the i-th (all) point(s).

B Numbers

B.1 Finite-Size Scaling of the Location of Pseudocritical Points

The following pages contain tables of full results of fits of pseudocritical points to

$$\lambda_{\mathrm{c}}^*(L) = \lambda_{\mathrm{c}} + bL^{-\theta}\,,$$

part of the result of fitting the zeroes of the twist parameter to the polynomial, as used in [141],

$$\lambda_{\mathrm{c}}^*(L) = \lambda_{\mathrm{c}} + aL^{-2} + bL^{-4} + cL^{-6}\,,$$

as well as a comparison of final results and preliminary estimates of $\lambda_{\mathrm{c}}(\Delta)$.

Table B.1: MA. Fit of zeros of the twist parameter to $\lambda^*(L) = \lambda_c + b/L^\theta$.

Δ	$L_{\min}$	$L_{\max}$	λ_c	b	θ	dof	χ^2/dof
0.0	24	384	0.735238(28)	−1.6(1.8)	2.17(33)	22	0.76
0.1	24	384	0.741376(17)	−2.1(1.1)	2.10(15)	22	0.88
0.2	24	384	0.746445(14)	−1.7(6)	1.95(9)	22	0.63
0.3	24	384	0.750608(11)	−2.2(5)	1.95(6)	22	1.34
0.4	24	384	0.753975(10)	−2.5(5)	1.92(5)	22	0.52
0.5	24	384	0.756677(9)	−3.3(5)	1.94(4)	22	0.76
0.6	24	384	0.758778(9)	−3.3(4)	1.89(3)	22	1.43
0.7	24	384	0.760328(8)	−4.3(3)	1.91(2)	22	1.58
0.8	24	384	0.761394(7)	−5.0(3)	1.89(2)	22	1.61
0.9	44	384	0.761988(9)	−7.3(7)	1.92(3)	17	0.87
1.0	44	384	0.762198(5)	−6.1(2)	1.79(1)	17	0.81

Table B.2: MA. Fit of crossing points of the twist parameter to $\lambda^*(L) = \lambda_c + b/L^\theta$.

Δ	$L_{\min}$	$L_{\max}$	λ_c	b	θ	dof	χ^2/dof
0.0	16	192	0.735001(201)	0.1(2)	1.33(42)	18	0.70
0.1	16	192	0.741220(96)	0.3(2)	1.48(21)	18	0.67
0.2	16	192	0.746402(58)	0.5(3)	1.69(18)	18	0.63
0.3	16	192	0.750623(38)	0.8(4)	1.82(14)	18	0.58
0.4	32	192	0.753947(57)	0.7(9)	1.78(32)	14	0.61
0.5	32	192	0.756696(39)	1.7(1.6)	1.99(26)	14	0.89
0.6	32	192	0.758782(35)	1.4(1.2)	1.93(23)	14	1.62
0.7	32	192	0.760340(29)	1.5(1.0)	1.96(19)	14	1.46
0.8	32	192	0.761417(22)	2.1(1.1)	2.05(15)	14	1.71
0.9	32	192	0.761949(31)	0.4(2)	1.60(13)	14	1.40
1.0	24	192	0.762177(15)	0.6(1)	1.71(5)	16	1.18

Table B.3: MA. Fit of zeros of the twist parameter to a third-order polynomial in L^{-2}.

Δ	$L_{\min}$	$L_{\max}$	λ_c	dof	χ^2/dof
0.0	24	384	0.735246(27)	21	0.79
0.1	24	384	0.741367(16)	21	0.62
0.2	24	384	0.746445(12)	21	0.65
0.3	24	384	0.750603(10)	21	1.38
0.4	24	384	0.753968(9)	21	0.53
0.5	24	384	0.756673(8)	21	0.78
0.6	24	384	0.758766(7)	21	1.39
0.7	24	384	0.760318(6)	21	1.69
0.8	24	384	0.761378(6)	21	1.81
0.9	24	384	0.761978(6)	21	0.94
1.0	64	384	0.762168(5)	13	0.63

Table B.4: MA. Fit of the maxima of the second-moment estimator of the correlation length ξ to $\lambda^*(L) = \lambda_\mathrm{c} + b/L^\theta$.

Δ	L_min	L_max	λ_c	b	θ	dof	χ^2/dof
0.0	20	384	0.735542(507)	−0.7(4)	1.18(14)	22	1.69
0.1	20	384	0.741374(204)	−2.1(1.2)	1.65(17)	22	1.61
0.2	20	384	0.746523(92)	−1.5(6)	1.61(12)	22	0.59
0.3	20	384	0.750744(56)	−1.4(6)	1.67(12)	22	0.59
0.4	20	384	0.754007(28)	−2.2(9)	1.89(11)	22	1.67
0.5	20	384	0.756659(16)	−8.7(3.8)	2.36(13)	22	0.81
0.6	20	384	0.758794(15)	−3.7(1.6)	2.14(12)	22	0.84
0.7	20	384	0.760323(12)	−5.3(1.9)	2.26(11)	22	1.02
0.8	20	384	0.761377(10)	−12.2(4.0)	2.52(10)	22	0.86
0.9	20	384	0.761995(9)	−13.6(3.8)	2.52(9)	22	1.56
1.0	32	384	0.762181(9)	−15.1(5.7)	2.51(11)	20	1.55

Table B.5: MA. Fit of the maxima of the susceptibility χ to $\lambda^*(L) = \lambda_\mathrm{c} + b/L^\theta$.

Δ	L_min	L_max	λ_c	b	θ	dof	χ^2/dof
0.0	12	384	0.735096(163)	−4.2(2.2)	2.1(2)	25	0.92
0.1	12	384	0.741580(88)	−4.9(2.3)	2.3(2)	25	1.21
0.2	12	384	0.746564(37)	−8(5)	2.7(3)	25	0.49
0.3	12	384	0.750715(21)	−33(30)	3.3(4)	25	0.66
0.4	12	384	0.754025(14)	−156(213)	4.0(6)	25	1.82
0.5	12	384	0.756702(10)	−1259(3164)	5(1)	25	1.44
0.6	12	384	0.758795(9)	−452(582)	4.5(6)	25	1.06
0.7	12	384	0.760326(8)	−92(76)	3.9(4)	25	1.14
0.8	12	384	0.761387(7)	−45(26)	3.5(3)	25	1.13
0.9	12	384	0.761992(6)	−31(11)	3.3(2)	25	1.14
1.0	12	384	0.762181(4)	−7.8(9)	2.65(4)	25	1.73

Table B.6: MB. Fit of zeros of the twist parameter to $\lambda^*(L) = \lambda_\mathrm{c} + b/L^\theta$.

Δ	L_min	L_max	λ_c	b	θ	dof	χ^2/dof
0.0	16	256	0.557448(54)	0.17(17)	1.64(33)	20	0.72
0.1	12	256	0.569761(31)	−3(9)	3.03(110)	21	0.68
0.2	20	256	0.580629(28)	−2.3(2.1)	2.26(28)	19	1.11
0.3	32	256	0.590136(28)	−2.9(2.3)	2.09(22)	16	1.01
0.4	32	256	0.598307(21)	−3.1(1.2)	2.00(11)	16	1.43
0.5	32	256	0.605228(16)	−4.2(8)	1.97(6)	16	2.21
0.6	32	256	0.610915(17)	−4.1(6)	1.88(4)	16	1.51
0.7	32	256	0.615312(14)	−6.2(6)	1.91(3)	16	0.81
0.8	32	256	0.618474(12)	−8.4(5)	1.92(2)	16	2.11
0.9	32	256	0.620407(12)	−9.6(4)	1.87(2)	16	1.20
1.0	40	256	0.621042(13)	−10.3(3)	1.76(1)	14	0.90

Table B.7: MB. Fit of crossing points of the twist parameter to $\lambda^*(L) = \lambda_c + b/L^\theta$.

Δ	$L_{\min}$	$L_{\max}$	λ_c	b	θ	dof	χ^2/dof
0.0	64	128	0.557260(196)			6	0.30
0.1	32	128	0.569707(148)			12	1.24
0.2	8	128	0.580740(128)	0.7(4)	1.97(21)	16	1.12
0.3	16	128	0.589824(256)	0.1(1)	1.22(27)	14	1.00
0.4	16	128	0.598264(95)	0.7(3)	1.68(14)	14	1.06
0.5	16	128	0.605133(66)	0.7(2)	1.65(8)	14	1.49
0.6	16	128	0.610838(57)	0.8(2)	1.66(7)	14	0.87
0.7	16	128	0.615202(47)	0.7(1)	1.59(5)	14	0.95
0.8	32	128	0.618411(60)	1.3(6)	1.76(12)	10	1.60
0.9	16	128	0.620230(38)	0.5(1)	1.48(4)	14	0.87
1.0	24	128	0.620846(42)	0.4(1)	1.42(5)	12	0.40

Table B.8: MB. Fit of zeros of the twist parameter to a third-order polynomial in L^{-2}.

Δ	$L_{\min}$	$L_{\max}$	λ_c	dof	χ^2/dof
0.0	12	256	0.557468(38)	20	0.72
0.1	12	256	0.569764(34)	20	0.72
0.2	16	256	0.580635(27)	19	1.11
0.3	20	256	0.590144(21)	18	0.91
0.4	20	256	0.598305(15)	18	1.29
0.5	20	256	0.605224(11)	18	1.94
0.6	20	256	0.610893(11)	18	1.23
0.7	24	256	0.615292(10)	17	0.68
0.8	24	256	0.618452(9)	17	1.90
0.9	32	256	0.620363(10)	15	1.06
1.0	56	256	0.620933(14)	10	0.83

Table B.9: MB. Fit of the maxima of the second-moment estimator of the correlation length ξ to $\lambda^*(L) = \lambda_c + b/L^\theta$.

Δ	$L_{\min}$	$L_{\max}$	λ_c	b	θ	dof	χ^2/dof
0.0							
0.1	12	256	0.572398(1074)	$-0.3(2)$	0.89(14)	21	2.01
0.2	12	256	0.580150(362)	$-1.8(1.1)$	1.72(23)	21	2.01
0.3	12	256	0.590008(233)	$-1.2(8)$	1.73(23)	21	0.72
0.4	16	256	0.598566(210)	$-0.2(2)$	1.26(23)	20	1.19
0.5	12	256	0.605186(49)	$-6.1(3.3)$	2.43(20)	21	0.61
0.6	12	256	0.610891(30)	$-3.6(1.3)$	2.29(13)	21	0.64
0.7	12	256	0.615332(19)	$-4.1(1.1)$	2.31(9)	21	0.45
0.8	20	256	0.618465(14)	$-7.8(4.4)$	2.54(17)	19	1.17
0.9	20	256	0.620409(14)	$-3.4(1.4)$	2.22(12)	19	0.85
1.0	36	256	0.620998(19)	$-5.0(4.2)$	2.25(23)	15	0.94

Table B.10: MB. Fit of the maxima of the susceptibility χ to $\lambda^*(L) = \lambda_\mathrm{c} + b/L^\theta$.

Δ	L_min	L_max	λ_c	b	θ	dof	χ^2/dof
0.0							
0.1	72	256	0.571422(307)			11	0.47
0.2	72	256	0.581519(221)			10	0.86
0.3	16	256	0.589517(823)	0.0(1)	0.67(27)	20	0.60
0.4	16	256	0.598227(175)	0.1(1)	1.04(21)	20	0.80
0.5	24	256	0.605120(101)	0.2(1)	1.21(18)	18	0.83
0.6	24	256	0.610910(37)	0.5(3)	1.62(15)	18	0.60
0.7	24	256	0.615288(30)	0.2(2)	1.48(15)	18	0.52
0.8	20	256	0.618410(23)	0.1(1)	1.38(13)	19	1.68
0.9	20	256	0.620378(11)	0.4(4)	2.01(32)	19	0.82
1.0	16	256	0.620982(7)	−15(10)	3.10(23)	20	1.14

Table B.11: Comparison of final estimates from exact diagonalization (ED), and the preliminary (1st center) and final estimates obtained from quantum Monte Carlo simulations.

	MA			MB		
Δ	ED	1st center	final	ED	1st center	final
0.0	0.73524	0.73522(7)	0.73524(2)	0.5540	0.54734(253)	0.55735(5)
0.1	0.74130	0.74147(5)	0.74137(2)	0.5673	0.56416(73)	0.56977(7)
0.2	0.74637	0.74643(3)	0.74645(2)	0.5790	0.57612(44)	0.58064(5)
0.3	0.75055	0.75057(2)	0.75062(2)	0.5890	0.58837(41)	0.59014(2)
0.4	0.75395	0.75396(2)	0.75398(2)	0.5976	0.59853(38)	0.59831(1)
0.5	0.75668	0.75668(1)	0.75668(1)	0.6048	0.60495(17)	0.60522(1)
0.6	0.75881	0.75876(1)	0.75878(1)	0.6107	0.61118(14)	0.61090(1)
0.7	0.76041	0.76033(1)	0.76032(1)	0.6153	0.61513(9)	0.61530(1)
0.8	0.76155	0.76138(1)	0.76139(1)	0.6187	0.61858(8)	0.61846(1)
0.9	0.76228	0.76199(1)	0.76199(1)	0.6210	0.62035(7)	0.62038(2)
1.0	0.76262	0.76219(1)	0.76218(1)	0.6223	0.62074(7)	0.62098(2)

B.2 Finite-Size Scaling of the Values at (Pseudo)Critical Points

The following pages contain tables of full results of FSS fits that yielded our final estimates of critical exponent ratios. Final results for γ/ν and β_x/ν, were obtained from double-log linear fits to

$$\ln \chi_{\max}(L) = \ln A + \frac{\gamma}{/}\nu \ln L\,,$$

with the exception of γ/ν at $\Delta = 1$, which was obtained from the subtraction method, i.e. fits to

$$\ln(\chi_{\max}(L) - \chi_{\max}(2L)) \sim \ln(A(1 - 2^{\gamma/\nu})) + \frac{\gamma}{\nu} \ln L\,.$$

Individual final estimates of $1/\nu$, were obtained from the double-log linear fits, but with unweighted datapoints. The errors have then been estimated by the jacknife method. Final results for α/ν, were obtained from non-linear fits to

$$c_\lambda(L; \lambda_{\mathrm{c}}) = B + AL^{\alpha/nu}\,.$$

Final results for β_z/ν, were obtained from non-linear fits to

$$D_z(L; \lambda_{\mathrm{c}}) = AL^{-\beta_z/\nu} + CL^{-1}\,,$$

and compared to results obtained from double-log linear fits, as well as to results of the quotients method, which fits

$$\frac{D_z(L; \lambda_{\mathrm{c}})}{D_z(2L; \lambda_{\mathrm{c}})} =\sim 2^{-\beta_z/\nu}\left(1 + \tilde{C}L^{-\omega}\right)\,,$$

Table B.12: MA, double-log linear fits of the maxima of the susceptibility to $\ln \chi_L = \ln A + \frac{\gamma}{\nu} \ln L$. At Δ, the result was obtained from the subtraction method (8.4).

Δ	$L_{\min}$	$L_{\max}$	$\ln A$	γ/ν	dof	χ^2_{dof}
0.0	32	384	0.0004(16)	1.6254(4)	19	1.34
0.1	32	384	−0.0934(12)	1.5993(3)	21	1.11
0.2	32	384	−0.1885(8)	1.5720(2)	21	0.59
0.3	32	384	−0.2753(9)	1.5431(2)	19	0.72
0.4	32	384	−0.3624(11)	1.5108(3)	21	1.11
0.5	56	384	−0.4408(13)	1.4754(3)	14	0.60
0.6	64	384	−0.5054(13)	1.4325(3)	15	0.48
0.7	64	384	−0.5598(14)	1.3813(3)	15	0.51
0.8	88	384	−0.6008(29)	1.3181(6)	12	0.96
0.9	176	384	−0.6020(98)	1.2321(18)	6	0.89
1.0	80	192	−0.2324(58)	1.0656(13)	8	0.59

Table B.13: Individual estimates of $1/\nu$ of MA, and the corresponding minimum chain length used in the jacknifed unweighted double-log linear fits. In all cases $L_{\max} = 384$. These estimates of $1/\nu$ have been put into the analysis of crosscorrelations in Sect. 8.2.

Δ	$L_{\min}$	$\frac{\mathrm{d}\ln\lvert D_z\rvert}{\mathrm{d}\lambda}$	$L_{\min}$	$\frac{\mathrm{d}\ln D_z}{\mathrm{d}\lambda}$	$L_{\min}$	$\frac{\mathrm{d}U_4}{\mathrm{d}\lambda}$	$L_{\min}$	$\frac{\mathrm{d}\ln D_x}{\mathrm{d}\lambda}$	$L_{\min}$	$\frac{\mathrm{d}\ln D_x^2}{\mathrm{d}\lambda}$
0.0	56	0.668(6)	80	0.672(10)	36	0.651(5)	24	0.689(23)	32	0.671(15)
0.1	56	0.741(4)	88	0.737(8)	56	0.734(5)	44	0.746(23)	44	0.761(13)
0.2	56	0.830(4)	64	0.833(5)	40	0.830(4)	72	0.833(21)	72	0.845(13)
0.3	64	0.905(3)	96	0.905(6)	56	0.906(4)	72	0.899(15)	72	0.912(11)
0.4	64	0.983(4)	56	0.992(4)	56	0.989(4)	88	0.990(17)	56	0.990(8)
0.5	72	1.053(4)	80	1.054(5)	80	1.058(5)	72	1.054(13)	88	1.043(12)
0.6	80	1.123(5)	80	1.127(5)	80	1.130(5)	56	1.128(10)	88	1.122(12)
0.7	88	1.203(7)	88	1.207(7)	88	1.214(7)	80	1.206(13)	80	1.212(11)
0.8	96	1.277(8)	96	1.281(8)	96	1.292(8)	80	1.264(14)	80	1.269(12)
0.9	96	1.371(8)	96	1.373(9)	96	1.391(9)	88	1.374(16)	88	1.360(14)
1.0	44	1.423(3)	56	1.426(3)	44	1.436(3)	112	1.411(11)	112	1.413(10)

Table B.14: MA, final results from a fit of finite-size data of the specific heat at the critical point to a power-law, $B + AL^{\alpha/\nu}$. $L_{\max} = 384$.

Δ	$L_{\min}$	B	A	α/ν	dof	χ^2/dof
0.0	12	0.426(2)	−0.18(4)	−0.71(9)	25	0.87
0.1	16	0.489(2)	−0.31(4)	−0.65(5)	24	0.52
0.2	16	0.619(7)	−0.35(2)	−0.33(3)	24	0.61
0.3	20	0.91(4)	−0.64(2)	−0.19(3)	23	0.98
0.4	20	3.4(1.3)	−3.08(1.3)	−0.04(2)	23	0.96
0.5	20	−0.9(3)	1.2(3)	0.09(2)	23	1.04
0.6	32	−0.2(2)	0.49(10)	0.23(3)	20	1.38
0.7	24	0.11(4)	0.24(2)	0.38(2)	22	0.83
0.8	24	0.22(3)	0.156(10)	0.510(10)	22	1.04
0.9	24	0.33(3)	0.099(7)	0.65(2)	22	1.48
1.0	56	0.50(4)	0.064(5)	0.75(2)	15	0.96

Table B.15: MA, final results from a fit of finite-size data of the longitudinal string observable D_z at the critical point to $AL^{\beta_z/\nu} + CL^{-1}$. $L_{\max} = 384$.

Δ	$L_{\min}$	A	β_z/ν	C	dof	χ^2_{dof}
0.0	24	2.53(3)	0.6684(15)	−1.17(5)	22	0.71
0.1	24	2.22(3)	0.6231(15)	−0.85(5)	22	1.00
0.2	24	2.06(2)	0.5859(12)	−0.72(4)	22	0.68
0.3	24	1.92(3)	0.5492(17)	−0.60(5)	22	1.45
0.4	24	1.79(2)	0.5137(10)	−0.50(3)	22	0.36
0.5	24	1.70(2)	0.4792(15)	−0.44(5)	22	0.76
0.6	32	1.61(3)	0.4451(25)	−0.40(9)	20	1.14
0.7	32	1.50(3)	0.4059(28)	−0.22(10)	20	1.42
0.8	32	1.43(3)	0.3702(27)	−0.20(10)	19	1.38
0.9	36	1.32(2)	0.3267(25)	−0.05(10)	19	0.91
1.0	40	1.16(1)	0.2672(15)	0.32(6)	18	1.08

Table B.16: MA, final results from double-log linear fits of finite-size data of the longitudinal string observable D_z at the critical point. $L_{\min} = 160$ and $L_{\max} = 384$.

Δ	$\ln A$	β_z/ν	dof	χ^2/dof
0.0	0.699(10)	0.641(2)	7	1.99
0.1	0.645(5)	0.604(1)	7	0.60
0.2	0.603(5)	0.571(1)	7	0.57
0.3	0.543(10)	0.535(2)	7	1.88
0.4	0.508(5)	0.504(1)	7	0.33
0.5	0.456(7)	0.469(2)	7	0.50
0.6	0.423(11)	0.437(2)	7	0.90
0.7	0.364(19)	0.400(4)	7	1.95
0.8	0.291(25)	0.359(5)	7	2.67
0.9	0.276(13)	0.326(3)	7	0.62
1.0	0.165(8)	0.270(2)	7	0.81

Table B.17: MA, final results of the quotients method for longitudinal string observable D_z at the critical point. $L_{\min} = 8$ and $L_{\max} = 384$.

Δ	β_z/ν	C	ω	dof	χ^2/dof
0.0	0.662(5)	−0.13(1)	0.43(5)	20	0.38
0.1	0.621(4)	−0.12(1)	0.45(5)	20	0.34
0.2	0.580(3)	−0.14(2)	0.58(6)	20	0.35
0.3	0.545(4)	−0.11(2)	0.57(9)	20	0.68
0.4	0.517(5)	−0.08(1)	0.44(7)	20	0.24
0.5	0.475(4)	−0.09(3)	0.65(14)	20	0.47
0.6	0.441(5)	−0.08(3)	0.65(20)	20	0.69
0.7	0.404(4)	−0.07(3)	0.74(26)	20	0.68
0.8	0.366(3)	−0.12(11)	1.18(46)	20	0.97
0.9	0.326(2)	−0.14(13)	1.39(48)	20	0.46

Table B.18: MA, final results from double-log linear fits of finite-size data of the transversal string observable D_x at the critical point. $L_{\max} = 384$.

Δ	$L_{\min}$	$\ln A$	β_x/ν	dof	χ^2/dof
0.0	32	0.179(3)	−0.249(1)	21	0.85
0.1	72	0.190(6)	−0.250(2)	14	1.31
0.2	56	0.193(4)	−0.249(1)	16	1.11
0.3	56	0.203(3)	−0.251(1)	16	0.41
0.4	56	0.198(4)	−0.249(1)	16	0.65
0.5	56	0.198(5)	−0.250(1)	16	0.92
0.6	56	0.181(6)	−0.247(2)	16	1.02
0.7	48	0.187(4)	−0.250(1)	17	0.51
0.8	72	0.174(12)	−0.251(3)	14	1.73
0.9	80	0.163(11)	−0.256(3)	13	0.91
1.0	72	0.189(6)	−0.274(2)	14	0.67

Table B.19: MB, double-log linear fits of the maxima of the susceptibility to $\ln \chi_L = \ln A + \frac{\gamma}{\nu} \ln L$. At Δ, the result was obtained from the subtraction method (8.4).

Δ	$L_{\min}$	$L_{\max}$	$\ln A$	γ/ν	dof	χ^2_{dof}
0.0	64	256	0.5975(32)	1.6689(7)	9	0.94
0.1	56	256	0.5000(19)	1.6472(4)	11	0.23
0.2	56	256	0.4019(26)	1.6266(6)	10	0.52
0.3	32	256	0.3006(11)	1.6036(3)	17	0.46
0.4	24	256	0.2094(15)	1.5773(4)	19	1.60
0.5	88	256	0.1098(32)	1.5482(7)	8	0.96
0.6	24	256	0.0194(14)	1.5096(4)	19	1.66
0.7	96	256	−0.0711(33)	1.4621(7)	7	0.58
0.8	88	256	−0.1497(36)	1.3967(8)	8	0.99
0.9	112	256	−0.1855(54)	1.2967(11)	6	0.83
1.0	40	128	0.2289(61)	1.0718(15)	9	0.92

Table B.20: Individual estimates of $1/\nu$ of MB, and the corresponding minimum chain length used in the jacknifed unweighted double-log linear fits. In all cases $L_{\max} = 256$, apart from estimates based on D_z-observables, where $L_{\min} = 192$.

Δ	$L_{\min}$	$\frac{\text{dln}\lvert D_z\rvert}{\text{d}\lambda}$	$L_{\min}$	$\frac{\text{dln}D_z}{\text{d}\lambda}$	$L_{\min}$	$\frac{\text{d}U_4}{\text{d}\lambda}$	$L_{\min}$	$\frac{\text{dln}D_x}{\text{d}\lambda}$	$L_{\min}$	$\frac{\text{dln}D_x^2}{\text{d}\lambda}$
0.0	72	0.516(11)	72	0.537(17)	48	0.475(11)				
0.1	64	0.618(17)	56	0.635(20)	56	0.603(17)				
0.2	64	0.664(10)	72	0.662(16)	56	0.643(11)				
0.3	64	0.730(9)	56	0.755(11)	64	0.723(10)				
0.4	48	0.811(4)	64	0.812(6)	48	0.808(5)	48	0.800(22)	56	0.794(15)
0.5	64	0.888(5)	64	0.898(6)	64	0.890(5)	64	0.907(19)	56	0.914(14)
0.6	64	0.987(5)	64	0.989(5)	64	0.994(5)	80	1.013(22)	80	1.016(16)
0.7	64	1.081(5)	64	1.091(5)	64	1.093(5)	72	1.102(16)	88	1.076(17)
0.8	96	1.186(10)	96	1.195(10)	96	1.202(10)	64	1.213(13)	72	1.201(13)
0.9	64	1.324(7)	64	1.330(7)	64	1.349(7)	64	1.327(16)	64	1.324(14)
1.0	64	1.421(6)	64	1.425(6)	64	1.433(6)	64	1.437(14)	64	1.439(12)

Table B.21: MB, final results from a fit of finite-size data of the specific heat at the critical point to a power-law, $B + AL^{\alpha/\nu}$. $L_{\max} = 256$.

Δ	$L_{\min}$	B	A	α/ν	dof	χ^2/dof
0.0	8	0.515(2)	−0.12(5)	−0.9(3)	22	1.25
0.1	8	0.554(2)	−0.17(4)	−0.77(10)	22	0.70
0.2	8	0.603(3)	−0.23(5)	−0.71(11)	22	1.81
0.3	16	0.681(6)	−0.28(5)	−0.51(8)	20	0.82
0.4	16	0.805(10)	−0.44(3)	−0.40(5)	20	0.86
0.5	16	1.11(4)	−0.72(2)	−0.22(3)	20	0.69
0.6	16	4.7(2.8)	−4.3(2.7)	−0.032(24)	20	1.84
0.7	24	−0.6(3)	1.0(3)	0.13(2)	18	1.06
0.8	24	0.21(6)	0.28(4)	0.35(2)	18	1.12
0.9	28	0.48(4)	0.117(10)	0.57(2)	17	0.92
1.0	56	0.74(8)	0.050(10)	0.77(4)	11	1.47

Table B.22: MB, final results from a fit of finite-size data of the longitudinal string observable D_z at the critical point to $AL^{\beta_z/\nu} + CL^{-1}$. $L_{\max} = 256$.

Δ	$L_{\min}$	A	β_z/ν	C	dof	χ^2_{dof}
0.0	24	3.03(15)	0.7443(60)	−1.47(21)	18	3.78
0.1	24	2.88(7)	0.7140(30)	−1.48(11)	18	0.85
0.2	24	2.53(4)	0.6723(20)	−1.10(7)	18	0.47
0.3	36	2.18(8)	0.6271(49)	−0.70(16)	15	1.53
0.4	24	2.14(4)	0.5982(24)	−0.81(7)	18	1.23
0.5	24	1.97(3)	0.5579(17)	−0.66(5)	18	0.77
0.6	24	1.75(3)	0.5103(20)	−0.35(6)	18	0.90
0.7	36	1.68(3)	0.4704(21)	−0.42(7)	15	0.46
0.8	36	1.58(4)	0.4230(38)	−0.43(13)	15	1.50
0.9	36	1.39(3)	0.3587(30)	−0.07(11)	15	0.84
1.0	36	1.16(2)	0.2720(17)	0.23(6)	15	0.59

Table B.23: MB, final results from double-log linear fits of finite-size data of the longitudinal string observable D_z at the critical point. $L_{\min} = 160$ and $L_{\max} = 256$.

Δ	$\ln A$	β_z/ν	dof	χ^2/dof
0.0	0.774(4)	0.707(1)	3	0.07
0.1	0.744(18)	0.677(4)	3	0.95
0.2	0.706(18)	0.646(4)	3	1.22
0.3	0.643(16)	0.610(3)	3	1.05
0.4	0.609(9)	0.578(2)	3	0.40
0.5	0.550(10)	0.540(2)	3	0.49
0.6	0.491(15)	0.500(3)	3	0.88
0.7	0.466(14)	0.463(3)	3	0.63
0.8	0.378(17)	0.410(4)	3	0.62
0.9	0.309(20)	0.356(4)	3	0.55
1.0	0.148(9)	0.270(2)	3	0.15

Table B.24: MB, final results of the quotients method for longitudinal string observable D_z at the critical point. $L_{\min} = 8$ and $L_{\max} = 256$.

Δ	β_z/ν	C	ω	dof	χ^2/dof
0.0	0.733(7)	−0.15(1)	0.45(6)	16	0.58
0.1	0.700(11)	−0.14(2)	0.44(10)	16	0.68
0.2	0.660(4)	−0.14(1)	0.52(5)	16	0.17
0.3	0.616(3)	−0.17(3)	0.70(9)	16	0.40
0.4	0.587(5)	−0.13(3)	0.61(11)	16	0.71
0.5	0.565(11)	−0.08(1)	0.35(10)	16	0.63
0.6	0.508(3)	−0.11(3)	0.71(13)	16	0.46
0.7	0.467(3)	−0.07(1)	0.61(10)	16	0.18
0.8	0.414(4)	−0.10(7)	0.96(37)	16	1.33
0.9	0.360(3)	−0.05(4)	0.83(40)	16	0.67

Table B.25: MB, final results from double-log linear fits of finite-size data of the transversal string observable D_x at the critical point. $L_{\max} = 256$.

Δ	$L_{\min}$	$\ln A$	β_x/ν	dof	χ^2/dof
0.0	80	0.160(5)	0.250(2)	9	0.55
0.1	32	0.168(4)	0.250(1)	15	0.56
0.2	40	0.180(5)	0.251(2)	15	1.29
0.3	40	0.183(3)	0.250(1)	15	0.49
0.4	28	0.192(3)	0.250(1)	18	0.84
0.5	64	0.193(5)	0.250(1)	11	0.55
0.6	64	0.184(6)	0.248(2)	11	0.88
0.7	64	0.191(7)	0.251(2)	11	0.88
0.8	64	0.181(6)	0.251(2)	11	0.53
0.9	112	0.114(22)	0.245(5)	6	0.79
1.0	160	0.096(38)	0.261(8)	3	0.49

C Some further points on the string observable D_z

Effective Background. The presence of a background is intimately related to a wrong estimate of the critical point. The string observable D_z is zero in the high-λ phase ($\lambda > \lambda_\mathrm{c}$) and non-zero in the low-λ phase ($\lambda < \lambda_\mathrm{c}$). Precisely at the critical point $D_z = 0$. The finite-size estimates at the critical point are nonzero but must converge to zero, which is the basis of our analysis. However, our estimates of critical points are necessarily wrong, in a strict sense. Even if we fix λ to our best estimate of λ_c, and that is exactly what we do, the argument $r_t = tL^{1/\nu} = (\lambda - \lambda_\mathrm{c})L^{1/\nu}$, will drive the datapoints away from the critical behaviour with growing system size L. A good estimate of λ_c certainly prevents this from happening up to sufficiently large L, by generating a small "amplitude" proportional to $(\lambda - \lambda_\mathrm{c})$. However, at some L_cr, the inaccuracy of the estimate of λ_c strikes and leads to a crossover from the finite-size equivalent of critical to that of non-critical behaviour. If we overestimate λ_c, we are in the $\langle D_z \rangle = 0$ phase, where finite-size datapoints still converge to zero, but, for $L \gg L_\mathrm{cr}$, with an exponent that is different from β_z/ν and is determined by the non-critical behaviour. Contrarily, if we underestimate λ_c, we are in what we call the ordered phase, and finite-size datapoints converge to the nonzero thermodynamic limit of the order parameter. In the FSS analysis, this latter case would generate a small but nonzero and *positive* background. Figure C.1 shows two examples of the dependence of the FSS analysis on the value of our estimate of the critical point, which represent the general tendency. The influence of the value of λ_c is visibly stronger a large Δ close to the isotropic point, where a variation of λ_c by three errorbars leads to significantly different estimates of the critical exponent ratio. This is not the case at small Δ.

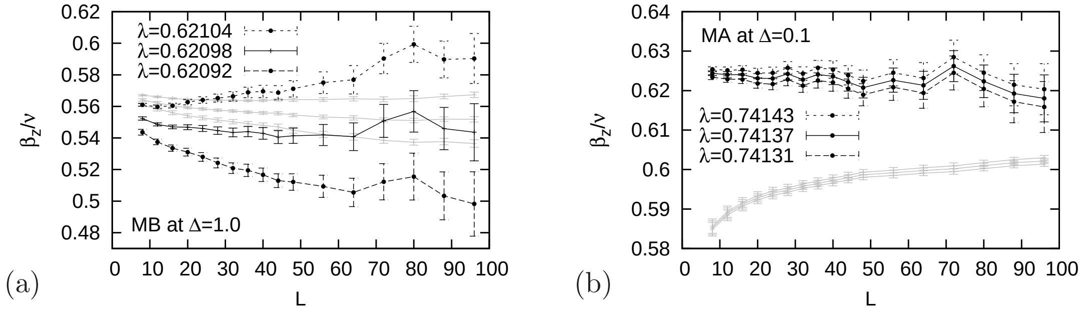

(a) (b)

Figure C.1: Examples of the dependence of results on the value of the critical points. Results of double-log linear fits (grey) to $\ln D_z(L) = \ln A + \beta_z/\nu \ln L$, at $\lambda = \lambda_\mathrm{c}$ and $\lambda = \lambda_\mathrm{c} \pm 3\sigma$, are compared to results of non-linear fits (black) to $D_z(L) = AL^{-\beta_z/\nu} + CL^{-1}$.

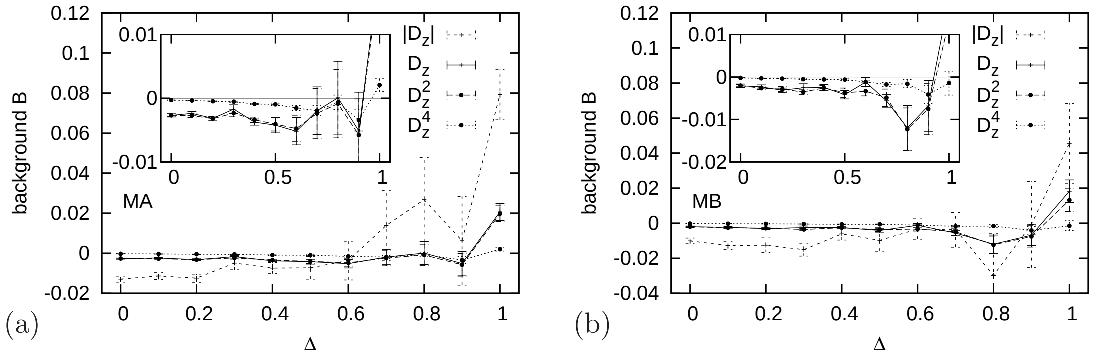

Figure C.2: The (L_{min}-dependent) effective background of the longitudinal string observables, obtained from non-linear fits to a single power-law, is, for $\Delta \leq 0.9$, negative or consistent with zero in both models, MA (**a**) and MB (**b**).

More importantly, however, is that from non-linear fits to a pure power-law with background we found, if at all, a very small negative background for roughly $\Delta < 0.7$. An effective background that is very small and nonzero but *negative* cannot, following our above discussion, be explained by the estimate of λ_{c} being seriously wrong. However, it can be the result of compensating for the presence of power-law corrections to FSS that have been neglected. We attribute the positive effective background that is visible at $\Delta = 1$, to the presence of logarithmic corrections.

Power-law corrections. The consideration of subleading power-law corrections to FSS means that we model the finite-size behaviour of D_z by

$$D_z(\lambda_{\mathrm{c}}; L) \sim AL^{-\beta_z/\nu}(1 + CL^{-\omega}) \,, \tag{C.1}$$

where A and C are the leading and sub-leading amplitudes, respectively. We present here the results of the *quotients* method [253]. Assuming absence of a background and presence of a single power-law correction, the quotients method is to fit suitable ratios of datapoints, e.g.

$$\frac{D_z(\lambda_{\mathrm{c}}; L)}{D_z(\lambda_{\mathrm{c}}; 2L)} = 2^{-\beta_z/\nu} \frac{1 + CL^{-\omega}}{1 + C(2L)^{-\omega}} \sim 2^{-\beta_z/\nu} \left(1 + \tilde{C}L^{-\omega}\right) \,, \tag{C.2}$$

where $\tilde{C} = (C - C/2^{\omega})$, and similar for the other moments of D_z. This results in a non-linear three-parameter fit, and the reduction of datapoints as well as error propagation lead to an increase of error estimates.

Estimates of $\beta_z^{(i)}/\nu$, that result from the quotients method are shown in Fig. C.3 where they replace the corresponding datasets in Figs. 8.20b and 8.21b from Sect. 8.4. In contrast to the fits in Sect. 8.4, we face the serious limitation, here, that we cannot, in most cases, arbitrarily raise L_{min} in the fits. This is partly due to the fact that we are looking at subleading effects, but also due to the reduction of data points, increase of errors *and* the exponent ω being a free parameter. What is most remarkable, is, however, that with the quotients method we observed a dramatic improvement in matching scaling relations in both models and all observables! For small L_{min} in

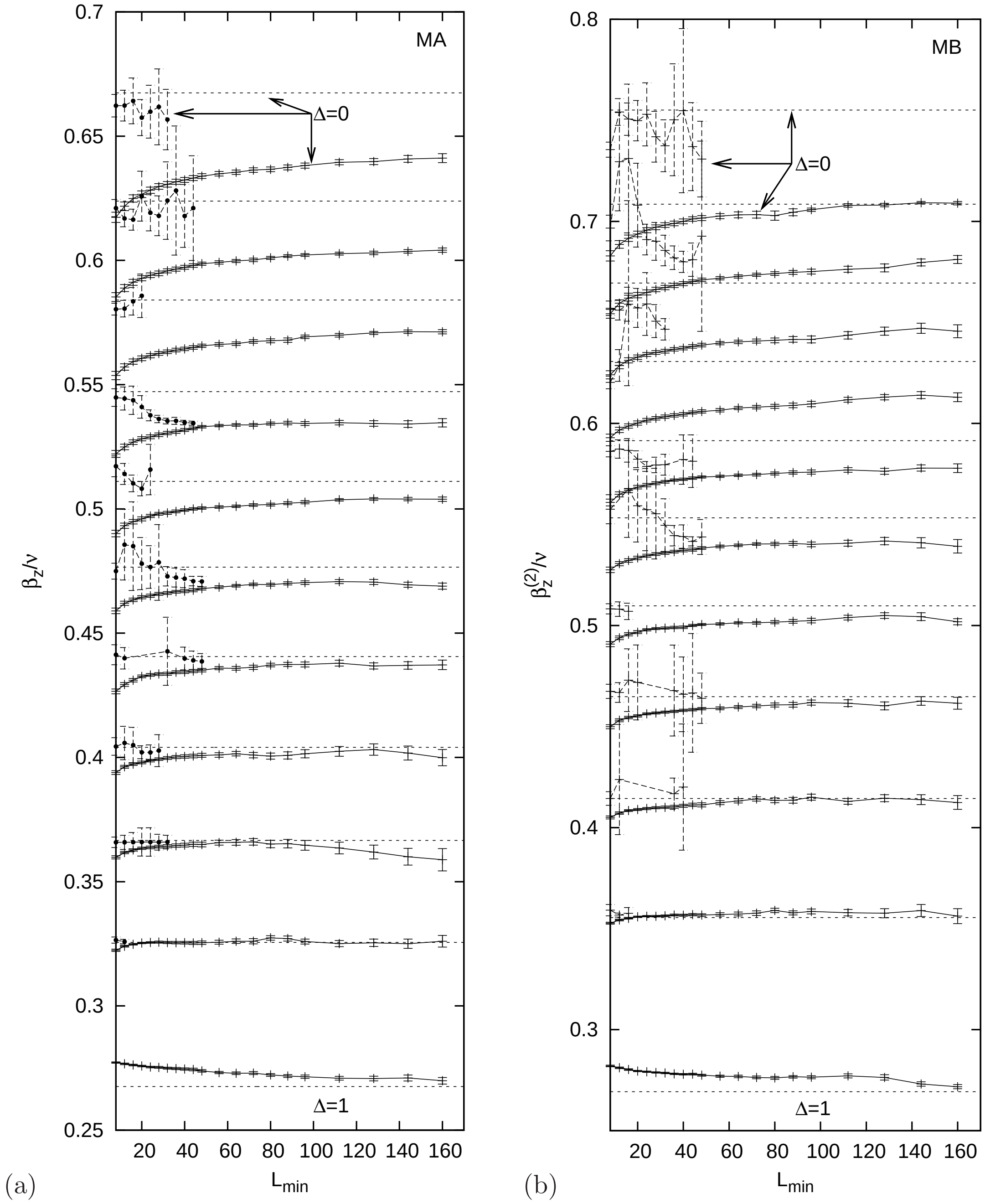

Figure C.3: MA, FSS analysis of D_z. (**a**) FSS behaviour at the critical point $\lambda_c(\Delta)$. (**b**) $L_{\min}$-dependence of the final estimate of β_z/ν from double-log linear fits. For all Δ, $L_{\max} = 384$. Results of double-log linear fits (datapoints connected by full lines) are compared to results of the quotients method (dots with dahsed errorbars). Dashed horizontal lines show the estimate β_z/ν obtained from γ/ν by Gaussian scaling relations and conjecture (8.22). Datasets correspond to $\Delta = 0 \dots 1$ from top to bottom in (**a**), and reversed in (**b**), as indicated by the labels.

Figure C.4: Illustration of the quotients method. Datasets converge to a "background" of value $2^{\beta_z/\nu}$. Compared to the data shown in, e.g., Figs. 8.20a and 8.21a, the errors are much more pronounced and the estimation of the parameter ω from non-linear fits (see insets) is far less accurate than that of the constant background. In particular, if L_{min} is set too large, a meaningful value of ω cannot be extracted.

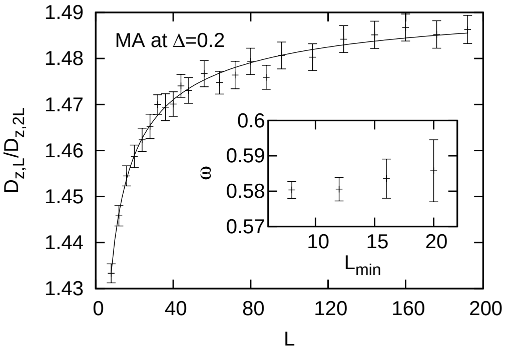

MA, the quotients method almost perfectly produced the values of β_z/ν that were to be expected (if we accept the drawback that it is twice as large as expected, in fact), and (8.22) to hold as equalities. For MB this is not the case, but there is a visible tendency into the expected direction. However, the corresponding datapoints also show the limitations. For D_z of MA at $\Delta = 0.3$ and 0.5, the estimate of β_z/ν of the quotients method visibly crosses over to match the estimate of the double-log linear fit. In those two cases, for example, we could indeed observe something like a convergence of the double-log linear fit in L_{min}. This could either mean, on one hand, that something was seriously wrong with our analysis, but, on the other hand, also that the observed convergence is a pseudo-convergence within the statistical (in)accuracy of the data, which the quotients method simply is not able to resolve anymore. Missing datapoints or datapoints with large errors, such as for MA at $\Delta = 0.6$, result from a missing or extremely shallow minimum of χ^2_{dof} in the corresponding non-linear fit, which underlines the delicateness of the task. We emphasize again, that it was subleading effects that we tried to quantify here. Our analysis showed that we need almost all chain lengths to be able to reach quantitatively meaningful results.

The quality of data that was to be fitted can be judged in Fig. C.4 which shows two examples. For $L_{\mathrm{min}} > 20$, it can be seen that any visible dependence on L drowns in the statistical inaccuracy of the data. What is further visible in the plots of Fig. C.4, is that the datapoints approach a limiting value from below. In the fits we used the asymptotic form of (C.2). With $\omega > 0$, an effective asymptotic amplitude $\tilde{C} < 0$ implies that also $C < 0$. A negative amplitude of the leading (or effective) correction may be an explanation for the observation of a negative effective background discussed above.

A graphical comparison of β_z/ν obtained from double-log linear fits with $L_{\mathrm{min}} = 160$ and β_z/ν from the quotients method with $L_{\mathrm{min}} = 8$, is most striking for MA (Fig. C.5, at the end of this section), where the value expected from conversion of γ/ν is included, while for MB (Fig. C.6, at the end of this section) it is by far not as convincing. The insets, however, show a significantly better satisfaction of (8.22) for $\Delta \leq 0.8$ in both models when the values from the quotients method are compared, which is why we conjecture (8.22) to hold as true equalities.

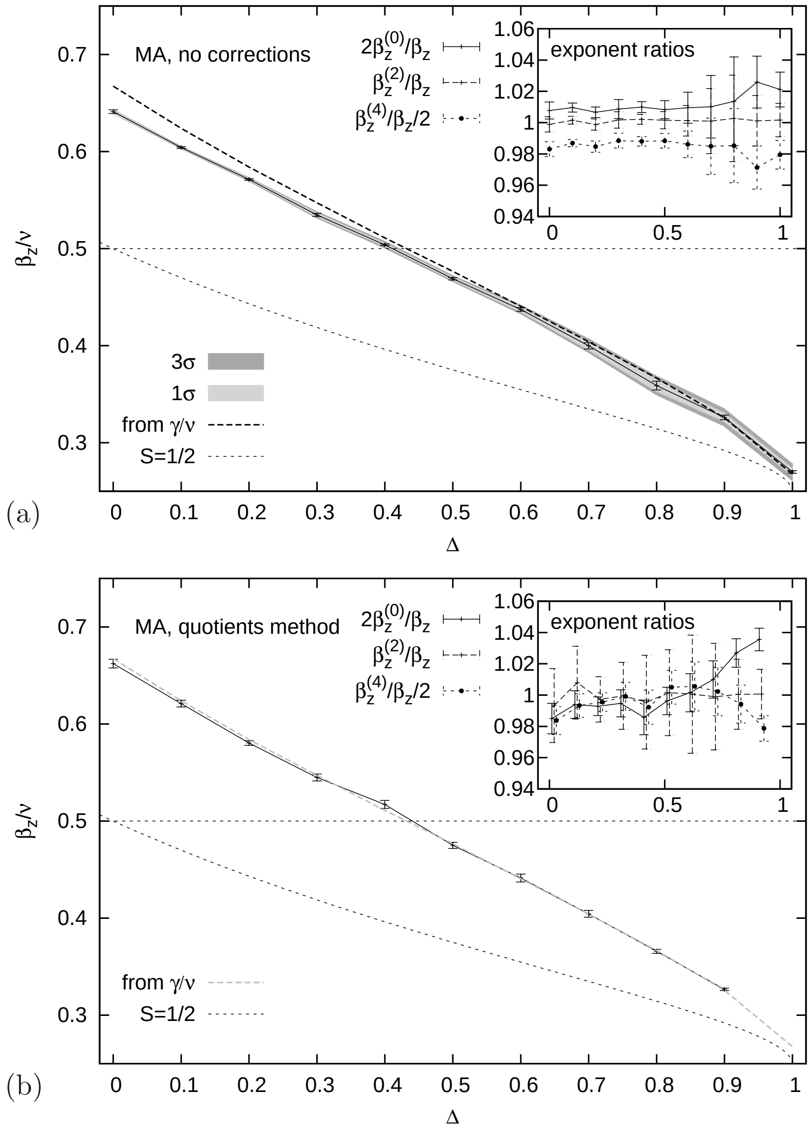

Figure C.5: MA. Final estimates of the critical exponent ratio β_z/ν of the longitudinal string observable D_z. Dashed curves show the exact value of β_z/ν for spin-$\frac{1}{2}$ chain (see main text). Dashed horizontal lines mark the pure XY-point of the spin-$\frac{1}{2}$ chain for comparison. The insets compare the exponents of the moments $|D_z|$, D_z^2 and D_z^4 to that of D_z itself. (**a**) Analysis without power-law corrections (double-log linear fits). Grey regions mark the variation, if our estimates of the critical points are varied by $\pm 1\sigma$ (light-grey) and $\pm 3\sigma$ (dark-grey). (**b**) Analysis with an effective power-law correction (quotients method).

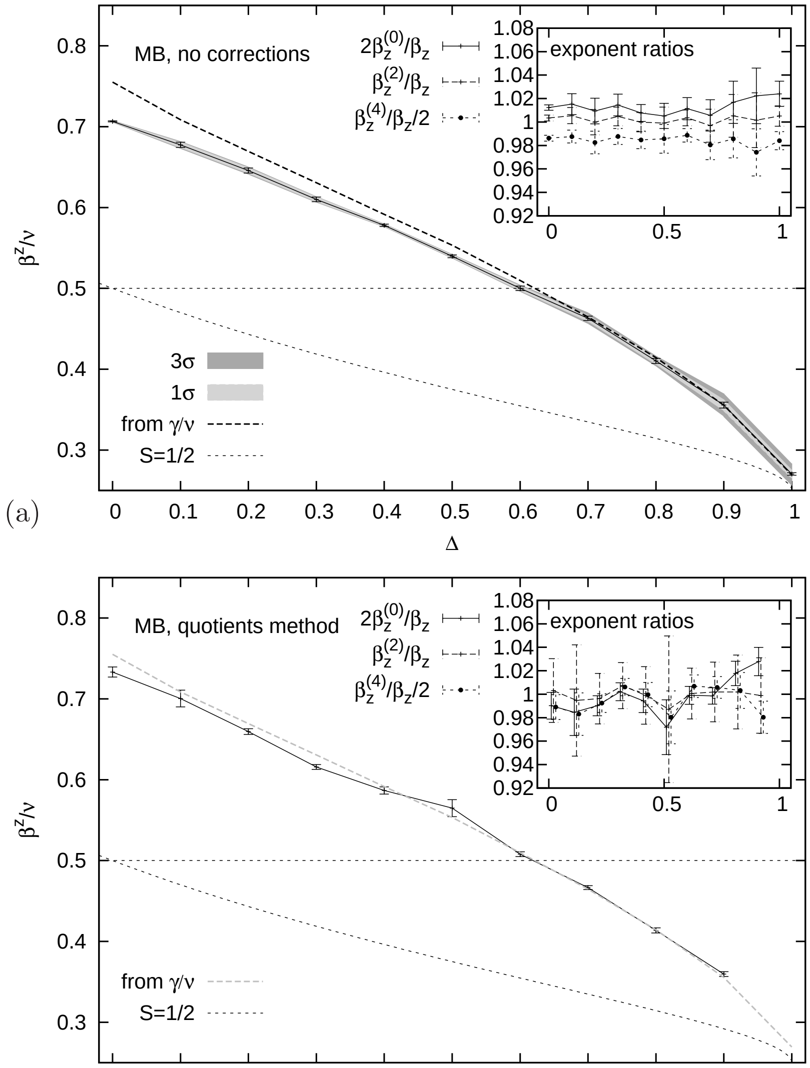

Figure C.6: Same as Fig. C.5, but for MB.

A flaw in the definition of D_z? In Sect. 8.4, we presented results of the critical exponent ratio β_z/ν that were obtained from fits to a FSS form that includes an additive correction term in L^{-1}. We were lead to try and fix the correction exponent ω in (C.1) by a comparison of the values for ω obtained from the quotients method to $-1/2\nu$, which is shown in Sect. 8.4 in Fig. 8.22. If $\beta_z/\nu = x_\lambda/2$, as our data suggests, the scaling relation $\beta_z/\nu + 1/2\nu = 1$, implies that

$$D_z(L) = AL^{-\beta_z/\nu}\left(1 + \mathcal{C}L^{-1/2\nu} + \cdots\right) = AL^{-\beta_z/\nu} + CL^{-1} + \cdots , \tag{C.3}$$

with $C = A\mathcal{C}$.

In the lack of an interpretation of a correction exponent that takes the values $1/2\nu$, we questioned reasons for an unusual additive L^{-1}-correction. And, indeed, we found a possible source in the very definition of the observable D_z itself. We will address this issue in more detail in the following.

The definition of the observable that we measured is $D_z = 2/L\sum_i D_{z,2i}$. The last term in this sum consists of all (sub)spins in the chain. With the groundstate being located in the sector with zero magnetization, it contains an equal number of subspins that are up and down if $L/2$ is even. Consequently, in the groundstate of all chains considered in this thesis, $D_{z,L} = 1$, always.

This means, that what we measure is

$$D_z = \frac{2}{L}\sum_{i=1}^{L/2} D_{z,2i} = \frac{2}{L}\left[\sum_{i=1}^{L/2-1} D_{z,2i} + D_{z,2L}\right] =: \frac{2}{L}\left[\left(\frac{L}{2} - 1\right)\tilde{D}_z + \langle D_{z,L}\rangle\right] , \tag{C.4}$$

where we have introduced a new truncated and normalized observable

$$\tilde{D}_z = \frac{1}{L/2-1}\sum_{i=1}^{L/2-1} D_{z,2i} , \tag{C.5}$$

and $\langle D_{z,L}\rangle = f(a, \xi_\tau^{-1}) \approx 1$, which is a function of the aspect ratio a and the energy gap, i.e. the inverse imaginary time correlation length $\xi_\tau^{-1} = E_1 - E0$, which depends on the chain length and the exchange anisotropy parameter Δ. If $\langle D_{z,L}\rangle$ really is responsible for the additive L^{-1}-correction, it would have been better to measure $\tilde{D}_z$ instead of D_z. Assuming $\tilde{D}_z \sim L^{-\beta_z/\nu}$, we would have had to consider

$$D_z(L) = AL^{-\beta_z/\nu} - 2AL^{-\beta_z/\nu-1} + 2\langle D_{z,L}\rangle L^{-1} + \cdots , \tag{C.6}$$

which yields an amplitude of the L_{-1}-term of approximately 2. But there is another term $\sim L^{-\beta_z/\nu-1}$. We did not consider this term in the fits, the results of which have been presented in Sect. 8.4. If it is significantly present but not considered, it will mix into the leading term and the L^{-1}-correction. Due its negative sign it is possible that it generates a negative effective amplitude C, if $\langle D_{z,L}\rangle < \tilde{D}_z$. Conversely, if $\langle D_{z,L}\rangle > D_z > \tilde{D}_z$, the supposedly sub-optimal constant $\tilde{D}_z$ added in the definition of D_z, generates a positive effective amplitude C. This would be in contradiction to our data (ignoring the fact that at the isotropic point the amplitude C is positive).

In our QMC simulations we have chosen the aspect ratio $a = \beta/L$, such that groundstate properties are measured only *almost* exclusively. Excited states with nonzero

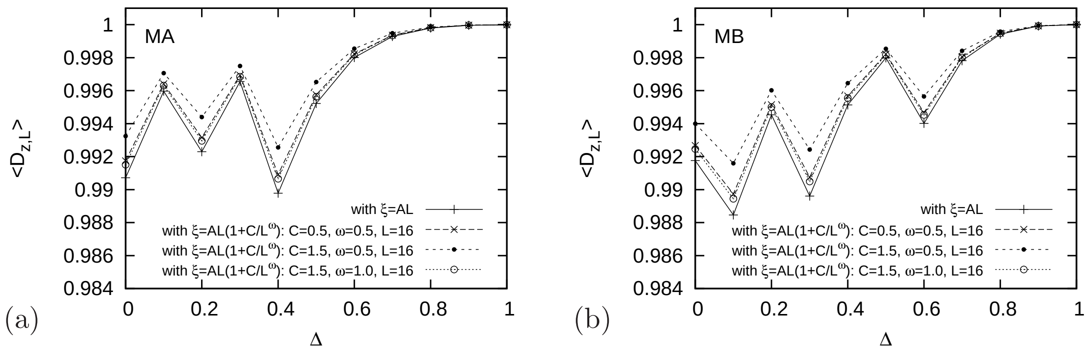

Figure C.7: Estimate of the expectation value $\langle D_{z,L}\rangle$ as approximately estimated by (C.8) for a small chain length $L = 16$. The estimate of the amplitude A has been taken from our analysis in Sect. 11.1, and reasonable values for ω and C, given in the legend, have been assumed.

magnetization inevitably mix in with a small contribution of $D_{z,L} = -1$. Thus, to finish this argument, we need to check if the finite inverse temperature in our simulations modifies the expectation value $\langle D_{z,L}\rangle$, such that $\langle D_{z,L}\rangle \approx 1$ is considerably violated. To this end, we estimate the expectation value $\langle D_{z,L}\rangle$, by considering only the two degenerate lowest eigenstates with $|M| = 1$ with energy E_1,[1]

$$\langle D_{z,L}\rangle = \frac{1}{Z}\left[\mathrm{e}^{-\beta E_0} - 2\mathrm{e}^{-\beta E_1} + \cdots\right] = \frac{1 - 2\mathrm{e}^{-\beta/\xi_\tau} + \cdots}{1 + 2\mathrm{e}^{-\beta/\xi_\tau} + \cdots}\,. \tag{C.7}$$

We now replace β by aL, with the aspect ratio a, and the inverse energy gap by a general FSS form $\xi_\tau \approx AL(1 + CL^{-\omega})$. The FSS amplitude A, of the correlation length has been estimated (two times for MA) in this thesis. In Sect. 10, it appeared as $A^{-1} = 2\pi v x_{1,0}$, with $x_{1,0}$ the scaling dimension of the scaling operators that generate the lowest excited levels. Implicitly, the amplitude of the fourth-moment estimator of the correlation length appear in Sect. 9 and explicitly in Sect. 11.1, where we also tried to extract the correction exponent ω. We may thus feed different estimates of various accuracy into

$$\langle D_{z,L}\rangle \approx \frac{1 - 2\mathrm{e}^{-a/(A(1+CL^{-\omega}))}}{1 + 2\mathrm{e}^{-a/(A(1+CL^{-\omega}))}} \approx \frac{1 - 2\mathrm{e}^{-a/A}}{1 + 2\mathrm{e}^{-a/A}}\,, \tag{C.8}$$

where the second approximation, from assuming absence of power-law corrections in the FSS behaviour of the correlation length, does not depend on L anymore. Figure C.7 shows that, in both mixed spin models, the deviation from $\langle D_{z,L}\rangle = 1$, is at most one percent, and that power-law corrections in $L^{-\omega}$, decrease the deviation further. With the values of the correction amplitudes and exponents that we estimated in Sect. 11.1, we conclude that $\langle D_{z,L}\rangle$ *cannot* explain the corrections to FSS observed in D_z, which shall therefore remain unexplained for the time being.

---

[1] At the isotropic point, the elementary triplet excitation is completely degenerate, which would lead to a slightly different approximation $(1 - \mathrm{e}^{-\beta/\xi_\tau} + \cdots)(1 + 3\mathrm{e}^{-\beta/\xi_\tau} + \cdots)$, in the following.

Bibliography

[1] W. Heisenberg, Z. Phys. **49**, 619 (1928).

[2] W. Blüm, H.-P. Dürr, and H. Rechenberg, eds., *Werner Heisenberg Gesammelte Werke*, A/I (Springer, Berlin Heidelberg, 1985).

[3] F. D. M. Haldane, Phys. Rev. Lett. **50**, 1153 (1983).

[4] W. J. L. Buyers, R. M. Morra, R. L. Armstrong, M. J. Hogan, P. Gerlach, and K. Hirakawa, Phys. Rev. Lett. **56**, 371 (1986).

[5] S. R. White and D. A. Huse, Phys. Rev. B **48**, 3844 (1993).

[6] A. M. Tsvelik, *Quantum Field Theory in Condensed Matter Physics* (University Press, Cambridge, 1995).

[7] A. O. Gogolin, A. A. Nersesyan, and A. M. Tsvelik, *Bosonization and Strongly Correlated Systems* (University Press, Cambridge, 1998).

[8] T. Giamarchi, *Quantum Physics in One Dimension* (Clarendon Press, Oxford, 2003).

[9] H. G. Evertz, G. Lana, and M. Marcu, Phys. Rev. Lett. **70**, 873 (1993).

[10] H. G. Evertz, Adv. Phys. **52**, 1 (2003).

[11] A. W. Sandvik, Phys. Rev. B **59**, R14157 (1999).

[12] S. Chattopadhyay, D. Jain, V. Ganesan, S. Giri, and S. Majumdar, Phys. Rev. B **82**, 094431 (2010).

[13] E. Canévet, B. Grenier, Y. Yoshida, N. Sakai, L.-P. Regnault, T. Goto, Y. Fujii, and T. Kawae, Phys. Rev. B **82**, 132404 (2010).

[14] V. N. Glazkov, A. I. Smirnov, A. Zheludev, and B. C. Sales, Phys. Rev. B **82**, 184406 (2010).

[15] V. N. Glazkov, T. S. Yankova, J. Sichelschmidt, D. Hüvonen, and A. Zheludev, Phys. Rev. B **85**, 054415 (2012).

[16] P. Calabrese, J. Cardy and B. Doyon, eds., J. Phys. A **42** (2009), Special Issue.

[17] C. D. E. Boschi, M. D. Dio, G. Morandi, and M. Roncaglia, J. Phys. A **42**, 055002 (2009).

[18] A. V. Sizanov and A. V. Syromyatnikov, Phys. Rev. B **84**, 054445 (2011).

[19] J. Tamaki and M. Oshikawa, Phys. Rev. B **85**, 134431 (2012).

[20] A. F. Albuquerque, C. J. Hamer, and J. Oitmaa, Phys. Rev. B **79**, 054412 (2009).

[21] S. Wenzel and W. Janke, Phys. Rev. B **80**, 054403 (2009).

[22] H. C. Jiang, F. Krüger, J. E. Moore, D. N. Sheng, J. Zaanen, and Z. Y. Weng, Phys. Rev. B **79**, 174409 (2009).

[23] X. Yan, W. Li, Y. Zhao, S.-J. Ran, and G. Su, Phys. Rev. B **85**, 134425 (2012).

[24] S. Sachdev, *Quantum Phase Transitions* (University Press, Cambridge, 1999).

[25] M. Henkel, *Conformal Invariance and Critical Phenomena* (Springer, Berlin Heidelberg, 2010).

[26] J. L. Cardy, *Scaling and Renormalization in Statistical Physics* (University Press, Cambridge, 1996).

[27] J. G. Bednorz and K. A. Müller, Z. Phys. B **64**, 189 (1986).

[28] B. Batlog, Phys. Today **44**, 44 (1991).

[29] K. Ishida, Y. Kitaoka, K. Asayama, M. Azuma, Z. Hiroi, and M. Takano, J. Phys. Soc. Jpn. **63**, 3222 (1994).

[30] H. Kuzmany, R. Pfeiffer, and F. Simon, Phys. Unserer Zeit **39**, 21 (2008).

[31] S. Venkataramani, U. Jana, M. Dommaschk, F. D. Sönnichsen, F. Tuczek, and R. Herges, Science **331**, 445 (2011).

[32] L. Barrios, D. Aguilà, O. Roubeau, P. Gamez, J. Ribas-Ariño, S. J. Teat, and G. Aromí, Chem. Eur. J. **15**, 11235 (2009).

[33] X.-H. Peng and D. Suter, Front. Phys. Chn. **5**, 1 (2010).

[34] A. Osterloh, L. Amico, G. Falci, and R. Fazio, Nature **416**, 608 (2002).

[35] V. S. Zapf, D. Zocco, B. R. Hansen, M. Jaime, N. Harrison, C. D. Batista, M. Kenzelmann, C. Niedermayer, A. Lacerda, and A. Paduan-Filho, Phys. Rev. Lett. **96**, 077204 (2006).

[36] S. A. Zvyagin, J. Wosnitza, A. K. Kolezhuk, V. S. Zapf, M. Jaime, A. Paduan-Filho, V. N. Glazkov, S. S. Sosin, and A. I. Smirnov, Phys. Rev. B **77**, 092413 (2008).

[37] W. Marshall, Proc. R. Soc. London Ser. **A 232**, 48 (1955).

[38] A. Auerbach, *Interacting electrons and quantum magnetism* (Springer, New York, 1994).

[39] G.-S. Tian and H.-Q. Lin, Phys. Rev. B **66**, 224408 (2002).

[40] G.-S. Tian and H.-Q. Lin, Phys. Rev. B **70**, 104412 (2004).

[41] T. Fukui and N. Kawakami, Phys. Rev. B **55**, R14709 (1997).

[42] T. Fukui and N. Kawakami, Phys. Rev. B **56**, 8799 (1997).

[43] K. Takano, Phys. Rev. B **61**, 8863 (2000).

[44] K. Takano, Phys. Rev. Lett. **82**, 5124 (1999).

[45] I. Affleck, T. Kennedy, E. H. Lieb, and H. Tasaki, Phys. Rev. Lett. **59**, 799 (1987).

[46] I. Affleck, T. Kennedy, E. H. Lieb, and H. Tasaki, Commun. Math. Phys. **115**, 477 (1988).

[47] C. K. Majumdar and D. K. Ghosh, J. Math. Phys. **10**, 1399 (1969).

[48] T. Tonegawa, T. Hikihara, M. Kaburagi, T. Nishino, S. Miyashita, and H.-J. Mikeska, J. Phys. Soc. Jpn. **67**, 1000 (1998).

[49] Z. Xu, J. Dai, H. Ying, and B. Zheng, Phys. Rev. B **67**, 214426 (2003).

[50] R. Bischof and P. R. Crompton, JETP Lett. **84**, 729 (2006).

[51] R. Bischof and W. Janke, in *Proc. 9th Int. Conf. Path Integrals – News, Trends and Perspectives*, edited by W. Janke and A. Pelster (World Scientific, Singapore, 2008), pp. 514–517.

[52] S.-B. Li, Z.-X. Xu, J.-H. Dai, and J.-B. Xu, Phys. Rev. B **73**, 184411 (2006).

[53] C. Lanczos, J. Res. Nat. Bur. Stand. **45**, 255 (1950).

[54] B. B. Beard and U.-J. Wiese, Phys. Rev. Lett. **77**, 5130 (1996).

[55] N. Prokof'ev, B. Svistunov, and I. Tupitsyn, Pis'ma v Zh. Eks. Teor. Fiz. (????).

[56] M. N. Barber, in *Phase Transitions and Critical Phenomena*, edited by C. Domb and J. L. Lebowitz (Academic Press, London, 1983), vol. 8.

[57] J. L. Cardy, ed., *Current Physics Sources and Comments Vol.2: Finite Size Scaling* (North Holland, Amsterdam, 1998).

[58] S. Todo and K. Kato, Phys. Rev. Lett. **87**, 047203 (2001).

[59] A. M. Ferrenberg and R. H. Swendsen, Phys. Rev. Lett. **61**, 2635 (1988).

[60] A. M. Ferrenberg and R. H. Swendsen, Phys. Rev. Lett. **63**, 1195 (1989).

[61] M. Troyer, F. Alet, and S. Wessel, Braz. J. Phys. **34**, 377 (2004).

[62] S. Blundell, *Magnetism in Condensed Matter* (University Press, Oxford, 2001).

[63] L.-P. Lévy, *Magnetism and Superconductivity* (Springer, Berlin Heidelberg, 2000).

[64] M. Takahashi, Y. Hosokoshi, H. Nakano, T. Goto, M. Takahashi, and M. Kinoshita, Mol. Cryst. Liq. Cryst. **306**, 111 (1997).

[65] M. Hase, I. Terasaki, and K. Uchinokura, Phys. Rev. Lett. **70**, 3651 (1993).

[66] J. P. Pouget, L. P. Regnault, M. Ain, B. Hennion, J. P. Renard, P. Veillet, G. Dhalenne, and A. Revcolevschi, Phys. Rev. Lett. **72**, 4037 (1994).

[67] T. M. Brill, J. P. Boucher, J. Voiron, G. Dhalenne, A. Revcolevschi, and J. P. Renard, Phys. Rev. Lett. **73**, 1545 (1994).

[68] Y. Fagot-Revurat, M. Horvati, C. Berthier, P. Ségransan, G. Dhalenne, and A. Revcolevschi, Phys. Rev. Lett. **77**, 1861 (1996).

[69] R. Peierls, *Quantum Theory of Solids* (University Press, Oxford, 1955).

[70] H. Manaka and I. Yamada, J. Phys. Soc. Jpn. **66**, 1908 (1997).

[71] H. Manaka, I. Yamada, and K. Yamaguchi, J. Phys. Soc. Jpn. **66**, 564 (1997).

[72] T. Masuda, A. Zheludev, H. Manaka, L.-P. Regnault, J.-H. Chung, and Y. Qiu, Phys. Rev. Lett. **96**, 047210 (2006).

[73] P. R. Hammar and D. H. Reich, J. Appl. Phys. **79**, 5392 (1996).

[74] G. Chaboussant, P. A. Crowell, L. P. Lévy, O. Piovesana, A. Madouri, and D. Mailly, Phys. Rev. B **55**, 3046 (1997).

[75] G. Chaboussant, M.-H. Julien, Y. Fagot-Revurat, M. Hanson, L. Lévy, C. Berthier, M. Horvatić, and O. Piovesana, Eur. Phys. J. B **6**, 167 (1998).

[76] M. Hagiwara, H. A. Katori, U. Schollwöck, and H.-J. Mikeska, Phys. Rev. B **62**, 1051 (2000).

[77] K. Izumi, T. Goto, Y. Hosokoshi, and J.-P. Boucher, Physica B **329-333**, 1191 (2003).

[78] Y. Yoshida, N. Tateiwa, M. Mito, T. Kawae, K. Takeda, Y. Hosokoshi, and K. Inoue, Phys. Rev. Lett. **94**, 037203 (2005).

[79] M. Kenzelmann, R. A. Cowley, W. J. L. Buyers, Z. Tun, R. Coldea, and M. Enderle, Phys. Rev. B **66**, 024407 (2002).

[80] C. Payen, P. Molinie, P. Colombet, and G. Fillion, J. Magn. Magn. Mat. **84**, 95 (1990).

[81] H. Mutka, J. L. Soubeyroux, G. Bourleaux, and P. Colombet, Phys. Rev. B **39**, 4820 (1989).

[82] H. Mutka, C. Payen, P. Molinié, J. L. Soubeyroux, P. Colombet, and A. D. Taylor, Phys. Rev. Lett. **67**, 497 (1991).

[83] J. P. Renard, M. Verdaguer, L. P. Regnault, W. A. C. Erkelens, J. Rossat-Mignod, J. Ribas, W. G. Stirling, and C. Vettier, J. Appl. Phys. **63**, 3538 (1988).

[84] Y. Koike, N. Metoki, Y. Morii, T. Kobayashi, T. Ishii, and M. Yamashita, J. Phys. Soc. Jpn. **69**, 4034 (2000).

[85] S. A. Zvyagin, J. Wosnitza, C. D. Batista, M. Tsukamoto, N. Kawashima, J. Krzystek, V. S. Zapf, M. Jaime, N. F. Oliveira, and A. Paduan-Filho, Phys. Rev. Lett. **98**, 047205 (2007).

[86] Y. Uchiyama, Y. Sasago, I. Tsukada, K. Uchinokura, A. Zheludev, T. Hayashi, N. Miura, and P. Böni, Phys. Rev. Lett. **83**, 632 (1999).

[87] A. Zheludev, T. Masuda, I. Tsukada, Y. Uchiyama, K. Uchinokura, P. Böni, and S.-H. Lee, Phys. Rev. B **62**, 8921 (2000).

[88] N. Tsujii, O. Suzuki, H. Suzuki, H. Kitazawa, and G. Kido, Phys. Rev. B **72**, 104402 (2005).

[89] A. I. Smirnov, V. N. Glazkov, T. Kashiwagi, S. Kimura, M. Hagiwara, K. Kindo, A. Y. Shapiro, and L. N. Demianets, Phys. Rev. B **77**, 100401 (2008).

[90] J. V. Alvarez, R. Valentí, and A. Zheludev, Phys. Rev. B **65**, 184417 (2002).

[91] J. V. Alvarez and R. Valentí, Eur. Phys. J. B **44**, 439 (2005).

[92] J. Darriet and L. P. Regnault, Solid State Commun. **86**, 409 (1993).

[93] J. DiTusa, S.-W. Cheong, C. Broholm, G. Aeppli, L. Rupp, Jr., and B. Batlogg, Physica B **194-196**, 181 (1994).

[94] T. Yokoo, T. Sakaguchi, K. Kakurai, and J. Akimitsu, J. Phys. Soc. Jpn. **64**, 3651 (1995).

[95] A. Escuer, R. Vicente, X. Solans, and M. Font-Bardia, Inorg. Chem. **33**, 6007 (1994).

[96] Y. Narumi, M. Hagiwara, R. Sato, K. Kindo, H. Nakano, and M. Takahashi, Physica B **246-247**, 509 (1998).

[97] M. Hagiwara, Y. Narumi, K. Kindo, M. Kohno, H. Nakano, R. Sato, and M. Takahashi, RIKEN Rev. **46**, 14 (2002).

[98] Y. Narumi, M. Hagiwara, M. Kohno, and K. Kindo, Phys. Rev. Lett. **86**, 324 (2001).

[99] M. Hagiwara, L. P. Regnault, A. Zheludev, A. Stunault, N. Metoki, T. Suzuki, S. Suga, K. Kakurai, Y. Koike, P. Vorderwisch, et al., Phys. Rev. Lett. **94**, 177202 (2005).

[100] M. Hagiwara, Y. Narumi, K. Kindo, M. Kohno, H. Nakano, R. Sato, and M. Takahashi, Phys. Rev. Lett. **80**, 1312 (1998).

[101] S. Demeshko, G. Leibeling, S. Dechert, S. Fuchs, T. Pruschke, and F. Meyer, ChemPhysChem **8**, 405 (2007).

[102] M. Belaïche, M. Bakhache, M. Benhammou, K. El-Mabrouke, and M. Bousmina, Physica E **40**, 574 (2008).

[103] O. Jeannin, R. Clérac, T. Cauchy, and M. Fourmigué, Inorg. Chem. **47**, 10656 (2008).

[104] P. J. Van Koningsbruggen, O. Khan, K. Nakatani, Y. Pei, J. P. Renard, M. Drillon, and P. Legoll, Inorg. Chem. **29**, 3325 (1990).

[105] M. Hagiwara, K. Minami, Y. Narumi, K. Tatani, and K. Kindo, J. Phys. Soc. Jpn. **67**, 2209 (1998).

[106] Z.-H. Ni, L.-F. Zhang, V. Tangoulis, W. Wernsdorfer, A.-L. Cui, O. Sato, and H.-Z. Kou, Inorg. Chem. **46**, 6029 (2007).

[107] C. Jing and S. Qiu, Trans. Met. Chem. **32**, 528 (2007).

[108] J. Yoo, A. Yamaguchi, M. Nakano, J. Krzystek, W. E. Streib, L.-C. Brunel, H. Ishimoto, G. Christou, and D. N. Hendrickson, Inorg. Chem. **40**, 4604 (2001).

[109] D. Li, H. Wang, S. Wang, Y. Pan, C. Li, J. Dou, and Y. Song, Inorg. Chem. **49**, 3688 (2010).

[110] F. Simon, H. Kuzmany, B. Náfrádi, T. Fehér, L. Forró, F. Fülöp, A. Jánossy, L. Korecz, A. Rockenbauer, F. Hauke, et al., Phys. Rev. Lett. **97**, 136801 (2006).

[111] J. Sloan, A. I. Kirkland, J. L. Hutchison, and M. L. H. Green, Chem. Commun. **13**, 1319 (2002).

[112] J. J. García-Ripoll, M. A. Martin-Delgado, and J. I. Cirac, Phys. Rev. Lett. **93**, 250405 (2004).

[113] S. E. Sebastian, D. Yin, P. Tanedo, G. A. Jorge, N. Harrison, M. Jaime, Y. Mozharivskyj, G. Miller, J. Krzystek, S. A. Zvyagin, et al., Phys. Rev. B **71**, 212405 (2005).

[114] K. Kodama, J. Yamazaki, M. Takigawa, H. Kageyama, K. Onizuka, and Y. Ueda, J. Phys. Cond. Mat. **14**, L319 (2002).

[115] K. Kodama, M. Takigawa, M. Horvatić, C. Berthier, H. Kageyama, Y. Ueda, S. Miyahara, F. Becca, and F. Mila, Science **298**, 395 (2002).

[116] T. Masuda, A. Zheludev, B. Sales, S. Imai, K. Uchinokura, and S. Park, Phys. Rev. B **72**, 094434 (2005).

[117] M. Hase, M. Matsuda, K. Kakurai, K. Ozawa, H. Kitazawa, N. Tsujii, A. Dönni, M. Kohno, and X. Hu, Phys. Rev. B **76**, 064431 (2007).

[118] H. Kleinert, *Path Integrals in Quantum Mechanics, Statistics, Polymer Physics, and Financial Markets* (World Scientific, Singapore, 2009).

[119] R. J. Baxter, *Exactly Solved Models in Statistical Mechanics* (Academic Press, London, 1982).

[120] T. Kashiwa, Y. Ohnuki, and M. Suzuki, *Path Integral Methods* (Clarendon Press, Oxford, 1997).

[121] R. J. Baxter, Phys. Rev. Lett. **26**, 832 (1971).

[122] R. J. Baxter, Ann. Phys. **70**, 193 (1972).

[123] F. Schwabl, *Statistische Mechanik* (Springer, Berlin Heidelberg, 2000).

[124] J. P. Sethna, *Statistical Mechanics: Entropy, Order Parameters and Complexity* (Clarendon Press, Oxford, 2010).

[125] J. M. Yeomans, *Statistical Mechanics of Phase Transition* (University Press, Oxford New York, 2000).

[126] G. Mussardo, *Statistical Field Theory* (University Press, Oxford New York, 2010).

[127] G. F. Mazenko, *Fluctuations, Order, and Defects* (John Wiley & Sons, New Jersey, 2003).

[128] L. P. Kadanoff, in *Phase Transitions and Critical Phenomena*, edited by C. Domb and J. L. Lebowitz (Academic Press, London, 1976), vol. 5a.

[129] R. J. Baxter and S. B. Kelland, J. Phys. C **7**, L403 (1974).

[130] A. Luther and I. Peschel, Phys. Rev. B **12**, 3908 (1975).

[131] L. P. Kadanoff, Phys. Rev. Lett. **39**, 903 (1977).

[132] L. P. Kadanoff and A. C. Brown, Ann. Phys. **121**, 318 (1979).

[133] M. P. M. den Nijs, Phys. Rev. B **23**, 6111 (1981).

[134] M. Vojta, Rep. Prog. Phys. **66**, 2069 (2003).

[135] A. Pelissetto and E. Vicari, Physics Reports **368**, 549 (2002).

[136] J. L. Cardy, in *Fields, Strings and Critical Phenomena, Les Houches, XLIX*, edited by E. Brézin and J. Zinn-Justin (North-Holland, Amsterdam, 1990).

[137] I. Affleck, Nucl. Phys. B **257**, 397 (1985).

[138] I. Affleck and F. D. M. Haldane, Phys. Rev. B **36**, 5291 (1987).

[139] Y. Kato and A. Tanaka, J. Phys. Soc. Jpn. **63**, 1277 (1997).

[140] M. Kohno, M. Takahashi, and M. Hagiwara, Phys. Rev. B **57**, 1046 (1998).

[141] M. Nakamura and S. Todo, Phys. Rev. Lett. **89**, 077204 (2002).

[142] M. den Nijs and K. Rommelse, Phys. Rev. B **40**, 4709 (1989).

[143] K. Hida, Phys. Rev. B **45**, 2207 (1992).

[144] M. Kohmoto and H. Tasaki, Phys. Rev. B **46**, 3486 (1992).

[145] K. Hida, Phys. Rev. B **46**, 8268 (1992).

[146] E. Lieb, T. Schultz, and D. Mattis, Ann. Phys. **16**, 407 (1961).

[147] M. Kohmoto, M. den Nijs, and L. P. Kadanoff, Phys. Rev. B **24**, 5229 (1981).

[148] M. Yamanaka, Y. Hatsugai, and M. Kohmoto, Phys. Rev. B **48**, 9555 (1993).

[149] A. Kitazawa, K. Nomura, and K. Okamoto, Phys. Rev. Lett. **76**, 4038 (1996).

[150] A. Kitazawa and K. Nomura, J. Phys. Soc. Jpn. **66**, 3944 (1997).

[151] K. Nomura, Phys. Rev. B **40**, 9142 (1989).

[152] J. M. Kosterlitz and D. J. Thouless, J. Phys. C **6**, 1181 (1973).

[153] D. P. Landau and K. Binder, *A Guide to Monte Carlo Simulations in Statistical Physics* (University Press, Cambridge, 2000).

[154] C. Fan, Phys. Rev. B **6**, 902 (1972).

[155] M. den Nijs, J. Phys. A **12**, 1857 (1979).

[156] M. Weigel and W. Janke, J. Phys. A **38**, 7067 (2005).

[157] R. Savit, Rev. Mod. Phys. **52**, 453 (1980).

[158] J. Ashkin and E. Teller, Phys. Rev. **64**, 178 (1943).

[159] M. Baake, G. von Gehlen, and V. Rittenberg, J. Phys. A **20**, L487 (1987).

[160] J. Salas and A. D. Sokal, J. Stat. Phys. **85**, 297 (1996).

[161] R. Mirman, *Group Theory: An Intuitive Approach* (World Scientific, Singapore, 2005).

[162] E. Fradkin and L. P. Kadanoff, Nucl. Phys. B **170**, 1 (1980).

[163] L. P. Kadanoff and M. Kohmoto, Nucl. Phys. B **190**, 671 (1981).

[164] F. C. Alcaraz, M. N. Barber, and M. T. Batchelor, Ann. Phys. **182**, 280 (1988).

[165] T. Kennedy and H. Tasaki, Phys. Rev. B **45**, 304 (1992).

[166] T. Kennedy and H. Tasaki, Commun. Math. Phys. **147**, 431 (1992).

[167] M. Oshikawa, J. Phys. Cond. Mat. **4**, 7469 (1992).

[168] F. C. Alcaraz and Y. Hatsugai, Phys. Rev. B **46**, 13914 (1992).

[169] M. Yajima and M. Takahashi, J. Phys. Soc. Jpn. **65**, 39 (1996).

[170] M. Yamanaka, M. Oshikawa, and S. Miyashita, J. Phys. Soc. Jpn. **65**, 1562 (1996).

[171] S. Yamamoto, Phys. Rev. B **55**, 3603 (1997).

[172] A. Kitazawa and K. Nomura, J. Phys. Soc. Jpn. **66**, 3379 (1997).

[173] T. Shun, H. Nakano, K. Kusakabe, and N. Suzuki, J. Phys. Soc. Jpn. **76**, 084714 (2007).

[174] T. Sakai and K. Okamoto, Phys. Rev. B **65**, 214403 (2002).

[175] F. C. Alcaraz and A. Moreo, Phys. Rev. B **46**, 2896 (1992).

[176] S. Yamamoto, Phys. Rev. B **51**, 16128 (1995).

[177] A. Moreo, Phys. Rev. B **36**, 8582 (1987).

[178] H. J. Schulz, Phys. Rev. B **34**, 6372 (1986).

[179] T. Giamarchi and H. J. Schulz, Phys. Rev. B **39**, 4620 (1989).

[180] J. Sólyom and J. Timonen, Phys. Rev. B **40**, 7150 (1989).

[181] I. Affleck, Nucl. Phys. B **265**, 409 (1985).

[182] K. Totsuka, Y. Nishiyama, N. Hatano, and M. Suzuki, J. Phys. Cond. Mat. **7**, 4895 (1995).

[183] A. Altland and B. Simons, *Condensed Matter Field Theory* (University Press, Cambridge New York, 2006).

[184] V. Knizhnik and A. Zamalodchikov, Nucl. Phys. B **247**, 83 (1984).

[185] F. C. Alcaraz and M. J. Martins, Phys. Rev. Lett. **61**, 1529 (1988).

[186] S. Yamamoto, Phys. Rev. B **52**, 10170 (1995).

[187] T. Ziman and H. J. Schulz, Phys. Rev. Lett. **59**, 140 (1987).

[188] A. Kitazawa and K. Nomura, Phys. Rev. B **59**, 11358 (1999).

[189] P. Jordan and E. Wigner, Z. Phys. A **47**, 631 (1928).

[190] T. D. Schultz, D. C. Mattis, and E. H. Lieb, Rev. Mod. Phys. **36**, 856 (1964).

[191] G. Spronken, B. Fourcade, and Y. Lépine, Phys. Rev. B **33**, 1886 (1986).

[192] H. J. Schulz, G. Cuniberti, and P. Pieri, in *Field Theories for Low-Dimensional Condensed Matter Systems*, edited by G. Morandi, P. Sodano, A. Tagliacozzo, and V. Tognetti (Springer, Berlin, 2000).

[193] K. Nomura, J. Phys. A **28**, 5451 (1995).

[194] M.-C. Cha, M. P. A. Fisher, S. M. Girvin, M. Wallin, and A. P. Young, Phys. Rev. B **44**, 6883 (1991).

[195] M. Wallin, E. S. Sørensen, S. M. Girvin, and A. P. Young, Phys. Rev. B **49**, 12115 (1994).

[196] J. des Cloizeaux and M. Gaudin, J. Math. Phys. **7**, 1384 (1965).

[197] J. D. Johnson, S. Krinsky, and B. M. McCoy, Phys. Rev. A **8**, 2526 (1973).

[198] C. J. Hamer, J. Phys. A **19**, 3335 (1986).

[199] A. Aharony and M. E. Fisher, Phys. Rev. B **27**, 4394 (1983).

[200] L. P. Kadanoff, Phys. Rev. B **22**, 1405 (1980).

[201] J. L. Black and V. J. Emery, Phys. Rev. B **23**, 429 (1981).

[202] R. R. P. Singh, M. E. Fisher, and R. Shankar, Phys. Rev. B **39**, 2562 (1989).

[203] I. Affleck, Phys. Rev. Lett. **62**, 839 (1989).

[204] I. Affleck and J. C. Bonner, Phys. Rev. B **42**, 954 (1990).

[205] A. L. Malevizzi and F. C. Alcaraz, J. Phys. Soc. Jpn. **64**, 4485 (1995).

[206] I. Affleck, D. Gepner, H. J. Schulz, and T. Ziman, J. Phys. A **22**, 511 (1989).

[207] D. C. Johnston, R. K. Kremer, M. Troyer, X. Wang, A. Klümper, S. L. Bud'ko, A. F. Panchula, and P. C. Canfield, Phys. Rev. B **61**, 9558 (2000).

[208] H. W. J. Blöte and M. P. Nightingale, Physica A **112**, 405 (1982).

[209] M. Nauenberg and D. J. Scalapino, Phys. Rev. Lett. **44**, 837 (1980).

[210] K. Nomura, Phys. Rev. B **48**, 16814 (1993).

[211] J. Salas and A. D. Sokal, J. Stat. Phys. **88**, 567 (2002).

[212] D. J. Amit, Y. Y. Goldschmidt, and S. Grinstein, J. Phys. A **13**, 585 (1980).

[213] J. L. Cardy, M. Nauenberg, and D. J. Scalapino, Phys. Rev. B **22**, 2560 (1980).

[214] L. N. Shchur, B. Berche, and P. Butera, Nucl. Phys. B **811**, 491 (2009).

[215] F. Woynarovich and H. P. Eckle, J. Phys. A **20**, L97 (1987).

[216] R. Kenna, D. A. Johnston, and W. Janke, Phys. Rev. Lett. **96**, 115701 (2006).

[217] R. Kenna, D. A. Johnston, and W. Janke, Phys. Rev. Lett. **97**, 155702 (2006).

[218] W. H. Press, S. A. Teukolsky, W. T. Vetterling, and B. P. Flannery, *Numerical Recipes* (University Press, Cambridge, 2007).

[219] A. Albuquerque, F. Alet, P. Corboz, P. Dayal, A. Feiguin, S. Fuchs, L. Gamper, E. Gull, S. Gürtler, A. Honecker, et al., J. Magn. Magn. Mat. **310**, 1187 (2007).

[220] J. Stoer and R. Burlisch, *Introduction to Numerical Analysis* (Springer, New York, 1980).

[221] M. Henkel and G. Schutz, J. Phys. A **21**, 2617 (1988).

[222] R. H. Swendsen and J.-S. Wang, Phys. Rev. Lett. **58**, 86 (1987).

[223] R. Brower, S. Chandrasekharan, and U.-J. Wiese, Physica A **261**, 520 (1998).

[224] O. F. Syljuåsen and A. W. Sandvik, Phys. Rev. E **66**, 046701 (2002).

[225] O. F. Syljuåsen, Phys. Rev. E **67**, 046701 (2003).

[226] K. Harada and N. Kawashima, Phys. Rev. E **66**, 056705 (2002).

[227] N. Prokof'ev and B. Svistunov, Phys. Rev. Lett. **87**, 160601 (2001).

[228] N. Prokof'ev, B. Svistunov, and I. Tupitsyn, Phys. Lett. A **238**, 253 (1998).

[229] A. W. Sandvik, Phys. Rev. Lett. **95**, 207203 (2005).

[230] A. W. Sandvik and H. G. Evertz, Phys. Rev. B **82**, 024407 (2010).

[231] E. Farhi and S. Gutmann, Ann. Phys. **213**, 182 (1992).

[232] J. Hoshen and R. Kopelman, Phys. Rev. B **14**, 3438 (1976).

[233] N. Kawashima and J. E. Gubernatis, Phys. Rev. Lett. **73**, 1295 (1994).

[234] J. V. Alvarez and C. Gros, Eur. Phys. J. B **15**, 641 (2000).

[235] S. Todo, M. Matsumoto, C. Yasuda, and H. Takayama, Phys. Rev. B **64**, 224412 (2001).

[236] F. Cooper, B. Freedman, and D. Preston, Nucl. Phys. B **210**, 210 (1982).

[237] W. Janke, in *Computational Many-Particle Physics*, edited by H. Fehske, R. Schneider, and A. Weiße (Springer, Berlin, 2008), vol. 739 of *Lect. Notes Phys.*, pp. 79–140.

[238] B. Efron and R. J. Tibshirani, *An Introduction to the Bootstrap* (Chapman and Hall, Boca Raton, 1998).

[239] M. E. J. Newman and G. T. Barkema, *Monte Carlo Methods in Statistical Physics* (University Press, Oxford, 1999).

[240] K. Binder, Phys. Rev. Lett. **47**, 693 (1981).

[241] K. Binder, Z. Phys. B **43**, 119 (1981).

[242] A. M. Ferrenberg and D. P. Landau, Phys. Rev. B **44**, 5081 (1991).

[243] F. J. Wegner, Phys. Rev. B **5**, 4529 (1972).

[244] V. Privman and M. E. Fisher, J. Phys. A **16**, L295 (1983).

[245] M. Henkel, S. Andrieu, P. Bauer, and M. Piecuch, Phys. Rev. Lett. **80**, 4783 (1998).

[246] C. N. Yang and C. P. Yang, Phys. Rev. **150**, 321 (1966).

[247] C. N. Yang and C. P. Yang, Phys. Rev. **150**, 327 (1966).

[248] J. L. Cardy, J. Phys. A **19**, L1093 (1986).

[249] N. Karbach and G. Müller, Comp. Phys. **11**, 36 (1997).

[250] N. Karbach, K. Hu, and G. Müller, Comp. Phys. **12**, 565 (1998).

[251] M. Weigel and W. Janke, Phys. Rev. Lett. **102**, 100601 (2009).

[252] M. Weigel and W. Janke, Phys. Rev. E **81**, 066701 (2010).

[253] L. A. Fernandez, A. Gordillo-Guerrero, V. Martin-Mayor, and J. J. Ruiz-Lorenzo, Phys. Rev. E **80**, 051105 (2009).

[254] A. W. Sandvik, Phys. Rev. B **56**, 11678 (1997).

[255] F. Alet and E. S. Sørensen, Phys. Rev. B **70**, 024513 (2004).

[256] D. Friedan, Z. Qiu, and S. Shenker, Phys. Rev. Lett. **52**, 1575 (1984).

[257] M. Führinger, S. Rachel, R. Thomale, M. Greiter, and P. Schmitteckert, Ann. Phys. **17**, 922 (2008).

[258] H. Bergknoff and H. B. Thacker, Phys. Rev. D **19**, 3666 (1979).

[259] K. Okamoto, J. Phys. Soc. Jpn. **56**, 912 (1987).

[260] H. Nishimori and K. Okamoto, J. Phys. Soc. Jpn. **56**, 1132 (1987).

[261] M. T. Batchelor, M. N. Barber, and P. A. Pearce, J. Stat. Phys. **49**, 1117 (1987).

[262] L. N. Shchur, B. Berche, and P. Butera, Eur. Phys. Lett. **81**, 30008 (2008).

[263] F. Jin, Z. Xu, H. Ying, and B. Zheng, J. Phys. Cond. Mat. **17**, 5541 (2005).

[264] S. Wessel and S. Haas, Phys. Rev. B **65**, 132402 (2002).

[265] N. Laflorencie, H. Rieger, A. W. Sandvik, and P. Henelius, Phys. Rev. B **70**, 054430 (2004).

[266] C. Yasuda, S. Todo, and H. Takayama, J. Phys. Soc. Jpn. **75**, 124704 (2006).

Bibliographische Beschreibung:

Bischof, Rainer
Gaussian Critical Line in Anisotropic Mixed Quantum Spin Chains
Universität Leipzig, Dissertation
252 S., 266 Lit., 89 Abb., 57 Tab.

Referat:

Das Interesse an niedrig-dimensionalen Quantenspinmodellen, und besonders an Quantenspinketten, hat eine lange Geschichte. Über die theoretische Bedeutung als fundamentale Beschreibung von quantenmagnetischen Phänomenen hinaus, reicht die Relevanz von der Modellierung von Hochtemperatur-Supraleitern über die Strukturchemie bis hin zum Quantencompouter und der theoretischen Untersuchung der Verschränkungsentropie. Im Speziellen wurden antiferromagnetisch gekoppelte, gemischte Spin-Dimere als Qubits für Quantencomputer vorgeschlagen. Zahlreiche Neuerungen in der numerischen Behandlung von Vielteilchensystemen wurden durch das Interesse an Quantenspinmodellen ausgelöst. Ein Meilenstein im Verständnis von Quantenspinketten war die exakte Lösung des 2-dimensionalen klassischen 8-Vertex Modells, welches in die anisotrope Quantenspinkette mit $S = 1/2$ transformiert werden kann. Für homogene Spinketten mit $S \geq 1$ existieren zahlreiche numerische und theoretische Arbeiten, jedoch keine exakt Lösung. Gemischte Quantenspinketten hingegen wurden bisher nur spärlich untersucht.

In der vorliegenden Arbeit werden, mittels numerischer Methoden, zwei spezifische Modelle anisotroper gemischter Quantenspinketten, bestehend aus Spins zweier unterschiedlicher Größen, $S^a = 1/2$ und $S^b = 1$ sowie $S^b = 3/2$, hinsichtlich ihrer kritischen Eigenschaften an Quanten-Phasenübergängen in einem ausgewählten Parameterbereich untersucht. Die Quantenspinketten sind aus Basiszellen zu vier Spins, gemäß der Struktur $S^a - S^a - S^b - S^b$, aufgebaut. Sie werden durch den XXZ Hamiltonoperator beschrieben, der das isotrope Quanten-Heisenberg Modell um eine variable anistrope Austauschwechselwirkung erweitert. Als zusätzlicher Kontrollparameter wird eine alterniernde Kopplungskonstante zwischen unmittelbar benachbarten Spins eingeführt. Die durch komplementäre Anwendung exakter Diagonalisierung und Quanten-Monte-Carlo Simulationen, sowie entsprechender Analyseverfahren, gewonnenen Erkenntnisse werden in das umfangreiche existierende Wissen über homogene Quantenspinketten eingebettet. Im Speziellen treten in anisotropen homogenenen Quantenspinketten Phasengrenzen mit kontinuierlich variierenden kritischen Exponenten auf, die *Gaußschen kritischen Linien*, auf denen neben den herkömmlichen auch erweiterte Skalenrelationen Gültigkeit besitzen. Umgewichtungsmethoden, speziell auch angewandt auf verbesserte Quanten-Monte-Carlo Schätzer, und Endlichkeitsskalenanalyse von Simulationsdaten liefern eine Fülle von numerischen Ergebnissen, die das Auftreten der Gaußschen kritischen Linie auch in den untersuchten gemischten Quantenspinketten bestätigen. Die Extrapolation exakter Daten bietet, neben der Bestätigung der Simulationsdaten, darüber hinaus Einblick in einen Teil des konformen Operatorinhalts des Modells mit $S^b = 1$.